2nd European sCO2 Conference 2018

DOI: https://doi.org/10.17185/duepublico/46074

URN: urn:nbn:de:hbz:464-20180912-120000-0

Link: https://duepublico.uni-duisburg-essen.de:443/servlets/DocumentServlet?id=46074

Conference Proceedings of the

2nd European sCO2 Conference 2018

Location:
Kraftwerksschule e.V. (KWS),
Deilbachtal 199,
45257 Essen, Germany

Date: 30-31 August 2018

Coordinator

Prof. Dr.-Ing. Dieter Brillert
University of Duisburg-Essen
Faculty of Engineering
Chair of Turbomachinery
Lotharstr. 1
D-47057 Duisburg
Email: sCO2@uni-due.de

Project Management Office

European Project Office Rhein-Ruhr
University of Duisburg-Essen
Science Support Centre
Universitätsstr. 2
D-45141 Essen
Email: maria.gies@uni-due.de

Imprint

Conference Proceedings of the 2nd European sCO2 Conference

ISSN 2510-7852

DOI 10.17185/duepublico/46074

URN: urn:nbn:de:hbz:464-20180912-120000-0

DuEPublico, Duisburg-Essen Publications Online
Universität Duisburg-Essen
http://duepublico.uni-duisburg-essen.de

2018

Agenda 30th August 2018

11:00 – 12:00	Welcome reception including lunch (KWS building)
12:00 – 12:20	Welcome note by Dieter Brillert and group photo
12:20 – 12:50	Keynote speech by Albannie Cagnac, Electricité de France (EdF)

13:00 – 14:30 sCO2-cycles and their applications (session 1)

Vojacek, Ales; Frybort, Otakar; Hacks, Alexander:
First Operational Experience From The Supercritical CO2 Experimental Loop
Noaman, Mohamed B.; Morosuk, Tatiana; Tsatsaronis, George:
Economic Forecasting For Solar-Energy Assisted Supercritical CO2 Brayton Cycle
Flaig, Wolfgang; Mertz, Rainer; Starflinger, Jörg:
Design, Control and Start-up of the sCO2 Test Facility Scarlett

13:00 – 14:30 Compressor / Turbine / Generator (session 2)

De Miol, Maxence; Bianchi, Giuseppe; Henry, Gabriel; Holaind, Norman; Tassou, Savvas A.; Leroux, Arthur:
Design Of A Single-Shaft Compressor, Generator, Turbine For Small-Scale Supercritical CO2 Systems For Waste Heat To Power Conversion Applications
Hacks, Alexander Johannes; Vojacek, Ales; Dohmen, Hans Josef; Benra, Friedrich-Karl; Brillert, Dieter:
Experimental Investigation of the sCO2-HeRo Compressor
Hacks, Alexander Johannes; Dohmen, Hans Josef; Benra, Friedrich-Karl; Brillert, Dieter:
Scaling Considerations for the Application of the sCO2-HeRo System in Nuclear Power Plants

14:30 – 15:00 Coffee break

15:00 – 16:30 sCO2-cycles and their applications (session 3)

Glos, Stefan; Schlehuber, Dominic; Wechsung, Michael; Wagner, Rebecca; Heidenhof, Andre:
Evaluation of sCO2 power cycles for direct and waste heat applications
Hájek, Petr; Vojacek, Ales; Hakl, Vaclav:
Supercritical CO2 Heat Removal System, - Integration into European PWR Fleet
Gampe, Uwe; Henoch, Jasmin; Gerbeth, Gunter; Hampel, Uwe; Hannemann, Frank; Rath, Sebastian:
Concept And Preliminary Design Of A 600 °C+ sCO2 Test Facility

15:00 – 16:30 Compressor / Turbine / Generator (session 4)

Kim, Min Seok; Oh, Bong Seong; Jung, Hwa-Young; Bae, Seong Jun; Lee, Jeong Ik:
Comparison of CO2 Critical Flow Model Based on Henry-Fauske Model with Two-phase Flow

Oh, Bong-Seong; Kim, Seong Gu; Cho, Seong Kuk; Bae, Seong Jun; Lee, Jeong Ik_
Start Up Modeling of S-CO2 Cycles Using Beta Line Method Of Turbomachinery Performance Map

Gregor, Klemencic; Werner, Andreas; Leibinger, Helmut; Steinschaden, Norbert; Nowack, Tim; Flegkas, Stylianos; Haider, Markus; Fellner, Thomas; Bergthaller, Thomas
Design and dynamic simulation of a 200 kwth laboratory sCO2-test rig

16:30 – 17:30 sCO2-HeRo lab tour (glass model)

19:00 – 22:30 Conference Dinner at “Brauerei Dampfe”

Agenda 31th August 2018

09:00 – 10:00 sCO2-cycles and their applications (session 5)

Weiland, Nathan T.; White, Charles W.; O'Connell, Andrew C:
Effects of Cold Temperature and Main Compressor Intercooling on Recuperator and Recompression Cycle Performance

Mecheri, Mounir:
Flow and Heat Transfer Characterization for Supercritical
CO2 During Heat Rejection

09:00 – 10:00 Heat transfer and heat exchanger (session 6)

Straetz, Marcel Ralf; Mertz, Rainer; Starflinger, Jörg:
Experimental Investigation On Heat Transfer Between Condensing Steam And sCO2 In Compact Heat Exchangers

Pandey, Sandeep; Laurien, Eckart; Chu, Xu:
Sco2 Closed Brayton Cycle For Coal-Fired Power Plant: An Economic Analysis Of A Previous Technical Optimization

10:00 – 10:30 Coffee break

10:30 – 12:00 sCO2-cycles and their applications (session 7)

Otero-Rodriguez, Gustavo; Patel, Ashish; Pecnik, Rene:
A Novel Approach To Accurately Model Heat Transfer To Supercritical Fluids

Buck, Reiner; Giuliano, Stefano:
Impact of CSP Design Parameters on sCO2-based Solar Tower Plants

Shah, Amit; Trivedi, Yagneshkumar; Dave, Ashish Kumar; Chauhan, Haresh; Patel, Kishan; Dave, Punitkumar; Mehta, Vishal:
Feasibility Study Of Supercritical Co2 Rankine Cycle For Waste Heat Recovery*

10:30 – 12:00 Heat transfer and heat exchanger (session 8)

Baik, Seungjoon; Lee, Jeong Ik:
Preliminary Experimental Study Of CO2 Based Mixture Supercritical Power Cycle

Lazova, Marija; De Paepe, Michel:
Investigating the heat transfer characteristics of supercritical HFC-125 in low temperature organic Rankine cycle

12:00 – 13:00 Lunch incl. some take away

* cancelled participation

Papers

2nd European supercritical CO2 Conference
August 30-31, 2018, Essen, Germany

2018-sCO2.eu-100

CHALLENGES IN SUPERCRITICAL CO2 POWER CYCLE TECHNOLOGY AND FIRST OPERATIONAL EXPERIENCE AT CVR

Ales Vojacek*
Research Centre Rez
Rez, Czech Republic
Email: ales.vojacek@cvrez.cz

Alexander Hacks
Universität Duisburg-Essen
Duisburg, Germany

Tomas Melichar
Research Centre Rez
Rez, Czech Republic

Otakar Frybort
Research Centre Rez
Rez, Czech Republic

Petr Hajek
Research Centre Rez
Rez, Czech Republic

ABSTRACT

CVR, Research Centre Rez, Czech Republic, is investigating advanced Brayton cycles using supercritical CO_2 (sCO_2) as working fluid, which has potential for high thermodynamic efficiency of a power plant. This innovative technology needs to be demonstrated and experimentally proven by numerous tests. For this purpose, CVR has built a sCO_2 experimental loop within Sustainable Energy project (SUSEN). This unique facility is flexible, modifiable and suitable for performance testing of key components of sCO_2 conversion cycles such as compressor, turbine, heat exchanger and valves together with material research with wide range of parameters: temperature up to 550°C, pressure up to 30 MPa and mass flow rate up to 0.35 kg/s. This paper covers literature survey on major challenges in sCO_2 development and the design of the loop with description of key components. The first operational experience is given as well as the discussion on the measured data set. Finally, it is outlined how the sCO_2 loop is involved in various research projects such as sCO_2-HeRo project (heat removal safety back-up system for LWR) for testing of sCO_2 turbomachine (TAC) and air sink heat exchanger (sink HX).

INTRODUCTION

In pursuit of inventing effective ways of generating electricity, researchers are experimenting with different working fluids as an alternative to the conventional water-steam in energy conversion cycles. Such a fluid is e.g. supercritical CO_2 and the idea of applying it in energetics using Brayton cycle is far not new. The advantages of the sCO_2 are coming from its real gas properties have been outlined and discussed during the 60's [1]-[2]. Over the past several decades there has been a prolific increase in research and development that make deployment of the sCO_2 systems more likely. Number of institutions have built their sCO_2 facility. Most of them are focusing on heat transfer (HT) near the critical region (7.4 MPa, 31°C) in simple circular heated geometries. First experimental data are dated to 60's. The very first HT research in sCO_2 was performed in USA and in former Soviet Union [3]-[4]. An exhaustive literature survey on an early research on supercritical HT is reported in [5]. Recently built experimental loops for sCO_2 HT investigation near pseudo-critical point found in literature are summarized in Annex A [6]-[16]. The main motivation of these facilities is to deliver new HT correlations, which could be transferred for the supercritical water as both media show similarities in pseudo-critical region and the parameters can be scaled from one supercritical media to another like proposed in [17] and [18]. To develop such a facility for sCO_2 is more economical than for water where the critical point is much higher (22.1 MPa, 374°C). Heat transfer at the supercritical pressure is very different from that at the subcritical pressure due to the drastic variations of the physical properties of fluids at around the pseudo-critical temperature. In addition, at heating sections oriented vertically with upward flow, the buoyancy effect reduces turbulence and shear stress causing heat transfer deterioration (HTD) [17]. The supercritical water enhances the efficiency of the fossil-fuel power plants already and supercritical water reactor design is part of the future nuclear reactors concepts (Generation IV). In such technologies, the problematic pseudo-critical point of water is being crossed in a heat source, i.e. boiler or nuclear reactor. Hence, HT become of great importance since HTD could lead to fuel overheating and in the worst case to core

DOI: 10.17185/duepublico/46075

meltdown. However, this is not the case for the sCO_2 energy applications. In the sCO_2 Brayton cycle, the pseudo-critical point will be crossed in a cooler. As far as for the HT, the heat transfer deterioration or enhancement would only lead to underestimated or overestimated size of the cooler, potentially decreasing/increasing the overall thermodynamic efficiency of the conversion cycle.

A number of researchers [19]-[43] have investigated heat transfer in the coolers using sCO_2 as an effective alternative refrigerant (in air-conditioning and heat pump systems using trans-critical cycles) to conventional substances such as chlorinated and fluorinated hydrocarbons, which are much more harmful to the environment and destroy the ozone layer. The very first research on HT is dated back to 1937 and was conducted in Germany. From the studies, it can be concluded that heat transfer is enhanced greatly in the near-critical region, with a maximum heat transfer coefficient occurring at the corresponding pseudocritical temperature and the maximum heat transfer coefficient decreases as the pressure increases. No HTD in the sCO_2 was found in literature. The experimental work on coolers in sCO_2 is shown in Annex B.

The sCO_2 Brayton cycle architecture has been largely studied since the choice of recommended cycle configuration is far not straightforward. Researchers are conducting theoretical studies on numerous sCO_2 configurations such as condensation, simple Brayton, precompression, recompression, split expansion, partial cooling, cascade, simple re-heat, double re-heat cycles [44]. For waste heat recovery application with sensible heat (e.g. flue gas combustion cycle), bottom cycle is needed to maximize the usable power. Various cascade like cycles are recommended [45]. However, the recompression cycle (operating at pressures of 20-25 MPa maximum temperature of 650°C) is perceived as the most promising cycle layout for the heat flux sources applications such as nuclear and solar power plants [46]. This is owing to the fact that the pinch point problem in the recuperator is in recompression cycle prevented by the lower mass flow at high pressure side of the low temperature recuperator, hence the heat capacity mass flow on both sides are equal and recuperation is prolonged. In order to prevent large HXs volume the introduction of effective compact HXs has to come in place to enable achieving a high degree of regeneration with recuperators of reasonable cost. The most compact of those presently available are Printed Circuit Heat Exchangers (PCHX) and they can be utilized in Brayton cycle as coolers (cooled by water for instance, but not by air because of too high pressure drop), yet more importantly as recuperators. This new type of HX has been developed by Heatric Pty Ltd over the last few decades [47]. Flat plates are photochemically etched with heat-transfer passages and then diffusion bonded together to form a solid block which can withstand high pressure and high temperature (700°C at 80 MPa/800°C at 35 MPa for Inconel 617 [48], 600°C at 20 MPa [49]) unlike the finned plate HX. A unique channel design requires optimization to maximize heat transfer while minimizing pressure drop. Based on the literature survey, the surface geometries of PCHXs can be categorized as either continuous or discontinuous-fin surfaces. Continuous fin surfaces include straight, sinusoidal, and zig-zag channels, while discontinuous surfaces include louver, S-shaped, and airfoil fin geometries. The experimental work performed in PCHX with sCO_2 is summarized in Annex C [50]-[58]. A comparison of a straight, two different zig-zag (40°/32.5° angle) and two types of airfoil (4/8.1 mm length) channel geometries at nearly equivalent cross-sectional area ratios have been made [55]. Based on this study, two airfoil geometries appear to perform much better than the zig-zag geometries, provided almost the same thermal performance with hydraulic losses reduced to almost the level of equivalent hydraulic straight channel.

The next task and likely the most challenging one is the sCO_2 turbomachinery design. The turbomachinery components claims to be highly compact due to significant power densities resulting in economically attractive solution. Sandia National Laboratory [59] has begun testing of sCO_2 compressors and turbines of power of few hundreds of kWe with poor efficiencies. The isentropic/polytrophic efficiencies of most power turbomachines increase with size and so does the sCO_2 machines. Hence, there is a need for bigger scale demonstrator in multi-MWe range in order to move the concept closer to market. Echogen [60] has developed sCO_2 10 MWe heat engine technology for waste heat recovery. However, there seems to be still some open issues, since they claim to have reached just 3 MWe for limited period of time. Within the SunShot program funded by Department of Energy, GE together with Southwest Research Institute aims to develop 10 MWe recompression sCO_2 cycle for CSP. In advance, they have built a simple recuperated Brayton cycle to test 1 MWe turbine [61]. There are several areas in which additional research is needed in order to make the sCO_2 cycle commercially viable. The impeller, diffusor and diaphragm need an advanced design to reach good efficiency and cope with the highly non-ideal behavior of the sCO_2 close to the critical point, possibly choked and two-phase flow conditions. Proper sealing is a key issue. Due to high pressure differences and design limitations (axial lengths) the labyrinth seals are not suitable. The dry gas seals are considered to have the best performance. The design of bearings to balance the thrust loads is challenging. Gas-foil thrust and journal bearings seem to be suitable option. They are widely used in small scale machines. However, the applicability for large scale machines needs to be tested. The rotation speed of sCO_2 turbomachines of 10 MW will likely be few times higher the standard 3000 rpm. Hence, design of gear box or high speed generators is required. If a shaft from a turbine is sealed, e.g. by dry gas seal, then commercial products of high speed generators/gear boxes are available.

Attractive thermal efficiencies of sCO_2 are reached at pressures as high as 25 MPa and temperatures as high as 650°C. Hence, material research is being conducted. Large number of corrosion data has been gained in University of Wisconsin. The corrosion behavior of commercial austenitic steels 800H and

DOI: 10.17185/duepublico/46075

AL-6XN and ferritic-martensitic steels F91 and HCM12A exposed to sCO_2 at 650°C and 20.7 MPa for up to 3000 hours was studied [55] with positive results. Further testing with various austenitic/ferritic steels is planned at CVR, Czech Republic and in Centro Sviluppo Materiali Spa, Italy, within the European H2020 project sCO2-Flex for 25MWe sCO_2 Brayton cycle coaled powered development.

A reliable operation of the sCO_2 Brayton cycle requires to carefully study the stability and control. The development and validation models that are capable of predicting operational performance characteristics in sCO_2 are important. Currently, there a few sCO_2 experimental loops equipped well enough to demonstrate sCO_2 Brayton cycle or at least a most part of it. It includes Echogen (waste heat recovery system, planned 10 MWe), SunShot (Simple recuperated cycle, 1 MWe and recompression cycle 10 MWe planned) Sandia National Laboratory (full Brayton recompression cycle, few hundreds of kWe reached), SCIEL loop in KAIST, South Korea (cycle for compressor testing, rest of the Brayton cycle on the way, few hundreds of kWe planned) and CVR, Czech Republic (Brayton cycle with piston pump and turbine substituted by reduction valve, 110 kW heat power). The experimental work performed in integral sCO_2 loops is summarized in Annex D [61]-[63].

CVR SCO2 EXPERIMENTAL LOOP DESCRIPTION

The sCO2 experimental loop was constructed within SUSEN (Sustainable Energy) project in 2017. This unique facility enables component testing of sCO2 Brayton cycle such as compressor, turbine, HX, valves and to study key aspects of the cycle (heat transfer, erosion, corrosion etc.) with wide range of parameters: temperature up to 550°C, pressure up to 30 MPa and mass flow rate up to 0.35 kg/s. The loop is designed to represent sCO_2 Brayton cycle behavior.

Annex E shows the piping and instrument diagram (PID) of the loop. The primary circuit is marked in thick red and it consists of following main components:

- The main pump (piston type), which circulates sCO_2 through the cycle with the variable speed drive for the flow rate control.
- The high and low temperature regenerative heat exchanger (HTR HX/LTR HX), which recuperates the heat, hence reduce the heating and cooling power.
- The 4 electric heaters (H1/1, H1/2, H2, H3), which have in total a maximum power of 110 kW and raise the temperature of sCO_2 to the desired test section (TS) inlet temperature up to 550°C.
- The reduction valve which consists of series of orifices to reduce the pressure and together with oil cooler (CH2) represent a turbine. Nominal temperature of oil (Marlotherm SH) is 140°C and flow rate is 0.4 kg/s. The oil is used due to the high temperatures of the exhaust heat (up to 550°C).
- The water cooler (CH1) cools down the sCO_2 at the inlet of the MP by water (nominal temperature 20°C, 1.4 kg/s flow rate of water).
- Air driven filling (reciprocating) compressor (gas booster station) which pumps the sCO_2 from the CO_2 bottles and also controls the operating pressure (the main parameters listed in Table 1).

Table 1: Parameters of the filling compressor.

Device	Filling compressor - DLE5-15-GG-C
Nominal inlet pressure of CO_2	0.5 MPa
Nominal outlet pressure	6.5 MPa
Maximum outlet pressure	30 MPa
Nominal flowrate	15 l_N/min
Nominal air pressure	0.6 MPa

The dashed blue line at the PID stands for the air cooled finned-tube sink HX testing layout and the green dash-and-dot line marks the modification for the turbomachinery performance testing.

The main operating parameters of the primary circuit are shown in Table 2.

Table 2: The main operating parameters of the sCO2 primary loop.

Maximum operation pressure	25 MPa
Maximum pressure	30 MPa
Maximum operation temperature	550°C
Maximum temperature in HTR	450°C
Maximum temperature in LTR	300°C
Nominal mass flow	0.35 kg/s

The sCO_2 loop layout is depicted in Figure 1 and the top view of the built facility is shown in Figure 2.

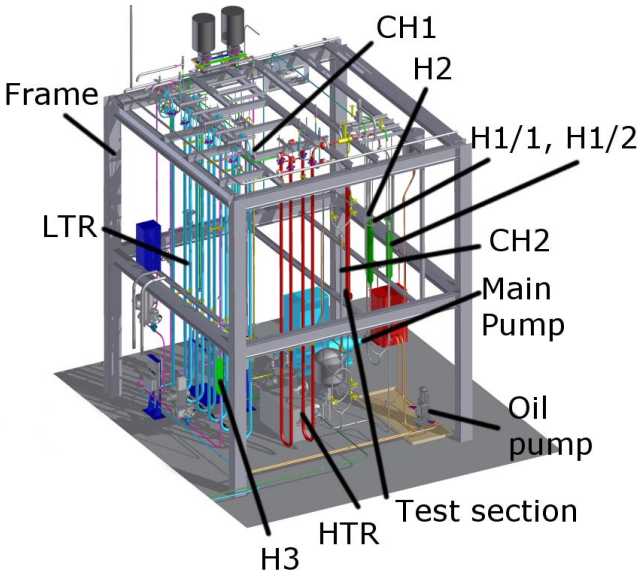

Figure 1: 3D CAD model of the sCO_2 loop.

DOI: 10.17185/duepublico/46075

Figure 2: A view from the top to the built sCO_2 loop.

Table 3 summarize parameters of MP and the schematic cross-section of MP is shown in Figure 3.

Table 3: Parameters of the main pump.

Device	Main Pump - PAX-3-30-18-250-YC-CRYO-drive 9/FM
Nominal inlet pressure	12.5 MPa
Nominal outlet pressure	25 MPa
Maximal outlet pressure	30 MPa
Nominal inlet temperature	25°C
Maximum inlet temperature	50°C
Nominal isentropic efficiency	0.7
Rotational speed	250÷1460 rpm
Volumetric flowrate	5÷30 l/min.

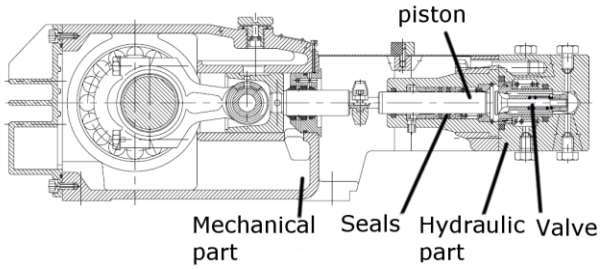

Figure 3: Cross-section of main pump.

The component geometry of the sCO_2 loop is described in Table 4.

Table 4: Component geometry of the sCO_2 loop

HTR + LTR (counter-flow shell and tube-type from SS)	Length of HTR = 20 m, Length of LTR = 60 m, Number of internal tubes = 7, Internal tube Ø 10 x 1.5 mm, Shell Ø 50 x 5 mm.
H1/1 + H1/2 (30 + 30 kW) (from SS)	Length = 0.95 m, Number of heating rods = 2 x 6, Diameter of a heating rod = 8 mm, Shell Ø 100 x 20 mm
H2 (30 kW) (from Inconel 625)	Length = 0.95 m, Number of heating rods = 2 x 6, Diameter of a heating rod = 8 mm, Shell Ø 73 x 6.5 mm
H3 (20 kW) (from SS)	Length = 0.75 m, Number of heating rods = 2 x 6, Diameter of a heating rod = 8 mm, Shell Ø 100 x 20 mm
CH1 (counter-flow shell and tube-type from SS)	Length = 7.5 m, Number of internal tubes = 7, Internal tube Ø 10 x 1.5 mm, Shell Ø 43 x 1.5 mm
CH2 (counter-flow shell and tube-type from Inconel 625/SS)	Length = 1.8 m, Number of internal tubes = 7, Internal tube Ø 10 x 1.5 mm, Shell Ø 43 x 1.5 mm
TS (from Inconel 625)	Length = 1.5 m, Shell Ø 73 x 6.5 mm
Pipeline from MP to T-junction LTR by-pass	Length = 4m, Tube Ø 22 x 4 mm
LTR by-pass	Length = 7 m, Tube Ø 22 x 4 mm
Pipeline from T-junction LTR by-pass to LTR	Length = 6 m, Tube Ø 22 x 4 mm
Pipeline from CH1 to MP	Length = 8 m, Tube Ø 20 x 3 mm

The electrical heater H3 with nominal power 20 kW is positioned at the bypass of the LTR in order to simulate the behavior of a recompression cycle.

OPERATIONAL PROCEDURES WITH SCO2 LOOP

The very first procedure necessary before starting-up the loop is vacuuming. It not only enables to eliminate all atmospheric gases, but also helps to remove unwelcome moisture. The system includes a vacuum pump which provides 20 kPa absolute pressure and is connected to an exhaust system to ambient. The loop is equipped with several joints from which it is possible to suck contaminants. The advantage is in an effective and economic handling of the CO_2 content. While some part of the loop needs to be opened and discharged the rest can stay full. In order to intensify the cleaning technique the CO_2 is let into the loop. The desired purity is checked by sampling. To assure that the loop is gas tight the created negative pressure should stay constant for several hours (obviously with vacuum pump switched-off).

The next process is the filling. To fill the loop with the required mass to achieve operating conditions, CO_2 vapor from

DOI: 10.17185/duepublico/46075

a standard pressurized bottle (where 2 phase CO_2 is stored) is introduced just before the water cooler CH1. The loop is initially filled quite quickly due to the high pressure difference in the bottle and the loop (approx. 60 bars). However, as the pressure in the system rises and the bottle content is decreasing, the process slows down. Hot air is used to heat up the bottle to speed up the filling. The weight of the bottle is measured in order to know how many CO_2 goes in. When a fixed mass based on model predictions gets near the normal operating mass which in our case is around 40 kg of CO_2 then the main circulation pump can start circulating the CO_2 content around. To adjust (increase) the pressure in the system the heaters are switched on. The maximum limit of 50 K/h temperature increase is controlled. As the system heats up and pressure rises the mass flow rate increases since the density at the inlet to the MP increases. If further mass adjustments are needed to reach desired parameters the air driven reciprocating compressor is used to boost the CO_2 to the loop and reducing the pressure can be performed through opening the bleeding valves with orifices installed in the pipe. For setting the inlet temperature to the MP a speed of a water pump is adjusted to control the water flow rate through the CH1 cooler.

The operation of the loop is controlled by the MP speed drive. Flow rate sCO_2 measured with a coriolis flow meter. It is possible to adjust the flow rate through the LTR by-pass so to simulate recompression cycle, as well as to adapt flow rate through the CH2 (simulating the turbine heat power release). The loop is divided into the low and high pressure part. The separation is performed by the reduction valve. The pressure in both parts is adjusted by the opening position of the valve.

To protect the loop against over pressure several pressure relief valves are installed at positions, where increase of pressure might occur. These are e.g. the heating parts equipped with closing valves both at the inlet and outlet as well as the pump.

The shut-down procedure is performed through the heating power control. The 50 K/h temperature change should be satisfied to bring the loop to the cold state (20°C). If there is a need for a repair the necessary part or the whole loop is evacuated trough the release valves and system of orifices to slow down the pressure change.

UTILIZATION OF THE CVR SCO2 LOOP

The CVR sCO_2 loop is involved in various research projects for testing of materials and equipment of the Brayton conversion cycle.

The CVR with 9 other European partners is involved in sCO_2-Flex project (2018-2020), where the main components of a 25 MWe Brayton cycle (boiler, HX, turbomachinery, instrumentation and control strategies) are being designed and optimized. The CVR role is to provide material tests, thermal-hydraulic tests of HXs (PCHXs and FPHX) and perform several design/off-design and abnormal operation to provide sufficient data for computational codes validation.

Within the European H2020 project sCO_2-HeRo (2016-2018) [64], six partners from three European countries are working on the assessment of this cycle. The goal is to numerically and experimentally prove the concept on a small-scale demonstrator which shall be incorporated in the PWR glass model at the Simulator Centre GfS in Essen, Germany. The sCO_2-HeRo is a system for safe, reliable and efficient removal of residual heat from nuclear fuel without the requirement of external power source.

Before assembling the small sCO_2-HeRo system in the GfS, each major component was tested in different institutions. The performance of the compact HX (micro channel type) was verified in the sCO_2 test loop (SCARLETT) in University of Stuttgart, while the air-cooled sink HX, compressor and turbine were measured in the CVR sCO_2 experimental facility.

Due to high flexibility of the loop layout, the loop might be easily modified and therefore can provide wide range of conditions for various experiments in terms of the operational parameters, geometry of test sections or thermal cycle simulations.

AIR COOLED SINK HEAT EXCHANGER TESTING

The heat transfer investigations in the air cooled sCO_2 finned-tube sink HX test configuration took place at CVR (Figure 4). Annex E shows the piping and instrument diagram (PID) of the sCO_2 loop and the dashed blue line stands for the sink HX testing modification to the existing loop.

Figure 4: The sink HX with measurements.

The nominal thermodynamic parameters of sink HX are shown in Table 5.

Table 5: Thermodynamic parameters of sink HX

pressure of sCO2 inlet to sink HX	7.83 MPa
temperature of sCO2 outlet of sink HX	33.0°C
temperature of sCO2 inlet to sink HX	166.0°C

DOI: 10.17185/duepublico/46075

mass flowrate of sCO2	0.325 kg/s
thermal power of sink HX	92.5 kW
temperature of air inlet to sink HX	25.0°C
temperature of air outlet of sink HX	50.0°C
volumetric flowrate of air outlet	12500.0 m^3/h
electric power of EC fans	0.33 kW

The measurement campaigns covered both supercritical and subcritical regions including transition through the pseudocritical region in the last stages of the sink HX. The critical point of the CO_2 is 7.39 MPa and 31.1°C. The controlled (independent) and resulted (dependent) parameters are summarized in Table 6.

Table 6: The main controlled and measured parameters for the performance tests

7 – 10 MPa	Pressure – inlet of sCO_2 in the sink HX – controlled
50 – 166°C	Temperature of sCO2 inlet to the sink HX – controlled
25 – 37°C	Temperature of sCO2 outlet from the sink HX – measured
0.1 – 0.32 kg/s	Mass flow rate of the sink HX – controlled
23 – 31°C	Temperature of air inlet to the sink HX – *controlled
31 – 65°C	Temperature of air outlet from the sink HX – measured
6 000 – 13 000 m^3/h	Volumetric flow rate of air outlet from the sink HX – controlled

* depends on the actual ambient temperature.

The experimentally determined heat balances from the measured parameters on both sides (sCO2 and air) are in fair agreement (±15 %) with each other which demonstrate good quality measurement. The results of calculated averaged overall heat transfer coefficients using correlations (Gnielinsky [65] for sCO_2 and IPPE [66] or VDI [67] for the air) and experimentally determined values shows for the performed tests reasonably low error of + 25 % and – 10 %. Hence, using the correlations for the estimation of the heat transfer in the sink HX with a similar design and similar conditions gives a fair error and thus is recommended. Utilizing the measured data with look-up tables for the HT of the sink HX is rather complicated to program. The analyzed correlations for heat transfer on the air side according to IPPE and VDI are in perfect match with each other. More detailed discussion of the performance is presented in the paper of Vojacek et al. [68].

TURBOMACHINE TESTING

The sCO_2 experimental loop is easy to modify and was thus used for two purposes in the sCO_2-HeRo project. After the component test of the heat sink it was also used for TAC testing. For TAC testing the sCO_2 experimental loop was redone in a way that the expansion valve was replaced with the turbine and the main pump (MP) with the compressor. The MP was then used for leakage feedback to regulate the pressure in the central housing around the bearings and the generator. The heater and recuperator arrangement was adjusted in a way that one of the recuperators (LTR) was bypassed. The reason is the lower inlet temperature of the turbine, which lies well below the cycle maximum temperature of 650 °C, and the resulting lower heating power. The complete thermodynamic design parameters of the sCO_2-HeRo TAC are summarized in Table 7. The TAC has an integrated design with turbine, generator and compressor in one casing. Thus, its general layout is similar to turbomachines of other small scale sCO2 test cycles such as the SNL RCBC, IST, TIT or SCIEL cycle, which are presented in the book of Brun et al. [61]. Mayor difference to the turbomachines of these cycles is, that the sCO2-HeRo cycle mass flow is even smaller (see Table 7). For detailed information on the TAC design please refer to Hacks et al. [69].

Table 7: Design parameters of the TAC

Component	**Parameter**	**Value**
Cycle	Mass flow	0.65 kg/s
Compressor inlet	Pressure	78.3 MPa
	Temperature	33 °C
Compressor outlet	Pressure	11.75 MPa
Turbine inlet	Pressure	11.75 MPa
	Temperature	200 °C
Turbine outlet	Pressure	7.83 MPa

Goals of the first component tests of the turbomachine in the modified loop are as follows:

- Gain experience in operating an sCO2-loop with a TAC
- Comparison of the predicted TAC behavior with the real behavior.
- Finding of a suitable strategy for turbomachine start-up and setting the operation point
- Measuring of the performance maps and comparison to the calculated performance

Prior to start-up of the TAC the cycle is brought to supercritical conditions by using the MP to circulate CO_2 through the cycle. The CO_2 is heated simultaneously to raise the pressure. Additionally, a booster pump or release valves are used for adjusting the pressure independent of the temperature and thus be more flexible in setting an operation point. Changing the pressure in the central housing to supercritical conditions reveled incompatibility of sCO_2 with grease used for lubrication. The bearings are designed as angular hybrid ball bearings. Therefore, CO_2 in the central housing must constantly be held in gaseous condition by reducing the pressure to subcritical conditions. This means that during start-up, the valves to the turbomachine are opened, only if gaseous

DOI: 10.17185/duepublico/46075

conditions are reached. At this point the pressure needs to be subcritical. If the valves are open the turbomachine is started by using the generator as motor to accelerate the shaft to the desired speed. Different acceleration rates were tested. Compared to the sCO_2 experimental loop the sCO_2-HeRo cycle design is a non-recuperated, simple Brayton cycle and thus has lower pressure losses. First performance tests showed that closed loop operation is not possible in the loop at CVR due to the additional pressure losses. This means, that the overall pressure losses would push the compressor operating point across the surge line. Performance tests of the compressor are therefore carried out in bypass operation using a control valve to throttle the flow. In this way pressure ratio and through flow rate could be adjusted. The measurements showed good agreement with the calculated performance map.
pressure ratio lies within the range of measurement uncertainty. Changing the inlet conditions further showed, that decreasing the inlet temperature increases the pressure ratio. More detailed discussion of the performance is presented in the paper of Hacks et al. [70].

CONCLUSIONS

This paper comprises a comprehensive literature review of the experimental work done in sCO_2 including heat transfer and pressure drops in HXs, turbomachinery, system behavior and materials. The results of this review can be summarized as follows. The heat transfer in the supercritical region varies greatly with temperature. There has been extensive research in heated surfaces. There in the vertical flow at high heat fluxes and low mass flow rates the heat transfer deterioration occurs at near pseudo critical region. This has to do with buoyant force which disturb the turbulence. Number of authors have investigated the cooling surfaces as well. All researches observed improvement of heat transfer during cooling at the pseudo critical region. Various types of compact heat exchangers have been discussed with focus on the most effective PCHXs. Based on the literature survey, comparisons between different channel geometries reveals that the airfoil geometries appear to perform much better than the zig-zag geometries. In the past 10 years, a number of sCO_2 Brayton cycles designs and prototypes have been developed. The experimental data from small test facilities (100 kWe range) indicate that the basic design and performance predictions are sound. A few multi-MWe range are in early stage operation. The most challenging is the turbomachinery. The design is very compact due to the high pressures resulting in highly dense gas which implies extreme loads on blades. The compact design requires also high speed which makes the bearing and seal design challenging. Additional difficulties are related with the stability of the cycle and operation in off-design region. Hence, progressive engineering research and development is required to improve existing prototypes and bring the technology closer to the market.

CVR works in the sCO_2 for several years now and operates sCO_2 loop for testing of Brayton cycle. The first operational experience with the turbomachine tests of a size of 10 kWe has been given along with the heat transfer investigations in the air cooled sCO_2 finned-tube sink HX. The compressor performance measurements of the pressure ratio matched well with the CFD calculations and the heat transfer at the sink HX is predictable using the conventional 1D empirical correlation (Gnielinsky [63] for sCO_2 and IPPE [66] or VDI [67] for the air).

The described first operational experience and the data obtained from different experiments proves operability and flexibility of the loop, which may be utilized within various experimental campaigns in the field of sCO_2.

NOMENCLATURE

Abbreviation	Description
CH	Cooler
CVR	Reseach Center Rez, Czech Rebublic
FPHX	Finned plate heat exchanger
H	Heater
HPC	High pressure compressor
HT	Heat transfer
HTD	Heat transfer deterioration
HTR	High temperature heat exchanger
HX	Heat exchanger
IPPE	Institute of Physics and Power Engineering
KAPL/BAPL	Knolls Atomic Power Lab/ Bettis Atomic Power Lab & Korea Atomic Energy Research Institute
KAERI & KAIST & POSTECH	Korea Advanced Institute of Science and Technology & Korea Atomic Energy Research Institute & Pohang University of Science and Technology
LPC	Low pressure compressor
LPT	Low pressure turbine
LTR	Low temperature heat exchanger
LWR	Light water reactors
MP	Main pump
PID	Piping and instrument diagram
PCHX	Printed circuit heat exchanger
RPM	Rotation per minute
SNL RCBC	Sandia National Laboratories recompression closed Brayton cycle
TAC	Turbomachine
TIT	Test loop at Tokyo Institute of

DOI: 10.17185/duepublico/46075

	Technology
SCIEL	Supercritical CO_2 Brayton Cycle Integral Experimental Loop

ACKNOWLEDGEMENTS

This project has received funding from the European research and training programme 2014 – 2018 under grant agreement No 662116.

REFERENCES

[1] DEKHTIAREV V.L.: On designing a large, highly economical carbon dioxide power installation. Elecrtichenskie Stantskii 1962;5:1-6.

[2] FEHER E.G.: The supercritical thermodynamic power cycle. In: Proceedings of the IECEC, Florida (USA) in 1967, 1:13e15.

[3] BRINGER, R.P.; SMITH, J.M.: Heat transfer in the critical region. AIChE J. 3 (1), 49–55, 1957.

[4] PETUKHOV, B.S.; KRASNOSCHEKOV, E.A.; PROTOPOPOV, V.S.: An investigation of heat transfer to fluids flowing in pipes under supercritical conditions. In: International Developments in Heat Transfer: Papers presented at the 1961 International Heat Transfer Conference, ASME, University of Colorado, Boulder, Colorado, USA, 8–12 January, Part III, Paper 67, pp. 569–578, 1961.

[5] DUFFEY, R.B.; PIORO, I.L.: Experimental heat transfer of supercritical carbon dioxide flowing inside channels (survey), Nuclear Engineering and Design 235 (2005) 913–924.

[6] BAE, Y.Y.; KIM, H.Y.; KANG, D.J.: Forced and mixed convection heat transfer to supercritical CO_2 vertically flowing in a uniformly-heated circular tube. Experimental Thermal and Fluid Science 34 (2010) 1295-1308.

[7] BAE, Y.Y.; KIM, H.Y.; YOO, T.H.: Mixed convection heat transfer to CO_2 flowing upward and downward in a vertical tube and an annular channel. IAEA Technical Meeting, Pisa, Italy, July 5-8, 2010.

[8] KIM, J. K.; JEON, H.K.; LEE, J.S.: Wall temperature measurements with turbulent flow in heated vertical circular/non-circular channels of supercritical pressure carbon-dioxide. International Journal of Heat and Mass Transfer 50 (2007) 4908-4911.

[9] KIM, J. K.; JEON, H.K.; YOO, J.Y.; LEE, J.S.: Experimental study on heat transfer characteristics of turbulent supercritical flow in vertical circular/non-circular tubes. The 11th International Topical Meeting on Nuclear Thermal-Hydraulics (NURETH-11), Avignon, France, October 2-6, 2005.

[10] KIM, D.E.; KIM, M.H.: Experimental study of the effects of flow acceleration and buoyancy on heat transfer in a supercritical fluid flow in a circular tube. Nuclear Engineering and Design 240 (2010) 3336-3349.

[11] JIANG, P.X.; ZHANG, Y.; SHI, R.F.: Experimental and numerical investigation of convection heat transfer of CO_2 at supercritical pressures in a vertical mini-tube. International Journal of Heat and Mass Transfer 51 (2008a) 3052-3056.

[12] JIANG, P.X.; ZHANG, Y.; SHI, R.F.: Convection heat transfer of CO_2 at supercritical pressures in a vertical mini tube at relatively low Reynolds numbers. Experimental Thermal and Fluid Science 32 (2008b) 1628-1637.

[13] JIANG, P.X.; ZHANG, Y.; SHI, R.F.: Experimental and numerical investigation of convection heat transfer of CO2 at supercritical pressures in a vertical tube at low Reynolds numbers. International Journal of Thermal Sciences 47 (2008c) 998-1011.

[14] JIANG, P.X.; XU, R.N.: Convection of carbon dioxide at SCP in various scales and geometries tubes. International Meeting of Specialists on Heat Transfer to Fluids at Supercritical Pressure, Manchester, UK, 30th June – 1st July 2014.

[15] LIU, G.; HUANG, Y.; WANG, J.: Experimental investigation of the basic characteristics of superficial carbon dioxide natural circulation in a rectangular channel. The 7th International Symposium on Supercritical Water-Cooled Reactors ISSCWR-7, Helsinki, Finland, 15-18 March 2015. ISSCWR7-2030.

[16] ETER, A.; GROENEVELD, D.; TAVOULARIS, S.: Experiments on heat transfer in rod-bundle flows of CO2 at supercritical pressures. 7th International Symposium on Supercritical Water-Cooled reactors ISSCWR-7 2015, 15th-18th March 2015, Helsinki, Finland. ISSCWR7-2070.

[17] JACKSON, J.D.; HALL, W.B.: Forced convection heat transfer to fluids at supercritical pressure. In: Kakac¸, S.; Spalding, D.B. (Eds.), Turbulent Forced Convection in Channels and Bundles, vol. 2. Hemisphere Publishing Corp., New York, USA, pp. 563–612.

[18] ZAHLAN, H.; GROENEVELD, D.; TAVOULARIS, S.: Fluid-to-fluid scaling for convective heat transfer in tubes at supercritical and high subcritical pressures, International Journal of heat and mass transfer, Volume 73, 274–283, 2014.

[19] SCHMIDT, K.: Untersuchungen über die Wärmeübergangszahl von Kohlensäure im kritischen Gebiet an eine Rohrwand Zeitschrift für die gesamte Kälte-Industrie, Berlin, 1937.

[20] KRASNOSHCHEKOV E.A.; PROTOPOPOV V.S.: Local heat transfer of carbon dioxide at supercritical pressure under cooling conditions. TVT, 1969, Vol.7, Issue 5, 922-930; High Temp. 7 (5), 856–861.

[21] TANAKA, H.; NISHIWAKI, N.; HIRATA, M.: Turbulent heat transfer to supercritical carbon dioxide, Proc. Japan Sot. Mech. Engrs Semi-lnt. Symp.. Tokyo, Heat Mass Transfer, Vol. 2, 127 (1967).

DOI: 10.17185/duepublico/46075

[22] BASKOV V.L.; KURAEVA I.V.; PROTOPOPOV V.S.: Heat transfer with the turbulent flow of a liquid at supercritical pressure in tubes under cooling conditions. High Temperature (translated from Teplofizika Vysokikh Temperatur) 1977; 15(1):81–6.
[23] PETROV, N.E.; POPOV, V.N.: Heat transfer and resistance of carbon dioxide being, cooled in the supercritical region, Thermal Engineering 32 (3) (1985).
[24] PETROV, N.E.; POPOV, V.N.: Heat transfer and hydraulic resistance with turbulent flow in a tube of water under supercritical parameters of state, Thermal Engineering 35 (5-6) (1988) 577-580.
[25] PITLA, S.S.; GROLL, E.A., ROBINSON, D.M.; RAMADHYANI, S.: Heat transfer from supercritical Carbone Dioxide in tube flow: A critical review, HVAC&R Research; Jul 1998; 4, 3; ProQuest Central pg. 281.
[26] PETTERSEN, J.; RIEBERER, R.; MUNKEJORD, S.T.: Heat transfer and pressure drop for flow of supercritical and subcritical CO2 in microchannel tubes, SINTEF Energy Research, Trondheim, February, 2000.
[27] OLSON, D.A.: Heat Transfer of supercritical Carbon Dioxide flowing in a cooled horizontal tube, NIST, Gaithersburg, May, 2000.
[28] ZINGERLI, A.; GROLL, E.A.: Influence of refrigeration oil on the heat transfer and pressure drop of supercritical CO2 during in-tube cooling, in: Proceedings of the Fourth IIR-Gustav Lorentzen Conference, Purdue, IN, 2000, pp. 269–278.
[29] YIN, J.M.; BULLARD, W.B.; HRNJAK, P.S.: R-744 gas cooler model development and validation. International Journal of Refrigeration 24 (2001) 692-701.
[30] LIAO, S.M.; ZHAO, T.S.: Measurement of heat transfer coefficients from supercritical carbon dioxide flowing in horizontal mini/micro channels, J. Heat Transfer 124 (2002) 413–420.
[31] GAO, L.; HONDA, T.: Experiments on heat transfer characteristics of heat exchanger for CO2 heat pump system, in: Proceedings of the Asian Conference on Refrigeration and Air Conditioning, Kobe, 2002, pp. 75–80.
[32] MORI, K.; ONISHI, J.; SHIMAOKA, H.; NAKANISHI, S.; KIMOTO, H.: Cooling heat transfer characteristics of CO2 and CO2–oil mixture at supercritical pressure conditions, in: Proceedings of the Asian Conference on Refrigeration and Air Conditioning, Kobe, 2002, pp. 81–86.
[33] YOON, S.H.; KIM, J.H.; HWANG, Y.W.; KIM, M.S.; MIN, K.; KIM, Y.: Heat transfer and pressure drop characteristics during the in-tube cooling process of carbon dioxide in the supercritical region, Int. J. Refrig. 26 (2003) 857–864.
[34] DANG, CH.; HIHARA, E.: In-tube cooling heat transfer of supercritical carbon dioxide. Part 1. Experimental measurement. International Journal of Refrigeration 27 (2004) 736–747.
[35] HUAI, XL; KOYAMA, S.; ZHAO, T.S.: An experimental study of flow and heat transfer of supercritical carbon dioxide in multi-port mini channels under cooling conditions, Chemical Engineering Science 60 (2005) 3337 – 3345.
[36] KUANG, G.: Heat transfer and mechanical design analysis of supercritical gas gooling process of CO2 in microchannels, Doctorate Thesis, University of Maryland. 2006.
[37] YUN, R.; HWANF, Y.; RADERMACHER, R.: Convective gas cooling heat transfer and pressure drop
[38] characteristics of supercritical CO2/oil mixture in a minichannel tube, Int. J. Heat Mass Transfer 50 (2007) 4796–4804.
[39] BRUCH, A.; BONTEMPS, A.; COLASSON, S.: Experimental investigation of heat transfer of supercritical carbon dioxide flowing in a cooled vertical tube, International Journal of Heat and Mass Transfer 52 (2009) 2589–2598.
[40] OH, H.K.; SON, C.H.: New correlation to predict the heat transfer coefficient in tube cooling of supercritical CO2 in horizontal macro-tubes, Experimental Thermal and Fluid Science 34 (8) (2010) 1230e1241.
[41] ELDIK, M.; HARRIS, P.M.; KAISER, W.H., ROUSSEAU, P.G.: Theoretical And Experimental Analysis Of Supercritical Carbon Dioxide, 15th International Refrigeration and Air Conditioning Conference at Purdue, July 14-17, 2014.
[42] GE, Y.T.; TASSOU, S.A.; SANTOSA, I.D.; TSAMOS, K.: Design optimisation of CO2 gas cooler/condenser in a refrigeration system. Applied Energy 2015;160:973–81.
[43] HO, D.; DANG, T.; LE, CH.; NGUYEN, T.: An experimental comparison between a microchannel cooler and conventional coolers of a C02 air conditioning cycle, in: 2017 International Conference on System Science and Engineering, Ho Chi Minh, Vietnam, July 21-23, 2017.
[44] ANGELINO G.: Carbon dioxide condensation cycles for power production. J Eng Gas Turb Power 1968;89(2):229-37.
[45] KIMZEY, G.; Development of a Brayton Bottoming Cycle using Supercritical Carbon Dioxide as the Working Fluid, Electric power research institute, Palo Alto, California, 2012.
[46] DOSTAL V.: A supercritical carbon dioxide cycle for next generation nuclear reactors [Ph.D. thesis]. Department of Nuclear Engineering, Massachusetts Institute of Technology (MIT); 2004
[47] JOHNSTON, A. ET AL.: Printed circuit heat exchangers for energy conservation, End of Grant Report No 519, National Energy Research, Development and Demonstration Program, Australia, 1985.
[48] SOUTHALL, D.; LE PIERRES, R.; DEWSON, S.J.: Design Considerations for Compact Heat Exchangers, Proceedings of ICAPP ’08, Anaheim, CA USA, June 8-12, 2008.
[49] LE PIERRES, R.; SOUTHALL, D.; OSBORNE, S.: Impact of Mechanical Design Issues on Printed Circuit Heat Exchangers, Proceedings of SCO2 Power Cycle Symposium 2011, University of Colorado at Boulder, CO, May 24-25, 2011.

DOI: 10.17185/duepublico/46075

[50] NIKITIN, K.; KATO, Y.; NGO L.: Printed circuit heat exchanger thermal–hydraulic performance in supercritical CO2 experimental loop. International Journal of Refrigeration 29, no. 5 (2006): 807-814.
[51] NGO, T.L.; KATO, Y.; NIKITIN K.; ISHIZUKA, T.: Heat transfer and pressure drop correlations of microchannel heat exchangers with S-shaped and zigzag fins for carbon dioxide cycles, Experimental Thermal and Fluid Science, vol. 32, no. 2, pp. 560-570, 2007.
[52] MOISSEYTSEV, A.; J. J. SIENICKI; CHO, D.H.; THOMASA, M.R.: Comparison of heat exchanger modeling with data from CO2-to-CO2 printed circuit heat exchanger performance tests. In Proceedings of the 2010 International Congress on Advances in Nuclear Power Plants-ICAPP'10. 2010.
[53] KRUIZENGA, A.M.: Heat transfer and pressure drop measurements in prototypic heat exchanger for the supercritical carbon dioxide Brayton power cycles, Ph.D. Thesis, University of Wisconsin – Madison, 2010.
[54] KATO, Y: How New Microchannel Heat Exchanger Reduced Pressure Drop to 1/6 Inheriting High Heat Transfer Performance, Supercritical CO2 Power Cycle Symposium, May 24-25, 2011, Boulder, Colorado.
[55] ANDERSON, M.; NELLIS, G.; CORRADINI, M.: Materials, Turbomachinery and heat exchangers for supercritical CO2 systems, University of Wisconsin – Madison, Award Number: 88234, Project Number: 09-778, Oct. 30, 2012.
[56] BAIK, S.; KIM, S.G.; SON, S.;KIM, H.T. LEE, J.I.:Printed Circuit Heat Exchanger Design, Analysis and Experiment, NURETH-16, Chicago, IL, August 30-September 4, 2015.
[57] RANJAN, D.: Fundamental study of key issues related to advanced sCO2 Brayton cycle: Prototypic HX development and cavitation, Final report for NEUP project 14-6670, Georgia Institute of Technology, Atlanta 2016.
[58] STRÄTZ, M.: Performance data of a compact heat exchanger, Deliverable 2.2, sCO2-HeRo-Project, Grant agreement No 662116, 2017.
[59] WRIGHT, S.A.; RADEL, R.F.; VERNON, M.E.; ROCHAU, G.E.; PICKARD, P.S.: Operation and Analysis of a Supercritical CO2 Brayton Cycle, SAND2010-0171, Albuquerque, New Mexico, Sep. 2010.
[60] HELD, T.J.: Commercialization of Supercritical CO2 (sCO2) Power Cycles, 1st European Seminar on "Supercritical CO2 Power Systems", TU Vienna, 29-30 Sep 2016.
[61] BRUN K.; FRIEDMAN P.; DENNIS R.: Fundamentals and Applications of Supercritical Carbon Dioxide (SCO2) Based Power Cycles. 1st edition, Elsevier Science & Technology, 2017.
[62] AHN, Y.; LEE, J.; KUM, S.G.; LEE, I.J.; CHA, J.E.; LEE, S.W.: Design consideration of supercritical CO2 power cycle integral experiment loop, Energy 86 (2015) 115-127.
[63] MOORE, J.; BRUN, K.; EVANS, N.; KALRA, C.: 2015. Development of 1 MWe supercritical CO2 test loop. In: Proc. ASME Turbo Expo GT2015-43771, Montreal, Canada.
[64] http://www.sco2-hero.eu/
[65] GNIELINSKI, V.: New equations for heat and mass transfer in turbulent, pipe and channel flow. Int Chem Eng 16:359–368, 1976.
[66] ZUKAUSKAS, A.A.: Konvektivnyj perenos v teploobmennikach. Nauka, Moskva 1982.
[67] VDI-Heat Atlas, Second edition, Springer-Verlag Berlin Heidelberg 2010.
[68] VOJACEK, A. ET. AL.: Performance test of the air cooled finned-tube sCO2 sink heat exchanger, ASME Journal of Heat Transfer, 2018, pending.
[69] HACKS, A. J.; SCHUSTER, S.; DOHMEN H. J.; BENRA F.-K.; BRILLERT D.: Turbomachine Design for Supercritical Carbon Dioxide within the sCO2-HeRo.eu Project. GT2018-75154, ASME Turbo Expo, Sweden, Oslo 2018.
[70] HACKS A. J.; VOJACEK A.; DOHMEN H. J.; BRILLERT D.: Experimental Investigation of the sCO2-HeRo Compressor. 2018-sCO2.eu-115, 2nd European supercritical CO2 Conference, August, 2018.

DOI: 10.17185/duepublico/46075

ANNEX A

RECENTLY BUILT EXPERIMENTAL SCO2 FACILITIES FOR HT INVESTIGATION TO HEATED SURFACES NEAR PSEUDO-CRITICAL POINT

Table 8: Recently built experimental sCO_2 facilities for HT investigation to heated surfaces near pseudo-critical point

Year	Country	Facility	Parameters	Geometry and flow
2005	South Korea	SPHINX (KAERI), [6]-[7]	7.75÷8.12 MPa, inlet 5÷39 °C, 285÷1200 kg/m2/s, 30÷170 kW/m2	Vertical upward/downward flow, Ø 4.4/4.57/6.32/ 9.0mm, annulus 8 x 10 mm
2008	China	Tsinghua University, [11]-[12] 2008	8.6 MPa, inlet 25÷30°C, 388÷582 kg/m2/s, 27÷549 kW/m2	Vertical upward/downward flow, Ø 0.27 mm
2008		Tsinghua University, [13] 2008	8.6 – 9.5 MPa, inlet 23 ÷ 36 °C, 6.3 – 6.6 kg/m2/s, 4.5÷94 kW/m2	Vertical upward/downward flow, Ø 2 mm
2010	South Korea	SPHINX (KAERI), [6]-[7]	7.75÷8.12 MPa, inlet 5÷39 °C, 285÷1200 kg/m2/s, 30÷170 kW/m2	Vertical upward/downward flow, Ø 4.4/4.57/6.32/ 9.0mm, annulus 8 x 10 mm
2010		Pohang University, [10]	7.5÷10.3 MPa, inlet 29 °C, 208÷874 kg/m2/s, 38÷234 kW/m2	Vertical upward flow, Ø 4.5 mm
2014	China	Tsinghua University, [14]	7.6 MPa, inlet 22÷34 °C, 230–354 kg/m2/s, 12÷63 kW/m2	Vertical upward/downward flow, Ø 1 mm
2015		Nuclear Power Institute of China, Sichuan, Natural circulation loop, [15]	8.2÷10.2 MPa, inlet 27÷30 °C, 245–393 kg/m2/s, 4÷53 kW/m2	Vertical upward flow, Ø 6 mm
2015	Canada	SCUOL Ottawa, [16]	6.6÷8.36 MPa, 11÷30 °C, 330÷1173 kg/m2/s, 56÷175 kW/m2	Vertical upward flow, 3 rods (Ø 10 mm) bundle in Ø 25.4 mm

ANNEX B

EXPERIMENTAL SCO2 FACILITIES FOR HT INVESTIGATION IN COOLERS

Table 9: Experiments in sCO2 facilities for HT investigation in coolers (chronologically ordered)

Year	Country	Facility	Parameters	Geometry and flow
1937	Germany	Berlin, [19]	6÷7.4 MPa, temperature close to critical temperature (no superheating), 0.05÷0.3 m/s	Vertical downward flow, Circular tube
1969	Russia	Moscow Power Engineering Institute [20]	8÷12 MPa, 29÷214 °C, Re=(900÷3200) x 10^3, 120÷1110 kW/m^2	Horizontal flow, Ø 2.22 mm
1967	Japan	University of Tokyo, [21]	-	Vertical downward flow, Circular tube Ø 6 mm
1977	Russia	Moscow Power Engineering Institute [22]	8÷12 MPa, 17÷212 °C, 1560÷4170 kg/m^2/s, up to 640 kW/m^2	Vertical upward/downward flow, Ø 4.12 mm
1985	Russia	Moscow, [23]	7.85÷12 MPa, 20÷248 °C, 450÷4000 kg/m^2/s,	-

DOI: 10.17185/duepublico/46075

			14÷1000 kW/m^2	
1985	Russia	Moscow, [24]	7.85÷12 MPa, 20÷248 °C, 450÷4000 kg/m^2/s, 14÷1000 kW/m^2	-
1998	USA	Purdue University, [25]	8.4÷11.4 MPa, 20÷124 °C, 1200÷2400 kg/m^2/s	Horizontal flow, Ø 4.7 mm
2000	Norway	SINTEF Energy Research, [26]	8.1÷10.1 MPa, 15÷70 °C, 600÷1200 kg/m^2/s, 10÷20 kW/m^2	Horizontal flow, Multi-port extruded circular tube, Ø 0.79 mm
2000	USA	NIST, [27]	7.8÷13.4 MPa, 23÷87 °C, 200÷900 kg/m^2/s, 1.78÷6.22 kW	Horizontal flow, Ø 10.9 mm
2000	USA	Purdue University, [28]	8÷12 MPa, 100÷125 °C, 1700÷5100 kg/m^2/s	Horizontal flow, Ø 2.75 mm
2001	USA	University of Illinois, [29]	7.7÷14.4 MPa, 33÷140 °C, 0.45÷0.71 kg/s	Horizontal flow, Multi-port extruded circular tube, Ø 0.79 mm
2002	China	Hong Kong, University of Science and Technology, [30]	7.4÷12 MPa, 20÷110 °C, 0.02÷0.2 kg/min., 10÷200 kW/m^2	Horizontal flow, Ø 0.5÷2.16 mm
2002	Japan	Tokyo, [31]	7.6÷9.6 MPa, 20÷100 °C, 330÷680 kg/m^2/s	Horizontal flow, Ø 5 mm
2002	Japan	Tokyo, [32]	9.5 MPa, 20÷70 °C, 100÷500 kg/m^2/s	Horizontal flow, Ø 4÷8 mm
2003	South Korea	Seoul, [33]	7.5÷8.8 MPa, 50÷80 °C, 225÷450 kg/m^2/s	Horizontal flow, Ø 7.7 mm
2004	Japan	Tokyo, National Institute of Advanced Industrial Science and Technology, [34]	8÷10 MPa, 5÷70 °C, 200÷1200 kg/m^2/s, 6÷33 kW/m^2	Horizontal flow, Ø 1÷6 mm
2005	China	Beijing, Chinese Academy of Science, [35]	7.4÷8.5 MPa, 22÷53 °C, 110÷420 kg/m^2/s, 0.8÷9 kW/m^2	Horizontal flow, Multi-port extruded circular tube, Ø 1.31 mm
2006	USA	University of Maryland, [36]	8÷10 MPa, 25÷50 °C, 300÷1200 kg/m^2/s, 20÷25 kW/m^2	Horizontal flow, Multi-port extruded circular tube, Ø 0.79 mm
2007	USA	University of Maryland, [37]	8.4÷10.4 MPa, 40÷80 °C, 200÷400 kg/m^2/s, 20÷25 kW/m^2	Horizontal flow, Multi-port extruded circular tube, Ø 1 mm
2008	France	CEA-Grenoble, Laboratoire Greth, [39]	7.4÷12 MPa, 15÷70 °C, 50÷590 kg/m^2/s	Vertical flow, upward/downward flow, Ø 6 mm
2010	South Korea	San, Pukyong National University, [40]	7.5÷10 MPa, 20÷100 °C, 200÷600 kg/m^2/s	Horizontal flow, Ø 4.55÷7.75 mm
2014	South Africa	Potchefstroom North-West University, [41]	8÷11 MPa, 34÷120 °C, Re = Re=(350÷680) x 10^3	Horizontal flow, Ø 16 mm
2015	UK	Brunel University, Uxbridge, [42]	7.6÷8.7 MPa, 30÷105 °C, 980÷1180 kg/m^2/s	Horizontal flow, finned tube HX Ø 6.7 mm
2017	Vietnam	HCMC University of Technology and Education, [43]	7.7÷8.6 MPa, 32÷56 °C	Horizontal flow, finned tube HX Ø 7.8/4.8 mm, finned plate HX – multiport micro-channel height 0.6 mm, width 1.2 mm

ANNEX C

EXPERIMENTAL SCO2 FACILITIES FOR HT INVESTIGATION IN PCHX

Table 10: Experiments in sCO2 facilities for HT investigation in PCHX (chronologically ordered)

DOI: 10.17185/duepublico/46075

Year	Country	Facility	Parameters	Geometry and flow
2005	Japan	Tokyo Institute of Technology, [50]	Hot side 2.2÷3.2 MPa, inlet 280÷300°C, 0.011÷0.022 kg/s, 65÷130 kg/m^2/s Cold side 6.5÷10.5 MPa, inlet 90÷108°C, 0.011÷0.022 kg/s, 161÷322 kg/m^2/s	Horizontal flow Zig-zag channel: Hot side fin gap 1.9 mm, channel depth 0.9 mm, wave length 9 mm, pitch 2.964 mm, angle 32.5°, Cold side fin gap 1.8 mm, channel depth 0.9 mm, wave length 7.24 mm, pitch 3.263 mm, angle 40°
2007	Japan	Tokyo Institute of Technology, [51]	Hot side 6 MPa, inlet 120°C, 0.011÷0.042 kg/s, 93÷356 kg/m^2/s Cold side 7.7÷12 MPa, inlet 35÷55°C, 0.011÷0.042 kg/s, 93÷356 kg/m^2/s	Horizontal flow S-shape channels: Hot/cold side fin gap 1.31 mm, channel depth 0.94 mm, wave length 7.565 mm, pitch 3.426 mm, angle 52°, Horizontal flow Zig-zag channels: Hot/cold side fin gap 1.31 mm, channel depth 0.94 mm, wave length 7.565 mm, pitch 3.426 mm, angle 52°
2010	USA	Argonne National Laboratory, [52]	Hot side 7.9÷8.5 MPa, inlet 154÷161°C, 0.085÷0.091 kg/s, Cold side 11.3÷20 MPa, inlet 40.7÷48.8°C, 0.054÷0.064 kg/s	Horizontal flow Zig-zag channels: Hot side fin gap 1.5 mm, channel depth 0.75 mm, angle 38°, 45° (estimated)
2010	USA	University of Wisconsin, [53]	Only 1 plate Hot side of sCO_2 (surrounded 2 plates top/bottom with cold water) 7.5÷8.1 MPa, inlet 20÷100 °C, 326÷762 kg/m^2/s, 12÷36 kW/m^2	Horizontal/vertical (downward/upward) flow Straight channel: Hot side fin gap 1.9 mm Zig-zag channel: Hot side fin gap 1.9 mm, channel depth 0.9 mm, wave length 9 mm, pitch 2.964 mm, angle 32.5°, Horizontal flow Zig-zag channel: Hot side fin gap 1.9 mm, channel depth 0.9 mm, wave length 7.24 mm, pitch 3.263 mm, angle 40°
2011	Japan	Tokyo Institute of Technology, [54]	-	Horizontal flow Zig-zag, sinuous curve, S-shape, modified louvered, louvered channels
2012	USA	University of Wisconsin, [55]	Only 1 plate (surrounded 2 plates top/bottom with cold water) 6÷12 MPa, inlet 16÷105 °C, 210÷1200 kg/m^2/s	Horizontal flow 8.1 mm NACA0020 4 mm NACA0020
2015	South	KAIST, [56]	Hot side sCO_2/cold side water	Horizontal flow

DOI: 10.17185/duepublico/46075

	Korea		7.3÷8.5 MPa, inlet 25÷40 °C, Re=2000÷58000	Zig-zag channel: Hot/cold side fin gap 1.8 mm, channel depth 0.75 mm, wave length 9 mm, pitch 2.964 mm, angle 32.5°
2016	USA	Atlanta, Georgia Institute of Technology, [57]	Only 1 plate (surrounded 2 plates top/bottom with cold water) 7.5÷8.1 MPa, inlet 12÷135 °C, 220÷660 kg/m^2/s	Horizontal flow 8.1 mm NACA0020 9 mm Offset fin
2017	Germany	SCARLETT, University of Stuttgart, [58]	sCO_2 heated up by steam 9.5÷11 MPa, inlet 40 °C, 1233÷2267 kg/m^2/s	Straight channel Hot side/cold side fin gap 2 mm, channel depth 1 mm

ANNEX D

THE DESIGN COMPARISON OF SCO2 INTEGRAL TEST LOOPS

Table 11: The design comparison of SCO2 integral test loops

Facility	**Turbomachinery**	**Cycle layout**	**Heat power [kW]**	**Efficiency [-]**	**Mass flow rate [kg/s]**	**Turbine intet temp. [°C]**	**Pressure ratio [-]**	**Rpm [rmp x 10^{-3}]**
SNL, [61], [62]	2 x TAC, (2x100 kWe net target),	Recompr.	780	0.315 (target)	3.5 (target) / 2.7(achieved)	537 (target) / 342(achieved)	1.8 (target) / 1.65 (achieved)	75 (target) / 52 (achieved)
KAPL / BAPL, [61], [62]	1 x TAC + 1 x turbine (target 100 kWe net), (40 kWe net achieved)	Simple recuper.	834.9	0.147 (target)	5.35 (target) / 3.54 (achieved)	300 (target)	1.8 (target) / 1.44 (achieved)	75(target)/60 (achieved)
TIT, [61], [62]	1 x TAC (10 kWe net achieved)	Simple recuper.	160	0.07 (achieved)	1.1 (achieved)	277 (achieved)	1.4 (achieved)	69 (achieved)
KAERI & KAIST & POSTECH (SCIEL), [61], [62]	1 x TAC (HPC&HPT), 1 x turbine (LPT), 1 x compressor (LPC), (250 kWe net target)	Simple recuper.	1320	0.225 (target)	6.4 (target)	500 (target)	2.67 (target)	75 (LPT), 70 (LPC), 68 (HPT & HPC) (target)
SunShot, [61], [63]	1 x compressor (standard), 1 x turbine (target 1 MWe net)	Simple recuper.	2600	-	8.4 (target)	715 (target)	2.9 (target)	27 (turbine) (target)
Echogen (EPS100), [61]	1 x TAC, 1 x turbine (10 MWe net target) (3 MWe net achieved)	Simple recuper.	25000 (target)	-	-	485 (target)	-	30

DOI: 10.17185/duepublico/46075

ANNEX E

EXPERIMENTAL SCO2 FACILITIES FOR HT INVESTIGATION IN PCHX RECUPERATORS

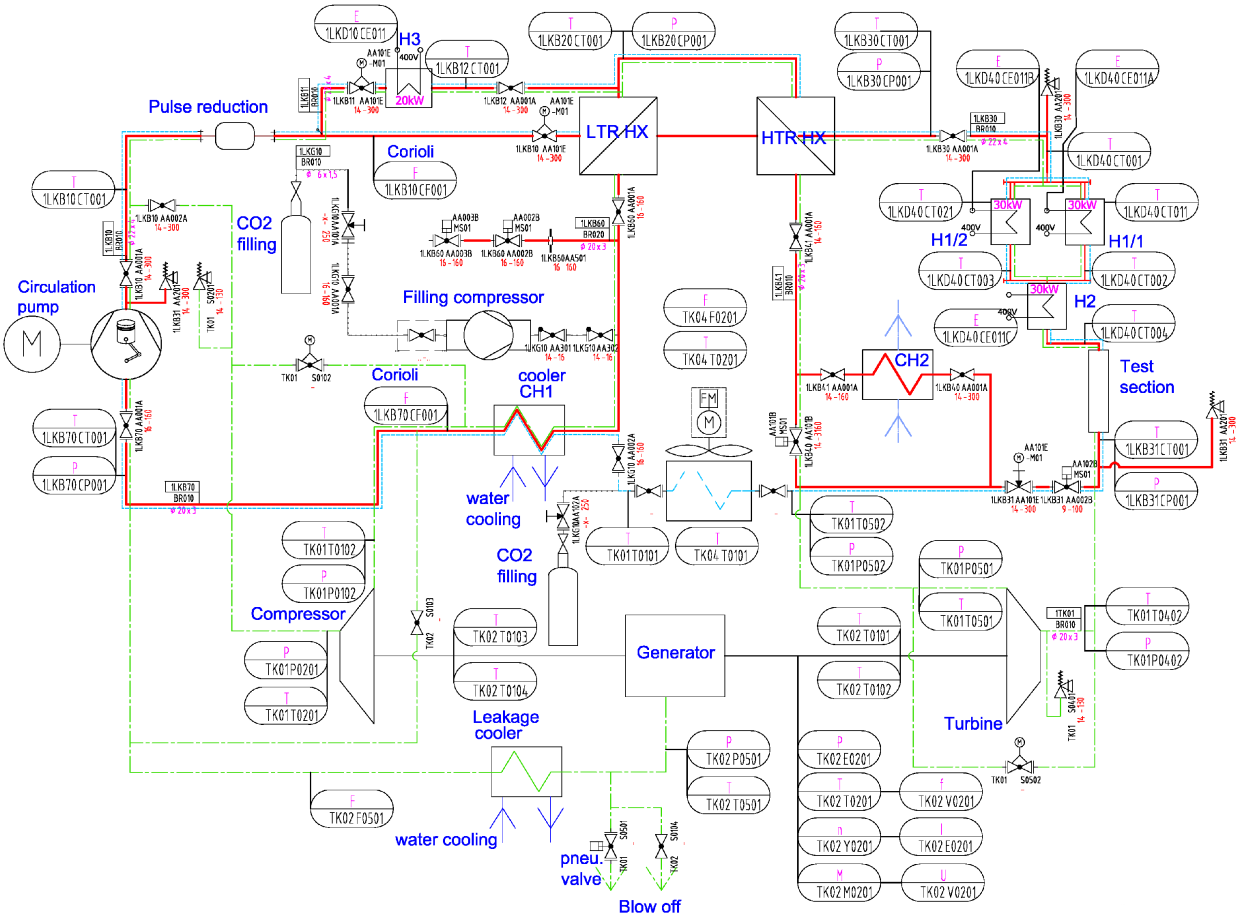

Figure 5: PID of the sCO2 loop in CVR

DOI: 10.17185/duepublico/46075

2nd European supercritical CO2 Conference
August 30-31, 2018, Essen, Germany

2018-sCO2.eu-130

ECONOMIC FORECASTING FOR SOLAR-ENERGY ASSISTED SUPERCRITICAL CO_2 CLOSED CYCLE

Mohamed Noaman*
TU Berlin
Berlin, Germany
Email: mohamed.noaman@tu-berlin.de

Tatiana Morosuk
TU Berlin
Berlin, Germany

George Tsatsaronis
TU Berlin
Berlin, Germany

ABSTRACT

In this paper, an economic forecast for two different system capacities is presented. This forecast is based on cost information gathered from various recently published literature and industry sources concerned with collector field and power cycle cost analysis. The forecast focuses on predicting the effect of introducing different setups for solar-energy assisted supercritical carbon dioxide (sCO_2) closed cycle to the power generation market assuming different scenarios for this technology within the market. Results show that the sCO_2 technology could help the concentrated solar power (CSP) industry to grow faster, increasing the potential of the sector not only for utility-scale power generation, but also for smaller community-scale projects. Further studies are recommended to improve the economic assessment and data collection of various components of the system.

INTRODUCTION

According to the US National Renewable Energy Laboratory (NREL), its CSP Gen3 demonstration roadmap [1], as well as other various research institutes, the sCO_2 power cycle has the potential to take over the conventional steam-Rankine cycle when operating at elevated temperatures of 700 °C or greater. In this paper, a supercritical CO_2 cycle was simulated and applied to a central and modular CSP tower design.

Recently, the price of utility bids for electricity generated from CSP commercial technology has decreased under 7 USD cents per kWh. The current commercialized CSP technology is based on a Rankine steam cycle. This paper focuses on the analysis and evaluation of the Rankine steam cycle and the recompression sCO_2 closed cycle in combination with a CSP tower. The recompression sCO_2 closed cycle has shown best efficiency vs. economic value when applied to a CSP tower technology for supplying base-load electricity. The sCO_2 closed cycle compared with air-based gas turbines, achieves better compressibility performance leading to an increase in the net produced electricity by 30%. This results in significantly less mirrors to be required for the solar field with a smaller receiver and tower, meaning a significant decrease in the capital cost required compared to current technological setups. The sCO_2 cycle also helps in creating smaller modular tower units, denoting a higher attractiveness to investors.

Previous research has explored the feasibility and potential of coupling supercritical carbon dioxide power cycle to CSP technologies [2, 3]. Such cycles are investigated also in combination with nuclear energy because they are simple, compact, less expensive, and they have a high efficiency, a small primary resource consumption, and shorter construction periods that reduces the interest on money during construction [4]. Likewise, in the case of solar thermal applications, a supercritical CO_2 closed cycle offers higher cycle efficiencies or equivalent to supercritical steam cycle at temperatures appropriate for CSP applications, however the high pressure required for sCO_2 makes coupling to parabolic trough fields challenging [5]. Therefore, it is better suited for integration with CSP tower technologies.

It is also mentioned that it is better to implement CSP tower in modular designs ranging from 5 to10 MW, because circulating high pressure sCO_2 through a large power tower would be a challenge due to the volume and pressure of fluid being moved, leading to excessive piping costs and huge reduction in overall efficiency [6]. Previous studies also investigated various elements when operated in supercritical phase and showed that CO_2 has a moderate critical pressure value, making it generally an appropriate working fluid to be used besides being stable and an inert gas (in the temperature range of interest) [4]. According to Southwest Research Institute (SwRI), using CO_2 results in a smaller turbo-machinery than helium or steam, it is more efficient than helium at medium temperatures, and it is 10 times cheaper than helium [7]. The significant difference in sizes and consequently in costs are shown in Figure 1. Supercritical CO_2 has high density (energy/volume and energy/weight) near its critical point, which reduces the compressor work and increases efficiency. The compact size of turbomachinery offers less weight, less size and lower thermal mass which results in reduction of the installation, maintenance and operation costs of the system.

The sCO_2 closed cycle is currently emerging as a promising track for high efficiency power production, where it is mostly required for solar thermal energy to achieve cost parity with conventional energy sources. The cycle has been proposed as

DOI: 10.17185/duepublico/46100

early as 1977 for shipboard applications [1], where a considerable fuel reduction was possible. Supercritical CO_2 test loops has already been constructed at Sandia National Laboratories in the US and at Tokyo institute of technology in Japan. The data from these tests indicates sound results as a preliminary design and relatively good performance predictions.

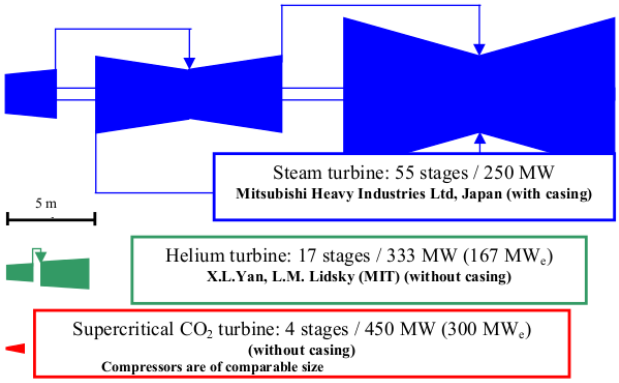

Figure 1: Turbine sizes for steam, helium and CO_2 [2]

Figure 2 shows a configuration of such a cycle with an integrated thermal energy storage system (TES). Because of the high-power density in the sCO_2 power generation rates, comparatively much lower volume flow rates are achieved compared to steam or air leading to lightweight, and low investment cost, where a modular design approach could be efficiently achieved in the range of 5 to10 MW.

In order to make this technology commercially viable, it is crucial to scale up these small laboratory tests onto multi Mega-watt range [3, 4]. In parallel also, some industry stakeholders are designing sCO_2 cycles to match current modular solar fields stating their high commercial competitiveness [5]. On top of that, the oil and gas industry has already developed technologies for compressing and pumping CO_2 at supercritical pressures leading to a decrease in the technological risk assessment of such systems [6].

The recompression configuration for the sCO_2 closed cycle have shown promising design efficiencies as well as good performance in demonstration test facilities stated earlier, together with using sCO_2 as both heat transfer fluid (HTF) in the solar field and working fluid within the power cycle, results into (a) relatively high temperatures at the solar receiver, (b) high degree of heat recuperation, (c) low average rejection temperature, (d) high fluid density near the compressor inlet (resulting in low compressor work), and (e) a low pressure ratio compared to a Rankine cycle [5].

There are three realization paths for such a solar tower/sCO2 power system, these are pathways based on the technology used in the design of the tower's receiver; molten salt, falling particle, or Gas-phase receivers. Based on current knowledge, all three have the potential to achieve grid parity. Pilot test loops and demonstration projects are needed to verify the technological feasibility. Research should also concentrate on checking the capability of each technology to satisfy the market requirements such as ramp rates, reliability, availability, and other standards [7]. In this paper, molten salt technology is used, as it represents the most mature technological approach.

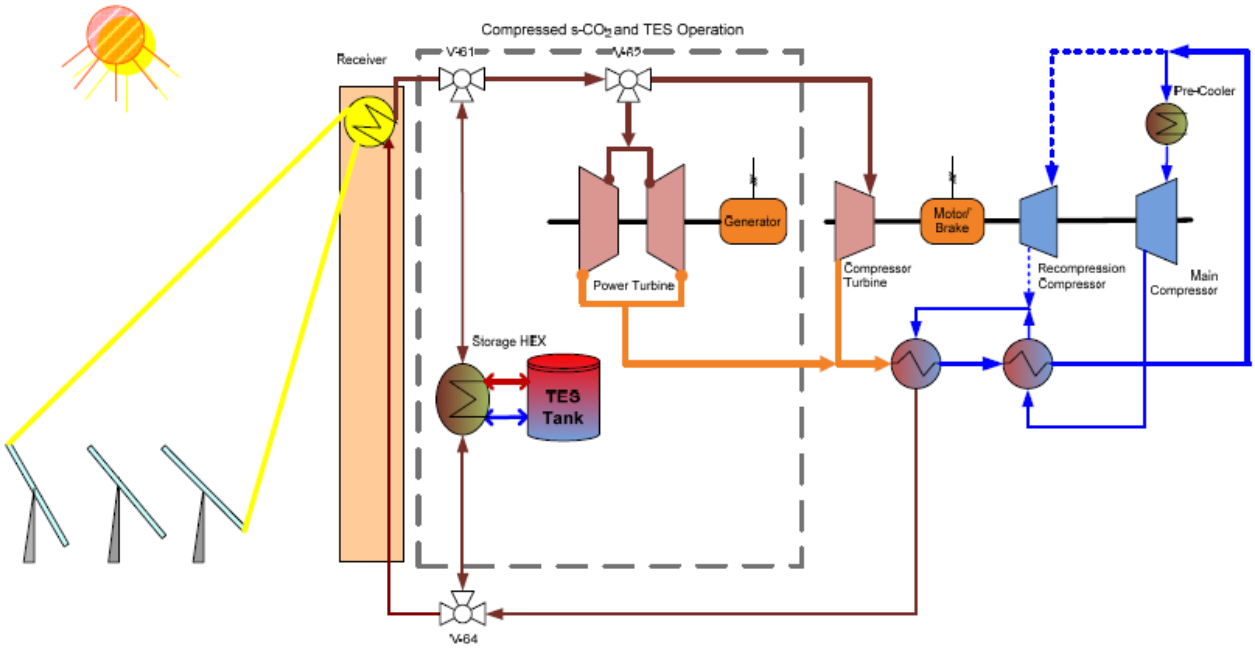

Figure 2: Dual shaft tower receiver sCO_2 closed cycle solar thermal power system with thermal energy storage [5]

DOI: 10.17185/duepublico/46100

METHODOLOGY

Based on the literature reviewed during the study, it was clear that several sCO_2 cycles have been proposed and developed during the last several years, with a focus on CSP applications. According to the data presented earlier, a sCO_2 closed cycle with recompression is selected as the most efficient cycle setup in order to compare it with the current commercial steam Rankine technology as a power block system for CSP applications.

The focus here is directed towards focusing on steam Rankine cycle representing the mature power cycle conversion technology which is now commercially available and used for every single CSP tower plant currently in operation, under construction or even in preparation, against sCO_2 closed recompression cycle representing a promising technology expected to lead the market in the future, which so far demonstrated high-efficiency results through lab demonstrations and received a lot of attention from the industry according to several studies mentioned previously.

The two cycles have been designed, simulated and assessed employing the Ebsilon software from STEAG GmbH. The cycles have had been compared with each other economically using the levelized cost of electricity index (LCOE), which was calculated using the total revenue requirement (TRR) method. A real design data for the steam Rankine cycle CSP case has been acquired from the "Solar Two" demonstration plant project [8]. The complete design schematic which was simulated on Ebsilon for the steam Rankine CSP system is shown in Annex A in addition to a table that shows the most important details for the system's design parameters and assumptions.

Since the focus in this study was only on the power block, the design of the solar field has been assumed based on SOLERGY computer code [9] which was used to predict the annual energy production of the power plant. This code was also selected because it gives a realistic estimate of the actual energy produced by the Solar Two demonstration plant [10, 11].

For a proper comparative analysis, the sCO_2 recompression closed cycle has been simulated at a capacity rating like that of the Rankine cycle design (125 MW). Also, a 10 MWe modular cycle has been proposed and simulated to explore the thermodynamic results obtained from such modular system, where it is also possible to have a solar park consisting of several modular towers all connected to a central TES system in case of supplying baseload.

The general selected design operating conditions are summarized in Table 1 and the design schematic for the simulated sCO_2 cycle is shown in Annex B. The turbine inlet temperature (TIT) was selected to be 550 °C to accommodate the technical limitation accompanied with the molten salt storage system that is coupled to the cycle and the CSP tower.

To be able to simulate a baseload case; two concepts are simulated: the first one is a default central receiver design consisting of two towers each with a rating capacity of 125 MWe, and the other one, consisting of 12 towers, is utilizing a modular design proposal, where a solar modular tower park is used (each tower would house its own turbo-machinery so that multiple towers could be assembled in a single solar park), and the whole park is connected to one TES system [5]. In order to consider the same power plant capacity simulated for the steam Rankine case and to be able to compare capital costs previously allocated, the power output from the modular designs are multiplied by a scale-up factor.

Table 1: Design conditions for the sCO_2 cycle

Design Parameter	**TIT 550°C**
Cycle Thermal Power (MW_{th})	318
Thermal Efficiency (%)	41
Net Efficiency (%)	39.3
Net Electric Power (MWe)	125
Compressor Outlet Pressure (bar)	200
Pressure Ratio	1.9
Turbine Inlet Temperature (°C)	550
Compressor Inlet Temperature (°C)	53
Cooling Water Inlet Temperature (°C)	43
Mass Flow Rate (kg/Sec)	2,300
Recompressed Fraction	0.3
Turbine Efficiency (%)	90
Main Compressor Efficiency (%)	89
Recompressing Compressor Efficiency (%)	89
Generator Efficiency (%)	98
Total Heat Exchanger Volume (m^3)	27.3

The recuperators used are Printed Circuit Heat Exchangers (PCHE), because one of the main goals is to keep the cycle compact, hence, this technology was selected since it is compact and has a small pressure drop. Shell and tube heat exchangers would not be suitable, because the tube wall would have to be thick to withstand the high-pressure difference between the high and the low cycle pressures and the heat exchanger would not be compact as required [2]. Table 2 includes detailed information about the recuperators and the air-coolers used in the designs based on this PCHE technology. The heat transfer coefficient for PCHE varies between 1,000-4,000 W/m^2K for gas cooler, and 7,000-10,000 W/m^2K for water/water [12].

Based on these two designs, the economic assessment for the two cases was then carried out through employing a comprehensive cost estimation, then the LCOE for the two cases was determined. The capital and the operation and maintenance costs used in the calculations were estimated based on some specific values obtained from the DOE Power Tower Roadmap (Industry input collected during a two-day workshop and combined with data from several cost studies). The roadmap enclosed a baseline economic calculation (what can be accomplished in commercial scale plants currently planned or under construction) vs. a workshop goal calculation (consensus values that are believed to be plausible given improvements in manufacturing and a more mature power tower industry) [13].

DOI: 10.17185/duepublico/46100

Table 2: Heat recovery at PCHE recuperators and air-coolers

Case	Heat Exchanger	Q (MW)	ΔT (K)	U (W/m^{2}K)	Area (m^2)
1st Case 125 MWe	LT Recuperator	190	9.6	3,000	6,500
	HT Recuperator	840	17.7	3,000	15,800
	Air-cooler	188	3.1	7,000	8,600
2nd Case 10 MWe	LT Recuperator	8	20	3,000	130
	HT Recuperator	43	4.8	3,000	3,000
	Air-cooler	10	4	7,000	350

RESULTS

The LCOEs for the steam Rankine cycle case and the two cases of the sCO_2 cycle were forecasted along the lifetime of the project (30 years). The result of this forecast is benchmarked against combined cycle gas fired power plants as an example for one of the most efficient conventional energy technologies. The average international price of natural gas during the last 10 years was around 4.7 $/MMBtu [14]. Also according to the international energy agency (IEA), the LCOE for combined-cycle gas turbine (CCGT) power plant technology is 63 $/MWhe levelized over 25 years lifetime [15] at an inflation rate of 2.5% per year for the US dollar, the LCOE produced from CCGT would be 85 $/MWhe at year 2019 (start of the project's lifetime). Based on these financial parameters, a forecasted benchmark was constructed for the resulted LCOE of the study cases under investigation against that of a gas-fired combined-cycle power plant (CCGT) as demonstrated in Figure 3.

Consequently, the results showed that the CCGT technology is expected to be less expensive than the three study cases until the year 2034 (15 years after the starting date), at which the LCOE for the recompression sCO_2 closed cycle integrated with a central tower case starts to level-up with that of a CCGT at 1.5% escalation rate of fuel. Then around the year 2037 (just 3 years later) the CCGT LCOE at 1.5% fuel escalation rate, again levels-up this time with that of the mature tower technology (molten-salt central tower integrated with default steam Rankine cycle). Finally, the LCOE for a CCGT at 1% fuel escalation rate would level-up with the sCO_2 central tower case on the year 2041.

It is evident as well, that at 0.5% fuel escalation rate the CCGT technology is expected to have a competitive edge over the three CSP study cases. However, the lifetime of a CCGT is assumed here to be 25 years only vs. 30 years for the three CSP study cases under investigation, leaving additional 5 years, at which the CSP plants would still be making stable profits. Moreover, the hypothetical CSP solar park (through aggregating sCO_2 closed modular towers) might become a profitable alternative as well 25 years (~2046) after the assumed starting date.

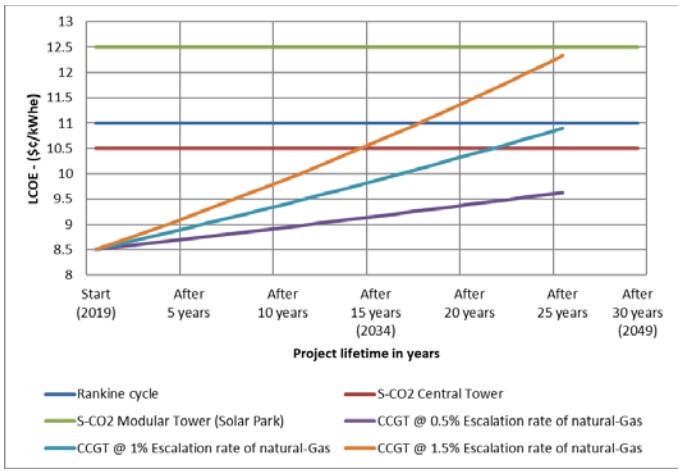

Figure 3: Calculated LCOEs for the three study cases vs. CCGT at different assumptions for fuel escalation rate

The fuel escalation rate assumed in this study is the periodic rate at which the global price of fuel increases minus the general inflation rate, which is the rate of increase in general consumer prices. The range assumed for the natural gas escalation rate from 0.5 to 1.5% is a very conservative forecast compared to the range of projected Henry Hub natural gas prices that depends on the assumptions about the availability of oil and natural gas resources and drilling technology. According to the US Energy Information Administration, natural gas prices are projected to double by the year 2040 [16].

CONCLUDING REMARKS

So far, only steady state analyses have been carried out, meaning that the behavior of the cycles, especially when integrated within the different setups mentioned above, is not known yet; however, some research studies take place currently in the US, Australia, Israel, Spain and in Germany particularly at the DLR [17]. This in return would help in understanding and selecting the most promising concepts and control strategies [2].

A comprehensive focus should also be directed toward developing materials suitable for the recompression sCO_2 closed cycle for the system components and the overall system to reach a high performance. This includes developing, testing and analyzing system components discretely as well as interconnected; corrosion experiments at high pressures (~200 bars) such as those assumed within the designs, material testing for turbine inlet temperatures reaching up-to 900 °C; and investigating the performance of PCHEs under the conditions stated in this study, especially the use of liquid metals as an alternative for thermal storage (instead of thermally limited molten-salts) reaching higher thermal storage temperatures (higher than 600 °C) in order to be compatible with the sCO_2 closed cycle designs [18].

From the economic viewpoint, air-based Brayton cycles, high-efficiency hybrid cycles as well as supercritical steam cycles are also feasible alternatives that should be economically evaluated against the research cases studied here, since these were mentioned in Sandia's tower roadmap to offer about 13%

DOI: 10.17185/duepublico/46100

improvement in efficiency and 25% decrease in capital costs in terms of $/kWe [13]. Additionally, the feasibility of tower receivers that withstand temperatures of approximately 700 °C and reaching 900 °C as well necessitate more thorough investigations that depend on the expected future technical breakthroughs [19]. On top of that, the feasibility of the presumed solar park proposal with a central integrated TES needs further investigation from the economic and technical viewpoints. The same applies to the central receiver setup integrated with the sCO_2 cycle (as the pipe losses were neglected), and to the economic burden of the intermediate heat exchanger between the primary HTF (molten-salt) loop and the secondary working fluid (sCO_2) loop.

LIST OF ACRONYMS

sCO_2	Supercritical Carbon Dioxide
CSP	Concentrated Solar Power
NREL	National Renewable Energy Laboratory
SwRI	Southwest Research Institute
SNL	Sandia National Laboratories
MIT	Massachusetts Institute of Technology
HTF	Heat Transfer Fluid
TES	Thermal Energy Storage System
LCOE	Levelized Cost of Electricity
TRR	Total Revenue Requirement method
TIT	Turbine Inlet Temperature
PCHE	Printed Circuit Heat Exchanger
DOE	US Department of Energy
HTR	High Temperature Recuperator
LTR	Low Temperature Recuperator
IEA	International Energy Agency
CCGT	Combined Cycle Gas Turbine
DLR	German Aerospace Center

REFERENCES

[1] O. Combs, *An Investigation of the Supercritical CO2 Cycle (Feher Cycle) for Shipboard Application,* Cambridge, Ma, USA: MIT, 1977.

[2] V. Dostal, M. J. Driscoll and P. Hejzlar, "Supercritical Carbon Dioxide Cycle for Next Generation Nuclear Reactors," The MIT Center for Advanced Nuclear Power Technology Program, Massachusetts, USA, 2004.

[3] B. Iverson, T. Conboy, J. Pasch and A. Kruizenga, "Supercritical CO2 Brayton cycles for solar-thermal energy," *Applied Energy,* pp. 111:957-70, 2013.

[4] Y. Kato, T. Nitawaki and Y. Muto, "Medium temperature carbon dioxide gas turbine reactor," *Nuclear Energy and Design,* no. 230, pp. 195-207, 2004.

[5] M. Zhiwen and C. S. Turchi, "Advanced Supercritical Carbon Dioxide Power Cycle Configurations for Use in Concentrating Solar Power Systems," in *Supercritical CO2 Power Cycle Symposium*, Boulder, 2011.

[6] M. Dunham and B. Iverson, "High-Efficiency Thermodynamic Power Cycles for Concentrated Solar Power Systems," *Renewable and Sustainable Energy Reviews,* pp. 758-770, 2014.

[7] M. Mehos, C. Turchi, J. Vidal and et al., "Concentrating Solar Power Gen3 Demonstration Roadmap," National Renewable Energy Laboratory (NREL), Golden, CO USA, 2017.

[8] A. B. Zavoico, "Solar Power Tower Design Basis Document," Sandia National Laboratories, Albuquerque, NM, USA, 2011.

[9] M. C. Stoddard, S. E. Faas, C. J. Chiang and J. A. Dirks, "SOLERGY - A Computer Code for Calculating the Annual Energy from Central Receiver Power Plants," Sandia National Laboratories, Livermore, CA, USA, 1987.

[10] D. J. Alpert and G. J. Kolb, "Performance of the Solar One Power Plant as Simulated by the SOLERGY Computer Code," Sandia National Laboratories, Albuquerque, NM, USA, 1988.

[11] E. Hugh and G. J. Reilly, "An Evaluation of Molten Salt Power Towers Including Results of the Solar Two Project," Sandia National Laboratories, Albuquerque, NM, USA, 2001.

[12] Heatric - Printed Circuit Heat Exchangers, "Typical characteristics of diffusion-bonded heat exchangers," 2017. [Online]. Available: https://www.heatric.com/typical_characteristics_of_PCHEs.html. [Accessed 02 12 2017].

[13] Sandia National Laboratories, "Power Tower Technology Roadmap and Cost Reduction Plan," Albuquerque, New Mexico, 2011.

[14] Energy Information Adminstration, "natural Gas Annual Prices," 2018. [Online]. Available: https://www.eia.gov/dnav/ng/hist/rngwhhdA.htm. [Accessed 06 12 2017].

[15] International Energy Agency, "Tackling Investment Challenges in Power Generation in IEA countries," IEA, head of publications service, Paris, France, 2007.

[16] US Energy Information Adminstartion, "Annual Energy Outlook 2017 with projections to 2050 (AEO 2017)," EIA, Washington, DC, 2017.

[17] M. Quero, R. Korzynietz, M. Ebert, A. Jimenez, A. Del Rio and J. Brioso, "Solugas – Operation experience of the first solar hybrid gas turbine system at MW scale," *Energy Procedia,* no. 49, pp. 1820-30, 2014.

[18] C. Forsberg, P. Peterson and H. Zhao, "High-temperature liquid-flouride-salt-closed-brayton-cycle solar power towers," *Sol Energy Eng,* vol. 129, pp. 141-6, 2007.

[19] K. H. Clifford and D. B. Iverson, "Review of high-temperature central receiver designs for concentrating solar power," *Renewable and Sustainable Energy Reviews,* no. 29, pp. 835-846, 2014.

DOI: 10.17185/duepublico/46100

[20] Solar Med Atlas, "Solar Med Atlas," 2018. [Online]. Available: http://www.solar-med-atlas.org/solarmed-atlas. [Accessed 03 05 2017].

[21] J. G. Kolb, "An Evaluation of Possible Next-Generation High Temperature Molten-Salt Power Towers," Sandia National Laboratories, Albuquerque, NM, USA, 2011.

[22] Arizona Public Service Company, Department of Energy, Pacific Gas and Electric Company, Bechtel National, "Solar Central Receiver Technology Advancement for Electric Utility Applications: Topical report. Phase IIA and IIB," Pacific Gas and Electric Company, San Francisco, CA, USA, 1992.

[23] K. Miner, "Pratt & Whitney Rocketdyne Receiver Overview, CSP Program Review Meeting," Albuquerque, NM, USA, February 9-11, 2010.

[24] C. Turchi, "Current and Future Costs for Parabolic Trough and Power Tower Systems in the US Market," in *Proceedings of the SolarPACES 2010 Conference*, Perpignan, France, 2010.

[25] C. Turchi, M. J. Wagner and C. F. Kutscher, "Water Use in Parabolic Trough Power Plants: Summary Results from WorleyParsons' Analyses," National Renewable Energy Laboratory, Golden, CO. USA, 2010.

[26] D. J. Chapman and D. Arias, "An Assessment of the Supercritical Carbon Dioxide Cycle for Use in a Solar parabolic Trough Power Plant," in *Proceedings on S-CO2 Power Cycle Symposium*, Troy, NY, 2009.

[27] D. S. Deffenbaugh, "Southwest Research Institute," 26 July 2012. [Online]. Available: https://www.swri.org/press-release/swri-industry-collaborators-receive-38-million-us-doe-develop-concentrating-solar. [Accessed 03 09 2017].

DOI: 10.17185/duepublico/46100

ANNEX A

STEAM RANKINE TOWER SCHEMATIC LAYOUT

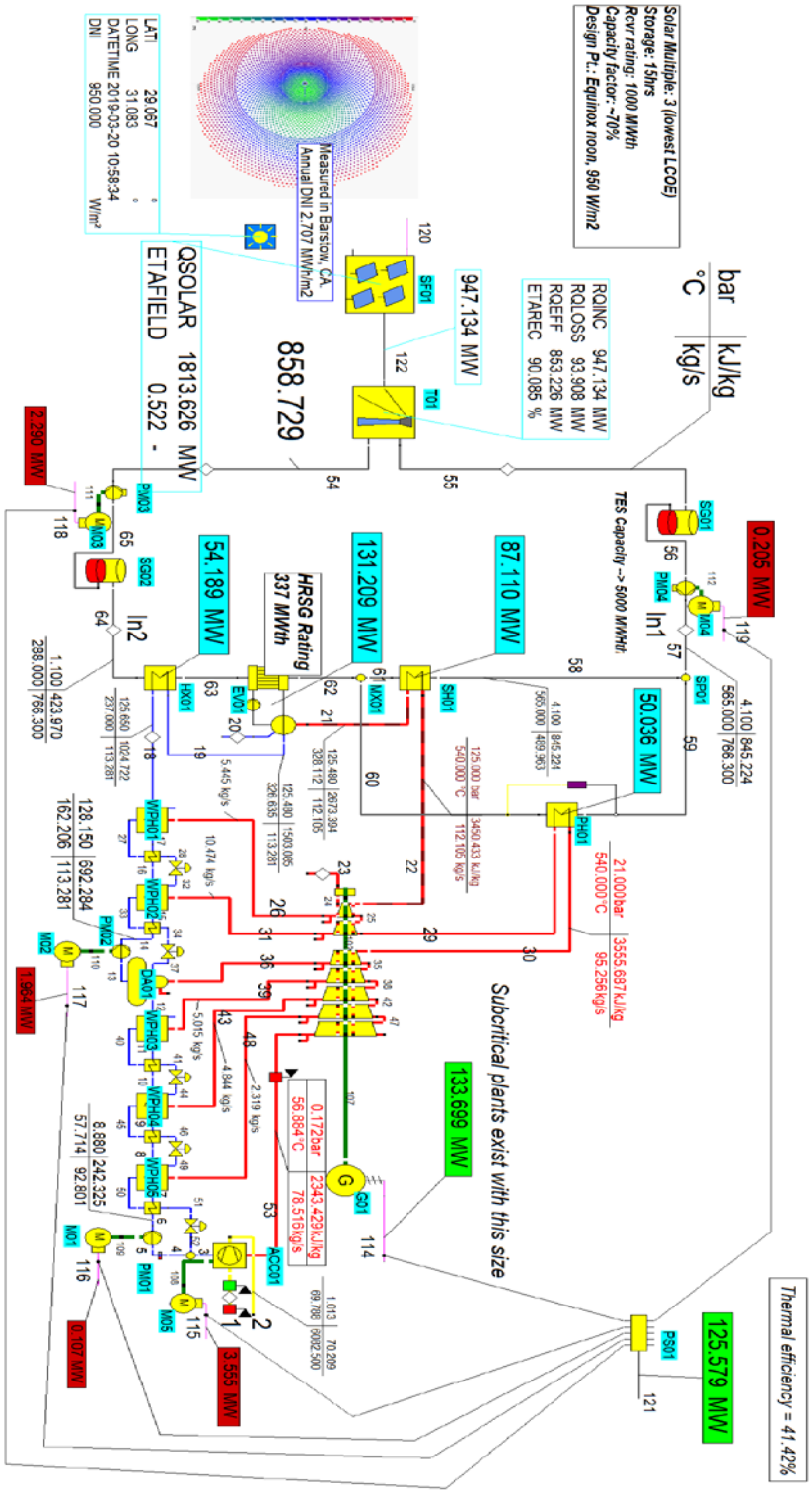

DOI: 10.17185/duepublico/46100

ANNEX A

RANKINE CYCLE PARAMETERS AND ASSUMPTIONS

Scope	Parameters	Assumptions	Additional Comments
Location details	Coordinates	Latitude 29.0667° Longitude 31.0833°	Location details obtained from solar med atlas website [20]
	Sunshine duration	9 hours average/day	
Ambient conditions	Wind speed	17 km/hour	
	Atmospheric pressure	0.95 bar	
	DNI at design point	950 W/m^2 (equinox)	Same as [21]
	DNI at coordinates	2.4 MWh/m^2/year	Obtained from solar med atlas [20]
	Plant design lifetime	30 years	Default for CSP plants
Solar Field details	Heliostat type/size	95 m^2 Advanced Thermal Systems Co (ATS)	Reliably operated for more than 20 years so far [21]
	Number of heliostats	~20 thousands	Calculated using Ebsilon 10
	Reflective area	~2 km^2	
	Heliostat field efficiency	~52%	[8]
Receiver	HTF	Molten-salt	Demonstrated at Solar Two and scale-up projects in operation and under construction
	Capacity	1,000 MW_{th}	Size similar to utility studies done in the USA [22]
	Peak solar flux	1 MW/m^2	Solar Two was 0.8 but current salt receivers have higher flux limits [23]
	Effectiveness	~90%	Same as [21]
Thermal Storage	Capability	15 hours	To insure a 70% capacity factor
	Storage capacity	5,000 MW_{th}	
Capital Cost Estimates	Heliostats	120 USD/m^2	These capital costs were compared against economic analysis present in next chapter
	Receiver/Tower	150 USD/kW_{th}	
	Storage System	25 USD/kW_{th}	
	Rankine power block	800 USD/kWe	
	O&M costs	50 USD/kW-year	
	Land cost	2 USD/m^2	
	Pricing year	2010	
	Analysis period	30 years	
	Inflation rate	2.5%	
Power Cycle	Plant Setup	Baseload – 24h operation	
	Capacity Factor	70% (SM3) Solar Multiple	Solar Two had SM1.2 but lowest LCOE occurs at 3 SM [24]
	Gross power rating	~134 MWe	Subcritical plants exist with this size in market
	Cooling method	Dry cooling condenser Design temp: 42.8 °C	Design condition: hottest time of the year [25]
Cycle efficiency	Wet-cooled	43%	
	Dry-cooled	41%	

DOI: 10.17185/duepublico/46100

ANNEX B

RECOMPRESSION SCO_2 CYCLE FOR CSP TOWER WITH TES TECHNOLOGY AT 550 °C TIT

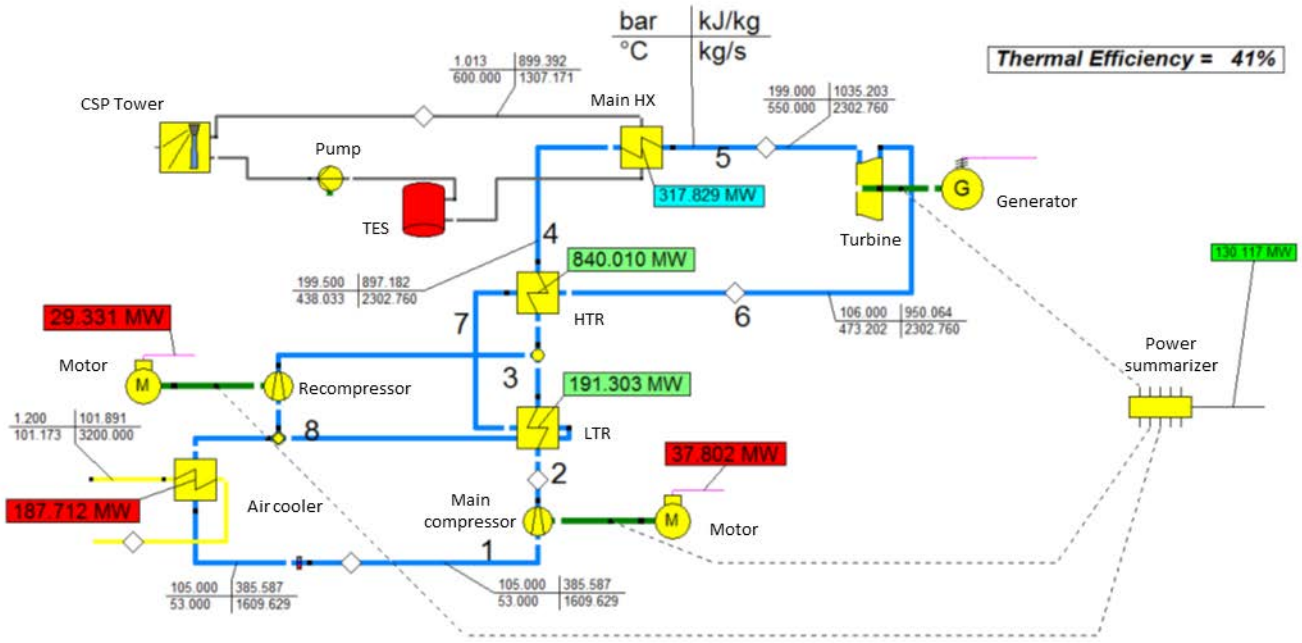

Cycle description

Recompression cycle offers high energetic efficiency with simple arrangement and minimum number of components. In this cycle, one additional compressor is added compared to the simple sCO_2 cycle configuration. The flow at point 8 is divided into two streams after leaving the low temperature recuperator. A fraction of the flow rejects heat to the cold sink at the air cooler and exits at (1) going to the main compressor near to critical point, while the other fraction is pressurized at the additional recompression compressor without cooling down. Then the two streams reach the same pressure and mix at point 3, and the mixed stream enters the high temperature recuperator (HTR) and leaving out at point 4. The cycle maximum temperature is achieved at the main heat exchanger (main HX) by absorbing the thermal energy from the molten salt fluid. Afterwards the flow at point 5 is expanded in the turbine to the low cycle pressure and enters the HTR and LTR to preheat the high-pressure stream.

The splitting ratio after point 8 should have the value, which offers the highest possible efficiency in the cycle. Hence, sensitivity analysis for the splitting ratio was conducted. Although the re-compressor requires extra energy, the overall efficiency is improved. Another important advantage is the improvement of the cycle's heat recovery. Splitting the flow after LTR decreases the heat capacity of the high-pressure side in LTR, which helps to avoid common pinch point problems.

DOI: 10.17185/duepublico/46100

2nd European supercritical CO2 Conference
August 30-31, 2018, Essen, Germany

2018-sCO2.eu-106

DESIGN, CONTROL PROCEDURE AND START-UP OF THE SCO2 TEST FACILITY SCARLETT

Wolfgang Flaig*
University of Stuttgart
Stuttgart, Germany
wolfgang.flaig@ike.uni-stuttgart.de

Rainer Mertz
University of Stuttgart
Stuttgart, Germany

Jörg Starflinger
University of Stuttgart
Stuttgart, Germany

ABSTRACT

Supercritical CO_2 (sCO_2) shows great potential as future working fluid for Joule Cycles. Compared to subcritical condition, sCO_2 shows advantages in the heat transfer due to its thermodynamic properties near the critical point, in particular high isobaric heat capacity, fluid-like density and gas-like dynamic viscosity. This can lead to the development of more compact and more efficient components, e.g. heat exchangers and compressors. Current research work at the Institute of Nuclear Technology and Energy Systems (IKE), University of Stuttgart, focuses on a retrofittable, self-propelling and self-sustaining heat removal system for nuclear reactors, based on a sCO2-turbine-compressor system, which is investigated in the frame of the EU-project He-Ro. IKE takes the leading role in the design; manufacturing and testing of a diffusion bonded compact heat exchanger, which enables the decay heat transfer from the reactor loop into the sCO2-cycle. The associated experiments are carried out in the multipurpose test facility, named SCARLETT – **S**upercritical **CAR**bon dioxide **L**oop at IK**E** Stu**TT**gart.

SCARLETT was built up for various experimental investigations of supercritical CO_2 in many different technical fields and is under operation now. It is designed to carry out experimental investigations with mass flows up to 0.110 kg/s, pressures up to 12 MPa and temperatures up to 150 °C.

SCARLETT consists of a closed loop, in which CO_2 is compressed to supercritical state and delivered to a test section. This test sections itself can be exchanged for various investigations. Downstream the test section, the CO_2 pressure will be reduced by an expansion valve and transported back into a pressure vessel, from where it is evaporated and compressed again. In opposite to many other sCO_2-facilities, the application of a high pressure pump or a circulation pump in combination with a pressurizer is refrained for the SCARLETT setup. Instead a piston compressor serves as the central component of the SCARLETT, which is responsible for the rise in pressure upstream the test section. The combined use of a compressor and an expansion valve makes a profound control strategy necessary to achieve constant and stable boundary conditions at the entrance of the test section. Additionally, the operation of SCARLETT is realised in remote control with high-grade automatization. This requires a control program and well-chosen signal routing. In order to support and complement the thermal-hydraulic design as well as the development of the control strategy, a zero dimensional model of SCARLETT was implemented in Matlab, with which the targeted stationary operating points were calculated.

This publication contains the description and the layout of the test facility, as well as the outline of the design. Furthermore the development of the control strategy is explained. Results of the start-up of SCARLETT in non-controlled and controlled mode and the modelling of the stationary operating points will be shown.

INTRODUCTION

The critical point of carbon dioxide (CO_2) is at p = 7.38 MPa and T = 30.98°C [1]. These moderate parameters compared to those of other working fluids like water (p = 22.06 MPa, T = 373.95°C [1]) favor the use of CO_2 as a substitute fluid easier to handle in current research work. Similar to all other supercritical fluids, near its critical point CO_2 shows a significant change in its thermophysical properties. Passing the pseudo-critical point with increasing temperature leads to a massive increase of the isobaric heat capacity and the decrease of the dynamic viscosity. Furthermore, the heat conduction coefficient and the density are initially similar to liquid values and then drop down after passing the pseudo-critical point with

DOI: 10.17185/duepublico/46081

higher temperature. This progression of the properties leads to a high Prandtl Number causing a significant peak in the Nusselt Number and in the heat transfer coefficient, respectively. This leads to high potential as working fluid in heat transfer near the critical point. Figure 1 shows the temperature-dependent progression of the heat transfer coefficient for CO_2, calculated with the Nusselt correlation for heated turbulent pipe flow by Dittus-Boelter [1], shown in Eq. (1):

$$Nu = \frac{\alpha \cdot d_h}{k_{layer}} = 0.023 \cdot Re^{0.8} \cdot Pr^{0.4} \qquad (1)$$

with the Nusselt number Nu, the heat transfer coefficient α, the hydraulic diameter d_h, the conductivity of the boundary layer k_{layer}, the Reynolds number Re, the Prandtl number Pr.

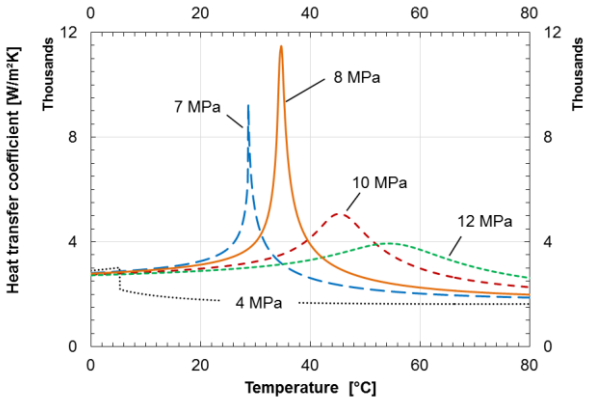

Figure 1: Calculated heat transfer coefficient according to Dittus-Boelter in dependence of the bulk temperature.

Pipe and channel flow under supercritical conditions with intensively heated walls are influenced by the significant change of fluid properties, e.g. density, viscosity, thermal conductivity. In the range of high heat flux combined with lower mass flow densities, the heat transfer strongly depends on heat flux, mass flow and other operation parameters [2]. This may trigger an unexpected and severe rise of the wall temperature, called Deteriorated Heat Transfer (DHT). The reasons for these phenomena are under scientific investigation right now and they are only understood qualitatively [3], [4], [5]. A prediction of the maximum wall temperature occurring under DHT is not possible until now.

Supercritical CO_2 flow with heat transfer has become of great interest lately, because it is suitable as a working fluid for power cycles. Dostal et al. [6] showed the possibility to realise such cycles with high efficiency and reasonable economic capital costs, if efficient and compact components, especially heat exchangers can be applied. But for the dimensioning of compact heat exchangers, it is necessary to know the heat transfer mechanisms and to obtain quantitative predictions of the necessary heat transfer. Different scientific research work focuses on a passive safety system based on a supercritical CO_2-Brayton cycle for nuclear reactors. This system is self-sustaining as well as self-propelling and able to transform the nuclear decay heat into waste heat, which will be emitted to the environment [7]. The components of this passive safety system have to be tested and numerical models for existing simulation programs have to be improved. The necessary software is partly developed, but there is still lack of experimentally validated models. In this context diffusion bonded plate heat exchangers (DBHE) as special type of compact heat exchanger are of great interest [8]. The technology seems very promising, particularly if supercritical CO_2 is used, because high heat transfer power is achievable, both on the pseudo-evaporation side and the pseudo-condensation side [9], [10].

TEST-FACILITY 'SCARLETT'

At Institut für Kernenergetik und Energiesysteme (IKE), a multipurpose test facility, named SCARLETT – **S**upercritical **CAR**bon dioxide **L**oop at IK**E** Stu**TT**gart, has been built for numerous investigations of supercritical CO_2 and is now in operation (Figure 2). This facility enables various experiments for fundamental research and applied science with supercritical CO_2. Separate test sections, which can be installed easily, provide a great variety of experimental investigations. The emphasis of the investigations will be on the validation of numerical flow simulations with supercritical fluids and the gathering of experimental data for validation of numerical simulations. The acquired knowledge and data will be used both in the nuclear field, and for non-nuclear applications, like low-temperature heat transfer, waste heat utilization, renewable energy sources and refrigeration engineering.

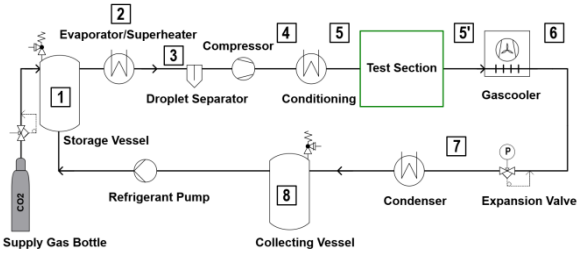

Figure 2: Scheme of the test facility SCARLETT.

Selection of Boundary Conditions. The layout data of the supercritical recompression cycle according to Dostal [6] are used as guideline for the testing facility. The high-pressure side is operating at a pressure of 20 MPa. Under these conditions, CO_2 shows a gas-like flow behavior, far off the critical point, which is not of interest for investigations about the special heat transfer phenomena. The low-pressure side in this cycle works with a pressure of 7.7 MPa and in a temperature range from 32 to 69°C for the precooler, and 69 to 157°C for the low-temperature recuperator. These conditions are near to the critical point and the base for future investigations. For a downscaled 1 MW cycle the mass flow is calculated to 11.9 kg/s. After the comparison of a typical compact heat exchanger [11], the mass flow has to be about 0.122 kg/s for the precooler and 0.027 kg/s for the low temperature recuperator. This

DOI: 10.17185/duepublico/46081

prototype allows the investigation of max. 30-50 channels per layer on a basis of max. 220 mm × 220 mm. This means a step forward compared to the investigations of Kruizenga et al. [12], who tested nine parallel channels.

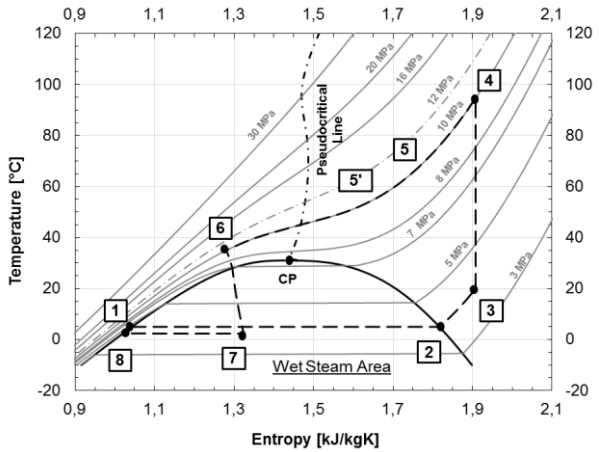

Figure 3: Temperature-entropy-diagram of the SCARLETT process.

In comparison to other sCO_2 facilities, the mass flow will not be compressed to supercritical pressure by a gear-pump or a membrane-piston-pump. Instead, a piston compressor is applied, also used by commercial refrigeration plants with a maximum mass flow of about 0.110 kg/s. This type of compressor limits the maximum achievable pressure to 14 MPa. In the SCARLETT facility, it will be possible to investigate several layers of a compact heat exchanger, which makes an appropriate value of the mass flow more import than a high pressure level. Hence, a maximum operation pressure of 12 MPa provides a suitable operation margin to the maximum pressure achievable. All other components are designed for a maximum pressure of 20 MPa, so that after an upgrading stage of the facility, a more powerful compressor can be implemented which is able to provide higher pressure up to 20 MPa.

The compressor outlet temperature of up to 160°C makes it necessary to cool the mass flow massively to work with lower test temperatures. Therefore, high thermal power has to be dissipated, which makes an adequate cooling system necessary.

The operating parameters of the facility are shown in Table 1. The power class of the planned facility fits to international existing research cycles with supercritical CO_2, e.g., cycles for fundamental research with lower mass flow but similar pressure level [10], [13] and [14]. There is also a CO_2-cycle at the University of Wisconsin, Madison for investigations on compact heat exchangers [15]. The maximum pressure of this cycle is higher (20 MPa vs. 12 MPa) but the mass flow is lower (0.015 kg/s vs. 0.110 kg/s).The test facility SCARLETT is smaller compared to the large cycles, which are used by the US Department of Energy (DOE) [16]. The cycle at the Bhaba Atomic Research Centre, Mumbai, is of interest regarding natural convection investigations with supercritical CO_2 [17]. The size and research capacity of SCARLETT fits well between the very small, single effect test facilities and the large power cycle facilities, closing this gap.

Table 1: Available experimental parameters for SCARLETT.

Parameter	Symbol	Value	Unit
Mass flow rate	$\dot{m}_{sCO_2}$	13-110	g/s
Temperature	T	5.0-150	°C
Pressure	p	7.5-12.0	MPa
Inner pipe diameter	d_i	10.0	mm

Facility Design. The technical objective of SCARLETT is to provide supercritical CO_2 at predefined temperatures and pressures to the test sections. This allows investigations in many different technical fields. Therefore, the facility is designed as a closed loop, in which CO_2 is circulating continuously. To fulfill this claim there are commonly used two types of basic facility designs in laboratory scale to shift CO_2 to the supercritical state [9], [12]. One type is using a stand-alone high pressure pump to raise the pressure, whereas the other type is consisting of a circulation pump in combination with a booster pump or a nitrogen pressurizer to hold the pressure and is applied in most cases. A third type uses a compressor and is similar to a refrigerant plant cycle. The advantage of this cycle is the availability of components and the operating efficiency of the compressor in the predefined pressure and mass flow range. Due to these reasons the compressor type facility design was chosen.

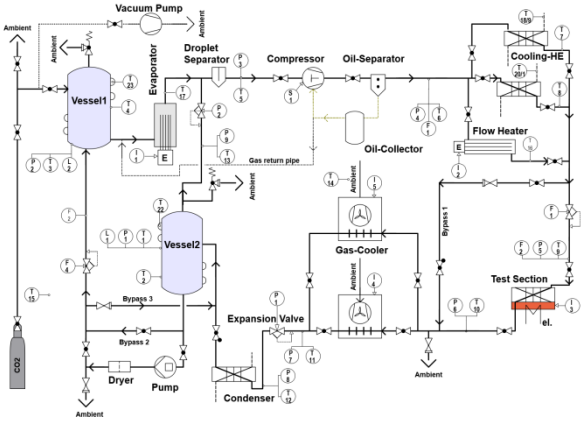

Figure 4: Piping and instrumentation diagram of the test-facility (according to EN ISO 10628).

If the SCARLETT facility is off-state, the CO_2 is stored as liquid in two pressure vessels, the storage vessel and the collecting vessel. The storage vessel can be refilled by CO_2 gas (standpipe) bottles. During operation the CO_2 passes through the SCARLETT facility, shown in Figure 2. First, it flows through an electrical heated evaporator, in which it will be isobarically evaporated and overheated of about 10 K to ensure a minimum of remaining liquid droplets in the CO_2 gas flow. After passing a droplet separator, for eliminating the last liquid droplets and to prevent the compressor from damages by liquid

DOI: 10.17185/duepublico/46081

strike, the CO_2 will be surged by a piston-compressor and compressed to supercritical pressure and temperature. Depending on the pressure ratio, outlet temperatures from 80 to 160°C are possible. After the compressor, the supercritical CO_2 flows through a heat exchanger, where it is either cooled or heated to the pre-defined test temperature (so called conditioning).

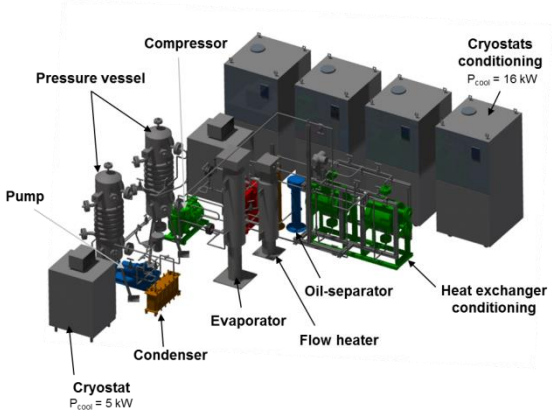

Figure 5: CAD-sketch of the test-facility SCARLETT.

At this point, the SCARLETT facility provides a user defined mass flow of sCO_2 at defined pressure and defined temperature to the test section, in which the experiments will be carried out. Because of the various conceivable investigations in the test section, it is illustrated as a box in Figure 2, which shows the scheme of the CO_2 loop. After leaving the test section the CO_2 is cooled to ambient temperature in a forced-ventilation gas cooler that is installed outside the laboratory building. Downstream of the coolers an expansion valve reduces the CO_2 pressure in an isenthalpic process to subcritical conditions into the wet steam area. Afterwards, the CO_2 is fully isobarically condensed in a plate heat exchanger and flows into the collecting vessel. A refrigeration pump installed between both pressure vessels delivers the liquid CO_2 back into the storage vessel closing the loop.

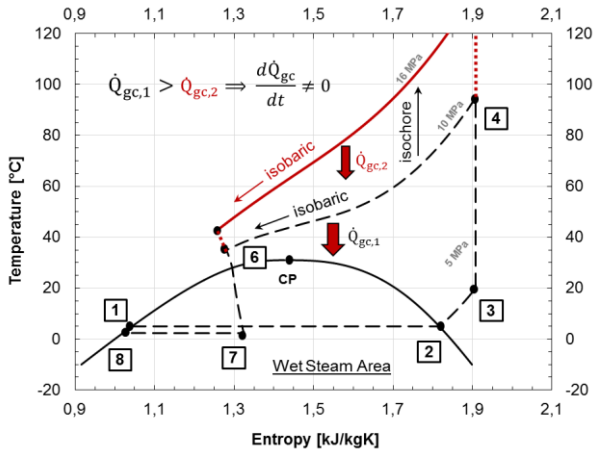

Figure 6: Influence of a transient on the SCARLETT process.

The thermodynamic cycle of the testing facility is plotted in Figure 3 by a temperature-entropy-diagram. In Figure 4, the detailed piping and instrumentation diagram of the facility is presented. Figure 5 shows a CAD-sketch of the CO_2 facility SCARLETT including peripheral components and the laboratory. Figure 7 shows pictures of the facility.

The test facility works similar to a refrigerant plant, this means, there are certain factors which influence the stationary behavior and thereby the experimental parameters, e.g. frequency of the current supplying the compressor, degree of opening of the expansion valve, coolant temperature at the inlet of the condenser, ambient temperature, speed of the gas cooler fan, conditioning cooling power. A variation of at least one parameter induces a temporary transient which leads finally to the adjustment of different stationary experimental parameters. This is exemplarily explained for a reduction of the gas cooler power (triggered by a higher ambient temperature e.g.) in Figure 6. The pressure raises after an isochoric change of state on the high pressure side due to the constrained heat power emission. The mass flow rate subsequently decreases due to the characteristic of the piston compressor. This has to be taken into account for the design and predicting of the stationary operating points.

The primary design equation is derived from an energy balance (Eq. (2)) and applied on heat transferring components, like heat exchangers, evaporator and condenser.

$$\dot{Q}_{HT} = \dot{m}_{sCO_2} \cdot \left(h_{in}(T,p) - h_{out}(T,p)\right) \qquad (2)$$

with the heat transfer rate $\dot{Q}_{HT}$, the sCO_2-mass flow $\dot{m}_{sCO_2}$, the specific enthalpy $h_{in}(T,p)$ at the entrance and the specific enthalpy $h_{out}(T,p)$ at the outlet of the component.

Figure 7: Current picture of the test-facility SCARLETT with an integrated experiment.

Furthermore the actual achievable heat transfer rate is given by Eq. (4) and linked with Eq. (3) to calculate the necessary heat transferring area.

$$\dot{Q}_{HT} = \alpha \cdot A \cdot \theta_{log} \qquad (3)$$

DOI: 10.17185/duepublico/46081

with heat transfer coefficient α, the heat transfer area A and the mean logarithmic temperature Θ_{log}.

The ejected mass flow of the compressor is not constant. It depends on the pressure ratio Π (high pressure p_1 to low pressure p_0) and the CO_2 density at the inlet of the compressor, according to Eq. (5):

$$\dot{m}_{sCO_2} = n \cdot V_{pd} \cdot \rho_0(T_s, p_0) \cdot \lambda(\Pi) \tag{4}$$

with the rotational speed n, the piston displacement V_{pd}, the density of the suction gas ρ_0 and the delivery rate λ.

The rotational speed can be calculated again by the effective frequency of the 3-phase current f_c and the number of magnetic poles in the induction motor m according to Eq. (5):

$$n = \frac{f_c}{m} \tag{5}$$

The change of state caused by the expansion valve is of isenthalpic nature. The induced pressure drop is calculated by Eq. (6).

$$\Delta p_{EV} = (p_1 - p_0) = \frac{1}{\rho_m} \cdot \left(\frac{\dot{m}_{sCO_2}}{K_V}\right)^2 \tag{6}$$

with the pressure drop of the expansion valve Δp_{EV}, the mean sCO_2 density between inlet and outlet ρ_m and the flow coefficient of the expansions valve K_v.

The outlet temperature and steam quality can be calculated with help of the CO_2 properties, delivered by Refprop , when p_0 and p_1 are known.

In order to receive a definite system of equations, Eq. (7) is applied, which considers that a change of the operating point of the facility induces a relocation of CO_2 mass from low pressure to high pressure side or vice versa.

$$\frac{dm_{HP}}{dt} = -\frac{dm_{LP}}{dt} \Rightarrow \frac{d\rho_{HP}(T,p) \cdot V_{HP}}{dt} = -\frac{d\rho_{LP}(T,p) \cdot V_{LP}}{dt} \tag{7}$$

with the total CO_2 mass on the high pressure and low pressure side $m_{HP/LP}$, as well as the density and the volume on both sides $\rho_{HP/LP}$, $V_{HP/LP}$.

Experimental results show, that the temperature of the coolant fluid (water/glycol mixture) on the secondary side of the condenser is affecting the CO_2 temperature and the corresponding CO_2 vapor pressure p_0 on the low pressure side. To simplify the calculations, $_{p0}$ can be assumed by the coolant temperature.

The pressure drop in the pipe is estimated by Eq. (8):

$$\Delta p_{Pipe} = \frac{1}{2} \cdot \dot{m}_{sCO_2}{}^2 \cdot f \cdot \frac{L}{A_{Pipe}^2 \cdot d_i \cdot \rho} \tag{8}$$

with the pressure drop of the expansion valve Δp_{EV}, the Darcy friction factor f, the length of the pipe L, the cross sectional area of the pipe A_{pipe} and the fluid density ρ.

The Darcy friction factor is calculated according to Colebrook for turbulent flow.

These equations were implemented in *Matlab* and used for a zero-dimensional model to design, predict and analyze the steady state behavior of the facility.

Mechanical stress of pressurized components is calculated according to standard DIN EN 13445-3 [18].

Oil Recirculation System. A piston compressor needs lubrication oil for preventing the compressor from mechanical damage, such as piston seizure. Refrigeration-machine oil based on Polyalkylenglykolen (PAG) is used according to the recommendation of the compressor manufacturer. The decomposition temperature of this oil is 180°C, which suits well to the maximum temperature of the compressor.

Part of this oil is entrained into CO_2, especially at supercritical state. Dang et al. [19] showed, that in experiments with oil concentrations of more than 1 %, pure oil is enriching at the tube walls, dissolving liquid CO_2 and subsequently influencing the pressure drop and the heat transfer significantly. In order to reduce these effects, an oil recirculation system is installed in SCARLETT, which is shown in Figure 4. This system works as follows:

An over-dimensioned coalescence separator is installed in the main pressure gas pipe right after the compressor. It extracts more than 99 percent of the oil from the sCO_2 gas flow. Additionally it serves as a buffer volume to smoothen inevitable oscillations that are deriving from the piston displacement. The removed oil, together with partly gaseous CO_2, flows into an oil collector vessel. The CO_2 fumes upwards and is released into the low pressure side of the test facility through a bypass pipe and a check valve. In case of an oil low level signal at the oil sump of the compressor, a magnetic valve opens and the oil flows back from the collector to the compressor, driven by pressure gradient. The remaining oil concentration will be obtained by a weighting procedure as described by Dang et al. [19]

Controlling. To obtain the user-given test condition at the entrance of the test-sections, the facility has to reach and stabilize defined operation parameters, i.e. temperature, pressure and mass flow. To fulfill this requirement, it is necessary to control all three parameters during operation. Because of the mutual influence of the parameters on each other, a decentralized Multi-Input-Multi-Output (MIMO) control strategy was chosen. This means temperature, pressure and mass flow are regulated by separate PID-controllers. The pressure is set by the flow resistance of the expansion-valve and the temperature by the cooling power of the cryostats supplying the conditioning heat exchanger. The mass flow can be varied by the rotation speed of the compressor engine, which is induced by a frequency converter. The main functions for the controlling and surveillance are concentrated in one program,

DOI: 10.17185/duepublico/46081

created by the software *Agilent-Vee*. All components are remotely controlled by this program processing analog or digital signals (hexadecimal code in complement representation) via serial ports. Eq. (9) shows the law of controlling for a PID.

$$u(t) = K_p \cdot \left(e(t) + \frac{1}{T_N} \cdot \int_0^T e(t)\, dt + T_{vh} \cdot \frac{de}{dt} \right) \qquad (9)$$

with the time continuous set value *u(t)*, the time continuous control deviation *e(t)*, the proportional control amplification K_p, the reset time T_N and the lead time T_{Vh}.

In order to implement a PID into the digital program, it has to be discretized by z-Transformation. Applying the difference rule afterwards leads to the position-algorithm in Eq. (10), which is calculated my means of measurement data to set the values for the expansion valve and the frequency converter.

$$\begin{aligned} u(k) = u(k-1) + e(k) \cdot \left(K_p + \frac{K_p \cdot \Delta t}{2 \cdot T_N} + \frac{K_p \cdot T_{vh}}{\Delta t} \right) \\ - e(k-1) \\ \cdot \left(K_p - \frac{K_p \cdot \Delta t}{2 \cdot T_N} + \frac{2 \cdot K_p \cdot T_{vh}}{\Delta t} \right) + e(k \\ - 2) \cdot \left(\frac{K_p \cdot T_{vh}}{\Delta t} \right) \end{aligned} \qquad (10)$$

with the time discrete set value *u(k)* and the time discrete control deviation *e(k)*.

The PID controllers for pressure and mass flow have been implanted digitally within the software *Agilent Vee*. In order to guarantee sufficient controlling quality, the pressure and mass signals have been investigated by a Fourier-transformation to detect the dominant frequencies. No relevant frequencies above 0.1 Hz were registered, which means that the clock cycle time of the Agilent system of 1.2 s is sufficient to fulfill the Nyquist-Shannon- sampling-theorem. Furthermore the integration time of the pressure and mass signal is raised on 100 net cycles to avoid aliasing.

The PID controller for the temperature is designed as an analog device, which is integrated into the cryostats and will set the temperature of the cooling fluid according to Eq. (9) as well.

Measurement Techniques. To control the test SCARLETT facility, several measurement instruments are available. All sensors are connected to an *Agilent 34980a* data acquisition system, which allows sending and receiving data to and from analogue devices. Table 2 gives an overview of the applied measurements instruments and their measuring range and their accuracy, respectively. Besides the described measurement devices, an observation window will be installed to enable optical measurements.

Table 2: Measurement devices applied in SCARLETT.

Parameter	Device	Range	Accuracy
Mass flow rate	Coriolis	13-130 g/s	0.5%
Temperature	Pt-100	-20-200 °C	0.15+0.002 T
Pressure	Piezoresistive	0-20 MPa	0.15%
Liquid-level	Difference Pressure	0.2-1 m	0.075%

Safety Installations. The threshold limit value of CO_2 at working place is 5000 ppm, defined for German workplaces by the German Government at TRGS 900 [20]. CO_2 is toxic for humans in concentration higher than 5 % of the breathing air. Furthermore, the high pressure in the facility can possibly be a safety risk in the case of a failure of single components. However, to ensure best possible safety for employees in the CO_2-laboratory, there are several arrangements, which have been applied to the operation of the facility:

- Gas detection devices to warn of a dangerous concentration of CO_2.
- Exhaust extraction system to maintain a low level of CO_2 concentration in the air.
- Inhabitancy in the CO_2-laboratory during operation is not permitted. Instead, the laboratory will be controlled from an adjacent laboratory.
- Safety valves are installed in the low- and high-pressure side to exclude an undue pressure peak. Furthermore, pipes flown through by liquid CO_2 are not lockable or equipped with safety valves.
- The controlling software is operating the facility with a minimum of human interventions. Especially, temperatures and pressures are surveilled steadily. Invalid values are countered automatically by shutting down the compressor and opening the expansion valve.
- Safety shutdown of compressor, evaporator and heaters via relays if there is no signal received from the controlling software for more than 10 s.

The complete facility is constructed according to the European Pressure Equipment Directive (guideline 97/23/EG) [21] and the standard (DIN EN 378) for refrigerating plants [22]. It has been certified by the German Technical Control Board (TÜV, Technischer Überwachungsverein).

RESULTS

The start-up of the test facility includes the implementing and testing of the controllers and the controlling software while bypassing the test section. The main measurement campaign concerning pressure loss and heat transfer of the DBHE is finished.

Start-Up of the Test-Facility. Figure 8 shows the compressor curve, derived by several experiments. The mass flow emitted by the compressor depends on two parameters, the compression ratio (high pressure to low pressure) and the

DOI: 10.17185/duepublico/46081

temperature of the condensate, which corresponds directly to the suction pressure. This means that an increasing test pressure (included in the compression ratio) influences the mass flow reciprocally, which is typical for a piston compressor. This result is emphasized by Eq. (6) for calculation of the emitted mass-flow of a piston compressor.

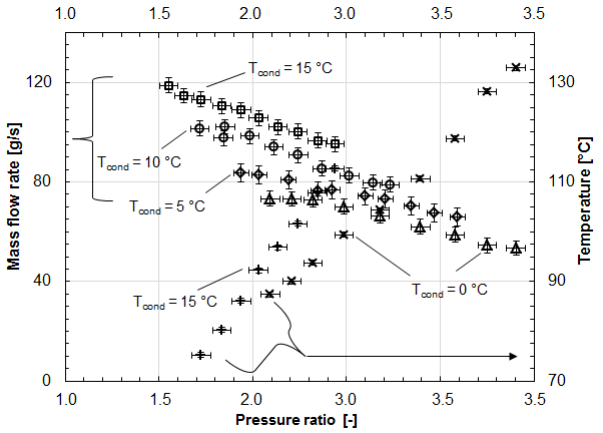

Figure 8: Characteristic line of the compressor Bitzer 4PTC.

Although the piston displacement is constant, the mass filling out this volume in one rotation depends on the density of the suction gas (depends on superheating temperature and low pressure again) and is inhibited by the delivery rate. The delivery rate takes mass loss and the decreasing of the density inside the compressor into account, which is mainly induced by a higher pressure ratio. Figure 8 shows furthermore that the emitting temperature of the compressor is raising with higher pressure ratio, with a lower temperature of the condensate or with lower suction pressure. This leads to the need to control the cooling power of the cryostats on the secondary side of the conditioning during operation as well.

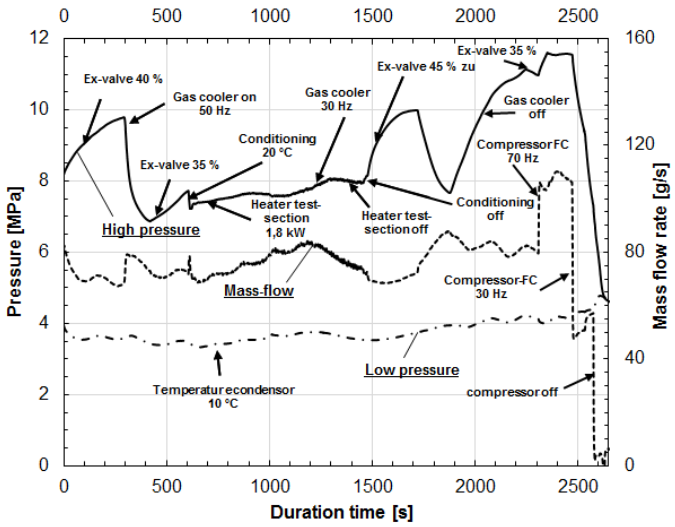

Figure 9: Process uncontrolled.

The described characteristic behavior of a compressor leads to an unsteady temporal behavior of the test pressures and the mass flow rate (like it is in a non-controlled refrigerant cycle), as can be seen in Figure 9. The pressure and mass flow rate are strongly influenced by several parameters like the rotation speed of the gas cooler fan, the condensing temperature, the cooling power and temperature in the conditioning and the heating power and temperature in the test-section.

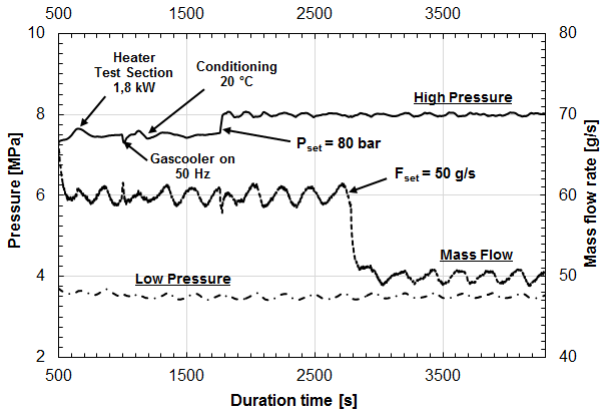

Figure 10: Process controlled.

The mass flow rate and the pressure are stabilized by changing the rotation speed and varying the opening of the expansion-valve, respectively, which is the task of the digital controllers. The results are shown in Figure 10, where the time–depended behavior of the control parameters pressure and mass flow rate can be seen, while PID-controllers are activated. Even under influence of disturbance value, like advanced heat emission at the gas cooler by starting the fan, the pressure and mass flow rate is constant and the disturbance suppressed by the controllers. After changing the set-points, the pressure and the mass flow rate are changing fast and continuously, confirming a reasonable operation of the facility by the settings of the controllers.

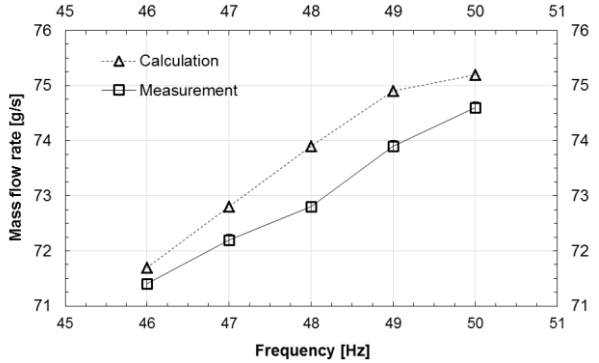

Figure 11: Dependency of the mass flow rate on the frequency of the compressor engine.

DOI: 10.17185/duepublico/46081

Figure 11 to Figure 13 show the comparison between the calculation, done for the SCARLETT design and the measurements of stationary operating points regarding exemplarily the mass flow rate. Figure 11 is dedicated to point out the influence of the 3-phase-frequency on the mass flow rate. Furthermore Figure 12 shows the effect of varying the degree of opening of the expansion valve on the mass flow rate. Figure 13 features the impact of the coolant temperature at the inlet of condenser on the mass flow rate.

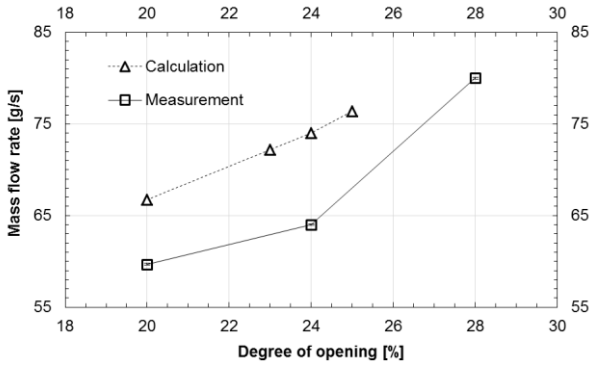

Figure 12: Dependency of the mass flow rate on the degree of opening of the expansion valve.

All three cases show a sufficient congruence between calculation by the zero dimensional *Matlab* model and the experimental data. The process of the mass flow rate during a variation of the influence parameters frequency, coolant temperature and degree of opening of the expansion valve is displayed well by the model. The quantitative accordance is given in general. The discrepancy between the calculated and the measured mass flow rate is less than 10 g/s in all three cases and less than 5 g/s for a variation of coolant temperature and frequency.

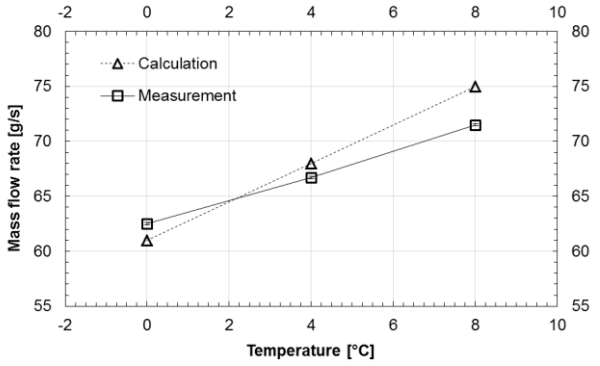

Figure 13: Dependency of the mass flow rate on the coolant temperature of the condenser.

SUMMARY

A multipurpose test facility for supercritical CO_2 has been built. Variable test sections, which can be exchanged easily, allow various experiments for fundamental and applied research, especially in the field of the validation of numerical models for turbulent flow with heat transfer, e.g. in compact heat exchangers in supercritical carbon dioxide. The test facility is designed as closed loop, which delivers a CO_2 mass flow up to 0.110 kg/s to the test section with a maximum pressure of 12 MPa. The test temperature can be set from 5 to 150°C. Depending on this temperature, the transferred thermal power of the facility can raise up to 50 kW.

A decentral PID controlling is implemented to enable stable values of test temperature, pressure and mass flow. A zero dimensional model of the test facility was used to design the facility and the targeted stationary operating points. The data calculated with the help of this model show sufficient congruence with experimental ones.

NOMENCLATURE

A	heat transferring area, m²
A_{pipe}	cross sectional area of pipe, m²
c_p	isobaric heat capacity, J/kg K
d_i	inner diameter, m
$e(k)$	control deviation discrete, Pa or kg/s
$e(t)$	control deviation time-continuous, Pa or kg/s
f	Darcy friction factor
f_c	frequency of the 3-phase current, Hz
F_{set}	setpoint of mass flow rate, kg/s
$h_{in/out}$	specific enthalpy at inlet/outlet; J/kg
k_{layer}	heat conductivity of the boundary layer, W/m K
K_p	proportional control amplification, -
K_v	flow coefficient of expansion valve, m²
L	length, m
m	number of magnetic poles, -
$m_{LP/HP}$	mass on low pressure/high pressure side, kg
$\dot{m}_{sCO_2}$	mass flow rate, kg/s
n	rotational speed, 1/s
p	pressure, Pa
p_0	pressure on low pressure side, Pa
p_1	pressure on high pressure side, Pa
P_{cool}	cooling power, W
P_{set}	setpoint of pressure, Pa
$\dot{Q}$	heat transfer rate, W
$\dot{Q}_{gc}$	heat transfer rate dissipated at gascooler, W
t	time, s
T	temperature, °C
T_{cond}	temperature of condenser cooling fluid, °C
T_N	reset-time, s
T_s	suction gas temperature, °C
T_{vh}	lead-time, s

DOI: 10.17185/duepublico/46081

$u(k)$	set-value discrete, - or Hz
$u(t)$	set value time-continuous, - or Hz
V_{LP}	volume of low pressure side, m³
V_{HP}	volume of high pressure side, m³
V_{pd}	volume of piston displacement, m³

Greek Letters

α	heat transfer coefficient, W/m² K
Δp_{EV}	pressure drop in expansion valve, Pa
Δp_{Pipe}	pressure drop in pipe, Pa
Δt	cycle time, s
η	dynamic viscosity, Pa s
Θ_{log}	mean logarithmic temperature, K
λ	delivery rate
Π	pressure ratio; $\left(\frac{p_1}{p_0}\right)$
ρ	density, kg/m³
ρ_{LP}	density on low pressure side, kg/m³
ρ_{HP}	density on high pressure side, kg/m³
ρ_0	density at compressor inlet, kg/m³
ρ_m	mean density, kg/m³

Non-Dimensional Numbers

Nu	Nusselt number; $\left(\frac{\alpha \cdot d_i}{k_{layer}}\right)$
Pr	Prandtl number; $\left(\frac{\eta}{c_p \cdot k_{layer}}\right)$
Re	Reynolds number; $\left(\frac{\dot{m}_{sCO_2} \cdot d_i}{A_{pipe} \cdot \eta}\right)$

Subscripts

amb	ambient
cool	cooling
cond	condenser
EV	expansion valve
gc	gas cooler
HP	high pressure side
i	inner
in	inlet
layer	boundary layer
log	logarithmic
LP	low pressure side
m	mean
N	reset time
out	outlet
P	proportional
pd	piston displacement
pipe	pipe
sCO_2	supercritical carbon dioxide
set	setpoint
v	valve
vh	lead time

Acronyms and Abbreviations

CAD	Computer Aided Design
CP	Critical Point
DBHE	Diffusion Bonded Heat Exchanger
DIN	Deutsches Institut für Normung
IKE	Institut für Kernenergetik und Energiesysteme
Pt-100	100 Ohm Platin resistance thermometer
SCARLETT	Supercritical CARbon dioxide Loop at IKE Universität StuTTgart
(s)CO_2	(supercritical) Carbon Dioxide
TRGS	Technische Regeln für GefahrStoffe, Guideline for dangerous Substances
TÜV	Technischer ÜberwachungsVerein, German Technical Control Board

ACKNOWLEDGEMENTS

This work was supported by a grant from the Ministry of Science, Research and the Arts of Baden-Württemberg (Az: 32-7533.-8-112/81) to Wolfgang Flaig. and by Deutsche Forschungsgemeinschaft (DFG).

The project leading to this application has received funding from the Euratom research and training programme 2014-2018 under grant agreement No 662116.

REFERENCES

[1] Verein Deutscher Ingenieure (VDI), VDI-Wärmeatlas, Düsseldorf: VDI-Verlag, 2013.

[2] M. E. Shitsman, "Impairment of the Transmission at Supercritical Pressures," *Teplofizika Vysokih Temperature,* vol. 1, no. 4, pp. 237-244, 1963.

[3] B. S. Shiralkar and P. Griffith, "Detoriation in heat transfer to fluids at supercritical pressures and high heat fluxes," *J. Heat Transfer, Trans. ASME,* vol. 91, no. 1, pp. 27-36, 1969.

[4] J. D. Jackson and W. B. Hall, "Forced Convection Heat Transfer to Fluids at Supercritical Pressues," *Turbulent Forced Convection in Channels and Bundles,* pp. 563-611, 1979.

[5] V. G. Razumovskiy, A. P. Ornatskiy and Y. M. Mayevskiy, "Local Heat Transfer and Hydraulic Behavior in Turbulent Channel Flow of Water at Supercritical Pressure," *Heat Transfer Soviet Research,* vol. 22, pp. 91-102, 1990.

[6] V. Dostal, M. Driscoll and P. Heijzlar, "A Supercritical Carbon Dioxide Cycle for Next Generation Nuclear Reactors," MIT- ANP-TR-100, Cambridge, Massachusetts, USA, 2004.

DOI: 10.17185/duepublico/46081

[7] J. Venker, "A Passive Heat Removal Retrofit for BWR's," *Nuclear Engineering International,* vol. 58, pp. 14-17, 2013.

[8] N. Tsuzuki, Y. Kato and T. Ishiduka, "High Performance Printed Circuit Heat Exchanger," *Applied Thermal Engineering,* vol. 27, no. 10, pp. 1702-1707, 2007.

[9] S. Pitla, E. A. Groll and S. Ramadhyani, "New Correlation to Predict the Heat Transfer Coefficient During In-Tube Cooling of Turbulent Supercritical CO2," *International Journal of Refrigeration,* vol. 25, no. 7, pp. 887-895, 2002.

[10] S. H. Yoon, J. H. Kim, Y. W. Hwang, M. S. Kim, K. Min and Y. Kim , "Heat Transfer and Pressure Drop Characteristics During the In-Tube Cooling Process of Carbon Dioxide in the Supercritical Region," *International Journal of Refrigeration,* vol. 26, no. 8, pp. 857-864, 2003.

[11] R. Le Pierres, D. Southall and S. Osborne, "Impact of Mechanical Design Issues on Printed Circuit Heat Exchangers," in *Proceedings of sCO2 Power Cycle Symposium 2011*, Boulder, CO, USA, May 24-25 2011.

[12] A. Kruizenga , M. Anderson, R. Fatima, M. Corradini, A. Towne and R. Devesh, "Heat Transfer of Supercritical Carbon Dioxide in Printed Circuit Heat Exchanger Geometries," *ASME Journal of Thermal Science and Engineering Applications,* vol. 3, no. 3, p. 031002, 2011.

[13] S. H. Song, H. Y. Kim, H. Kim and Y. Y. Bae, "Heat Transfer Characteristics of a Supercritical Fluid Flow in a Vertical Pipe," *Journal of Supercritical Fluids,* vol. 44, no. 2, pp. 164-171, 2008.

[14] P. C. Simoes, J. Fernandes and J. P. Mota, "Dynamic Model Supercritical Carbon Dioxid Heat Exchanger," *Journal of Supercritical Fluids,* vol. 35, no. 2, p. 2005, 167-173.

[15] M. D. Carlson, A. Kruizenga , M. Anderson and M. Corradini, "Measurements of Heat Transfer and Pressure Drop Characteristics of Supercritical Carbon Dioxide Flowing in Zig-Zag Printed Circuit Heat Exchanger Channels," in *Supercritical CO2 Power Cycle Symposium*, Boulder, Colorado, USA, May 24-25, 2011.

[16] S. A. Wright, R. F. Radel, M. E. Vernon, G. E. Rochau and P. S. Pickard, "Operation and Analysis of a Supercritical CO2 Brayton Cycle," Sandia National Laboratories, Albuquerque, New Mexico, USA, 2010.

[17] B. T. Swapnalee, P. K. Vijayan, M. Sharma and D. S. Pilkhwal, "Steady State Flow and Static Instability of Supercritical Natural Circulation Loops," *Nuclear Engineering and Design,* vol. 245, pp. 99-112, 2012.

[18] Deutsches Institut für Normung (DIN), "Unbefeuerte Druckbehälter-Teil 3: Konstruktion," Beuth Verlag, No. EN 13445-3:2011-2, Berlin, 2011.

[19] C. Dang, K. Hoshika and E. Hihara, "Effect of lubricating oil on the flow and heat-transfer characteristics of supercritical carbon dioxide," *International Journal of Refigeration,* vol. 35, pp. 1410-1417, 2012.

[20] Bundesministerium für Arbeit und Soziales, Technische Regeln für Gefahrstoffe, TRGS 900, Berlin: Gemeinsames Ministerialblatt BArBl, 2006.

[21] Das Europäische Parlament und der Rat der Europäischen Union, Richtlinie 97/23/EG des Europäischen Parlaments und des Rates vom 29. Mai 1997 zur Angleichung der Rechtsvorschriften der Mitgliedsstaaten über Druckgeräte, Brüssel: ABl 181, 1997.

[22] Deutsches Institut für Normung (DIN), "Kälteanlagen und Wärmepumpen-Sicherheitstechnische und Umweltrelevante anforderungen," Beuth Verlag, EN 378-1:2008+A2:2012, Berlin, 2012.

DOI: 10.17185/duepublico/46081

2nd European supercritical CO_2 Conference
August 30-31, 2018, Essen, Germany

2018-sCO_2.eu-112

DESIGN OF A SINGLE-SHAFT COMPRESSOR, GENERATOR, TURBINE FOR SMALL-SCALE SUPERCRITICAL CO_2 SYSTEMS FOR WASTE HEAT TO POWER CONVERSION APPLICATIONS

Maxence De Miol
Enogia SAS
Marseille, France

Giuseppe Bianchi*
Brunel University London,
Uxbridge, United Kingdom
Email: giuseppe.bianchi@brunel.ac.uk

Gabriel Henry
Enogia SAS
Marseille, France

Norman Holaind
Enogia SAS
Marseille, France

Savvas A. Tassou
Brunel University London,
Uxbridge, United Kingdom

Arthur Leroux
Enogia SAS
Marseille, France

ABSTRACT

Waste heat to power conversion is a promising approach to reduce the carbon intensity in industry and manufactured goods. In this framework, bottoming thermodynamic cycles using supercritical carbon dioxide as working fluid (sCO_2) might be a suitable and efficient technology to consider especially for heat sources characterized by streams at high temperatures (>300°C). The compactness of sCO_2 turbomachinery is one of the advantages of sCO_2 systems over the conventional technologies; on the other hand, the reduced dimensions limits the bottom end of the power size achievable with such systems. The scarce amount of scientific and industrial literature for electrical power sizes between 50 and 100 kW further demonstrates this. The current research work summarizes the design procedure as well as the technical and technological challenges involved in the design of a single-shaft compressor, generator, turbine unit (CGT) for a sCO_2 system with a 50kWe nominal power output. First an overview of the High Temperature Heat To power Conversion facility (HT2C) under construction at Brunel University London will be presented. Then, highlights of the CGT design are presented in terms of structural and packaging aspects as well as with regards to the ancillary lubrication, drainage and cooling loops.

INTRODUCTION

In the last decades, the need of lowering the environmental impact as well as of optimizing industrial processes has driven research to innovative concepts and equipment with regards to three major areas: energy efficiency, energy saving and energy recovery. Out of these strategies, the energy recovery theoretically implies no changes in the existing energy system but rather aims at converting part of the energy that these systems currently reject to the environment in different forms.

With regards to thermal energy, latest reports state that most the waste processes involve heat sources with temperatures below 300°C [1]. However, the well-known Carnot efficiency states that the potential of a heat source depends on its exergy content and ultimately to its temperature. According to [1], high temperature industrial waste heat potential has been estimated as 3367 TWh worldwide. Using the same methodology, the authors analyzed the European scenario concluding that high temperature industrial waste heat potential amounts to 275 TWh, from nonmetallic minerals (glass, cement), nonferrous materials (aluminum) as well as iron and steel (the industrial sectors where most of the high-grade waste heat processes can be found).

Unlike direct use heat recovery systems, which may require severe modifications to the industrial process in order to use the thermal power recovered within the industrial site or export it over the fence, grid-connected heat to power conversion systems do not necessarily need a local heat user or a storage system. Also, recovery in electrical form can provide greater CO_2 emission savings than recovery in thermal form as for instance in UK, recovering 1 kWh of thermal energy saves 0.204 kg of CO_2 while if the 1 kWh was electrical the savings would be equal to 0.348 kgCO_2 [2].

Existing heat to power conversion systems have mostly addressed medium grade waste heat sources (100-300°C) through steam or Organic Rankine Cycle (ORC) systems. However, for high-grade heat sources, these approaches become less suitable due to the high energy losses involved with two-phase heat recovery or because of the degradation of the organic fluid properties currently employed in these systems. On the other hand, a Joule-Brayton cycle working with CO_2 in supercritical phase would allow to achieve better efficiencies than a steam Rankine Cycle at lower temperatures [3, 4] and at

DOI: 10.17185/duepublico/46086

lower capital and operating costs. Operating with very dense fluids would indeed lead to compact equipment that would also require less maintenance [5]. Furthermore, the sCO_2 technology would allow a better thermal matching between the temperature glides of working fluid and heat source and thus would achieve a higher 2nd law (exergy) efficiency [6]. For these reasons, simplified or more complex configurations of sCO_2 power cycles are being considered for the next nuclear and fossil fuel power generation (500 to 1000 MWe) [7-9], modular nuclear power generation (300 MWe) [10–13], solar thermal power generation (10 to 100 MWe) [14–21], shipboard propulsion, geothermal, oxy-combustion (1 to 100 MWe) [22–31], and industrial scale waste heat recovery (1 to 10 MWe) [32,33]. The technical feasibility of such systems has been so far assessed mostly at theoretical level and it has been focused on cycle analyses of large power scale sCO_2 systems for power generation applications.

The research presented in this paper, on the other hand, addresses one of the most challenging areas of the sCO_2 heat to power conversion field by presenting the design of one of the first experimental sCO_2 facilities in Europe. The focus is on the design of a small-scale sCO_2 system in the power range around 50 kWe.

OVERVIEW OF THE HT2C FACILITY

The I-ThERM project, funded by the European commission within the h2020 research and innovation program, aims at demonstrating, among the other technologies, the feasibility of a plug&play sCO_2 system for high grade heat to power conversion applications. Accordingly, an industrial scale High Temperature Heat To power Conversion facility (HT2C) has been designed at Brunel University London taking into account not only research challenges but also industrialization aspects.

Unlike existing experimental sCO_2 facilities, whereas the heat input to the working fluid is provided through electrical resistance heaters, a novel feature of the current research is the investigation and development of direct recovery heat exchangers using flue gas as heat source. In order to do that, HT2C is equipped with a process air heater whose main features are listed in Table 1 and shown in Figure 1. Noteworthy ones are the high flexibility of operation as well as power size, which allows to test bottoming systems with power outputs in the order to tens of kilowatts.

Inlet conditions to the high temperature test section, where the sCO_2 system will be installed, are controlled with a proprietary system which relies on primary fan speed and flue gas flow rate as control signals while temperature downstream the process air heater and air flow rate are used for control feedback. A similar control architecture is repeated for the low temperature test section, whose provision is beyond the sCO_2 project.

As heat sink for the H2TC facility, a dry cooler system will be employed. Its features are listed in Table 2 and shown in Figure 2.

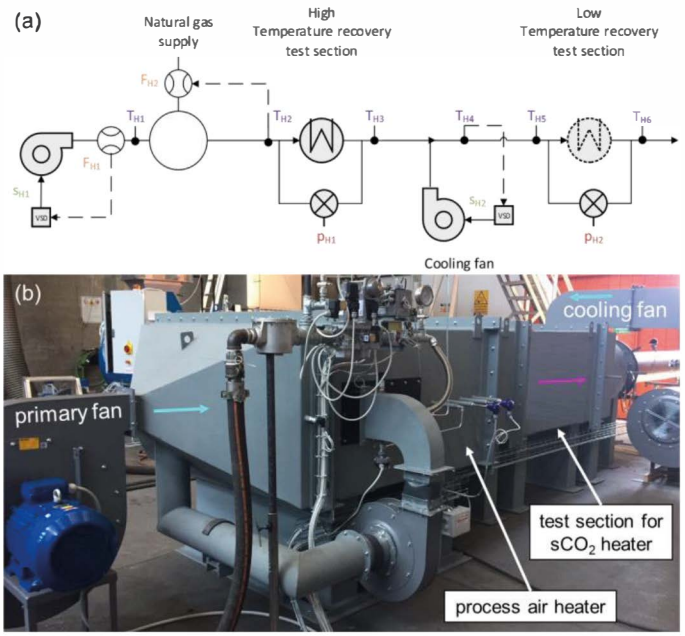

Figure 1: P&ID (a) and picture (b) of the heat source

Table 1: Heat source specifics.

Net max power supplied	830 kW
Maximum operating temperature	780 °C
Pressure drop allowed for primary heat exchanger	70 mbar
Fuel	Natural Gas (G20)
Gas input peak design	83.5 Nm³/h

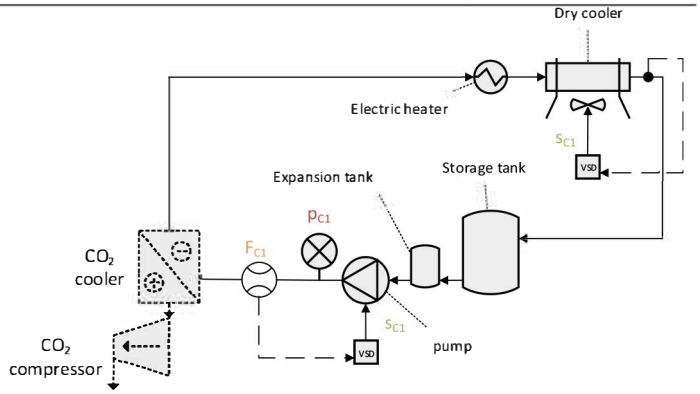

Figure 2: P&ID of the heat sink.

Table 2: Heat sink specifics.

Total cooling duty	500 kW
Water on temperature	60 °C
Water off temperature	20 °C
Mono-Ethylene glycol	25%
Total airflow at standard conditions	35.7 kg/s
Total fin and tube surface area	850 m²
Maximum fluid temperature	100 °C

DOI: 10.17185/duepublico/46086

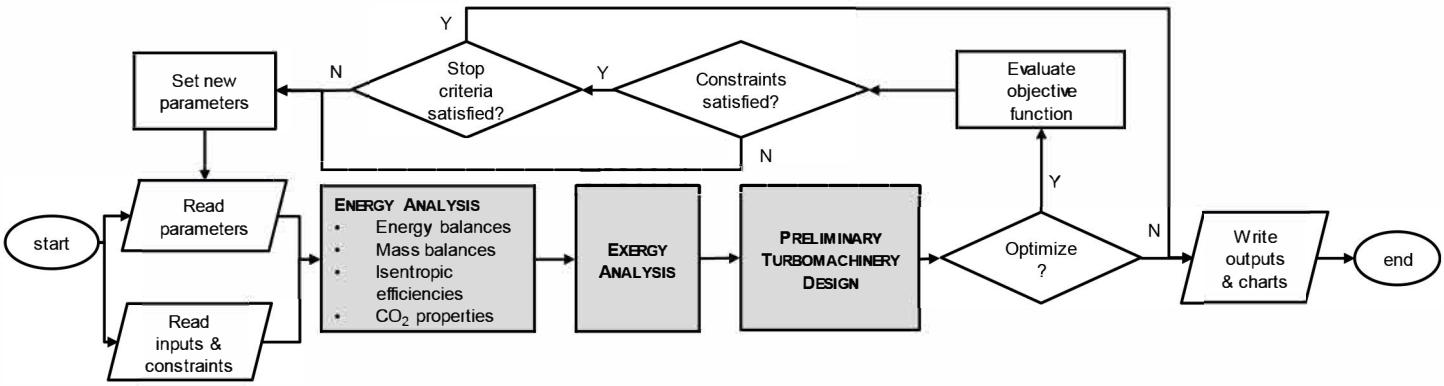

Figure 3: Thermodynamic design procedure

The dry cooler employs variable speed drives for the pump and the fans. A noteworthy feature of the chosen layout is the presence of an electric heater to warm-up the auxiliary fluid in the cooling loop to be used during the startup phase of the tests.

DESIGN OF THE SCO_2 SYSTEM

Within the scope of the I-ThERM project and the testing capabilities of the HT2C facility, the design of the bottoming sCO_2 system was bounded by several constraints that influenced its design. With reference to a theoretical study in which the authors compared several sCO_2 cycle layouts considering technical and economic figures, for the power range of interest it resulted that the most suitable system configuration for the current application was the simple regenerated layout [34]. This architecture requires the lowest number of components (3 heat exchangers, 1 compressor and 1 turbine) and therefore allows to minimize the investment cost of the heat to power conversion unit. In order to further lower the number of components, a single shaft architecture was considered for the Compressor-Generator-Turbine unit (CGT). As a consequence, the strict link between compressor and turbine performances leads to greater control, sealing and lubrication challenges.

As per Figure 3, which summarizes the design steps undertaken, the thermodynamic design of the sCO2 system has been carried out through a general design platform for simple regenerated layouts whose development has been presented in [35]. The in-house design code is based on energy and mass balances and it embeds turbomachinery design correlations based on the similarity analysis that allow to estimate speed and diameters of the impellers of the radial turbomachines.

The optimization libraries of the Engineering Equation Solver environment [36], in which the design platform has been developed, were used to identify the nominal operating conditions of the sCO_2 systems that are listed in Table 3.

These specifics were eventually used to design the heat exchangers as well as the turbomachinery. In particular, the

Table 3: Design point of the sCO_2 system.

min/max pressure [bar]	min/max Temperature [°C]	CO_2 mass flow rate [kg/s]
75/127.5	35/400	2.25

printed circuit technology was considered for the recuperator but not for the cooler due to recent developments in plate heat exchangers for refrigeration systems which have made this technology able to withstand high pressures at temperatures up to 250°C. This allowed a significant saving in the overall costs of the sCO_2 unit. The recuperator is shown in Figure 4. The CO_2 loop has additional connections to a CO_2 gas cooler to investigate the effects of a direct heat rejection at later stages of this research activity.

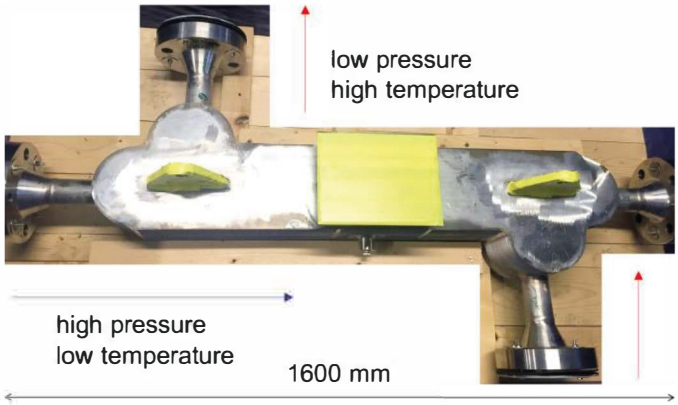

Figure 4: Printed circuit heat exchanger used as recuperator

The CO_2 heater had to fulfill requirements of compactness, low pressure drop on both sides and relatively low cost. These design trade-offs are expected to be achieved using a novel micro-tube heat exchanger technology which can easily be adapt to many high temperature heat to power generation applications.

DOI: 10.17185/duepublico/46086

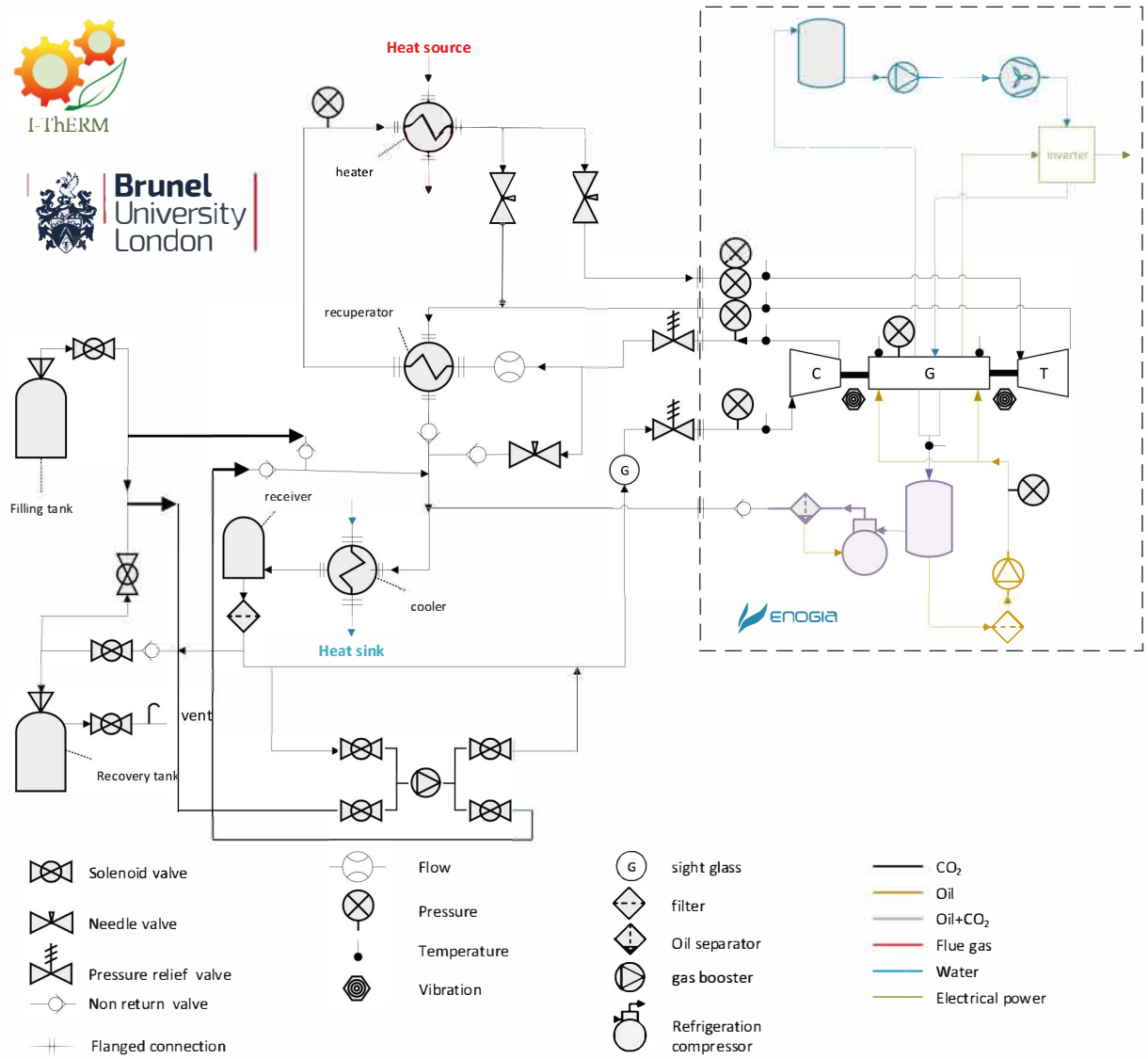

Figure 5: Process & Instrumentation Diagram.

To conceive the process and instrumentation diagram (P&ID) reported in Figure 5, startup, transient operation and shutdown modes had to be considered. In this step, precious pieces of scientific literature were the references [37] and [38], in which the research group of the US Naval Nuclear Laboratory shared their expertise about their testing activities on a 100 kWe two shaft recuperated closed sCO_2 Brayton cycle. In order to support the development of suitable controls for such complex apparatus, a transient model of the experimental rig using the methodology presented in [39] is being developed. In terms of hardware, motorized needle valves are installed downstream the compressor and the heater. According to [37], acting on the recirculation valve downstream the compressor proved to be the most effective strategy to operate the rig during off-design conditions; this device sends part of the compressed working fluid upstream the cooler but not directly to the compressor inlet to prevent any temperature shift from the critical region. As concerns the set of valves downstream the heater, their purpose is to either by-pass or to throttle the flow conditions upstream the turbine.

With regards to the ancillaries of the sCO_2 loop, two vessels and a gas booster were considered to charge the system beyond the critical pressure as well as to potentially vary the charge during operation. The gas booster is also meant to ease the startup procedure by providing a little flow at low heat conditions such that any liquid within the circuit is vaporized before starting the turbomachinery. Reasons for choosing a gas booster against a CO_2 piston pump was mainly cost, around 15 times higher in the second case. Pressure relief and solenoid valves complete the configuration together with static components such as filters, receiver, oil separators and sight glass

Design codes taken into account for all the components and the whole CO2 loop were the ASME BPV Code Section VIII Division 1 or the PD 5500 directives.

DOI: 10.17185/duepublico/46086

THE COMPRESSOR-GENERATOR-TURBINE UNIT

The Compressor, Generator and Turbine unit, herein referred as to CGT, is the core of the sCO_2 heat to power conversion system. Its design involved varies expertise and it is summarized in the following paragraphs. The first step of the procedure was to select the most suitable turbomachinery technology based on the design specifics of Table 3.

The selection of the turbomachinery type and architecture was performed with reference to technical and economic criteria. Based on the non-dimensional theory for turbomachinery, proposed by Balje [40] and applied to the sCO_2 field by Fuller [41], a first conclusion that was drawn was to discard positive displacement machines which are mainly suitable for high pressure ratios and small flow rates. As concluded in [41], for low power sCO_2 turbomachinery (<0.3MWe) single stage radial turbine is preferable. In fact, an axial multistage turbine would have lower speed and high efficiency but it would also require additional costs that can be justified only for large scale systems. On the other hand, a radial outflow turbine would have low revolution speeds but also low efficiency, high axial loads and high bending stresses. Instead, a radial inflow turbine should have a high efficiency for low pressure ratio, but also high revolution speed and high axial loads. Additional selection criteria for the turbomachinery technology were efficiency and cost. After a comparison made with the support of Table 4, the radial inflow turbine appeared to be the most suitable architecture for the current application.

Table 4: CGT architecture comparison.

	Axial multistage	Radial outflow	Radial inflow
Efficiency	+ + +	+	+ +
Cost	- - -	-	-
Ranking	3	2	1

A synchronous permanent magnet machine was selected for the electrical generator due to the high revolution speeds of the turbomachines as well as the authors' know-how on the design of such devices for small-scale ORC applications. To minimize the costs of the CGT unit, a single shaft arrangement was considered and resulted in the architecture shown in Figure 6. The Figure also shows the shaft guidance systems and passive seals. The pressure reduction to minimize windage losses is made by the creation of a cavity around the generator, surrounded by passive seals. A drain continuously vacuums this central part and keeps it at sub-critical pressure. The good efficiency of the static passive seals is ensured by the compact architecture which allows an accurate placing, close to the rotating shaft. The thermal insulation coupled with active cooling protects the bearing system located on the turbine side and ensures proper operation of the generator.

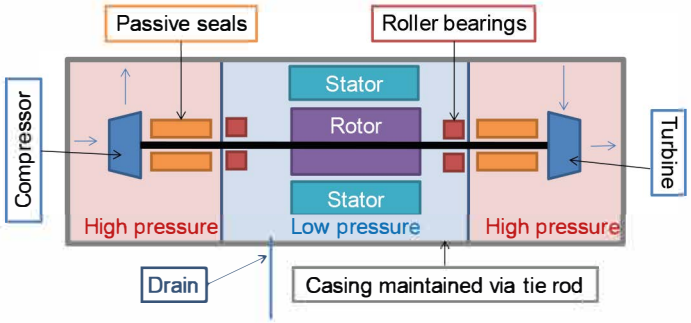

Figure 6: CGT layout.

AERODYNAMIC DESIGN

Several methodologies of varying complexity were employed for the design of the radial compressor and turbine. The design procedure is summarized in Figure 7 while more extensive details are provided in reference [35].

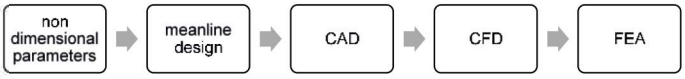

Figure 7: Turbomachinery design procedure.

Preliminary speed and dimensions of the impellers were determined from the non-dimensional theory [40] with the relevant equations included in the thermodynamic design shown in Figure 3. Based on these figures and the design specifics resulting from the cycle analysis (pressure ratio, mass flow rate, isentropic efficiencies), a mean-line design of the turbomachines was carried out to calculate blade angles and overall dimensions of the flow passages. Three-dimensional geometries of the impellers and of the diffusers were generated through CAD and CFD studies set up in in Star-CCM+ package. In particular, using 3D steady state RANS CFD simulations, based on the mixing plane approach and taking into account real gas properties for CO_2 [35], more accurate estimations of the isentropic efficiencies were made and compared to the ones assumed in the cycle analysis. Iterations were subsequently carried out to maximize the isentropic efficiency and to avoid inconsistences with the cycle analysis. The results of this procedure are summarized in Table 5.

Table 5: Summary of the aerodynamic design.

		Compressor	Turbine
Rotor	Diameter	55 mm	72 mm
	Number of blades	7	14
Nozzle	Number of blades	11	17
Isentropic efficiency (total-static)		76%	70%

DOI: 10.17185/duepublico/46086

Figures 8 and 9 show the compressor and turbine impellers which are unshrouded and machined from material block and milled to desired shapes derived from the aerodynamic design.

Figure 8: Compressor impeller

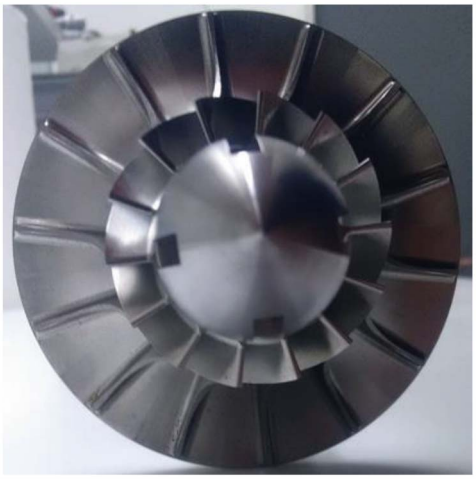

Figure 9: Turbine impeller

STRUCTURAL DESIGN

The rotating speed directly affects the rotational guidance technology. In order to optimize performance and reliability, high precision roller bearings have been employed. The natural frequencies and gyroscopic effect on the rotating parts are simulated by Finite Element Analysis (FEA). The stiffness of the bearings was simulated according to manufacturer's data and calculated load.

This study allowed to retrieve the frequency spectrum and, in turn, to identify the safe operating regime in terms of revolution speed. Furthermore, the analysis allowed to design the shaft. As shown in Figure 10, it has a bigger diameter in the central part due to the permanent magnets of the electrical generator. As an example, Figure 10.b, shows the stress induced by a white noise load.

The structural design of the CGT included also included FEA simulations to verify the structural integrity of static parts like the casing. These analyses were carried out assuming a pressure 1.5 times the maximum value at nominal operating conditions. Figure 11, shows local Von Mises stress in the casing. This picture further enables visualization of the openings for the electrical generator, the drainage as well as the lubrication channels for the bearings. Figure 12, shows the full CGT assembly whose overall dimensions are 290x290x502mm (WxHxL).

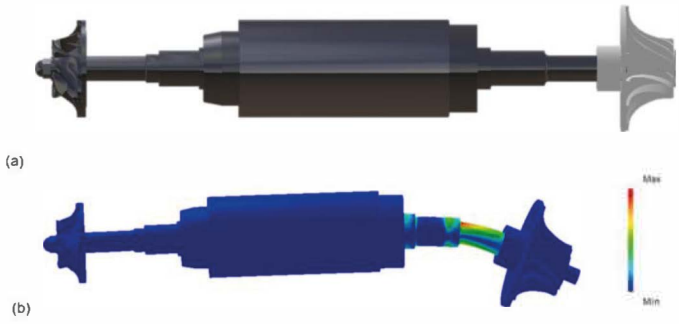

Figure 10: Shaft layout (a) and FEA simulation results to white noise load profile (b).

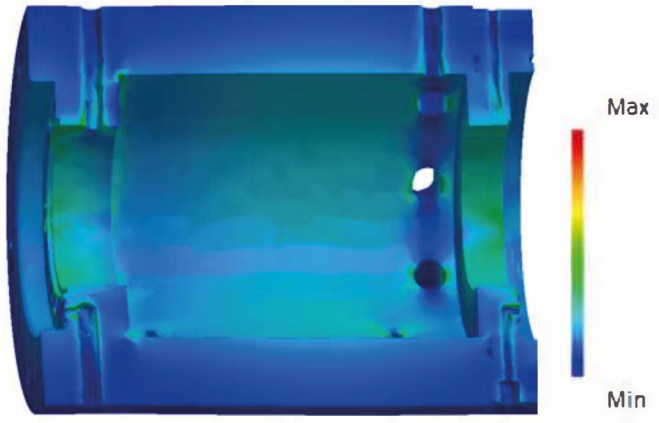

Figure 11: Von Mises stress on the casing.

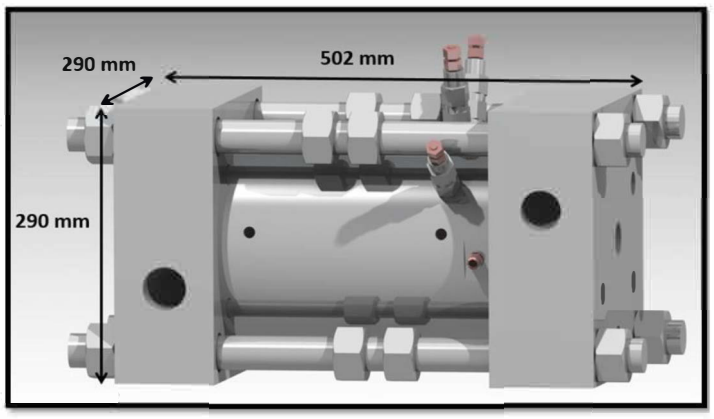

Figure 12: Final design of the CGT

DOI: 10.17185/duepublico/46086

ANCILLARIES LAYOUT

To ensure a proper operation of the CGT during any operation mode (idle, transient, steady), a number of auxiliary loops were considered. The complete P&ID chart of the CGT is shown in Figure 5. In order to reduce costs and enhance reliability, most of the ancillaries are off-the-shelf components specially designed for CO_2 refrigeration applications.

The cooling loop controls the inverter and generator temperatures using water as a cooling medium and a dry cooler to reject the heat to the ambient. The lubrication loop provides oil to the bearings of the CGT. It consists of an oil tank, and oil pump which supplies oil to the bearings. The oil is recovered inside the generator cavity by the draining loop, and then directed back to the oil tank.

The ancillary loops and the CGT will be housed in a common enclosure. The enclosure will also house the electrical cabinet and instrumentation that monitors pressure, temperature and vibration of the installation. The instrumentation will be connected to the electrical cabinet PLC which monitor and control the operation of the CGT.

CONCLUSIONS & FUTURE WORK

Supercritical CO_2 (sCO_2) power systems are promising candidates for the replacement of conventional steam power plants in any high-grade heat to power conversion application. In addition to the large-scale applications, where the power size of sCO_2 plants will be in the order of megawatts, an attractive power range is also the one between tens and few hundreds of kilowatts. The high compactness of sCO_2 equipment in this range of capacities, however, involves additional design challenges that the current research activity aims to tackle. In particular, this paper has shown the methodology through which a 50 kWe sCO_2 heat to power conversion unit has been designed. The sCO_2 system is based on a simple regenerative Joule-Brayton cycle architecture with pressure ratio of 1.7 and a single shaft Compressor-Generator-Turbine (CGT) unit. This configuration, together with the employment of a plate heat exchanger as CO_2 cooler and of a micro-tube CO_2 heater, allows to lower the investment costs without a substantial reduction in system performance. A future challenge of this research will be an extensive test campaign at steady and transient operating conditions to assess the actual performance of the sCO_2 system as well as its reliability for future industrialization.

ACKNOWLEDGEMENTS

The research presented in this paper has received funding from the European Union's Horizon 2020 research and innovation programme under grant agreement No. 680599. Aspects of the work are also funded by the Centre for Sustainable Energy Use in Food Chains (CSEF). CSEF is an End Use Energy Demand Centre funded by the Research Councils UK, Grant No: EP/K011820/1.

REFERENCES

[1] Forman C, Muritala IK, Pardemann R, Meyer B. Estimating the global waste heat potential. Renew Sustain Energy Rev 2016;57:1568–79. doi:10.1016/J.RSER.2015.12.192.

[2] UK Government GHG Conversion Factors for Company Reporting, 2017, https://www.gov.uk/government/publications/greenhouse-gas-reporting-conversion-factors-2017

[3] Persichilli M, Kacludis A, Zdankiewicz E. Supercritical CO2 Power Cycle Developments and Commercialization: Why sCO2 can Displace Steam Ste. Power-Gen India & 2012.

[4] Huck P, Freund S, Lehar M, Peter M. Performance comparison of supercritical CO 2 versus steam bottoming cycles for gas turbine combined cycle applications.

[5] Parks C. Corrosion of candidate high temperature alloys in supercritical carbon dioxide 2013.

[6] Sarkar J. Second law analysis of supercritical CO2 recompression Brayton cycle. Energy 2009;34:1172–8. doi:10.1016/J.ENERGY.2009.04.030.

[7] Johnson G, McDowell M. Issues Associated With Coupling Supercritical CO2 Power Cycles to Nuclear, Solar and Fossil Fuel Heat Sources. Proc Supercrit CO2 Power Cycle 2009.

[8] Weiland NT, White CW. Techno-economic analysis of an integrated gasification direct-fired supercritical CO 2 power cycle. Fuel 2018;212:613–25. doi:10.1016/j.fuel.2017.10.022.

[9] Ahn Y, Bae S, Kim M, Cho S, Baik S, Lee J. Cycle layout studies of S-CO2 cycle for the next generation nuclear system application. Trans 2014.

[10] Vitale Di Maio D, Boccitto A, Caruso G. Supercritical carbon dioxide applications for energy conversion systems. Energy Procedia 2015;82:819–24. doi:10.1016/j.egypro.2015.11.818.

[11] Dostal V, Driscoll M, Hejzlar P. Supercritical CO2 cycle for fast gas-cooled reactors. Expo 2004 … 2004.

[12] Moisseytsev A, Sienicki JJ. Recent Developments in S-Co2 Cycle Dynamic Modeling and Analysis At Anl. 4th Int Symp - Supercrit CO2 Power Cycles 2013;53:1689–99. doi:10.1017/CBO9781107415324.004.

[13] Turchi CS, Ma Z, Dyreby J. Supercritical Carbon Dioxide Power Cycle Configurations for Use in Concentrating Solar Power Systems. Vol. 5 Manuf. Mater. Metall. Mar. Microturbines Small Turbomachinery; Supercrit. CO2 Power Cycles, ASME; 2012, p. 967. doi:10.1115/GT2012-68932.

[14] Iverson BD, Conboy TM, Pasch JJ, Kruizenga AM. Supercritical CO2 Brayton cycles for solar-thermal energy. Appl Energy 2013;111:957–70. doi:10.1016/j.apenergy.2013.06.020.

[15] Singh R, Kearney MP, Manzie C. Extremum-seeking control of a supercritical carbon-dioxide closed Brayton cycle in a direct-heated solar thermal power plant. Energy 2013;60:380–7. doi:10.1016/j.energy.2013.08.001.

[16] Singh R, Rowlands AS, Miller SA. Effects of relative volume-ratios on dynamic performance of a direct-heated supercritical carbon-dioxide closed Brayton cycle in a solar-thermal power plant. Energy 2013;55:1025–32. doi:10.1016/j.energy.2013.03.049.

DOI: 10.17185/duepublico/46086

[17] L'Estrange T, Truong E, Rymal C, Rasouli E, Narayanan V, Apte S, et al. High flux microscale solar thermal receiver for supercritical carbon dioxide cycles. ASME 2015 13th Int. Conf. Nanochannels, Microchannels, Minichannels, American Society of Mechanical Engineers; 2015, p. V001T03A009. doi:10.1115/ICNMM2015-48233.
[18] Silva-Pérez MA. Solar power towers using supercritical CO2 and supercritical steam cycles, and decoupled combined cycles. Adv. Conc. Sol. Therm. Res. Technol., Elsevier Inc.; 2016, p. 383--402. doi:10.1016/B978-0-08-100516-3.00017-4.
[19] Atif M, Al-Sulaiman FA. Energy and exergy analyses of solar tower power plant driven supercritical carbon dioxide recompression cycles for six different locations. Renew Sustain Energy Rev 2017;68:153–67. doi:10.1016/j.rser.2016.09.122.
[20] Besarati SM, Goswami DY. Supercritical CO2 and other advanced power cycles for concentrating solar thermal (CST) systems. Adv. Conc. Sol. Therm. Res. Technol., Elsevier Inc.; 2016, p. 157–78. doi:10.1016/B978-0-08-100516-3.00008-3.
[21] Sabau A, Yin H, Qualls A, McFarlane J. Investigations of supercritical CO2 Rankine cycles for geothermal power plants 2011.
[22] McClung A, Brun K, Delimont J. Comparison of Supercritical Carbon Dioxide Cycles for Oxy-Combustion. Vol. 9 Oil Gas Appl. Supercrit. CO2 Power Cycles; Wind Energy, ASME; 2015, p. V009T36A006. doi:10.1115/GT2015-42523.
[23] Allam R, Martin S, Forrest B, Fetvedt J, Lu X, Freed D, et al. Demonstration of the Allam Cycle: An Update on the Development Status of a High Efficiency Supercritical Carbon Dioxide Power Process Employing Full Carbon Capture. Energy Procedia 2017;114:5948–66. doi:10.1016/j.egypro.2017.03.1731.
[24] Huang X, Wang J, Zang J. Thermodynamic analysis of coupling supercritical carbon dioxide brayton cycles 2016;37:34–8. doi:10.13832/j.jnpe.2016.03.0034.
[25] Wang J, Huang Y, Zang J, Liu G. Preliminary design and considerations of a MWE scale supercritical Co2 integral test loop. Vol. 9 Oil Gas Appl. Supercrit. CO2 Power Cycles; Wind Energy, vol. 9, American Society of Mechanical Engineers (ASME); 2016, p. V009T36A002. doi:10.1115/GT2016-56426.
[26] Yuansheng L, Jun W, Can M, Chunhui D, Zhenxing Z, Mo T. Design and analysis of key instruments of supercritical carbon dioxide Brayton cycle in future nuclear power field. vol. 2, American Society of Mechanical Engineers (ASME); 2017. doi:10.1115/ICONE2567155.
[27] Manjunath K, Sharma OP, Tyagi SK, Kaushik SC. Thermodynamic analysis of a supercritical/transcritical CO2 based waste heat recovery cycle for shipboard power and cooling applications. Energy Convers Manag 2018;155:262–75. doi:10.1016/j.enconman.2017.10.097.
[28] Sharma OP, Kaushik SC, Manjunath K. Thermodynamic analysis and optimization of a supercritical CO2 regenerative recompression Brayton cycle coupled with a marine gas turbine for shipboard waste heat recovery. Therm Sci Eng Prog 2017;3:62–74. doi:10.1016/j.tsep.2017.06.004.
[29] Vesely L, Dostal V. Effect of multicomponent mixtures on cycles with supercritical carbon dioxide. Vol. 9 Oil Gas Appl. Supercrit. CO2 Power Cycles; Wind Energy, vol. 9, American Society of Mechanical Engineers (ASME); 2017, p. V009T38A016. doi:10.1115/GT2017-64044.
[30] Levy EK, Wang X, Pan C, Romero CE, Maya CR. Use of hot supercritical CO2 produced from a geothermal reservoir to generate electric power in a gas turbine power generation system. J CO2 Util 2018;23:20–8. doi:10.1016/j.jcou.2017.11.001.
[31] McClung A, Brun K, Chordia L. Technical and economic evaluation of supercritical oxy-combustion for power generation. Supercrit CO2 Power … 2014.
[32] Kim MS, Ahn Y, Kim B, Lee JI. Study on the supercritical CO2 power cycles for landfill gas firing gas turbine bottoming cycle. Energy 2016;111:893–909. doi:10.1016/j.energy.2016.06.014.
[33] Kacludis A, Lyons S, Nadav D, Zdankiewicz E. Waste Heat to Power (WH2P) Applications Using a Supercritical CO 2 -Based Power Cycle.
[34] Marchionni M, Bianchi G, Tsamos K, Tassou S, Techno-economic comparison of different cycle architectures for high temperature waste heat to power conversion systems using CO2 in supercritical phase, Energy Procedia, Volume 123, 2017, Pages 305-312, ISSN 1876-6102, doi:10.1016/j.egypro.2017.07.253.
[35] Hoiland N, Bianchi G, De Miol M, et al., Design of radial turbomachinery for supercritical CO2 systems using theoretical and numerical CFD methodologies, Energy Procedia, Volume 123, 2017, Pages 313-320, ISSN 1876-6102, doi:10.1016/j.egypro.2017.07.256
[36] Klein SA, Alvarado FL. Engineering equation solver. F-Chart Software, Madison, WI. 2002;1.
[37] Clementoni EM, Cox TL, King MA, Rahner KD. Transient Power Operation of a Supercritical Carbon Dioxide Brayton Cycle. ASME. Turbo Expo: Power for Land, Sea, and Air, Volume 9: Oil and Gas Applications; Supercritical CO2 Power Cycles; Wind Energy ():V009T38A001. doi:10.1115/GT2017-63056.
[38] Clementoni, E. M., T. L. Cox, and M. A. King. Initial Transient Power Operation of a Supercritical Carbon Dioxide Brayton Cycle with Thermal-hydraulic Control. 5th International Symposium on Supercritical CO2 Power Cycles, San Antonio, TX, March. 2016.
[39] Marchionni, M., Bianchi, G., et al., Dynamic modeling and optimization of an ORC unit equipped with plate heat exchangers and turbomachines. Energy Procedia, Volume 129, 2017, Pages 224-231, ISSN 1876-6102, doi: 10.1016/j.egypro.2017.09.146
[40] Balje, O. E. Turbomachines-A guide to design, selection, and theory. John Wiley & Sons, 1981.
[41] Fuller, R., Preuss, J. and Noall, J., 2012, June. Turbomachinery for supercritical CO2 power cycles. In ASME Turbo Expo 2012 (pp. 961-966). American Society of Mechanical Engineers.

DOI: 10.17185/duepublico/46086

2nd European supercritical CO2 Conference
August 30-31, 2018, Essen, Germany

2018-sCO2.eu-115

EXPERIMENTAL INVESTIGATION OF THE SCO2-HERO COMPRESSOR

Alexander Hacks
University of Duisburg-Essen
Duisburg, Germany
Email: Alexander.Hacks@uni-due.de

Ales Vojacek
Research Centre Řež
Řež, Czech Republic

Hans Josef Dohmen
University of Duisburg-Essen
Duisburg, Germany

Dieter Brillert
University of Duisburg-Essen
Duisburg, Germany

ABSTRACT

Supercritical CO_2 (sCO2) is widely used in many industrial applications. The utilization of sCO2 power cycles has been gaining attention and first prototypes of the order of few MWe are being built. A European consortium led by University of Duisburg-Essen is investigating a sCO2 heat removal system (sCO2-HeRo) as a back-up cooling system, which efficiently removes residual heat from nuclear fuel without the requirement of external power sources. The sCO2-HeRo system applies a simple sCO2 Brayton cycle. This technical paper presents the first test results of the sCO2 turbomachine (TAC). The paper focuses on the validation of the calculated performance maps of the centrifugal compressor. The tests were performed in the newly built sCO2 experimental loop, which was constructed within the SUSEN (Sustainable Energy) project at Research Centre Řež (CVR).

INTRODUCTION

Raising nuclear reactor safety to a higher level, the sCO2 heat removal system (sCO2-HeRo) is developed within a EU funded project. The objective of this project is to build a small-size demonstrator sCO2 cycle and install it at the PWR glass model at the Gesellschaft für Simulatorschulung mbH (GfS) in Essen, Germany. The glass model allows to simulate different accident scenarios. Thus, the operation of the downscaled unit will demonstrate the maturity of the sCO2-HeRo cycle. The self-propellant, self-sustaining sCO2-HeRo simple Brayton cycle includes a compressor, heat exchanger (steam to sCO2), turbine and sink heat exchanger, whereby the compressor and turbine impellers are mounted onto one shaft with a generator in between [1]. Each of the components is pre-tested before final assembling into the sCO2-HeRo cycle at GfS. The turbomachine pre-tests were conducted at CVR to validate the calculated performance maps and gain knowledge on the machine behaviour.

DESCRIPTION OF TURBOMACHINE-SET FOR THE GLASS MODEL

The tested TAC has an integrated design and consists of three major components turbine, alternator and compressor. The cross section of the TAC and pictures of the impellers are presented in Figure 1. Figure 1 also includes the flow directions of the sCO2 through the machine and gives an impression on the impeller dimensions. As shown in Figure 1 the compressor is on the left and the turbine on the right, while the alternator is in the middle. The bearings are realized by angular hybrid ball bearings in between the impellers and the generator respectively. The thrust bearing is on the side of the compressor. Both compressor and turbine consist of one stage and have shrouded impellers with 2D-radial blading. This allows for labyrinth seals to be applied, which reduce the leakage losses. These losses have a significant influence on the components efficiency due to the small mass flow within the cycle. Table 1 contains the cycle mass flow and further thermodynamic conditions. The mass flow is limited by the heating power of the glass model, while the maximum temperature at the turbine inlet refers to the operating conditions of a nuclear power plant for emergency cooling. The compressor inlet lies close to the critical point reducing the compression work. For further information on the test cycle and cycle parameters please refer to Benra et al. [1]. Due to the given thermodynamic parameters and maximum mass flow the type and dimension of the compressor and turbine (shown in Figure 1) are chosen. The nominal rotational speed of the shaft is 50,000 rpm with an electrical power of the motor of 7 kW. For more information on the TAC design and the design procedure please refer to Hacks et al. [3].

DOI: 10.17185/duepublico/46088

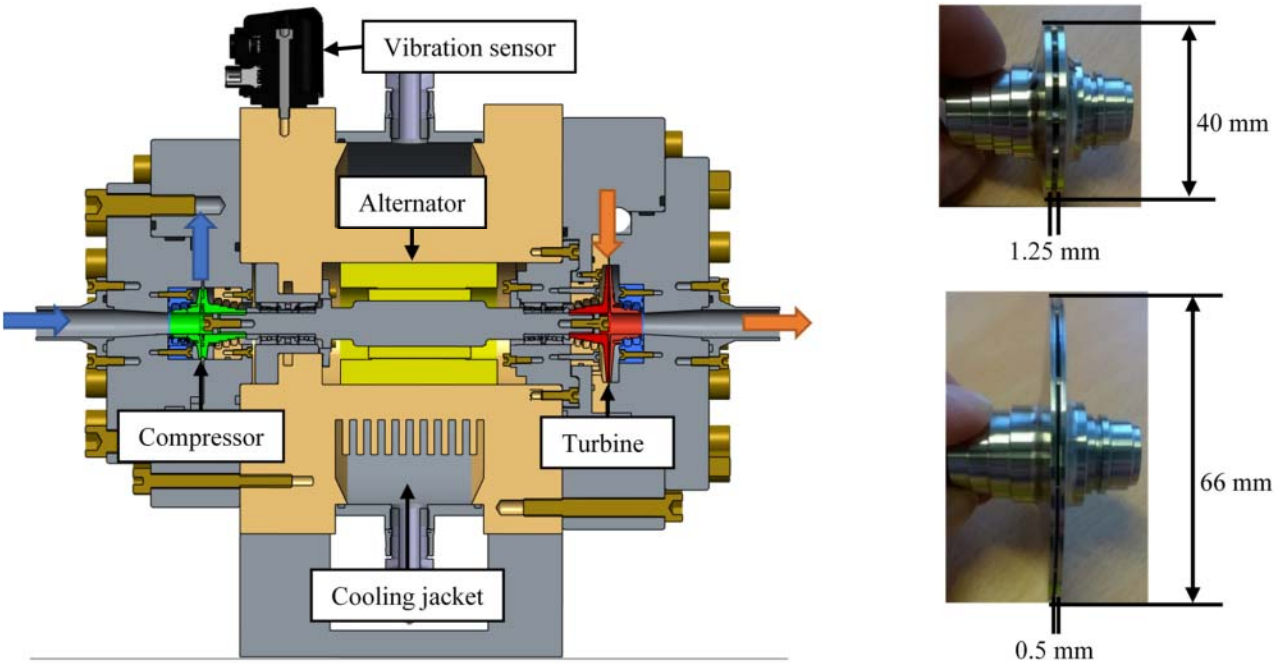

Figure 1: Cross section and impellers of the TAC with flow directions and dimensions

Table 1: Nominal conditions at cycle interfaces

Component	Parameter	Value
Compressor inlet	Pressure	78.3 bar
	Temperature	33 °C
	Mass flow	0.65 kg/s
Compressor outlet	Pressure	117.5 bar
	Mass flow	0.65 kg/s
Turbine inlet	Pressure	117.5 bar
	Temperature	200 °C
	Mass flow	0.65 kg/s
Turbine outlet	Pressure	78.3 bar
Leakage	Pressure	65 bar

TEST FACILITY

The turbomachine performance test took place at Research Centre Rez, using the SUSEN sCO2 experimental loop. This unique facility enables to study key aspects of the cycle (turbomachines, heat transfer, erosion, corrosion etc.) with a wide range of design parameters [7]:

- Temperature: up to 550°C
- Pressure: up to 300 bar
- Mass flow rate: up to 0.35 kg/s (limited by the circulation piston pump) As the sCO2-HeRo compressor is used the mass flow is raised to 0.65 kg/s

Figure 2 shows the piping and instrument diagram (PID) of the loop. The part of the primary circuit used for the TAC measurement is marked by the red connection lines. The main components are:

- The turbomachine (TAC), which consist of the turbine, alternator and compressor [3].
- The circulation piston pump returns the leakage from the TAC back to the cycle and is used for circulation during cycle warm-up.
- The high and low temperature regenerative heat exchanger (HTR HX/LTR HX) reduce the heating and cooling power.
- The 4 electric heaters (H1/1, H1/2, H2, H3) have in total a maximum power of 110 kW.
- The water coolers CH1 and the leakage cooler.

The heat exchangers HTR HX and LTR HX are designed as counter-flow shell and tube-type from stainless steel. Each heater concludes of 12 heating elements made from specially designed electric heating rods, which are encapsulated in austenitic steel (for H1/1, H1/2, H3) or Inconel (for H2) pressure boundary. The pressure in the system is controlled either by the electric heaters, i.e. by the temperature in the circuit, or by inventory control strategy. This concludes of the filling compressor and the release valves (to the outside atmosphere), by which it is possible to control the amount of CO2 in the loop and thus the pressure. To protect the loop several pressure relief valves are installed at different positions. Excess pressure is expected e.g. at the outlet of the heating parts as well as the compressor and the pumps.

DOI: 10.17185/duepublico/46088

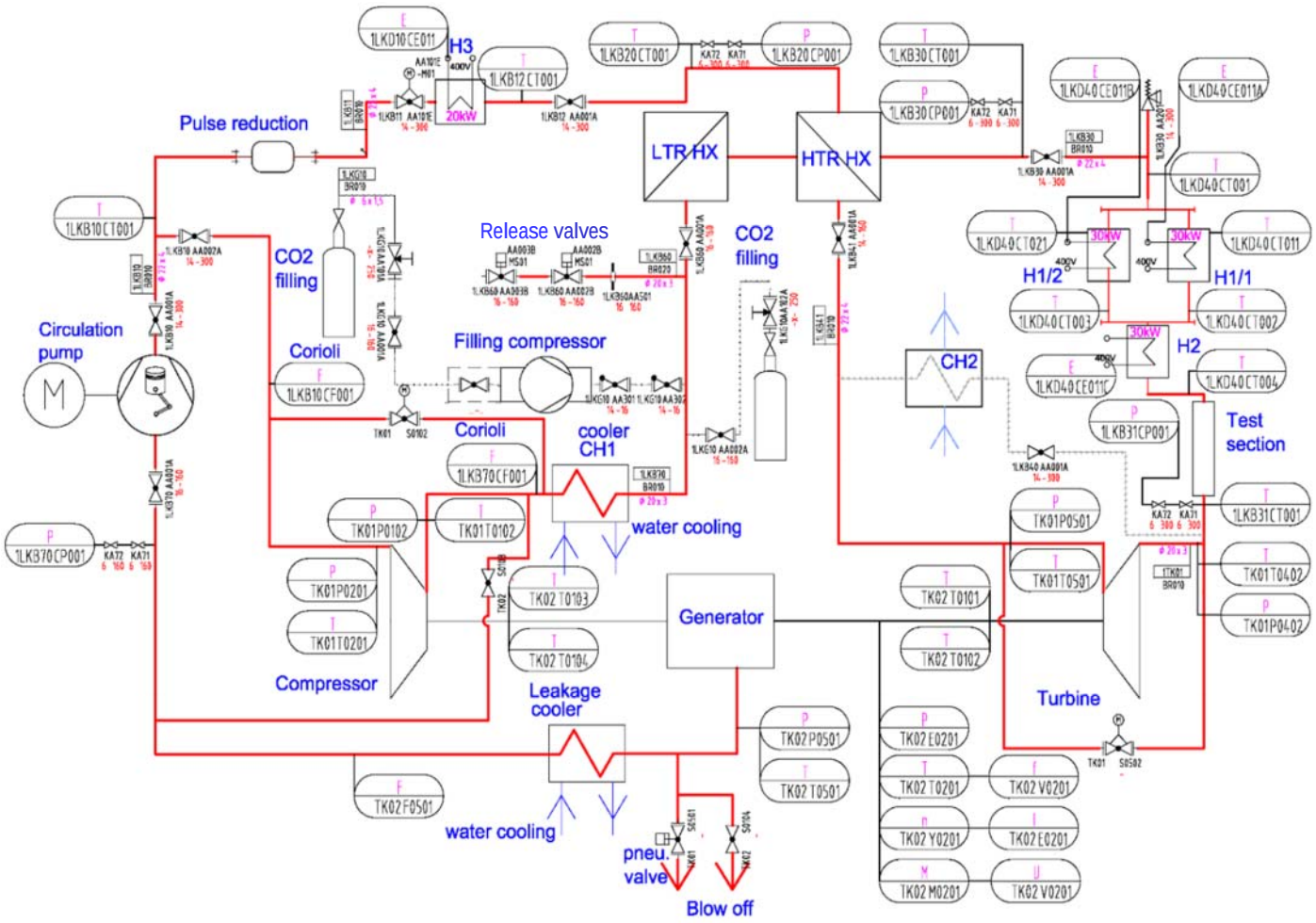

Figure 2: PID of the sCO2 loop with TAC at CVR

MEASUREMENT DEVICES AND ERRORS

Measuring the momentum or power of the motor to determine the compressor power is not possible in the machine configuration shown in Figure 1, because the turbine is mounted to the same shaft and windage losses have a significant influence on the required motor power. Figure 2 shows the piping and installation diagram (PID diagram) of the modified sCO_2 loop with the main components together with all installed measurement devices. These are mass flow meters, Pt-100 sensors, thermocouples, pressure sensors, vibration sensors etc. The nomenclature of the measurement devices respects the KKS identification system for power plants. The uncertainties provided by the measurement devices, transducers, input cards and the control system are summarized in Table 2. The errors correspond to calibration certificates and the manufacturer's instructions. The error propagations of the measuring errors are described in Annex A.

DOI: 10.17185/duepublico/46088

Table 2: Installed measurement devices and errors (in percent of range)

Description	Variable	Range	Unit	Device error	Transducer error	Input card error	Control system error	Total error
Mass flow rate 1LKB70CF001, 1LKB10CF001 Rheonik (RHM12)	$\dot{m}_{comp\_in}$ $\dot{m}_{comp\_out}$	0 – 0.7	kg/s	0.15 % from 1.66 kg/s	Rawet – PX310S	Siemens SM 331	ABB freelance	+/- 0.007 kg/s
					0.1 %	0.4 %	0.1 %	
Compressor inlet temperature, JSP (Pt 100)	T_{comp_in}	15 – 45	°C	0.15 %	Rawet – PX310S	Siemens SM 331	ABB freelance	+/- 0.26 K
					0.1 %	0.4 %	0.1 %	
Compressor outlet temperature, JSP (Pt 100)	T_{comp_out}	15 – 60	°C	0.15 %	Rawet – PX310S	Siemens SM 331	ABB freelance	+/- 0.35 K
					0.1 %	0.4 %	0.1 %	
Turbine inlet/outlet and leakage temperature, TC (type K) , Omega	T_{turb_in} T_{turb_out} $T_{leakage}$	0 – 600	°C	0.275 %	Rawet – PX310S	Siemens SM 331	ABB freelance	+/- 5.1 K
					0.1 %	0.4 %	0.1 %	
Compressor pressure inlet/outlet, Turbine pressure outlet, GE (UNIK 5000)	p_{comp_in} p_{comp_out} p_{turb_out}	0 – 150	bar	0.15 %	Rawet – PX310S	Siemens SM 331	ABB freelance	+/- 1.1 bar
					0.1 %	0.4 %	0.1 %	
Turbine pressure inlet, leakage pressure, GE (UNIK 5000)	p_{turb_in} $p_{leakage}$	0 – 300	bar	0.15 %	Rawet – PX310S	Siemens SM 331	ABB freelance	+/- 2.3 bar
					0.1 %	0.4 %	0.1 %	

PERFORMANCE TESTS

The main objective of the performance tests is the validation of the calculated performance maps of both compressor and turbine. The performance maps are introduced into the German nuclear code ATHLET to predict the cycle behaviour and thus introduce the HeRo safety system into nuclear power plants. In general, performance maps show the characteristic behaviour of compressors and turbines. Usually the pressure ratio, specific work or efficiency is plotted against the flow rate or flow coefficient for different rotational speeds. Figure 3 shows an example of such a performance map showing the pressure ratio over the flow coefficient for different speeds. The pressure ratio and efficiency are combined into one diagram. In general compressor performance maps also include the surge line (b) and choke line (c). Figure 3 additionally includes the blow-off (d) and stability line (a). Point A represents the design point. The stability and surge line represent the lower border of flow rate at a given speed for which the flow through the compressor gets unstable due to flow separation at the suction side of the blades. The choke line on the other hand represents the upper border at which the flow through the compressor gets choked. The blow-off line indicates the flow rate at which measures, such as blowing-off a part of the gas flow, should be taken to prevent unstable operation and surge. To measure the performance map, the inlet and outlet conditions of the compressor or turbine need to be measured as well as the rotational speed. The TAC shall start-up by itself, if a station blackout occurs. Further, the decay heat reduces during operation. It is therefore necessary to know the behaviour of the machine at off-design conditions. The performance maps are thus measured for different inlet conditions.

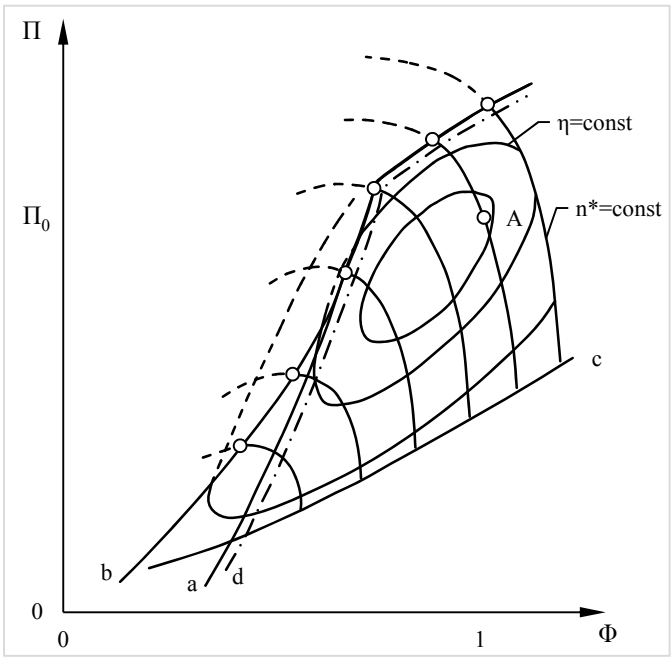

Figure 3: Compressor performance map according to Traupel (Abb. 13.2.1. Page 104 [6])

DOI: 10.17185/duepublico/46088

MEASUREMENT PARAMETERS

The performance test shall give insight in the machine performance within the expected range of operation and the general machine and cycle behaviour. As the dependency of fluid properties of sCO2 on pressure and temperature is especially large close to the critical point the performance map of the compressor regarding different inlet conditions is of great importance. The performance testing is separated in several test sequences. Each covers a certain objective leading to a certain range of parameters. Measurements are taken at stationary conditions meaning without fluctuations in mass flow, pressure and temperature and then compared to the regarding CFD calculations. The approach to the CFD calculations is described by Hacks et al. [3] and Schuster et al. [5]. The test sequences and the regarding parameters are summarized in Table 3. The main objectives and the approaches are as follows.

1) **Objective**: Find a strategy for starting the cycle including the TAC and bringing it to nominal conditions.
Approach: Fill the loop with CO_2 from the bottle. Then bring the loop to nominal conditions by heating up the CO_2 and thus also increasing its pressure (because the loop is a closed volume) to reach supercritical conditions and start the TAC using the generator as motor.

2) **Objective**: Measure the compressor performance map.
Approach: Bring the compressor inlet conditions to the desired conditions using knowledge from test sequence 1. Vary the conditions at the compressor inlet. The turbine conditions are also monitored but turbine inlet conditions do not need to be stationary. At speeds higher than 30000 rpm the turbine is used to provide auxiliary power to turn the compressor

3) **Objective**: Measure the turbine performance map.
Approach: Bring the turbine inlet conditions to the desired conditions using knowledge from test sequence 1 and 2. Vary the conditions at the turbine inlet. The turbine mass flow and inlet pressure are dependent on the compressor performance. The mass flow through the turbine is set by splitting up the mass flow through the compressor and let a fraction bypass the turbine.

4) **Objective**: Check bearing operation in sCO2.
Approach: In the previous tests the central housing is held at constant subcritical pressure of 65 bar. Now pressure is varied by changing the mass flow through the leakage pump.

Table 3: Test sequences and parameters

Test sequence	Test parameters						
	Mass flow $\dot{m}_{sCO2}$ (kg/s)	**Compressor p_{in} (bar)**	**Compressor T_{in} (°C)**	**Turbine p_{in} (bar)**	**Turbine T_{in} (°C)**	**Leakage p_{out} (bar)**	**Speed n (rpm)**
1 – Start-up test	resulting	resulting	resulting	resulting	resulting	65 (max.)	0-50,000
2 – Compressor test	0.3 - 0.7	77.3 - 79.3	31.5 - 34.5	resulting	resulting	65 (max.)	10,000-50,000
3 – Turbine test	0.3 - 0.7	78.3	33	resulting	150 - 200	65 (max.)	10,000-50,000
4 – Central housing test	resulting	78.3	33	resulting	150	55 - 117.5	10,000

EXPERIMENTAL RESULTS AND DISCUSSION

The previously described test plan was taken as basis for the actual testing. Test sequence 1 regarding the start-up and test sequence 4 regarding the pressure in the central housing showed limitations of testing in the SUSEN loop at CVR. For start-up testing the cycle is filled from CO_2 bottles to a pressure of up to 60 bar. The circulation pump is used to circulate the CO2 in the cycle and through the heaters. The turbomachine is bypassed. During circulation the CO_2 is heated up until the cycle reaches supercritical conditions. During this procedure the valves to the turbomachine are opened as soon as gaseous inlet conditions are reached at all turbomachine inlets. Thus, also the turbomachine is preheated. To set the desired compressor inlet conditions CO_2 is either added or released by the filling compressor or release valves respectively. Then the turbomachine is started. During first start-up, it was noticed that the overall pressure drop in the cycle is too big for the turbine to be tested in closed loop configuration together with the compressor. The reason for the high pressure losses is that the test facility is originally designed for a lower flow rate and for high temperatures, which require recuperators to reduce the heating and cooling power. Therefore, the compressor is tested in bypass configuration employing valve TK02 S0102 (see Figure 2) as a throttle. The turbine tests are dismissed and will be done at the GfS. Pressure rise in the central housing and thus sCO2 at the bearings showed that the grease lubricated bearings cannot operate in sCO2 and that it must be ensured that the CO_2 in the central housing is always gaseous. Thus, the pressure in the central housing is limited to

DOI: 10.17185/duepublico/46088

68 bar by a pressure relieve valve. To ensure delivery to GfS within the target time frame and because of the very limited auxiliary power of the turbine caused by the low turbine mass flow (leakage only), performance map testing was only carried out for a rotational speed of up to 30,000 rpm.

Affinity laws

It is found that affinity laws according to Bohl and Elmendorf [2], as stated in Table 4, are sufficiently accurate to predict the performance for other operation conditions such as other compressor inlet conditions and other rotational speeds. Figure 4 indicates this for 30,000 rpm, showing the measured pressure ratio at 30,000 rpm versus the pressure ratio for 30,000 rpm calculated by the affinity laws from the pressure ratio measured for 20,000 rpm and 25,000 rpm respectively. The maximum difference between the pressure ratio predicted by the affinity laws and the actual measured pressure ratio is less than 0.003 or an error of 2 % regarding the measured pressure increase across the compressor. As a conclusion the performance data for one rotational speed is measured for three different inlet conditions. Measurements are taken once for the design conditions with the nominal density at the compressor inlet and once for higher and lower density respectively. The desired performance data for other inlet conditions is calculated by the affinity laws. This allows implementation into the nuclear code ATHLET by implementing the measured data and interpolating this data using the affinity laws.

Table 4: Parameters for affinity laws [2]

Speed ratio	$k_n = \frac{n_I}{n_{II}}$	(1)
Size ratio	$k_d = \frac{d_I}{d_{II}}$	(2)
Density ratio	$k_\rho = \frac{\rho_I}{\rho_{II}}$	(3)
Mass flow	$\frac{\dot{m}_I}{\dot{m}_{II}} = k_d^3 * k_n * k_\rho$	(4)
Pressure difference	$\frac{\Delta p_I}{\Delta p_{II}} = k_d^2 * k_n^2 * k_\rho$	(5)
Efficiency[1]	$\frac{\eta_I}{\eta_{II}} = 1 \ or$ $Pfleiderer: \frac{1-\eta_{II}}{1-\eta_I} = \left(\frac{Re_I}{Re_{II}}\right)^{0.1}$ $Re = \frac{d^2 * \omega}{\nu}$	(6)
Power	$\frac{P_I}{P_{II}} = k_d^5 * k_n^3 * k_\rho$	(7)

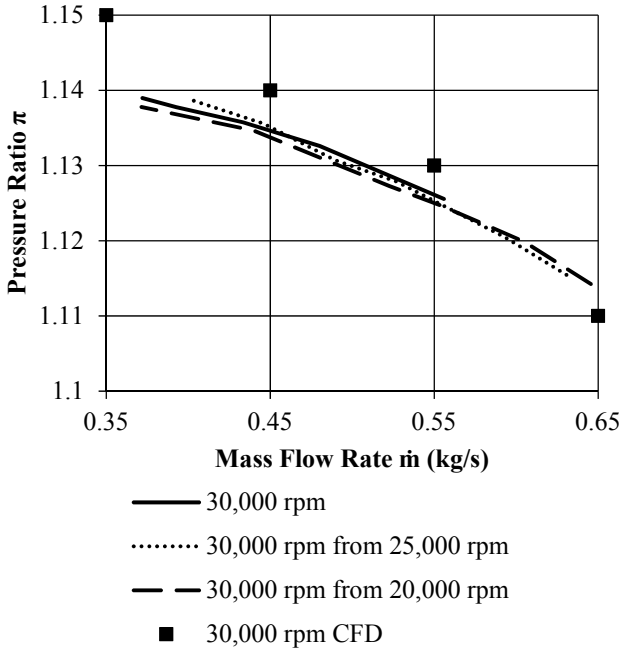

Figure 4: Affinity law applied for 30000 rpm

Compressor performance map

Figure 5 shows the pressure ratio performance map of the compressor in terms of pressure ratio versus compressor inlet mass flow for three different inlet conditions indicated by different symbols. The inlet conditions refer to the minimum and maximum as well as the nominal inlet density into the compressor. This means inlet conditions with maximum inlet temperature and minimum pressure, minimum inlet temperature and maximum pressure and nominal conditions according to Table 3. The error bars are calculated according to the formulas in Annex A. They are similar for different inlet conditions and thus only shown for the nominal inlet conditions to improve readability of the diagram. The surge line indicates the position at which the calculated performance lines have their maximum. The pressure ratio thus raises from the working point towards the predicted surge line in accordance with API Standard 617 (Lüdtke [4]). The calculated performance lines and the surge line are for nominal inlet conditions only. Figure 5 presents that the measured pressure ratios for nominal inlet conditions correspond closely to the pressure ratios calculated using CFD. They tend to underestimate the CFD results only for higher speeds. Still the values calculated with CFD lie within the uncertainty range indicated by the error bars. These get especially large due to error propagation, if affinity laws are applied. In general affinity laws consider constant efficiency. Increase in efficiency can be expected with increasing speed according to the formula of Pfleiderer [2]. Anyhow, this increase is not considered in the

[1] Formula of Pfleiderer is taken from the book of Bohl and Elmendorf [2]

DOI: 10.17185/duepublico/46088

calculation of the pressure ratio. Therefore, the pressure ratios for 40,000 rpm and 50,000 rpm are conservative values.

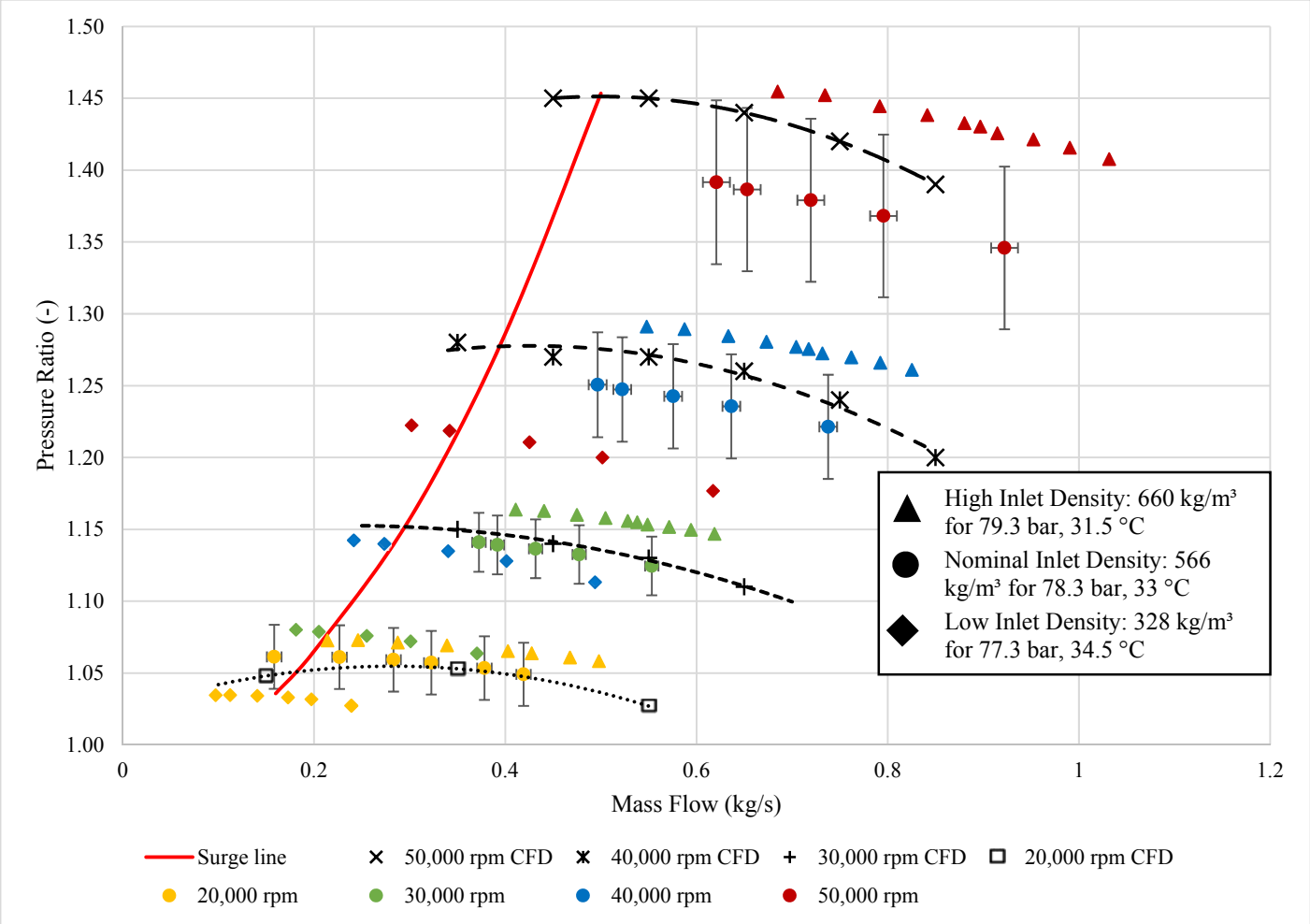

Figure 5: Compressor performance map – Pressure ratio

It is found that the pressure ratio raises with the inlet density and vice versa. The differences in the measured pressure ratio are large with respect to changing inlet conditions. But on the other hand, this shows that changing the inlet conditions in a way that the inlet density increases also raises the pressure ratio. The previously mentioned difference between calculated and measured pressure ratio at high rotational speeds can therefore be balanced by reducing the temperature at the compressor inlet. The isentropic efficiency and the power of the compressor calculated from the measured pressures and temperatures show huge uncertainties. They are caused by the small enthalpy difference between compressor inlet and outlet combined with the strong dependency of the enthalpy on the inlet conditions. As the uncertainties are as big as the calculated value itself neither the isentropic efficiency nor the calculated power is presented here. The measurements at GfS will be used to get further insight into the compressor power and efficiency. Systematical measurement errors must be minimized and all measurement devices must be calibrated in assembled conditions.

CONCLUSIONS

The turbomachine tests at CVR gave insight in the cycle behaviour and showed a possible start-up procedure of the sCO2 cycle, which can also be applied for the HeRo cycle at GfS. It is found that grease lubricated ball bearings need to be operated in gaseous CO_2 to ensure operability.

The compressor performance measurements of the pressure ratio matched well with the CFD calculations. Strategies to increase pressure ratio were found. To increase the pressure ratio the temperature at the compressor inlet can be decreased and thus also the density increased. It is therefore possible to adjust the compressor pressure ratio, if it is required, for further testing at GfS.

DOI: 10.17185/duepublico/46088

Calculated efficiency and power are not presented as the uncertainties of the measurements are large. For calculating these parameters accurately, the pressure and temperature measurements need to be very accurate. Calibration of the measurement devices connected to the control system is essential.

NOMENCLATURE

Measurement in KKS code	Description
TK01T0102	Inlet temperature to the compressor
TK01T0201	Outlet temperature of the compressor
TK01P0102	Inlet pressure to the compressor
TK01P0201	Outlet pressure of the compressor
TK01T0402	Inlet temperature to the turbine
TK01T0501	Outlet temperature of the turbine
TK01P0402	Inlet pressure to the turbine
TK01P0501	Outlet pressure of the turbine
TK02T0501	Leakage temperature
TK02P0501	Leakage pressure
1LKB70CF001	Mass flow rate inlet to the compressor
1LKB10CF001	Mass flow rate outlet from the compressor to the loop without the recirculating part which bypass the loop
TK02F0501	Leakage mass flow rate

Abbreviations	Description
CH1	Water cooler
CH2	Oil cooler
CVR	Research Centre Řež
GfS	Gesellschaft für Simulatorschulung mbH in Essen, Germany
H1/1, H1/2, H2 and H3	Electric heaters
HTR	High temperature regenerative heat exchanger
LTR	Low temperature regenerative heat exchanger
PID	Piping and installation diagram
sCO2	Supercritical carbon dioxide
sCO2-HeRo	Supercritical carbon dioxide heat removal system
SUSEN	Sustainable Energy project
TAC	Turbomachine

Variable	Unit	Description
cp	kJ/(kg*K)	Isobaric heat capacity
d	mm	Diameter
h	kJ/kg	Enthalpy
k_n	-	Speed ratio
k_d	-	Size ratio
k_ρ	-	Density ratio
$\dot{m}$	kg/s	Mass flow rate
n	1/min	Rotational speed
p	bar	Pressure
Δp	bar	Pressure drop
P	kW	Power
Q	m^3/s	Volume flow
Re	-	Reynolds number
T	K	Temperature
η	%	Efficiency (isentropic)
ν	m^2/s	Kinematic viscosity
π, Π	-	Pressure ratio
ρ	kg/m^3	Density
σ	n.a.	Error propagation
Φ	-	Flow coefficient
ω	1/s	Angular velocity

Subscripts	Description
comp	Compressor
in	Inlet
is	Isentropic
leakage	Leakage
out	Outlet
turb	Turbine
I	Target parameter for calculation by affinity law
II	Base parameter for calculation by affinity law

ACKNOWLEDGEMENTS

This project has received funding from the European research and training programme 2014 – 2018 under grant agreement No 662116.

DOI: 10.17185/duepublico/46088

REFERENCES

[1] Benra, F.-K., Brillert, D., Frybort, O., Hajek, P., Rohde, M., Schuster, S., Seewald, M. & Starflinger, J. (2016). A supercritical CO2 low temperature Brayton-cycle for residual heat removal. *The 5th International Symposium - Supercritical CO2 Power Cycles*, San Antonio, Texas, USA

[2] Bohl, W. & Elmendorf, W. (2013). *Strömungsmaschinen 1. Aufbau und Wirkungsweise* (Vol. 11). Würzburg: Vogel

[3] Hacks, A. J., Schuster, S., Dohmen H. J., Benra F.-K. & Brillert D. (2018). Turbomachine Design for Supercritical Carbon Dioxide within the sCO2-HeRo.eu Project. *ASME Turbo Expo*, Oslo, Norway

[4] Lüdtke, K. H. (2004) *Process Centrifugal Compressors – Basics, Function, Operation, Design, Application*. Springer Science and Business Media

[5] Schuster, S., Benra, F.-K., Brillert, D. (2016) Small scale sCO2 compressor impeller design considering real fluid conditions. *The 5th International Symposium - Supercritical CO2 Power Cycles*, San Antonio, Texas, USA

[6] Traupel, W. (2001) *Thermische Turbomaschinen 2* (Vol 4). Springer-Verlag

[7] Vojacek, A., Hacks, A. J., Melichar, T., Frybort, O. & Hajek, P. (2018). "First Operational Experience from the Supercritical CO2 Experimental Loop. *2nd European supercritical CO2 Conference*, Essen, Germany

DOI: 10.17185/duepublico/46088

ANNEX A

ERROR PROPAGATION

The following shows the calculation off the error propagation of pressure ratio and mass flow for direct calculation from the measurements and for application of the affinity laws.

Pressure difference: $$\sigma_{\Delta p} = \sqrt{\left(\sigma_{p_{in}}\right)^2 + \left(\sigma_{p_{out}}\right)^2} \tag{8}$$

Pressure ratio: $$\sigma_{\pi} = \sqrt{\left(-\frac{p_{out}}{p_{in}^2} * \sigma_{p_{in}}\right)^2 + \left(\frac{1}{p_1} * \sigma_{p_{out}}\right)^2} \tag{9}$$

For the calculation of the error propagation due to the use of the affinity laws the following assumptions are taken as simplification:

$$\sigma_{k_d} = \sigma_{k_n} = \sigma_{k_\rho} = 0 \tag{10}$$

Further the machine is always the same, which implies:

$$k_d = 1 \tag{11}$$

Mass flow by affinity law: $$\sigma_{\dot{m}_I} = k_n * k_\rho * \sigma_{\dot{m}_{II}} \tag{12}$$

Pressure ratio by affinity law: $$\sigma_{\Delta p_I} = \sqrt{\left(\frac{1}{p_{in}} * k_n^2 * k_\rho * \sigma_{\Delta p_{II}}\right)^2 + \left(-\frac{\Delta p_I}{p_{in}^2} * \sigma_{p_{in}}\right)^2} \tag{13}$$

DOI: 10.17185/duepublico/46088

2nd European supercritical CO2 Conference
August 30-31, 2018, Essen, Germany

2018-sCO2.eu-116

SCALING CONSIDERATIONS FOR THE APPLICATION OF THE SCO2-HERO SYSTEM IN NUCLEAR POWER PLANTS

Alexander Hacks
University of Duisburg-Essen
Duisburg, Germany
Email: Alexander.Hacks@uni-due.de

Dieter Brillert
University of Duisburg-Essen
Duisburg, Germany

ABSTRACT

The supercritical CO_2 heat removal system (sCO2-HeRo) project aims to develop and test a safety system for nuclear power plants with boiling water reactor (BWR) and pressurized water reactor (PWR) reactors for the case of a station blackout with loss of the ultimate heat sink. The safety system is based on a closed Brayton cycle using supercritical CO_2 (sCO2) as working fluid. The project focuses on the experimental proof of the concept and thereby reaching Technology Readiness Level 3 (TRL 3). As the demonstration cycle has a heat source of 200 kW only, the developed turbomachine for the demonstration cycle is a small-scale model. The system in the nuclear power plant (sCO2-NPP) needs to remove up to 60 MW_{th} leading to larger component sizes. The paper shall give an insight in the steps and considerations to proceed from the small-scale model to the actual safety system in the NPP. This includes the evaluation of the aerodynamic efficiency of the turbomachine and the windage losses. Furthermore, concepts of the bearings and generator cooling are investigated regarding possible improvements and required modifications.

INTRODUCTION

Cycles using sCO2 as working fluid have attracted considerable attention due to their compactness and proposed thermodynamic efficiency. The application in a back-up safety system for NPPs however is unique. Most of current research in this field is focused on designing more cost effective and flexible cycles for power generation. The sCO2-HeRo system however is designed to remove residual heat of nuclear fuel in the case of a station blackout with loss of the external power supply and the heat sink. The application requires that the used unrecuperated Brayton cycle is self-launching, self-propelling and self-sustaining. Furthermore, it should be possible to retrofit it to existing NPPs (Benra et al. [1]). The concept of the system is tested in the newly built sCO2 cycle at the PWR glass model at the Gesellschaft für Simulatorschulung (GfS) in Essen, Germany. The sCO2 HeRo cycle is connected to PWR glass model, which allows to demonstrate the function of the system for different emergency cases in NPPs. However, the heating power available for the demonstration cycle is only 200 kW. Compared to around 60 MW, which need to be removed in a NPP, this is rather small. It leads to a very small mass flow and consequently a very small turbomachine. As addressed by Sienicki et al. [9] all the different components of the turbomachine must be examined, when scaling turbomachines over a wide range of power output. Both the efficiency and applicability of technologies such as impellers, bearings, seals, motors, etc. must be investigated. In this paper the scaling procedure of the very small sCO2-HeRo turbomachine to the full-scale sCO2-NPP turbomachine is explained. For this purpose, both the sCO2-HeRo turbomachine and the requirements for the sCO2-NPP turbomachine are presented. The scaling procedure is described in detail with special attention to the requirements as a safety cooling system.

DESCRIPTION OF TURBOMACHINE-SET FOR THE GLASS MODEL

The turbomachine (TAC), which is implemented in the glass model, has an integrated design and consists of the three major components turbine, alternator and compressor. Figure 1 presents the cross section of the TAC with the flow directions of sCO2 and pictures of the impellers. The compressor is on the left and the turbine on the right, while the alternator is in the middle. The bearings are realized by angular hybrid ball bearings in between the impellers and the generator respectively. The thrust bearing is on the side of the compressor. Both compressor and turbine consist of one stage and have shrouded impellers with 2D-radial blading. This allows to apply labyrinth seals to reduce leakage losses. These losses have a significant influence on the components efficiency due to the small cycle mass flow. Table 1 contains the cycle mass flow and further thermodynamic conditions. The mass flow is limited by the heating power of the glass model test cycle. The maximum temperature at the turbine inlet refers to the operating conditions of the cycle in a NPP for

DOI: 10.17185/duepublico/46089

emergency cooling. The compressor inlet lies close to the critical point to reduce the compression work. For further information on the test cycle and cycle parameters please refer to Benra et al. [1]. Because of the given thermodynamic parameters and mass flow the type and dimension of the compressor and turbine (shown in Figure 1) are chosen. The nominal rotational speed of the shaft is 50,000 rpm with an electrical power of the generator of 7 kW. The cooling of the generator is realized by the compressor leakage. For more information on the TAC design and the design procedure please refer to Hacks et al.[4].

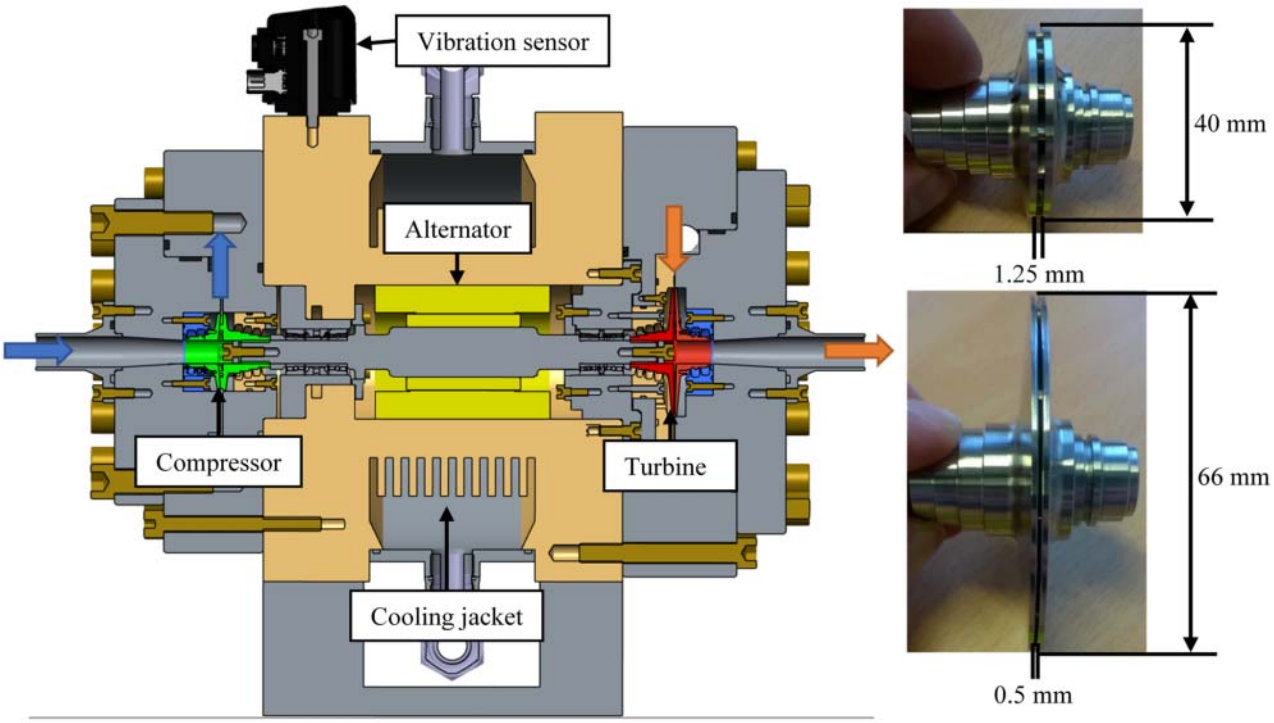

Figure 1: Cross section and impellers of the TAC with flow directions and dimensions

Table 1: Nominal conditions in the glass model

Component	Parameter	Value
Cycle	Mass flow	0.65 kg/s
Compressor inlet	Pressure*	78.3 bar
	Temperature*	33 °C
Compressor outlet	Pressure*	117.5 bar
Turbine inlet	Pressure*	117.5 bar
	Temperature*	200 °C
Turbine outlet	Pressure*	78.3 bar
Leakage	Pressure*	65 bar

*static

REQUIREMENTS TO THE TURBOMACHINE IN A NPP

The turbine inlet temperature of the sCO2-HeRo cycle is set by evaluating different options for the heat removal in an emergency case in in a NPP. Different concepts on how to remove the heat from the nuclear core were analysed resulting in different temperatures at the turbine inlet of up to 280 °C (Venker [10]). For simplification the different options of heat removal and corresponding turbine inlet temperatures are not considered, as it does not influence the general scaling procedure. It shall be assumed that the pressure and temperature of the sCO2-NPP cycle at the compressor and turbine inlet are the same as for sCO2-HeRo cycle. The amount of heat, which needs to be removed strongly depends on the size of the power plant, the time that passes after a station blackout before the sCO2-HeRo system takes over and other measures taken during that period. Venker [10] shows that the residual heat, which needs to be removed directly after the station black out, is around 60 MW_{th} for a power plant with a nominal power of around 4 GW_{th}. However, after one hour the heat drops to around 30 MW_{th} and after around 8 hours to 20 MW_{th}. The decay heat drives the sCO2-NPP cycle. The strong drop in heating power, especially in the first hours, thus request a suitable control strategy for the cycle. It is decided to divide the sCO2-NPP system in several units. Single units are then switched off step by step with decreasing decay heat. Each unit consist of one complete sCO2 cycle. The thermal energy of one sCO2-NPP unit is set to 5 MW_{th}. As the pressures and temperatures are assumed to be constant the increase in thermal power corresponds to an equivalent increase in cycle mass flow (see Figure 2). Assuming a constant pressure ratio and increased mass flow, the resulting generator power in the NPP is around 180 kW.

DOI: 10.17185/duepublico/46089

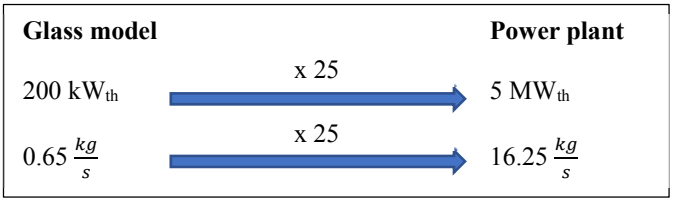

Figure 2: Mass flow – From sCO2-HeRo to sCO2-NPP size

TURBOMACHINE LAYOUT

The first thing to decide in the scaling process is whether the overall layout of the TAC is suitable for the new operation conditions. The system needs to have a simple design with a small turbomachine to retrofit existing power plants with it. The integrated design of compressor and turbine together in one casing represents the most compact machine and theoretically allows a machine without any external leakage. It is therefore desirable to keep the overall design of the sCO2-HeRo TAC as presented in Figure 1. Sienicki et al. [9] give an overview on suitable technologies for sCO2 turbomachinery in terms of size given in electrical power output. The electrical output of the sCO2-NPP turbomachine is below 1 MW$_e$, even if the thermal power per unit is raised to 10 MW$_{th}$ or 20 MW$_{th}$. According to Figure 3 the technologies applied in the sCO2-HeRo TAC, such as one stage compressor and turbine, labyrinth seals and a high-speed generator are also applicable for the sCO2-NPP machine. Thus, the integrated TAC design is considered to be suitable.

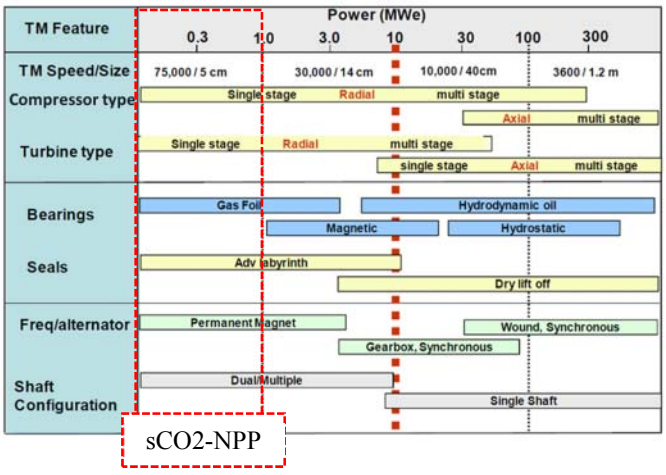

Figure 3: Technologies for sCO2 turbomachinery according to Sienicki et al. (Figure 1, [9])

AERODYNAMIC SCALING

Due to the higher mass flow the size of the TAC needs to increase. The following explanations focus on the compressor but are valid for the compressor and the turbine. A basic approach on designing a new compressor uses the Cordier diagram as presented in Figure 4. It shows the type of the impeller, and the expected efficiency of the compressor over the specific speed and specific diameter. The red dot in Figure 4 indicates the position of the sCO2-HeRo compressor. As discussed by Hacks et al. [4] the rotational speed of the compressor must be well above 150,000 rpm for the compressor to lie within a region of good efficiency because of the low mass flow. As this is not a feasible option because of excessive windage losses, the rotational speed is reduced leading to a low specific speed and large specific diameter. This causes a low flow coefficient and low efficiency according to Figure 4. A usual procedure to design a machine based on an existing design is to scale the machine according to the affinity laws. This means the machines are similar in geometry, velocities and dynamic forces (see Bohl and Elmendorf [3]). During this procedure the dimensionless parameters such as specific speed and diameter, flow and head coefficient stay constant. The scaled compressor is thus at the same position in Figure 4. As the expected efficiency is low for the sCO2-HeRo compressor (red dot), it seems not reasonable to apply scaling according to the affinity laws, but rather to shift the compressor in Figure 4 further towards higher efficiencies. To stick to the TAC design of the sCO2-HeRo with shrouded impellers and labyrinth seals, only the indicated region of radial impellers is considered (see red dotted line). To decide for the final position in Figure 4 the following influences must be considered.

1. Efficiency of the compressor and turbine
2. Windage losses
3. Leakage flow for generator cooling

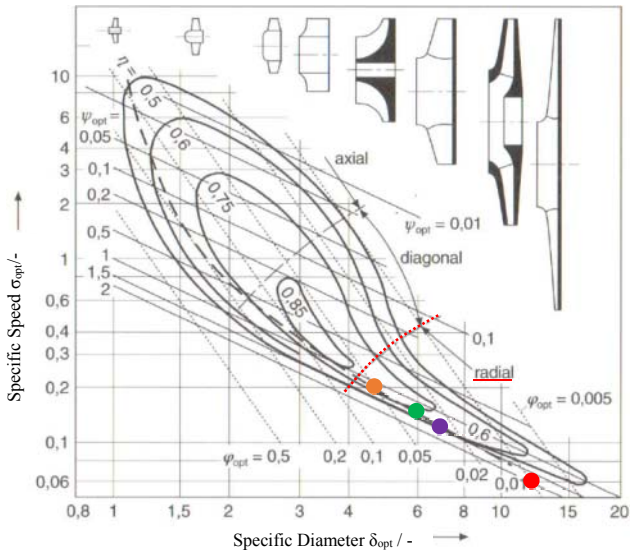

Figure 4: Cordier diagram for turbo-compressors [3][1]

[1] Labels of axes translated from German into English, Data according to Balje O. E., Turbomachines: A Guide to Design, Selection and Theory, John Wiley & Sons Inc., 1981 edited by Bohl and Elmendorf. Please note that the definition of head coefficient, specific speed and specific diameter vary from the definition of Balje by a constant factor of 2, 0.34 and 1.05 respectively.

DOI: 10.17185/duepublico/46089

The following explanations are based on the compressors and turbines given in Annex A and the motors in Annex B. Further, presented power differences are related to the power of the machine scaled by affinity laws (red dot). Because of the affinity laws, the efficiency is assumed to be the same as in the sCO2-HeRo machine and compressibility effects are neglected. All diagrams show power over rotational speed. The speed refers to a certain compressor, turbine and motor design in the tables in Annex A and Annex B. The dots that mark special operation points are presented in the following diagrams and Figure 4.

Compressor and Turbine Efficiency

As already mentioned the efficiency of compressor and turbine are expected to increase when moving the operating point along the Cordier line from the red dot towards the orange dot in Figure 4. The increase of compressor efficiency of more than 25 % from the red to the orange dot according to Figure 4 however, seems to be too large. Design CFD calculations for the sCO2-HeRo showed isentropic efficiencies of the compressor and turbine of around 66 % and 75 % already. More information on the calculations is given by Hacks et al. [4] and Schuster et al. [8]. The increase in power in Figure 4 is thus estimated by assuming a linear increase of efficiency of 5 % from the red dot towards the orange dot. This is of course a rough assumption but is deemed sufficient to present the scaling concept. Figure 5 shows that the improved efficiency causes an increase of the net-power by about 30 kW. This is caused by lower power consumption of the compressor of about 10 kW and increased turbine power of about 20 kW.

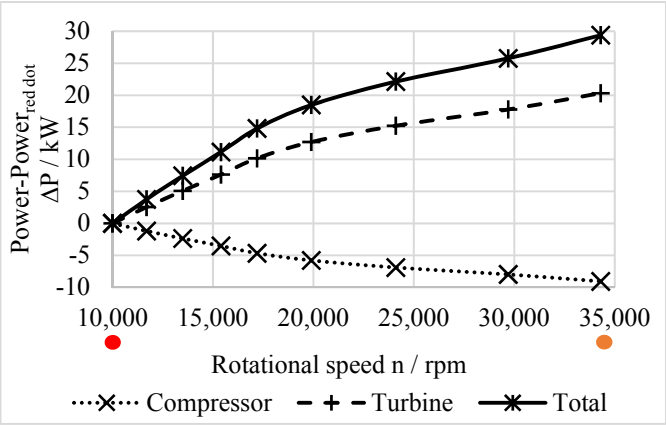

Figure 5: Power difference depended on efficiency

Windage losses

Hacks et al. [4] and others explain the high influence of windage losses on the overall efficiency of sCO2 turbomachinery. Therefore, the increased net-power must be compared to the development of the windage losses. The windage losses are determined applying the windage models of von Kármán [7] and Bilgen and Boulos [2] for the impellers and the generator respectively. The losses at the shaft seals and bearings are neglected, because they strongly depend on the chosen bearing type and shaft geometry. As direct leakage feedback without additional pump is desired and the windage losses are smaller for lower pressure, the pressure in the central housing is set to the compressor inlet pressure. The dimensions of the compressor and turbine impellers are determined using the Cordier diagram and summarized in Annex A. The motor dimensions are summarized in Annex B and retrieved using the motor type sheets of the company e+a Elektromaschinen und Antriebe AG, which supplied the motor for the sCO2-HeRo TAC. Appling equation (1) and (2) for the impeller discs indicates, that the windage losses of the impellers decrease towards higher specific speed along the Cordier line in Figure 4 (red dot towards orange dot). For the motor however, this is different. Even though the motor size decreases with increasing speed, the windage losses according to equation (3) and (4) increase. Figure 6 presents that there exists a speed, at which the windage losses reach a minimum. This speed is the optimal speed regarding windage losses, which is indicated by the purple dot in Figure 4. The losses at higher speed and smaller dimensions (orange dot) are even bigger as for the larger machine at lower speed.

Impellers:

$$c_m = \frac{0.07288}{Re^{0.2}} \quad (1)$$

$$P_{fG} = 0.5 * \pi * c_m * \rho * \omega^3 * \left(\frac{D}{2}\right)^5 \quad (2)$$

Generator:[2]

$$c_m = \frac{0.065 * \left(\frac{b}{\frac{D}{2}}\right)^{0.1}}{Re^{0.2}} \quad (3)$$

$$P_{fG} = 0.5 * c_m * \rho * \omega^3 * \left(\frac{D}{2}\right)^4 * L \quad (4)$$

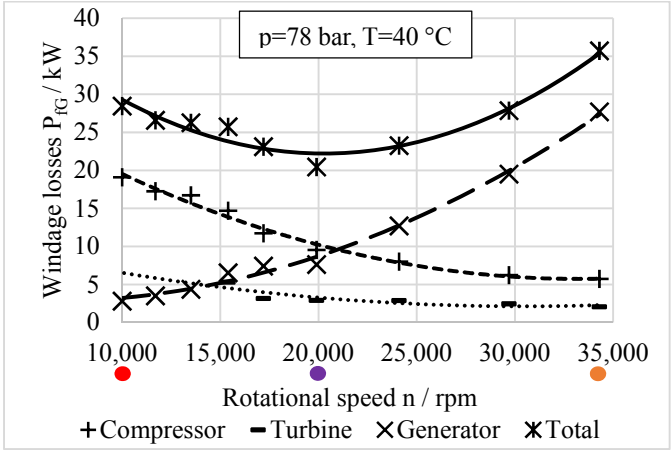

Figure 6: Windage losses at the motors and impellers

[2] Bilgen and Boulos [2] define $Re = \frac{\rho * \omega * \frac{D}{2} * b}{\mu}$. The formula for c_m is changed to fit the given definition of the Reynolds number.

DOI: 10.17185/duepublico/46089

Cooling requirements

The cooling of the generator is realized by leading the leakage of the compressor through the generator cavity and having additional cooling fins in the casing. Design calculations (see Hacks et al. [4]) and first tests showed that the concept is sufficient for generator cooling of the sCO2-HeRo TAC. Therefore, no additional cooling system is required, but a minimum leakage flow must be provided, which has influence on the compressor performance. The larger TAC has a larger generator, which produces higher power losses. The total losses of the generator consist of the previously described windage losses and the electrical losses. To approximate the required leakage flow, the necessary cooling power is calculated by equation (5). As a conservative approach the effect of the cooling fins is neglected.

$$P_{Cooling} = P_{fG} + P_{eG} \quad (5)$$

The electrical losses of the generator are approximated by the required efficiency of class IE4 of DIN EN 60034-30-1, which is 97 %. For the expected 180 kW_e of the generator this means approximately 5,4 kW of electrical losses. This represent the maximum losses, which are, for simplicity, used for all speeds. Together with the windage losses the leakage flow must remove about 3 kW to 28 kW of heat from the generator. Other windage losses along the flow path of the leakage such as the bearings and seals are neglected. To avoid large temperature gradients across the motor the maximum temperature increase of the leakage flow is set to 15 °C, which is comparable to the temperature increase in the sCO2-HeRo TAC. The inlet temperature into the cavity is 35 °C. Thus, the minimum mass flow of sCO2 to remove the heat can be approximated. It is maximally 0.5 kg/s or 3 % of the design mass flow. Hence, the influence on the overall efficiency is expected to be relatively small and generator cooling can be realized by the leakage flow. The influence on choosing the operational speed is deemed neglectable.

Scaling summary

Shifting the compressor point in Figure 4 to better efficiency causes higher rotational speed and a decreasing diameter of the impellers. Analysis of the windage losses shows, that those at the impellers decrease, while the windage losses at the generator increase. Thus, an operational speed with minimal windage losses exists. The increase in turbine and compressor efficiency causes higher shaft power. The optimal operating point is, where the power of the generator reaches its maximum. Further, the generator is cooled by the leakage flow of the compressor. Increasing windage losses require more cooling and thus a larger leakage flow from the compressor, which decreases its efficiency. It is shown that a reasonable fraction of the compressor flow is sufficient for generator cooling. Therefore, the leakage mass flow is not considered for determining the operating point. Figure 7 shows the development of the power output for different operating points. The power difference is calculated with respect to the machine, which is scaled by affinity laws having the same dimensionless parameters as the sCO2-HeRo TAC. The combination of both the development of windage losses and the power increase due to the higher compressor and turbine efficiency clearly shows an optimum operating point (green dot in Figure 7). The so found operating point is then used for detailed mechanical design of the TAC including the bearings and rotordynamics as well as blading design. As the dimensionless parameters change, it can be expected, that the sCO2-HeRo blades must be modified. Applying a 1D program considering leakage flows is required to reliably predict the compressor and turbine efficiency and power.

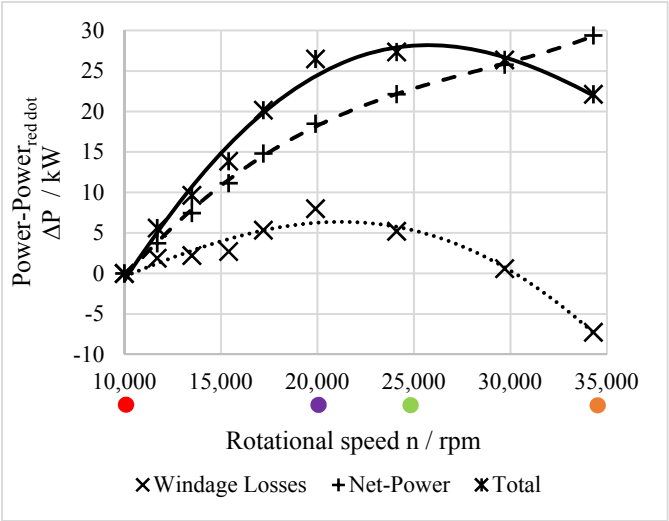

Figure 7: Development of power for different operation points

BEARINGS

The sCO2-HeRo TAC uses grease lubricated ball bearings due to size constraints and rotordynamic (see Hacks et al.[4]). First tests show that grease lubricated bearings cannot be used in sCO2 environment. Thus, a pump for pressure reduction in the central housing is required. As for a safety system in a NPP it is desirable to reduce the amount of auxiliary systems, the bearing concept needs to be changed to bearings that can operate in sCO2 environment. The characteristics of three bearing types with respect to the sCO2-NPP TAC are summarized in Table 2. As the sCO2-NPP system consist of several units, it is possible to use different strategies in the separate units. For example, very robust bearings can be used to initialise the whole system. Such bearing can be sCO2-lubricated ball bearings, which do not need to be controlled during start-up and do not have minimum speed. Therefore, they have no acceleration requirements. Initialisation means that a TAC with these bearings is used to produce little amount of electricity. The electricity then serves to start up a control system for magnetic bearings or to provide auxiliary power for rapid acceleration of the shaft using the motor for the application of gas foil bearings. As the units are switched off one after another, a machine, which employs roller bearings and thus has a low service life, is still a feasible option.

DOI: 10.17185/duepublico/46089

Table 2: Comparison of bearing concepts

	Roller bearings	Gas foil bearings	Magnetic bearings
Operating speed restrictions	Restriction of maximum speed	Need minimum speed	
Service life	Limited	Unlimited	Unlimited
Auxiliary Units	Leakage pump	Non	Control system for active control of the bearings
Design	Standard	High dependency of load capacity on fluid properties and speed	Active control of the shaft position is required
Robustness	Grease and Oil are dissolved by sCO2	Strong dependency of load capacity on fluid conditions and rotational speed	Electricity shortage means that bearings do not work (active component)
Start-Up	Allows rotation also at low speeds	Rapid start-up until minimum speed	Critical speeds can be avoided with suitable control

Roller bearings

These bearings are probably the most robust bearings as the do neither need lift-off speeds or active control. When grease or oil lubricated bearings are employed, a leakage pump is required. Initial tests of the sCO2-HeRo TAC show that, even if the grease inside the bearings is removed by sCO2, the bearings can still operate for a certain time. As the lubrication effect of the sCO2 is limited the time is short. However, the required service life for the application is maximally a few days. Thus, it seems reasonable to believe that sCO2-lubricated roller bearings can be employed if the maximum speed of the TAC and the bearing load is appropriate.

Gas foil bearings

This is the type of bearing proposed by Sienicki et al. [9] for the size range of the sCO2-NPP TAC. These bearings require a minimum lift-off speed to operate, which requires fast start-up and rapid acceleration of the shaft. Ongoing tests of the sCO2-HeRo address the start-up of the system to determine the required time and procedure. The load capacity of the bearings is strongly dependent on the rotational speed and very limited at low speed. The bearings therefore need to be carefully designed and the operation range must be set leaving sufficient margin towards higher loads and low speeds to allow save operation. Additionally, the gap between the stator and rotor parts is very narrow causing high losses when operated in sCO2. The key advantage for the safety system is, that gas foil bearings can operate without additional auxiliary units and without wearing off.

Magnetic bearings

These bearings need to be controlled when in operation and thus need a fully operational control system during start-up of the safety system. They need to be as carefully designed as foil bearings but allow a wider operation range regarding rotational speed. This means, that they do not need a minimum speed to operate and are additionally able to actively avoid critical speeds by altering their stiffness and damping behaviour. Further the gap between rotor and stator is larger as for gas foil bearings causing lower losses. The service life is basically unlimited. As a loss of the control system makes the bearings stop working, additional catcher bearings such as non-lubricated ball bearings must be employed to safe the shaft from falling into the stator.

ROTORDYNAMICS

Finally, also rotordynamics need to be considered. The increasing speed means that during start-up critical speeds need to be considered. For the application as safety system generally a wide range of operational speed with low influence of critical speeds is desired. The generated electrical power is not the key requirement of the cycle. Therefore, it might be better to stick to low rotational speeds, even if the efficiency is lower. If the bearing system is known rotordynamic considerations such as avoiding critical speeds can directly be included in the process of choosing an operational speed. As this is not yet the case for the sCO2-NPP system it is not considered in this paper.

CONCLUSION

It is presented, that for the scaled sCO2-NPP TAC the same design approach can be used as for the sCO2-HeRo TAC. Scaling following the affinity laws means that the efficiency of the sCO2-NPP TAC is low. To increase efficiency the operating point can be shifted in the Cordier diagram. The operating point is found by iterative calculation and comparison of the compressor and turbine efficiency and the windage losses. The cooling requirement is manly dependent on the windage losses. The required leakage flow for generator cooling is small compared to the main flow in the cycle. Therefore, it is not necessary to consider it for choosing the operation point. More detailed calculations such as rotordynamics, which consider the operational restrictions such as critical speeds can be included, too. For this it is necessary to define the appropriate bearing type. The sCO2-NPP TAC shall operate with sCO2 in the central housing. Different bearing types are compared with considering the requirements of the safety system. The most appropriate bearing type is dependent on the machine behaviour and control strategy especially during start-up. This is subject to the ongoing tests of the sCO2-HeRo TAC and no decision can be made yet.

DOI: 10.17185/duepublico/46089

NOMENCLATURE

Symbol	Unit	Description
b	m	Cavity height
c_m	-	Moment coefficient
D	m	Diameter
L	m	Length
$\dot{m}$	kg/s	Mass flow
n	1/s	Rotational speed
P	kW	Power
Q	m³/s	Volume flow
$Re = \frac{\rho * \omega * \left(\frac{D}{2}\right)^2}{\mu}$		
u	m/s	Circumferential speed
y	J/kg	Specific flow work
$\delta_{opt} = \frac{\psi_{opt}^{\frac{1}{4}}}{\sqrt{\varphi_{opt}}} = D * \sqrt[4]{\frac{2*y}{Q^2}} * \frac{\sqrt{\pi}}{2}$	-	Specific diameter
η	%	Isentropic Efficiency
μ	Pa*s	Dynamic viscosity
ρ	kg/m³	Density
$\sigma_{opt} = \frac{\sqrt{\varphi_{opt}}}{\psi_{opt}^{\frac{3}{4}}} = n * \frac{2*\sqrt{\pi}*\sqrt{Q}}{(2*y)^{\frac{3}{4}}}$	-	Specific speed
$\varphi_{opt} = \frac{c_m}{u} = \frac{4*Q}{\pi^2*D^3*n}$	-	Flow coefficient
$\psi_{opt} = \frac{2*y}{u^2} = \frac{2*y}{\pi^2*D^2*n^2}$	-	Head coefficient
ω	Rad/s	Angular speed

Abbreviation	Description
BWR	Boiling water reactor
GfS	Gesellschaft für Simulatorschulung mbH
NPP	Nuclear power plant
PWR	Pressurized water reactor
sCO2	Supercritical CO_2
sCO2-HeRo	The supercritical CO_2 heat removal system for the glass model
sCO2-NPP	The supercritical CO_2 heat removal system for a nuclear power plant
TAC	Turbine, alternator, compressor system

Subscript	Description
e	Electrical
f	Friction
G	Generator
th	Thermal

ACKNOWLEDGEMENTS

This project has received funding from the European research and training programme 2014 – 2018 under grant agreement No 662116.

REFERENCES

[1] Benra, F.-K., Brillert, D., Frybort, O., Hajek, P., Rohde, M., Schuster, S., Seewald, M. & Starflinger, J. (2016). A supercritical CO2 low temperature Brayton-cycle for residual heat removal. *The 5th International Symposium - Supercritical CO2 Power Cycles*, San Antonio, Texas, USA

[2] Bilgen, E. & Boulos, R. (1973). Functional Dependence of Torque Coefficient of Coaxial Cylinders on Gap Width and Reynolds-Numbers. *Journal of Fluids Engineering*, 95(1), 122-126

[3] Bohl, W. & Elmendorf, W. (2013). *Strömungsmaschinen 1. Aufbau und Wirkungsweise* (Vol. 11), Würzburg: Vogel

[4] Hacks, A. J., Schuster, S., Dohmen H. J., Benra F.-K. & Brillert D. (2018). Turbomachine Design for Supercritical Carbon Dioxide within the sCO2-HeRo.eu Project. *ASME Turbo Expo*, Oslo, Norway

[5] e+a Elektromaschinen und Antriebe AG (2017). Asynchron-Elan types – 4-pole – 08/2017

[6] e+a Elektromaschinen und Antriebe AG (2017). Asynchron-Standard types – 4 pole – 06/2017

[7] Kármán, Th v. (1921) Über laminare und turbulente Reibung. *ZAMM-Journal of Applied Mathematics and Mechanics/Zeitschrift für Angewandte Mathematik und Mechanik*, 1(4), 233-252.

[8] Schuster S., Benra F.-K., Brillert D. (2016) Small scale sCO2 compressor impeller design considering real fluid conditions. *The 5th International Symposium - Supercritical CO2 Power Cycles*, San Antonio, Texas, USA

[9] Sienicki, J. J., Moisseytsev, A., Fuller, R. L. Wright, S. A. & Pickard, P. S. (2011). Scale Dependencies of Supercritical Carbon Dioxide Brayton Cycle Technologies and the Optimal Size for a Next-Step Supercritical CO2 Cycle Demonstration. *SCO2 Power Cycle Symposium*, Boulder, Colorado, USA

[10] Venker, J. (2015). Development and validation of models for simulation of supercritical carbon dioxide Brayton cycles and application to self-propelling heat removal systems in boiling water reactors. *IKE (Institut für Kernenergetik und Energiesysteme), Universität Stuttgart*, Stuttgart, Germany

DOI: 10.17185/duepublico/46089

ANNEX A

COMPRESSOR AND TURBINE PARAMETERS

The compressor and turbine parameters are determined with help of the Cordier diagram. First the dimensionless parameters of the compressor are read out of the Cordier diagram along the Cordier line from the red to the orange dot in Figure 4. Then diameter and speed are calculated by the given formulas. Secondly the dimensionless turbine parameters are determined for rotational speeds calculated before. The Cordier line for turbines on page 79 in the book of Bohl and Elmendorf [3] is used. The pressure ratio and inlet conditions are assumed to be constant. The highlighted points in the Figure 4 to Figure 7 are marked. Additionally, the tables contain the compressor and turbine data for all other points shown in the diagrams Figure 5 to Figure 7 marked as support points.

Table 3: Comparison of the basic parameters of the compressor

Position in Figure 4	**Rotational speed n (rpm)**	**Impeller Diameter D (mm)**	**Mass Flow ṁ (kg/s)**	**Isentropic Efficiency η (%)**	**Specific diameter δ_{opt} (-)**	**Specific speed σ_{opt} (-)**	**Flow coefficient φ_{opt} (-)**	**Head coefficient ψ_{opt} (-)**
sCO2-HeRo	50,000	40	0.65	66.3	12.4	0.06	0.009	1.8
Red dot (scaled by affinity laws)	10,000	200	16.25	66.3	12.4	0.06	0.009	1.8
Support point	11,600	178	16.25	66.8	11	0.07	0.011	1.7
Support point	13,400	162	16.25	67.3	10	0.08	0.012	1.5
Support point	15,100	146	16.25	67.8	9	0.09	0.015	1.4
Support point	16,800	130	16.25	68.3	8	0.10	0.019	1.4
Purple dot	19,400	114	16.25	68.8	7	0.12	0.024	1.4
Green dot	23,300	98	16.25	69.3	6	0.15	0.032	1.3
Support point	28,600	82	16.25	69.8	5	0.18	0.045	1.2
Orange dot	32,800	74	16.25	70.3	4.5	0.21	0.053	1.1

Table 4: Comparison of the basic parameters of the turbine

Position in Figure 4	**Rotational speed n (rpm)**	**Impeller Diameter D (mm)**	**Mass Flow ṁ (kg/s)**	**Isentropic Efficiency η (%)**	**Specific diameter δ_{opt} (-)**	**Specific speed σ_{opt} (-)**	**Flow coefficient φ_{opt} (-)**	**Head coefficient ψ_{opt} (-)**
sCO2-HeRo	50,000	66	0.65	74.8	10.9	0.07	0.011	1.6
Red dot (scaled by affinity laws)	10,000	330	16.25	74.8	10.9	0.07	0.011	1.6
Support point*	11,600	282	16.25	75.3	9.3	0.09	0.015	1.6
Support point*	13,400	231	16.25	75.8	7.6	0.10	0.023	1.8
Support point*	15,100	181	16.25	76.3	6	0.11	0.042	2.3
Support point	16,800	151	16.25	76.8	5	0.12	0.066	2.7
Purple dot	19,400	135	16.25	77.3	4.5	0.14	0.079	2.6
Green dot	23,300	120	16.25	77.8	4	0.17	0.094	2.3
Support point	28,600	102	16.25	78.3	3.4	0.20	0.125	2.1
Orange dot	32,800	90	16.25	78.8	3	0.23	0.160	2.1

*Extrapolated from Cordier diagram

DOI: 10.17185/duepublico/46089

ANNEX B

MOTOR SIZES

Table 5 contains the rotor diameter and length including the end rings for different rotational speeds. The motor parameters were extracted from the type overview of 4 pole asynchronous motors (see [5] and [6]) and the "Motor Scout" offered by e+a Elektromaschinen und Antriebe AG for an approximated power of 180 kW. The outer rotor diameter is approximated by the inner stator diameter. The rotor length is calculated from the stator stack length, determined using the "Motor Scout" of e+a Elektromaschinen und Antriebe AG according to the names in Table 5, and the rotor ring length in the type overview.

Table 5: Motor Sizes for the determination of windage losses in Figure 6

Speed (rpm)	Name	Outer Rotor Diameter (mm)	Total Rotor Length (mm)
10,000	mW 20/36-4-s2r5	130	396
11,600	mW 20/26-4-s3r3	130	296
13,400	mW 20/26-4-s3r3	130	296
15,100	mW 20/26-4-s3r3	130	296
16,800	mW 17/40-4-s2r5	110	432
19,400	mW 17/25-4-s2r5	110	282
23,300	mW 17/25-4-s2r5	110	282
28,600	mW 17/20-4-s2r5*	110	232
32,800	mW 17/20-4-s2r5*	110	232

* Maximum speed of the motor is 29,000 rpm. No motors are available in the type overview for speeds above 29,000 rpm.

DOI: 10.17185/duepublico/46089

2nd European supercritical CO2 Conference
August 30-31, 2018, Essen, Germany

2018-sCO2.eu-107

EVALUATION OF SCO_2 POWER CYCLES FOR DIRECT AND WASTE HEAT APPLICATIONS

Stefan Glos*
Siemens AG, Power and Gas Division
Mülheim an der Ruhr, Germany
Email:Stefan.glos@siemens.com

Michael Wechsung
Siemens AG, Power and Gas Division
Mülheim an der Ruhr, Germany

Rebecca Wagner
University Duisburg-Essen
Duisburg, Germany

Andre Heidenhof
University Duisburg-Essen
Duisburg, Germany

Dominic Schlehuber
Siemens AG, Power and Gas Division
Mülheim an der Ruhr, Germany

ABSTRACT

Supercritical CO_2 (sCO_2) power systems may improve cycle efficiencies of future power plants significantly while reducing size and costs of the related components. This paper provides a thermodynamic evaluation of sCO_2 power cycles compared to conventional power cycles based on water/steam. Different plant layouts for direct and waste heat applications are assessed and the impact of process parameters such as upper and lower process temperatures is evaluated by variational calculations. The results are compared with reference values based on water/steam derived from a state-of-the-art concentrated solar power plant and combined cycle power plants respectively. An optimized cycle layout results in significant efficiency advantages of the sCO2 power cycles. Regardless of the application, the investigations show that these advantages are strongly dependent on the characteristic values of the components such as TTD, pressure losses and expansion efficiencies.

INTRODUCTION

Power generation based on supercritical carbon dioxide (sCO_2) Brayton cycles has been the object of numerous research studies during the last years. Improved cycle efficiencies and lower component costs compared to conventional Rankine cycles are claimed in various publications [1-4]. Depending on the application type, different cycle layouts have been proposed in literature. A recently published, comprehensive review of investigated cycle configurations is given in [5]. For direct heated applications such as coal fired, concentrated solar or nuclear power plants recompression cycles have been identified as most beneficial [3, 6]. For waste heat applications and combined cycle power plants cascaded cycles are the best choice for high cycle performance [4, 5]. However, theoretically calculated cycle efficiencies are highly dependent on assumed characteristic values such as turbine efficiencies, pressure losses and terminal temperature differences and may not necessarily reflect economics and practical performance limits. The comparison of published cycle efficiencies with reference values based on water/steam is thus often difficult.

This paper evaluates for both, primary and waste heat applications, the performance of sCO_2 cycles in comparison with state-of-the-art water steam cycles. Basic design estimations such as turbine design are carried out and compared with the equipment used in the reference cycles. The sensitivities of characteristic values on performance and equipment are investigated.

SIMULATION AND MODELING

Thermodynamic cycle simulations were carried out by using the simulation software Cycle-Tempo [7] in combination with REFPROP property tables [8] considering the physical properties of CO_2 and water/steam. The performance values of the reference cycles based on water/steam were calibrated to results derived by SIEMENS in-house simulation software. Initial sCO_2 turbine design calculations were performed with internal software using a simplified fluid property model [8]. In the operating range of the turbines, i.e. the gaseous single phase region, this model, which is actually valid for gaseous fluid mixtures, is in good agreement with the properties derived by REFPROP.

DIRECT HEAT APPICATIONS

A 150 MW solar tower power plant was chosen as reference for direct heated application. The general cycle layout is shown in figure 1. It consists of three LP preheaters, one deaerator and two HP preheaters. The turbo set consists of high efficient SST700 and SST900 steam turbine modules. Live steam and reheat temperature were varied between 545 °C 605 °C. Live steam and reheat pressures are 140 bar and 27 bar respectively. The HP pressure loss across boiler and main steam piping is approximately 12 % and reheat pressure loss 10 %.

DOI: 10.17185/duepublico/46082

The terminal temperature difference of the condenser was set to 3 K. Cooling water inlet temperatures were varied between 10 °C and 45 °C.

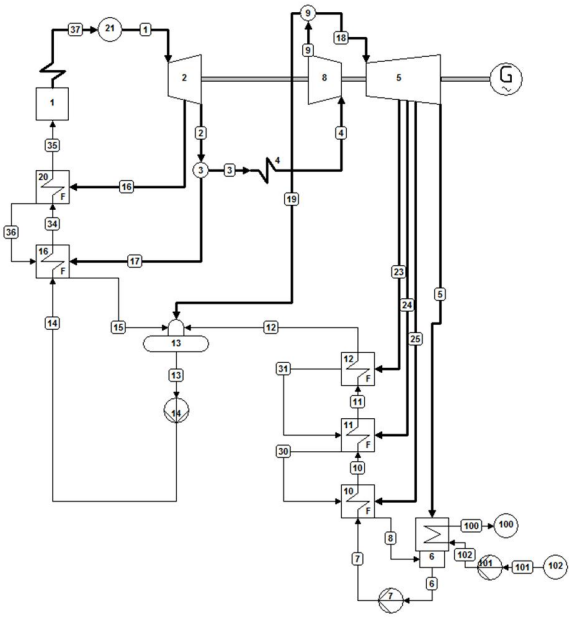

Figure 1: Heat balance diagram of reference cycle, a 150 MW CSP Rankine cycle, modeled with Cycle-Tempo.

The thermodynamic cycle of a simple recuperated, reheated sCO_2 Brayton cycle is illustrated in figure 2. Comparing the mean temperatures of heat input and heat sink for the Brayton and the reference Rankine cycle the advantage of direct heated Brayton cycle becomes obvious.

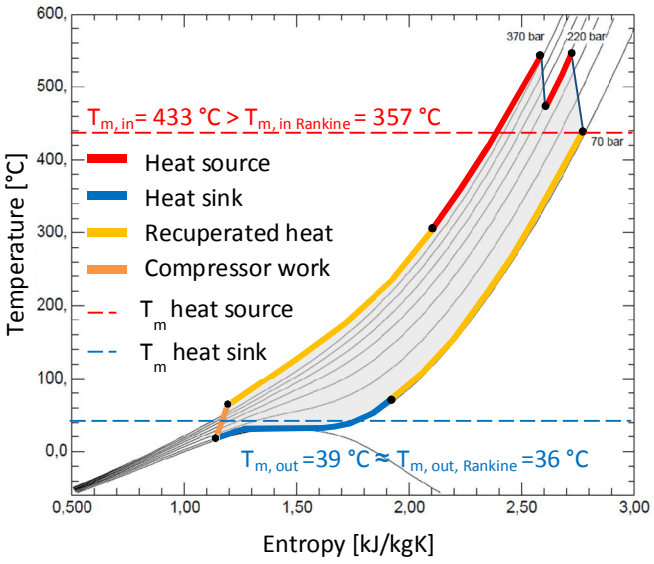

Figure 2: T-s diagram of recuperated sCO_2 cycle for a reheat power cycle with 545 °C as live steam and reheat temperature.

While the mean temperature of the heat sink differs only marginally, the mean temperature of the heat source is significantly higher in the Brayton cycle. Introducing the Carnot efficiency according to equation 1 the idealized benefit of the sCO_2 cycle can be expressed in a $\Delta\eta_{Carnot} \approx 5$ % for this case.

$$\eta_{Carnot} = (1 - \frac{T_{Heat\ Sink}}{T_{Heat\ Source}}) \quad (1)$$

However, for comparing the Brayton cycle with a Rankine cycle and thus for assessing the thermodynamic benefits, the exergy losses of the process have to be considered. The characteristic values such as pressure losses, turbine and compressor efficiencies and terminal temperature differences (TTD) of the heat exchangers which were used in initial cycle calculations are summarized in table 1. The values for pressure losses, TTD and compressor efficiency were chosen in line with published data [3, 4, 6]. A sensitivity study of these values as well as first turbine design considerations, from which the turbine efficiency was derived, is presented in detail later in this paper.

Two cycle architectures were considered. A simple recuperated cycle with reheat is shown in figure 3 and a recompressed, reheated cycle with single stage intercooling, which is shown in figure 4. The inlet pressure of the first turbine was set to 370 bar and the lower pressure level at the compressor inlet was set to 70 bar. The initial recompression ratio is 25 % which means that only 75 % of the total mass flow is led to the heat sink.

Table 1: Characteristic values for efficiencies, pressure losses and terminal temperature differences used for the initial thermodynamic cycle calculations.

Parameter	Value	Unit
Pressure loss recup., boiler, reheat, cond.	2	%
Terminal temperature difference heat sink	3	K
Terminal temperature difference recup.	5	K
Efficiency turbines	91	%
Efficiency compressors	85	%
Efficiency generator	98,25	%

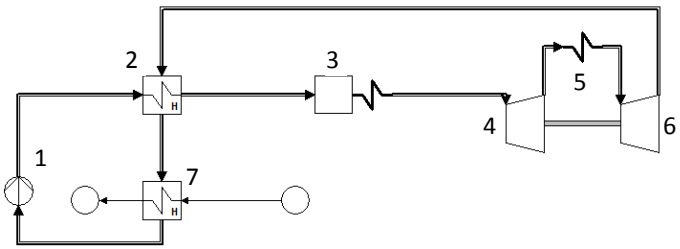

Figure 3: Layout of a simple recuperated, reheated sCO_2 cycle. 1-compressor, 2-recuperator, 3-boiler, 4-high pressure turbine, 5-reheat, 6-reheat turbine, 7-heat sink.

DOI: 10.17185/duepublico/46082

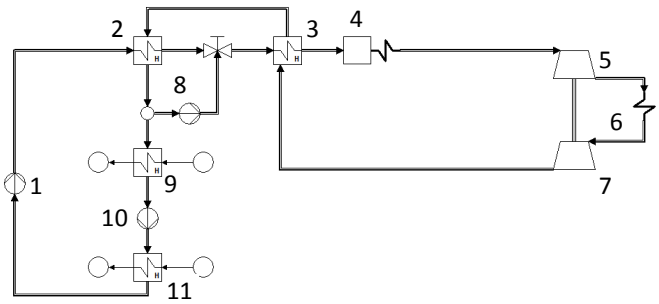

Figure 4: Layout of a recompressed, intercooled and reheated sCO_2 cycle. 1-compressor, 2-low temperature recuperator (LTR), 3-high temperature recuperator (HTR), 4-boiler, 5-high pressure turbine, 6-reheater, 7-reheat turbine, 8-compressor, 9-heat sink, 10-compressor, 11-intercooler.

Since the cycle performance depends significantly on the lower process temperature, cycle calculations were carried out with varying cooling water inlet temperatures for both the water/steam cycle and the sCO_2 cycle. As the cooling water temperature rises, the losses in the condenser and compressor also increase, as these process steps are completely shifted to the right side of the critical point. By increasing the back pressure, this can be corrected and the losses can be reduced. For simplification the calculations were carried out with constant expansion and compression efficiencies. In figure 5 the deviation of the sCO_2 net efficiency values from the reference values based on water/steam are shown.

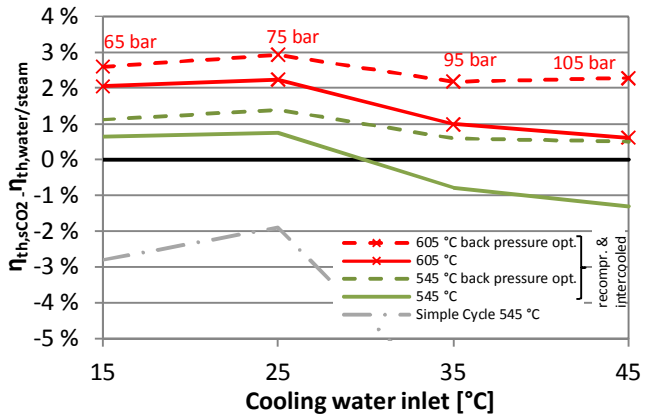

Figure 5: Deviations of net efficiency values compared to reference values based on water/steam. The initial back pressure was 75 bar. The optimized back pressures are given for 605 °C. Further process parameters were kept constant.

The main contributor for the significant lower performance of the simple recuperated Brayton cycle compared to the reference values is the large exergy loss in the recuperator based differences in isobaric specific heat capacity of the hot and cold stream. By introducing the recompression cycle these losses can be reduced significantly which increases the overall process efficiency as shown in figure 6. This improvement is, however, associated with an increase of the heat transfer surface. A sensitivity study is described later in this paper.

However, with increasing cooling water temperature and thus with increasing compressor inlet temperature the efficiency drops considerably because the thermodynamic condition at the compressor inlet changes from a “as-liquid-state” to an “as-gaseous state”.

Thus, the compressor work and losses as well as the exergy losses in the heat sink are increasing significantly. This effect can be compensated by increasing the lower pressure level of the process, i.e. the compressor inlet pressure. In figure 5 the calculation points for the optimized backpressures (dashed line) are labeled with the chosen pressure values.

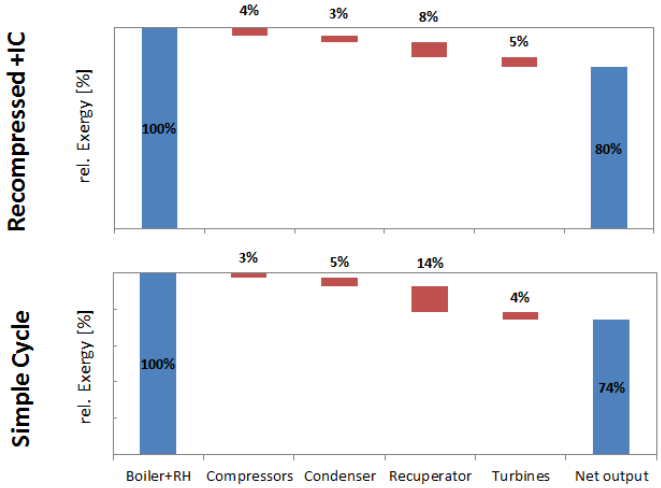

Figure 6: Exergy losses in a simple recuperated cycle and in a recompressed, intercooled cycle. The amount of supplied exergy in the boiler and reheater is set to 100 %.

The impact of the upper and lower process pressure on the thermal efficiency is shown in figure 7 exemplarily for a turbine inlet temperature of 605 °C and a cooling water inlet temperature of 25 °C. In this case, the thermodynamic condition of the compressor inlet is close to the liquid phase as shown in figure 2 leading to an optimum backpressure of approximately 75 bars.

DOI: 10.17185/duepublico/46082

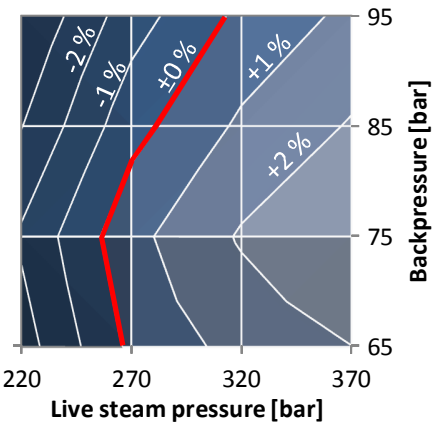

Figure 7: Deviation of net efficiency values compared to reference values based on water/steam depending on upper and lower process pressure for a design point of 605 °C turbine inlet temperature and 25 °C cooling water temperature.

It can be also concluded from figure 7 that the turbine inlet pressure has to be higher than approximately 255 bars to get a performance benefit compared to the reference performance based on water/steam. With decreasing inlet pressure the recuperated heat is increasing and thus the exergy loss rises significantly.

The sCO_2 turbine modules were derived from the standard steam turbine product portfolio. Both, the high pressure turbine and the reheat turbine are high efficient barrel type turbines as shown in figure 8. Due to the small enthalpy drop in the Brayton cycle the number of stages and thus the axial length is significantly lower compared to the reference turbines. Whereas the high pressure inlet volume flow is even higher compared to the water/steam cycle, the exhaust volume flow at the lower pressure side is considerably smaller compared to the exhaust flow of the low pressure steam turbine, which leads to smaller component sizes at the cold end. However, the high pressure level in the sCO_2 turbines leads to large wall thicknesses in casings, valves and piping in comparison to the steam turbines. Improvements concerning performance and economics can be gained from the implementation of advanced sealing technologies such as dry gas seals and the development of a single casing turbine design and must be addressed in future development activities.

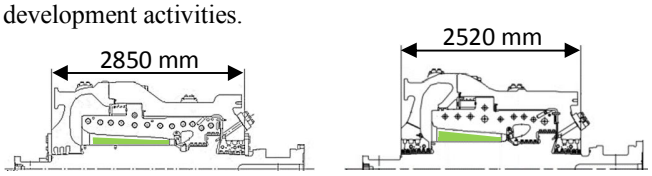

Figure 8: Illustration of high pressure sCO_2 turbine (left) and reheat turbine (right).

Table 2: Comparison of enthalpy differences as well as volume flows at the inlet and the outlet of the turbines in the CO_2- and the reference cycle based on water/steam.

Turbine		Water/Steam	sCO_2
HP	$\dot{V}_{inlet}$ [m³/s]	2,7	4,6
	$\dot{V}_{outlet}$ [m³/s]	9,3	8,5
	Δh [kJ/kg]	415	108
Reheat	$\dot{V}_{inlet}$ [m³/s]	13,5	10
	$\dot{V}_{outlet}$ [m³/s]	1841,5	18
	Δh [kJ/kg]	1210	97

A central component in a supercritical CO_2 Brayton cycle is the recuperator which transfers the heat from the exhaust flow of the turbine to the high pressure flow before it enters the boiler. The thermodynamic effect on the cycle efficiency is comparable to the feedwater preheating in a Rankine cycle. However, the amount of transferred heat is significantly higher in the Brayton cycle. In order to achieve a good overall cycle efficiency the TTD in the recuperator has to be kept small leading to a considerable high transfer capability (kA values) and thus to high heat transfer surfaces. Thus, the necessity of high efficient heat exchangers with high surface densities and low specific costs becomes obvious. In table 3 the characteristic data of the recuperating/ preheating can be compared.

Table 3: Comparison of recuperated heat and transfer capability in the CO_2 and the reference cycle based on water/steam.

	Water/Steam	sCO_2 Recompressed & Intercooled
Recuperated heat [MW]	79	505
$kA_{LP\,/\,LTR}$ [MW/K]	3,8	23
$kA_{HP\,/\,HTR}$ [MW/K]	3,4	10,5

Based on these results, the impact of the recompression bypass ratio and TTD on both the cycle efficiency and the heat transfer surface can be studied. The heat transfer surfaces in the recuperators were approximated by applying Nusselt-correlations for counter-flow tube-in-tube-heat exchangers. Lowering the bypass value from the initial value of 25 % by e.g. 5 % leads to an efficiency drop of approximately 1,1 % as shown in figure 9. On the other hand with this reduction the heat transfer surface in the recuperator can be reduced by approximately 30 % as illustrated in figure 10.

DOI: 10.17185/duepublico/46082

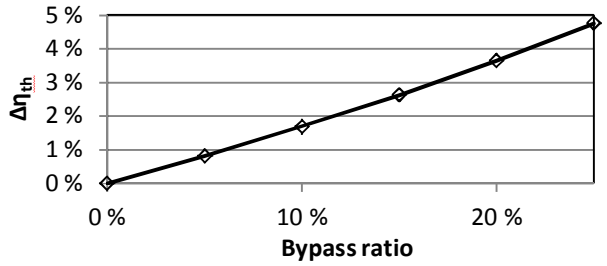

Figure 9: Deviation of the cycle efficiency as a function of the recompression bypass ratio.

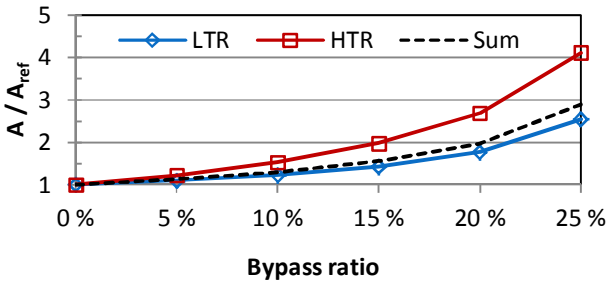

Figure 10: Deviation of the relative heat transfer surface in the low temperature heat exchanger (LTR) and the high temperature heat exchanger (HTR) as a function of the recompression bypass ratio.

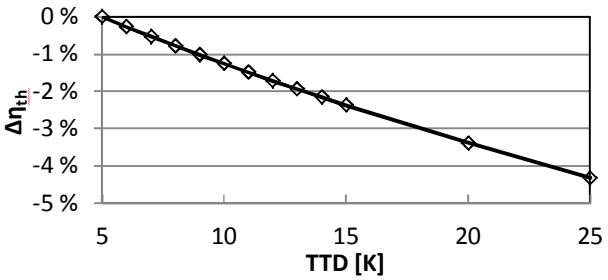

Figure 11: Deviation of the cycle efficiency depending on the terminal temperature difference

The sensitivity of the cycle efficiency and the heat transfer surface depending on the chosen terminal temperature difference is shown in figure 11 and figure 12 respectively. Increasing the terminal temperature difference from the initial value of 5 K to e.g. 10 K leads to an efficiency drop of approximately 1,3 % whereas the heat transfer surface could be reduced by about 40 %.

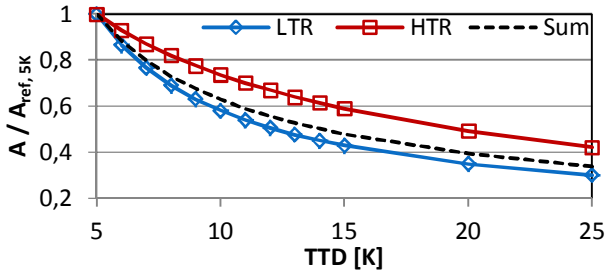

Figure 12: Deviation of the relative heat transfer surface in the low temperature heat exchanger (LTR) and the high temperature heat exchanger (HTR) as a function of the terminal temperature difference.

The initial pressure loss for each recuperator and the boiler was set to 2 % as listed in table 1. Thus, the pressure loss of the high pressure flow amounts to 6 % compared to 12 % in the reference cycle as written before. Assuming the same relative pressure loss of 12 % leads to an efficiency drop of approximately 1,1 % as shown in figure 13. Keeping in mind the fact of the higher pressure level and the larger volume flow at the turbine inlet, the necessity of a compact plant layout with short pipe length becomes obvious.

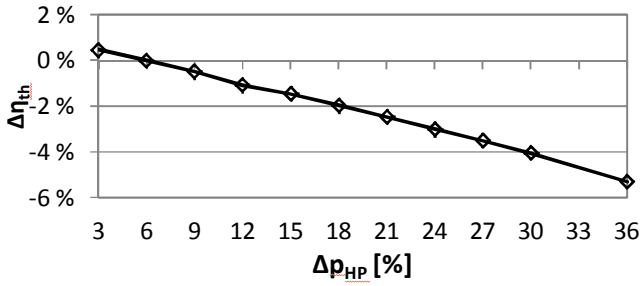

Figure 13: Deviation of the cycle efficiency depending on the assumed pressure loss of the high pressure flow (compressor outlet to HP turbine inlet).

In conclusion it can be stated that a supercritical Brayton cycle may lead to a significant performance benefit for the investigated 150 MW CSP application. Mandatory prerequisite is an optimized cycle architecture (recompressed and intercooled) with small terminal temperature differences, small pressure losses, high efficient turbo machinery, high turbine inlet pressures and optimized backpressures depending on the cooling conditions. Furthermore an increasing benefit with increasing upper process temperature can be noted. However, the shown performance benefit for the sCO_2 cycle cannot be generalized. For applications with high power output e.g. large coal fired power plants where supercritical Rankine cycles are beneficial, the results might be different and should be evaluated separately.

The necessary economic assessment and optimization of a sCO_2 power plant for a solar application needs to be done in a subsequent step considering the overall plant configuration including solar field, receiver etc.

DOI: 10.17185/duepublico/46082

WASTE HEAT APPLICATIONS

Two Combined Cycle Power Plants were chosen for the assessment of sCO_2 bottoming cycles in comparison to reference cycles based on water/steam. In the first reference cycle a dual pressure Rankine cycle recovers the waste heat coming from an aero derivative Trent60 gas turbine. The exhaust gas temperature is 431 °C. The second case is based on an SGT800 gas turbine with an exhaust gas temperature of 567 °C. Table 4 summarizes the design parameter of the two reference cycles.

Table 4: Design parameter of the reference cycles.

Parameter	Trent60	SGT800
Exhaust gas temperature [°C]	431	567
Exhaust gas mass flow [kg/s]	151,4	269,4
TTD HRSG [K]	10	10
Pressure loss HRSG HP part [%]	13,0	11,6
Bottoming cycle net output [MW]	14,6	50,0
Efficiency generator [%]	100	100

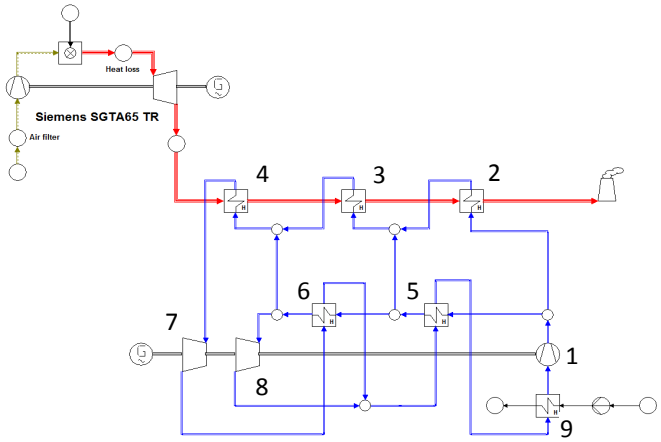

Figure 14: Layout of a dual split cascaded sCO_2 cycle. 1-compressor, 2, 3, 4-waste heat exchanger, 5-low temperature recuperator (LTR), 6-high temperature recuperator (HTR), 7-main turbine, 8-secondary turbine, 9-heat sink.

Cascaded sCO_2 cycles have been identified for high cycle performance in waste heat applications. In comparison to Rankine cycles the exergy losses in the heater can be minimized leading to a performance benefit of the bottoming cycle [4, 5, 9]. In figure 14 the cycle layout is shown exemplarily for the Trent60 bottoming cycle. It consists of one compressor, two recuperators, two turbines, one cooler and three heaters. After the compression, the fluid is split to two separate streams. The main stream passes through the heaters which recover the heat from the exhaust gas. After the expansion in the main turbine, it flows through two recuperators where the heat of the main turbine exhaust is transferred to the second stream which expands in the secondary turbine.

Since the specific heat of sCO_2 decreases with increasing temperature, the exergy losses in a single heater would be significantly high. By splitting up the heater and adding split flows from the second stream the temperature differences across the heat exchangers and thus the exergy losses can be minimized as shown in figure 15. The corresponding TTD as well as the TTD of the recuperators, the assumed pressure losses, turbine and compressor efficiencies and thermodynamic parameters for both the Trent60 and the SGT800 are listed in table 5.

Table 5: Design parameters of the sCO2 cycles.

Parameter	Trent60	SGT800
Back pressure [bar]	75	65
Cooling water inlet temperature [°C]	15	15
Pressure loss heaters, recu., cond. [%]	2	2
TTD waste heat exchanger [K]	10	10
TTD HTR [K]	10	10
TTD heat sink [K]	5	5
Turbine inlet pressure [bar]	220	255
Turbine inlet temperature [°C]	387	516
Efficiency main turbine [%]	86,2	89,2
Efficiency secondary turbine [%]	79,5	86,2
Efficiency compressors [%]	80	80
Efficiency generator [%]	100	100

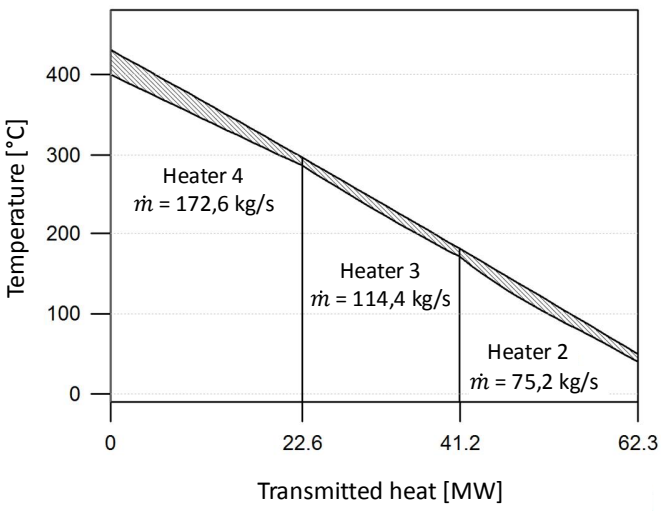

Figure 15: T-Q Diagram of heat recovery in a dual split sCO_2 cycle (example: Trent60). The diagram contains the CO_2 mass flow values in each heater.

The turbine inlet pressures and temperatures were optimized based on variational calculations. The turbine efficiencies were derived from first design calculations which are described subsequently. The influence of varying pressure

DOI: 10.17185/duepublico/46082

losses and TTD were investigated which is also presented in detail later in this paper.

The exergy analysis for both, the cascaded sCO_2 cycle and the reference cycle illustrates the potential of the cascaded sCO_2 cycles, i.e. the significant lower exergy losses in heaters/HRSG and stack as shown in figure 16. The benefit is partly compensated by the losses in the recuperator, however with the assumed parameters for TTD and pressure losses a performance benefit can be noted for the Trent60 case at 25 °C cooling water inlet temperature.

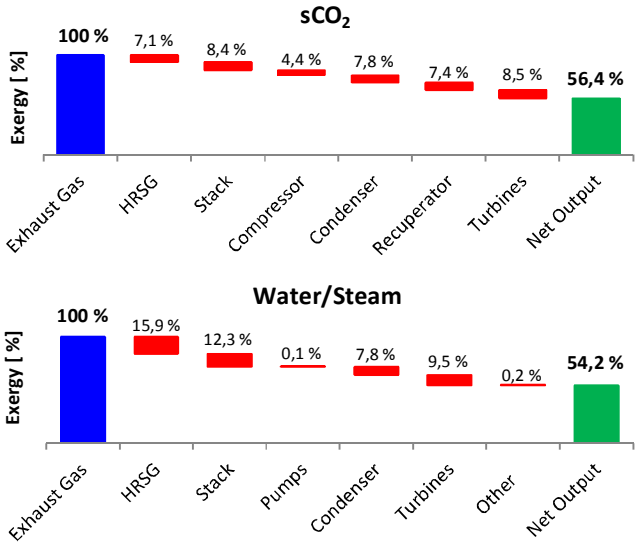

Figure 16: Comparison of relative exergy losses of the cascaded sCO_2 cycle and the dual pressure reference cycle. The calculations are based on the Trent60 CCPP with a cooling water inlet temperature of 25 °C.

The CO_2 turbine modules for both the Trent60 and the SGT800 bottoming cycle were derived by applying scaling laws on high pressure steam turbine modules. For each application dual casing turbines were considered each connected with a gear box. Since the power range and thus the volume flows of both cases are small, the resulting efficiencies are significantly lower compared to the previously described, direct heated application. The dominant losses in these small scaled turbine cylinders are the leakage losses related to both, the bladepath and the shaft sealings. Thus, appropriate measures for improving the performance need to be addressed in further development activities. Potential measures are the application of innovative sealing technologies and new turbine concepts such as single casing turbines in order to reduce the number of shaft sealings whereby the second measure would make a considerable contribution to cost savings.

Cycle calculations were carried out with varying cooling water inlet temperatures for both the water/steam cycles and the sCO_2 cycles. For simplification purpose, the impact of the ambient conditions on the gas turbine output and exhaust gas conditions were neglected. Furthermore the turbine efficiencies for both the sCO_2- and the reference cycles were kept constant. In figure 17 and 18 the deviation of the sCO_2 power output and the combined cycle efficiency values from the reference values based on water/steam are presented for the Trent60 and the SGT800 case respectively.

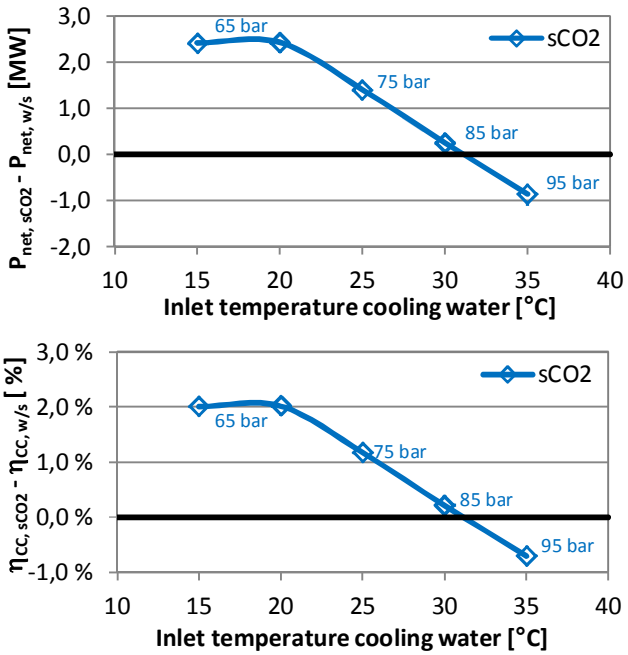

Figure 17: Deviation of the power output and cycle efficiency values compared to reference values based on water/steam (Trent60). Only the back pressure was optimized at each cooling water temperature.

For both applications, a performance benefit at cold cooling water inlet conditions can be determined. With increasing cooling water temperature and thus with increasing compressor inlet temperature the efficiency benefit drops considerably leading to a performance disadvantage at high cooling water inlet temperatures even with optimized backpressures in the sCO_2 cycle. In analogy to the direct heated application this can be explained by the thermodynamic condition at the compressor inlet which changes from a “as-liquid-state” to an “as-gaseous state” when the inlet temperature is exceeding the critical temperature of the fluid.

DOI: 10.17185/duepublico/46082

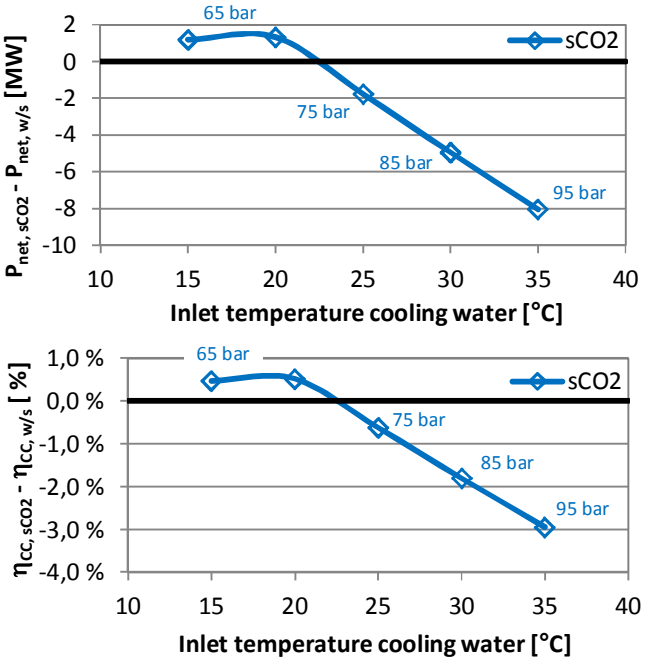

Figure 18: Deviation of the power output and cycle efficiency values compared to reference values based on water/steam (SGT800). Only the back pressure was optimized at each cooling water temperature.

Comparing figure 17 and figure 18 it is obvious that a sCO_2 bottoming cycle is more beneficial for the Trent60 than for the SGT800. Introducing the exergy loss analysis for the SGT800 bottoming cycles as shown in figure 19, it can be concluded that the exergy losses in HRSG and stack for the reference cycle of the SGT800 are clearly lower compared to the Trent60 reference cycle (figure 16). A similar result can be found in [10] i.e. the potential of a sCO_2 bottoming cycle in a combined cycle power plant is decreasing with increasing temperature level of the exhaust gas.

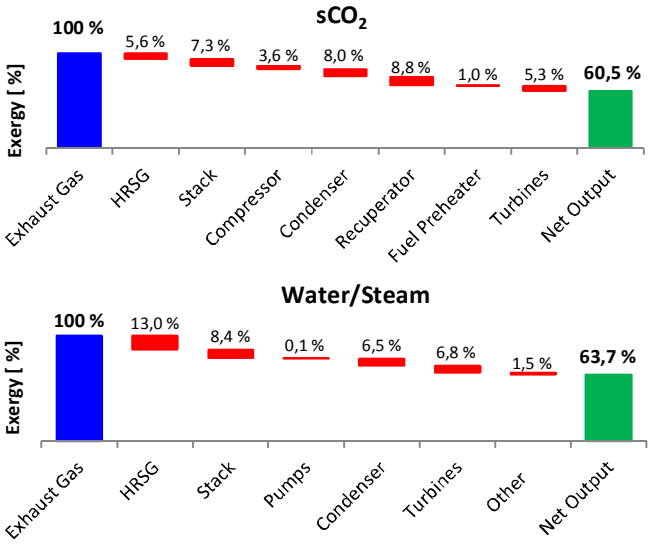

Figure 19: Comparison of relative exergy losses of the cascaded sCO_2 cycle and the dual pressure reference cycle. The calculations are based on the SGT800 CCPP with a cooling water inlet temperature of 25 °C.

The above discussed performance results are based on the assumed parameters listed in table 5. The resulting heat transfer surfaces of the heaters, the recuperators and the condenser were approximated by applying Nusselt-correlations for cross-flow shell-and-tube-heat exchangers. The comparison of the heating surface of the sCO_2 cycle and the reference cycle as well as the impact of varying the TTD of HRSG and recuperator are shown in figures 20 and 21 respectively.

It is obvious that a TTD of 10 K combined with an optimized dual split cascaded heater leads to small temperature differences and thus to heating surface which are approximately three times higher than the heating surfaces in the HRSG of the reference cycle. By doubling the TTD in the heater the heating surface can be nearly halved, however associated with a performance loss of approximately 1 MW. Equivalently, increasing the TTD of the recuperator from 10 K to 20 K the related heating surfaces can be almost halved but a significant performance loss of approximately 1,3 MW has to be taken into account.

Furthermore, a variation of the pressure loss within the heat exchangers was carried out. The result is shown in Figure 22. Low pressure losses, as specified in table 5, lead to low flow velocities and thus to larger heat transfer surfaces compared to water/steam. Therefore, a smaller surface area is required for higher pressure losses. As the analysis of the deviation of the power output values shows, low losses are nevertheless necessary to generate a performance benefit with sCO_2. As a result, doubling the pressure loss of all heat exchangers on the high and low pressure side of the cycle reduces the advantage by more than 1 MW. In comparison, a corresponding change in the pressure drop only on the high pressure side reduces the performance advantage approximately by half.

DOI: 10.17185/duepublico/46082

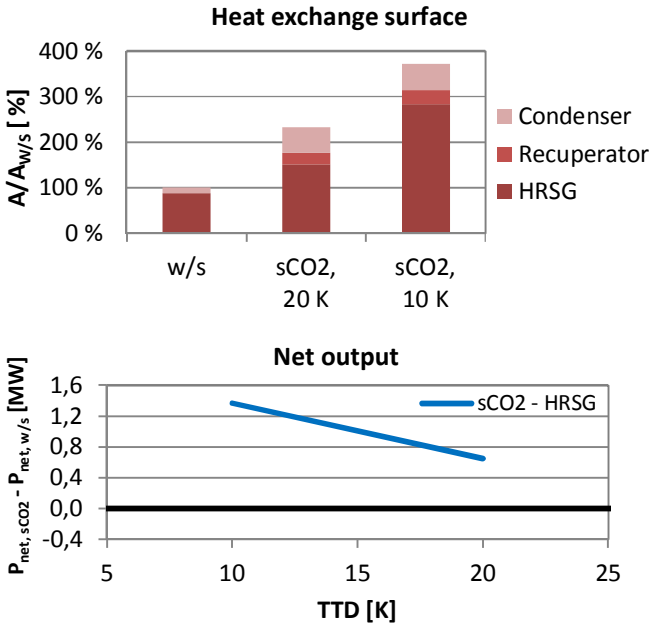

Figure 20: Heat transfer surface and deviation of the power output values depending on the TTD of the HRSG compared to reference values based on water/steam.

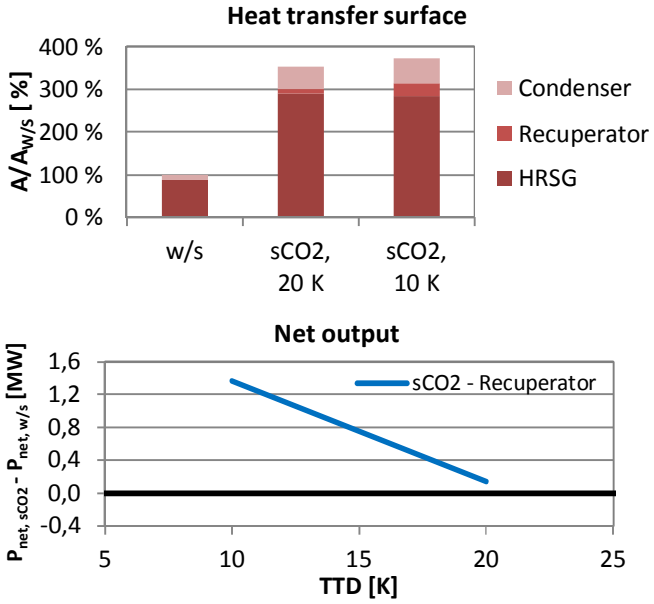

Figure 21: Heat transfer surface and deviation of the power output values depending on the TTD of the recuperator compared to reference values based on water/steam.

In summary, it can be emphasized that supercritical sCO_2 Brayton cycles may improve the performance of waste heat recovery processes, whereby the performance potential is decreasing with increasing temperature of the heat source. Further improvements can be gained by optimized design of the turbines. A cascaded cycle architecture minimizes the exergy losses in the heater resulting in large heat exchanger surfaces. The optimization of the backpressures may compensate the efficiency drop at high cooling water inlet conditions.

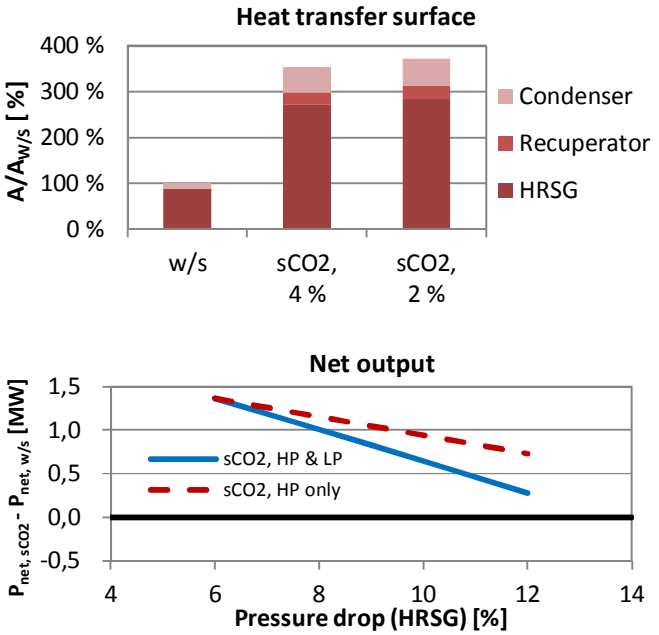

Figure 22: Heat transfer surface and deviation of the power output values depending on the pressure drop of the heat exchangers compared to reference values based on water/steam.

SUMMARY AND CONCLUSION

sCO_2 power cycles have been evaluated for a concentrated solar power plant and two combined cycle power plants and have been compared with reference cycles based on water/steam. A performance benefit can be noted for the CSP application in particular at turbine inlet temperatures above approximately 600 °C. For waste heat applications the potential for sCO_2 power cycles is rising with lower heat source temperatures. In all cases the performance benefits are associated with large heating surfaces, which make the development of high efficient and cost effective heat exchangers necessary. Initial turbine design calculations result in significant lower stage numbers compared to the reference turbines in the Rankine cycles. Much smaller turbine exhaust volume flows reduce the turbine sizes at the cold end. However, increased wall thicknesses in casings, valves and piping on the higher pressure side have to be considered. Furthermore optimized turbine designs and plant layouts must consider the large impact of the pressure losses on the cycle efficiency. In a subsequent step the economic assessment and optimization of the cycles as well as the development of high efficient and cost balanced components needs to be addressed.

DOI: 10.17185/duepublico/46082

OUTLOOK

An industrial-scientific partner consortium has joined forces with regard to the technological development of the sCO2 cycles. In addition to a pilot plant for method development and basic research, the development of a prototype for a waste heat recovery application is planned in order to contribute to further improvement of the technologies. In a preceding step, the thermo-economic evaluation of the applications under consideration will be carried out.

NOMENCLATURE

A	Heat transfer surface [m^2]
CSP	Concentrated Solar Power
h	Mass-specific Enthalpy [kJ/kg]
HP	High Pressure
HTR	High Temperature Recuperator
HRSG	Heat Recovery Steam Generator
k	Heat transition coefficient
LP	Low Pressure
LTR	Low Temperature Recuperator
p	Pressure [bar]
P	Power output [MW]
ref	Reference
sCO_2	Supercritical Carbon Dioxide
T	Temperature [°C or K]
T_m	Mean Temperature [°C or K]
TTD	Terminal Temperature Difference [K]
$\dot{V}$	Volume flow [m^3/s]
w/s	Water/Steam
Δ	Difference
η	Efficiency
η_{th}	Thermal Efficiency

ACKNOWLEDGEMENTS

The authors would like to thank Maike Bruckhaus for carrying out preliminary numerical investigations.
They further would like to thank Prof. Brillert, University Duisburg-Essen, Prof. Colonna, University Delft and Prof. Gampe, University Dresden for their suggestions and discussions.

REFERENCES

[1] Dostal, V., Driscoll, M. J., Hejzlar P. (2004). A supercritical Carbon Dioxide Cycle for Next Generation Nuclear Reactors. MIT-ANP-TR-100. USA, Boston.
[2] Brun, K., Friedmann, P., Dennis, R. (2017). Fundamentals and Applications of Supercritical Carbon Dioxide (sCO2) Based Power Cycles. Woodhead Publishing, USA, San Antonio.
[3] Mecheri, M.; Le Moullec, Y. (2016). Supercritical CO2 Brayton Cycles for Coal-fired Power Plants. Energy 103, 758–771, France, Chatou.
[4] Persichilli, M., Kacludis, A., Zdankiewicz, E., Held, T. (2012). Supercritical CO2 Power Cycle Developments and Commercialization: Why sCO2 can Displace Steam. Presented at Power-Gen India & Central Asia 2012, India, New Delhi.
[5] Crespi, F., Gavagnin, G., Sánchez, D., Martínez, G. S. (2017). Analysis of the Thermodynamic Potential of Supercritical Carbon Dioxide Cycles: A Systematic Approach. Journal of Engineering for Gas Turbines and Power 140, Issue 5. Spain, Seville.
[6] Miller, J. D., Buckmaster, D. J., Hart, K., Held, T. J., Thimsen, D., Maxon, A., Phillips, J. N., Hume, S. (2017). Comparison of Supercritical CO2 Power Cycles to Steam Rankine Cycles in Coal-fired Applications. Presented at ASME Turbo Expo 2017. USA, Charlotte.
[7] http://www.asimptote.nl/software/cycle-tempo/. Current status of Cycle Tempo by Asimptote, 2018.
[8] Wilkes, J. Allison, T., Schmitt, J., Bennett, J., Wygant, K., Pelton, R., Bosen, W. (2017). Application of an Integrally Geared Compander to an sCO2 Recompression Brayton Cycle. Presented at the 5th International Symposium - Supercritical CO2 Power Cycles, USA, San Antonio.
[9] Cho, S. K., Kim, M., Baik, S., Ahn, Y., Lee, J. I. (2015). Investigation of the Bottoming Cycle for High Efficiency Combined Cycle Gas Turbine System with Supercritical Carbon Dioxide Power Cycle. Presented at ASME Turbo Expo 2015. Canada, Montréal.
[10] Kimzey, G. (2012). Development of a Brayton Bottoming Cycle using Supercritical Carbon Dioxide as the Working Fluid. USA, Palo Alto.

DOI: 10.17185/duepublico/46082

2nd European supercritical CO2 Conference
August 30-31, 2018, Essen, Germany

2018-sCO2.eu-109

SUPERCRITICAL CO_2 HEAT REMOVAL SYSTEM - INTEGRATION INTO EUROPEAN PWR FLEET

Petr Hajek
ÚJV Řež, a. s.
Hlavni 130, Řež,
250 68 Husinec, Czech Republic
petr.hajek@ujv.cz

Ales Vojacek
ÚJV Řež, a. s.
Hlavni 130, Řež,
250 68 Husinec, Czech Republic

Vaclav Hakl
ÚJV Řež, a. s.
Hlavni 130, Řež,
250 68 Husinec, Czech Republic

ABSTRACT

This technical report describes the basic principles for integration of possible sCO2-HeRo loops in to the European PWR reactors fleet. This technical report is focused on integration to the VVER 1000 reactor design on existing operational units. The integration of sCO2-HeRo loops is described to level of detail in conceptual study. In this technical report there is specified initial information for design and design basis. There are summarized safety and reliability requirements, safety assurance principles, safety classification together with thermodynamic analyses supporting the selected technical solution.

INTRODUCTION

In the report the basic information is given about the possibility of integrating sCO2-HeRo loop into PWR design as well as information about the selected design for this integration and thermodynamic analyses supporting the selected technical solution.

The basic idea is to use the steam from the reactor in BWR or from the SG (Steam Generator) in PWR design as source of heat in heat exchanger of sCO2-HeRo loop and to return the condensed water back to the reactor or SG. This idea ensures the cooling of the reactor core and there is no need for feed water supply, no loss of coolant inventory, use of saturated steam allowing using evaporation heat and the use of small and compact heat exchangers.

The potential of sCO2-HeRo design is significant. The utilization of sCO2-HeRo exceeds SBO (Station BlackOut) accidents. It is expected that this system has a capability to be employed as a system for removal of heat from containment of NPP's. In case of LOCA (Loss Of Coolant Accident) or SA (Severe Accident) the containment vessel will contain a huge amount of mixed air and saturated water vapor. In emergency state as LOCA there are installed sprays systems for removing of this heat and for handling SA there are no systems available in current NPP's design. The only way on current NPP's, how to remove heat from containment to prevent its damage, is containment ventilation or cooling of containment inner wall. The heat exchangers of sCO2 HeRo loop can possibly act as heat removal device for containment cooling system.

In the process of developing integration of possible sCO2-HeRo loops in to the European PWR reactors fleet the two following concepts of sCO2-HeRo deployment have been worked out.

- Design of SBO-SG_HRS (Heat Removal System)
- Design of Containment_HRS

SBO-SG_HRS is a design in case of a SBO and the system draw steam from main steam line and condensed water is fed back to SG via normal feed line pipe. For more details see chapter 2 "Basic design".

Containment_HRS design is based on the installation of additional heat exchangers inside the containment, which will be condensing vapor from containment atmosphere on its outer surface. Condensed water can be used in case of LOCA in containment sump for emergency cooling systems and in case of SA according the used strategy for reactor vessel cooling (IVR) or corium cooling (ExVR).

BASIC DESIGN

1. SBO-SG_HRS

Progress of typical SBO event on VVER1000 units:

After a SBO on VVER 1000 unit there is an automatic reactor shut down by falling regulating rods. Meanwhile, in the active zone residual heat is produced. By nature, natural circulation is established in the primary circuits, which transfers

DOI: 10.17185/duepublico/46083

this heat to the SG and evaporates its water content. Generated steam is released by battery operated Atmospheric Exhaust Station (PSV) or by SG Pilot Operated Pressure Relief Valve (PRV). During a SBO accident without sources of electric energy, it is not possible to feed water to SG, so the level on SG secondary side steadily decreases. Parameters in primary loops are steady till the moment when the tube bundle in the SG starts to be uncovered by water (and only by vapor). After that the temperature and pressure in the primary loop starts to rise. According to analyses it takes about 50 – 60 minutes, till the tube bundle in the SG will be totally uncovered and cooling primarily coolant by evaporation SG water content is severely limit. The temperature in primary circuit starts to rise dramatically and primary coolant is released to the containment by pressure relieve valves. Eventually, it leads to SA.

The impact of SBO-SG_HRS on SBO progress:

The SBO-SG_HRS extracts the heat from the evaporated SG water and the generated condensate is fed back (driven by natural draft) to the SG secondary side. This process prevents the reduction of water content on the secondary side of the SG and enables the removal of the residual heat for a long period of time. The heat is conveyed to UHS (Ultimate Heat Sink - air).

An important role in the design of the SBO-SG_HRS system plays the balance between generated heat and SBO-SG_HRS heat removal capacity. The design of the SBO-SG_HRS system is based on basic requirements of heat removal capacity systems. The basic design of the nominal capacity of the heat removal system design was selected for 5 MW for one unit and on one NPP. It is planned to install 4 units in total.

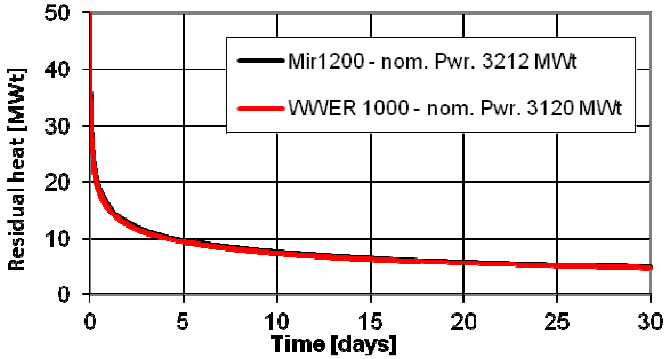

Figure 1-1 Residual heat for MIR 1200 and VVER 1000 types of reactors.

Figure 1-1 shows a graph of residual heat dependence on time. According to this graph it is possible to find out, that the proposed basic heat removal capacity of 20 MW is adequate of reactor core residual heat production after **8 hours** after reactor shut down (VVER 1000 unit).

The capacity of one system unit with regulation of the bypass over the turbine is 4.2 – 8.4 MW. The total possible capacity of 33.6 MW (4 times 8.4 MW) is sufficient for heat removal after **1 hour** after the reactor shut down. Within this period of time the water level in SG decreases below the tube bundle; however, the water deposit in primary circuit stays intact yet. The inventory of coolant on secondary site of the SG without emergency feeding corresponds to cooling reactor core for 1 hour by evaporation. From this mass and energy balance follows the requirement to start these systems at latest in **45 minutes** from SBO and reactor trip.

The water content from the SG which was released to the atmosphere till the SBO-SG_HRS starts to operate, can be restored to nominal SG water level by special SBO feed water pumps (Emergency supply pump to SG), which are already installed on units as result of Stress test procedures solution. Power for their operation can be produced by SBO-SG_HRS.

The requirements on the proposed systems are to enable a long term heat removal for at least 72 hours according the requested capability of the unit withstand all possible emergency situations without assistance from outside of the plant site. On top of that the design of the sCO2-HeRo aims for long term of residual heat removal systems in terms of weeks or month. This is possible due to the modular distribution of the system to 4 units, capable of independent operation and regulation of removed residual heat as in.

1.1. System description

As you can see in Fig. 1.1-1 and Fig. 1.1-2**Chyba! Nenalezen zdroj odkazů.** the SBO-SG_HRS (Station BlackOut heat Removal System from Steam Generators) is composed of three parts.

First part – the steam/water part is used to remove the heat from the secondary side of the steam generators. It is connected to the main steam line pipe in front of the fast acting valves (FAV, these valves are pneumatically operated valves with the purpose to separate the loop from the steam generator in case of a main steam pipe rupture) on the side, which is permanently connected to the SG. Next to it are the loop isolation valve and compact heat exchanger (CHX) for steam condensation. The Condensate leaves the CHX in the pipeline which is connected through the containment localization group of valves to the main feedwater line. The circuit is driven by the natural convection force. The position of the heat exchangers is selected in such manner (higher than the steam generators) so that the natural circulation works.

Second part – the CO2 loop extracts the heat from the compact heat exchanger through the sCO2-HeRo turbo machinery to the air cooled sink heat exchanger. The sCO2 loop is a simple Brayton cycle with a compressor, a turbine, a CHX and a sink HX. The positive energy balance of this cycle enables to extract electric energy which can be used for energy supply to essential instrumentation and control system or to

DOI: 10.17185/duepublico/46083

emergency supply pump for the SG feed water to recover water level inside the SG.

Third part – the air cooling loop serves as heat sink for the whole system and dissipates heat to the atmosphere. The fan is used for forced air flow through the sink heat exchanger to increase the heat transfer efficiency and is powered by the electric energy produced by turbine.

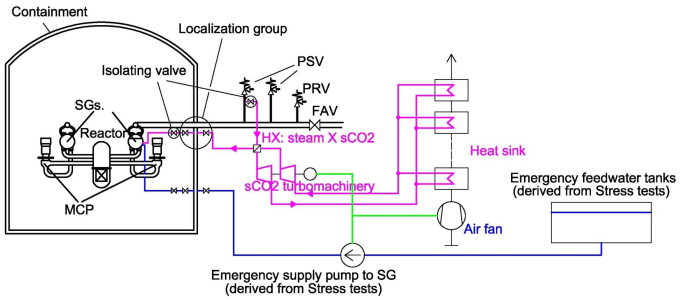

Figure 1.1-1 SBO-SG_HRS (Station Blackout heat Removal System from Steam Generators) – one unit structure.

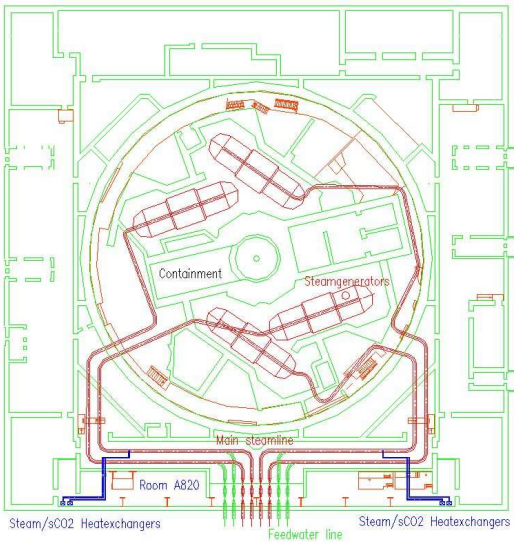

Figure 1.1-2 SBO-SG_HRS – Arrangement of four units on SG and main pipe lines

Arrangement of four units in containment

The System of heat removal in conditions of SBO consists of two independent systems. The description of the individual system is stated above. The system is divided to this "sub systems" to cope with all range of residual heat of a shutdown of the reactor. With a gradual cooling down of the core, the amount of residual heat is obviously decreasing so it is gradually coming to the point when only one sub-system is sufficient. Hence, the other sub system is from this moment further disconnected.

Each sub-system is connected to the main steam line of one steam generator. The heat which is generated in the core is equally distributed into the steam generators, so there is no need to connect the system to all main steam pipelines (steam generators).

For a further operability of the system, each sub system has 2 heat exchangers steam/sCO2, which can be in operation both or just one of them, depending on the situation. Each heat exchangers steam/sCO2 is then connected with its 1 unit of the sCO2 turbomachinery 5 MWth and with the sink HXs (altogether 6 for each 5 MWth unit).

This is the main part of the SBO-SG_HRS which takes care about the CO_2 circulation and the production of electric energy.

1.2. System functions

The SBO-SG_HRS (Station BlackOut heat Removal System from Steam Generators) is designed for operation under design extension conditions (DEC).
Under design extension conditions, the SBO-SG_HRS shall perform the function of heat removal via the secondary circuit:

- residual heat removal and cooldown of the reactor plant under conditions of NPP blackout.
- residual heat removal and cooldown of the reactor plant under conditions of total feedwater loss.
- ensuring the reserve by the active safety systems

1.3. System requirements

This chapter summarizes the basic requirements on the designed systems from the point of view of safety assurance principles (passive/active, redundancy, diversity, separation, actuation, independence…), safety classification (safety functions, safety classes) and reliability requirements.

The SBO-SG_HRS (Station BlackOut heat Removal System from Steam Generators) is designed for operation under design extension conditions (DEC).
Under design extension conditions, the SBO-SG_HRS shall perform the function of heat removal via the secondary circuit:

- residual heat removal and cooldown of the reactor plant under conditions of NPP blackout.
- residual heat removal and cooldown of the reactor plant under conditions of total feedwater loss.
- ensuring the reserve by the active safety systems
-

1.4. Operational regimes and parameters

The system has four operational modes:

Normal operation

During the normal operation the SBO-SG_HRS is in a standby mode. The first part (steam/ water loop) is filled with

DOI: 10.17185/duepublico/46083

water on normal condition. The CO2 loop is filled with CO2 to stand-by pressure, which must be determined.
Isolation valves are closed.

Start up:

There is a possibility to start up by electricity from electric accumulators by converting the generator into an electromotor. Another possibility is to use pressure tanks with CO_2 and use this stored energy to start the initial circulation in loop. The solution which would be used in final design of loop will be done in further phase of this project.

Fulfilling of safety function:

In the first part of the loop the steam naturally circulates and condensates to water in the heat exchanger. The condensate is fed back to the SG. The CO_2 loop works as a Bryton cycle. Forced air circulation is powered by produced electricity by circulation fan.

In case external conditions will be changed, like for example the outside temperature, it is possible to add or disconnect sections of the heat exchanger CO_2 / air

Shut down:

It is possible to switch the system off by closing the isolation valve on line from the main steam pipeline to the heat exchanger.

1.5. Power supply

A battery source for the initial valves operation must be integrated into the system to control the system operation and for the system start.

The energy source for the start-up (electric energy in batteries or compressed gas in bottles) should be sufficient for 2-3 attempts to start the system.

During the operation of the systems there will be an adequate production of electric energy for self-consumption and for powering external appliances.

2. CONTAINMENT_HRS

As well as the SBO-SG_HRS the Containment_HRS is initially designed for the removal of 5 MW of residual heat for one modular unit and altogether it is planned to install it within four units. It well corresponds with the curve of active zone residual heat production.

The difference between the Containment_HRS and the SBO-SG_HRS is that in case of a SBO the inherent capacity of water in the SG, capable to withdraw residual heat by its evaporation, is adequate only for less than one hour. Hence, the SBO-SG_HRS must be started up very quickly.

On the other hand, in case of a LOCA or a SA inside the containment, there is a much higher heat capacity reserve in all internal materials (water, concrete, steel …). According to previously made analyses, the pressure in the containment rises to the level corresponding to the containment strength (5 bars) in about 15 hours.

On the other hand, parameters in the containment after a LOCA (like temperature, pressure, vapor content) are steadily rising after the primary circuit brake, but the first moments aren't sufficient for the Containment_HRS for a self-propellant, self-sustaining operation. The startup time of these systems must be adapted to the immediate situation inside the containment.

The requirement on the proposed systems is to enable a long term heat removal for at least 72 hours according the requested capability of the unit to withstand all possible emergency situations without assistance from outside of the plant site. On top of that the design of the sCO2-HeRo is aiming for long term of residual heat removal systems, in terms of weeks or month. This is possible due to the modular distribution of the system to four units, capable of independent operation and regulation of removed residual heat.

It is possible to use the CO_2 loop unit for regulation by the mean of turbine bypass, as in the SBO-SG_HRS. It is expected that the result in heat removal capacity range will be similar, which has to be shown in the future.

It is supposed that this active control is not necessary for the Containment_HRS, because of the containment high heat capacity, which enables regulation by the mean of switching of whole modular units of the Containment_HRS.

2.1. System description

The Containment_HRS (Containment heat Removal System) is composed of two parts. See **Chyba! Nenalezen zdroj odkazů.**.

First part – consists of a heat exchanger for the extraction of the heat from the air/steam atmosphere mixture inside the containment and the CO_2 loops transferring the heat, from this heat exchanger, due to turbo machinery to the air cooled heat exchanger. This loop is designed as a simple Brayton cycle with compressor, turbine and generator on one shaft. The slightly positive energy balance of this cycle enables to extract electric energy, which can be used for energy supply to systems essential measuring and control system and for the powering of the electric air fan.

On the CO_2 lines penetration through the containment wall will be grouped isolation valves. One of them, near by the

DOI: 10.17185/duepublico/46083

containment wall will be connected to the wall by double wall pipe to confine leakage in case of a tube rupture.

Second part – an open air cooling loop serves as a heat sink for the whole Containment_HRS and dissipates heat to the atmosphere. The fan is used for forced air flow true heat exchanger to increase the efficiency and it is powered by the electric energy produced by turbine.

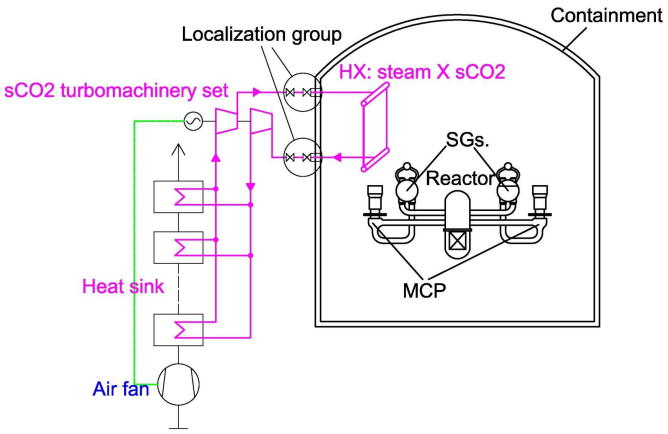

Figure 2.1-1 CONTAINMENT_HRS (Containment Heat Removal System) – one unit structure.

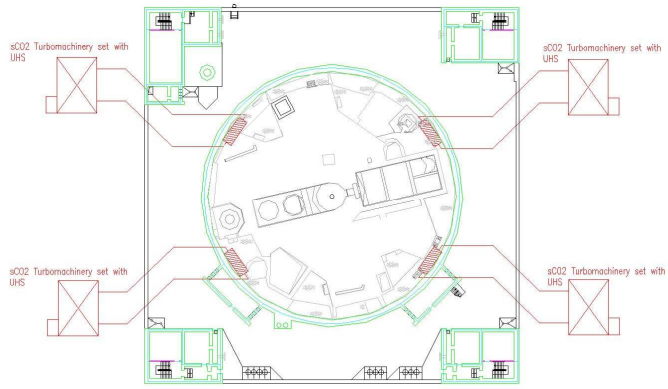

Figure 2.1-2 SBO-Containment_HRS – Arrangement of four units in containment.

Arrangement of four units in containment

The system consists of 4 individual trains. The description of an individual train is listed above. The containment heat exchangers (one for each 5 MWth unit) are placed at the top head of the containment at regular intervals around the circumference of the containment approximately at level +46m. The pipeline with supercritical CO_2 medium goes through the containment by new hermetic penetration to the rooftop of the surrounding building and then to the ground level. The situation is well displayed at **Chyba! Nenalezen zdroj odkazů.**. On the ground level the modular configuration of the sCO2 turbomachinery of 5 MWth are placed (one for each 5 MWth unit) together with the sink HXs (altogether 24 for each 5 MWth unit). The integration of the system into the civil part of an existing unit and the connection to the technology is described in the following chapter.

2.2. System functions

The Containment_HRS (Containment heat Removal System) is designed for the operation under design basis accidents conditions (DBA LOCA) and in Beyond design basis accidents (Severe accidents SA) conditions.
Under DBA an SA condition, the Containment_HRS shall perform the function:

- Heat removal from containment inner atmosphere.

2.3. Operational regimes and parameters

The system has four operational modes:

Normal operation:

During the normal operation, the Containment_HRS is in a standby mode. The CO_2 loop is filled with CO_2 to stand-by pressure, which must be determined. The isolation valves are closed.

Start-up:

The principle of the Containment_HRS power up isn't decided yet. It. There is a possibility to start up by electricity from electric accumulators by converting the generator into an electromotor. Another possibility is to use pressure tanks with CO_2 and to use this stored energy to start the initial circulation in the loop. The final solution which will be used in the final design of the loop will be found at a later time of this project.

Fulfilling of safety function:

The CO_2 loop works as a Brayton cycle. The heat from the containment is withdrawn by CO_2 and potential steam in the containment atmosphere is condensed. Forced air circulation is powered by produced electricity by a circulation fan.
In case external conditions are changing, e.g. the outside temperature, it is possible to add or disconnect sections of the heat exchanger CO_2 / air.

Shut down:

The system can be switched off by closing the valve on the CO_2 loop isolation group on the containment wall.

2.4. Power supply

A battery source for the initial valves operation must be integrated into the system for control system operation and for the startup of the system.

DOI: 10.17185/duepublico/46083

The energy source for the startup (electric energy in batteries or compressed gas in bottles) should be sufficient for 2-3 attempts to start the system.

During the systems operation, there will be an adequate production of electric energy for self-consumption and for powering external appliances.

3. POSSIBILITY OF SELF-LAUNCHING SYSTEM

This chapter evaluates the possibilities in order to design the SBO_HRS and the Containment_HRS scenarios to be self-launching.

Generally, it must be considered that either both the SBO_HRS and the Containment_HRS will be added to currently operating units or these systems will be designed for newly built VVER (PWR) units.

- Newly built VVER units - For a newly built NPP it is possible to integrate the SBO-SG_HRS and Containment_HRS to the DID logic sequence, because it will be newly developed in the design phase of a project. If these systems should be self-launching, the condition and limitation of a system start-up have to be exactly addressed.
- Currently operating units VVER units – There are challenges to determine whether the SBO-SG_HRS and Containment_HRS could be operated in a self-launching or in a manually operated mode. Originally, in the NPP design the DEC - Postulated multiple failure events, beyond design basis accidents and severe accident were not considered.
    - SBO-SG_HRS - As a result of the European Stress Test, severe accident mitigation measures have been implemented in VVER plant. All such measures dealing with SBO DG stations, SBO SG feed water pumps or SBO-accidents in general are actuated and operated manually by the operator from special control workplaces. The HeRo System operating under SBO conditions would have the same restraints. A challenge here is, e.g. defining procedures how to manually operate systems together with the sCO2-HeRo-system. Such investigations are on the agenda for the 3rd year of the project when improved ATHLET simulations will be carried out with improved models.
    - Containment_HRS – For currently operating VVER units, severe accident management strategies are currently being prepared. The design and operation conditions of a sCO2-HeRo-system will depend on the accident management strategy, i.e. In-Vessel or Ex-Vessel retention scenarios, resulting in different atmospheric conditions at different times of an accident. A definition of starting conditions will depend on the outcome of the analysis of the accident scenario.

The possibility of a self-launching system is generally conditional upon solving problems:

- Definition of groups of events for which the system will be designed. In the designs, specific events must be addressed in a logic sequence DID for which the system should be used. A list of symptoms which definitely and unmistakably distinguish these events has to be set up.
- Evaluation of failure of other possible resources intended for this project event. There can be another system designed for the same purpose. It has to be clear, that the new system only starts if it clearly demonstrates that the primary systems fail to fulfill their function.
- Evaluation of launching point. Some parameters and set points must be given, which result in system start up when exceeded.
- Transitions between the phases of self-launching procedure. The start-up procedure will consist of several phases and has to define conditions verifying the fulfillment of the previous phase and enabling the transition to the next phase.

Considered self-launching process phases:

1. Filling of CO_2 to the system to the operational level.
2. Configuration of CO_2/Air heat exchanger for corresponding ambient temperature. Selection of needed sections and opening corresponding valves.
3. Start up by electricity from electric accumulators by converting the generator into an electromotor or usage of pressure tanks with CO_2 and use this stored energy to start initial circulation in loop.
4. Connection to the electric grid.
5. Optimization of operational parameters for CO_2 loops.

THERMODYNAMIC ANALYSIS

CYCLE CALCULATION – OPTIMIZATION PARAMETERS

The following chapter is devoted to the optimization of the thermodynamic cycles both for CONTAINMENT_HRS and SBO-SG_HRS systems. The optimization is based on searching a compressor inlet and compressor outlet pressure of the cycle to receive the highest efficiencies of the cycle. There were assumed expected isentropic efficiencies of the compressor and turbine as well as expected inlet temperature and pressure to the compressor and to the turbine. This optimization is extremely

DOI: 10.17185/duepublico/46083

important and determines whether the system will have a chance to be self-propellant or not.

The sCO2-HeRo cycle is designed as a simple Brayton cycle. At this preliminary state, neither the implementation of recuperation nor other improving elements such as modification of the cycle, e.g. recompression cycle (considered as the most promising conversion cycle for sCO2 with the highest efficiency) were considered, although there is an added value of these improvements in terms of higher electric power output since the efficiency of the cycle is increased. This would lead to rising up the mass flow rate in the system in order to keep the thermal power (decay heat removal) constant, thus increasing the power of the compressor and the turbine by the ratio of mass flow rates (simple Brayton cycle/enhanced cycle).

In no human endeavor, one can ever guarantee failure-free operation. The system and human failures are inevitable. The likelihood of any failure is higher for more complicated systems. Keeping this in mind, it leads to a rather small and safer simple Brayton sCO2 conversion cycle rather than more complicated enhanced cycles.

Table 1 gives the thermodynamic values of the CONTAINMENT_HRS and SBO-SG_HRS cycle which were considered.

The cycle calculation starts at the compressor inlet. The temperature and pressure are specified at that point. Both were parametric inputs. The compressor efficiency is an input variable parameter. It varies according to the common values depending on the sizes, rotation speed and pressure ratios. The compressor outlet pressure is specified also as a parameter.

Table 1 Thermodynamic values of the CONTAINMENT_HRS and SBO-SG_HRS cycle.

Variable	*Value*	*Unit*
inlet temperature sCO2 to the compressor	30, 40, 50	°C
inlet temperature sCO2 to the turbine CONTAIMENT_HRS/SBO-SG_HRS	114/280	°C
inlet pressure sCO2 to the compressor	75, 100, 125, 150	bar
inlet pressure sCO2 to the turbine	100, 150, 200, 300	bar
thermal power of heat source	5000	kW
isentropic efficiencies of the compressor	0.65, 0.75 and 0.8	-
isentropic efficiencies of the turbine	0.75, 0.85 and 0.9	-

CONCLUSION

This technical report describes the basic principles for integration of possible "supercritical CO_2 heat removal system" into the European PWR reactors fleet. This technical report is focused on integration to the VVER 1000 reactor design on existing operational units. The integration of sCO2-HeRo loops is described to a level of detail in a conceptual study. In this technical report, initial information is specified for design and beyond design basis. Safety and reliability requirements are summarized, safety assurance principles, safety classification together with thermodynamic analyses supporting the selected technical solution.

ACKNOWLEDGMENTS

This project has received funding from the European research and training programme 2014 – 2018 under grant agreement No 662116.

DOI: 10.17185/duepublico/46083

2nd European supercritical CO2 Conference
August 30-31, 2018, Essen, Germany

2018-sCO2.eu-110

CONCEPT AND PRELIMINARY DESIGN OF A 600 °C+ SCO_2 TEST FACILITY

Gampe, Uwe*
TU Dresden
Dresden, Germany
Email: uwe.gampe@tu-dresden.de

Henoch, Jasmin
TU Dresden
Dresden, Germany

Rath, Sebastian
TU Dresden
Dresden, Germany

Gerbeth, Gunter
Helmholtz Zentrum
Dresden-Rossendorf
Dresden, Germany

Hampel, Uwe
Helmholtz Zentrum
Dresden-Rossendorf
Dresden, Germany

Hannemann, Frank
Siemens AG, Power & Gas
Division Erlangen/Mülheim,
Germany

Glos, Stefan
Siemens AG, Power & Gas
Division Erlangen/Mülheim,
Germany

ABSTRACT

Supercritical carbon dioxide as working fluid in thermal power generation involves numerous new challenges. However, basic design features of the power plant architecture remain nearly unaffected. Consequently, technology development can be based on existing design roots and calculation methods, which need to be adapted and developed in any event. This requires an experimental basis allowing both generic experiments and testing of individual modules or complete system components.

A consortium of industrial and scientific partners has started technology development targeting application in bottoming cycles behind gas turbines, industrial waste heat recovery and Concentrated Solar Power (CSP). This requires that design and evaluation methods are constantly undergoing further development and improvement. A test facility is being prepared to contribute to methodology development on the experimental side and to contribute in basic research.

The test facility is designed in a modular approach. Maximum design pressure will be 300 bar and maximum mass flow rate is intended to range between 3 and 4 kg/s. This enables boundary conditions for testing of modules and complete components, such as heat exchanger and turbo machinery. Moreover, a modular architecture of the test facility will also allow experimental investigations in the test section at smaller mass flow rates.

We present the overall concept and the architecture of the test facility. Special attention is devoted to flow scheme, instrumentation, modular heater, recirculation blower and cooler for controlled cooling conditions. We present technical solutions, concepts and design data.

INTRODUCTION

It is well known that supercritical carbon dioxide (sCO_2) offers a range of advantages compared to current technologies applied in thermal power generation. Higher thermal efficiency represents increased utilization of primary energy. This causes reduced emissions at exploitation of heat sources based on thermochemical energy conversion and reduced heat release to the atmosphere with resulting lower ecological foot print. Moreover, smaller size of components with lower costs and higher operational flexibility are further advantages. Finally, lower water consumption in the power generation process is an important benefit.

An additional advantage of sCO_2 as working fluid for secondary heat sources is the lack of vaporization plateau in comparison to subcritical water-steam-cycles. Figure 1 shows schematically two temperature heat load diagrams with the same flue gas temperature for a water/steam and a sCO_2 cycle. The hatched area indicates the loss due to temperature differences. Due to the vaporization plateau of the subcritical water/steam cycle, this area is visibly larger than for the sCO_2 cycle, where a better thermal coupling inside the steam generator can be achieved. This shows that sCO_2 can lead to higher efficiency and therefore to an improved heat utilization. Even better results can be accomplished by the utilization of cascaded sCO_2 cycles for heat recovery.

DOI: 10.17185/duepublico/46084

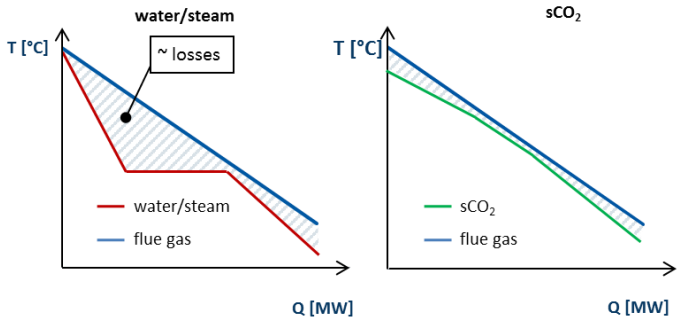

Figure 1: Comparison of water/steam and sCO_2 cycle for a defined secondary heat source and indication of occurring losses

Figure 2 shows the exergetic efficiency η_{ex} of a heat recovery steam generator (HSRG) for three different cycles as a function of the live steam temperature in the range of 400°C to 600°C.

$$\eta_{Ex} = \frac{\dot{E}_{working\ fluid}}{\dot{E}_{flue\ gas}} \qquad 1\text{-}1$$

The black line indicates the supercritical CO_2 cycle, the red line a triple-pressure steam cycle and the blue line a dual-pressure steam cycle. Generic cycle calculations based on simplified cycle models were performed. Minimal pinch point and neglected pressure losses were set as boundary conditions [1].

It is well known, that higher live steam temperatures lead to a higher exergetic efficiency and triple-pressure steam cycle is more efficient than dual-pressure steam cycle, as shown in Figure 2. The advantage of the exergetic efficiency of the sCO_2 cycle compared to the triple-pressure steam cycle gets smaller with higher temperatures. The diagram also shows, that for lower temperatures (400°C) the benefit of the sCO_2 cycle is more distinct.

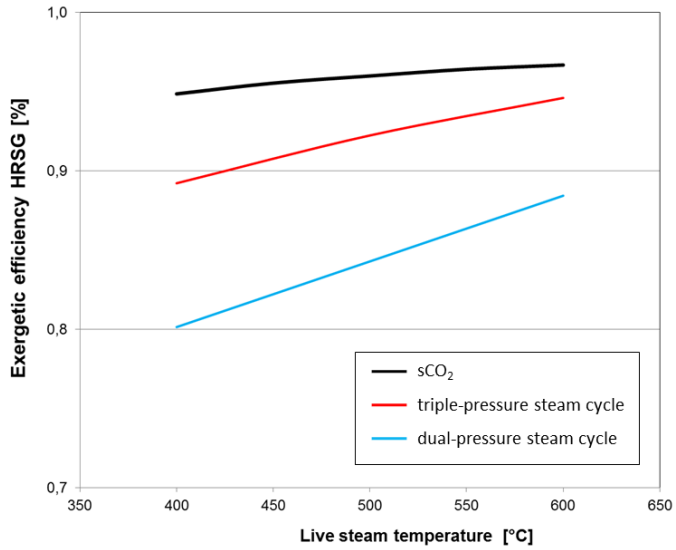

Figure 2: Exergetic efficiency of a heat recovery steam generator (HSRG)

Comparative analysis has also been conducted for application of sCO_2 for primary heat sources, e.g. concentrated solar power (CSP). In contrast to state-of-the-art fossil power plants with supercritical steam parameters, which are not in the focus of the authors, solar thermal power plants are based on subcritical steam cycles.

Figure 3 shows the temperature entropy diagram of a latest state of technology 150 MW molten salt tower power plant with water/steam cycle. The Carnot efficiency is calculated with the average temperatures of the heat sink and the heat source.

$$\eta_{Carnot} = 1 - \frac{T_{m,heat\ sink}}{T_{m,heat\ source}} \qquad 1\text{-}2$$

Maximum cycle temperature is 550°C. The Carnot efficiency of this cycle with reheat is 51%.

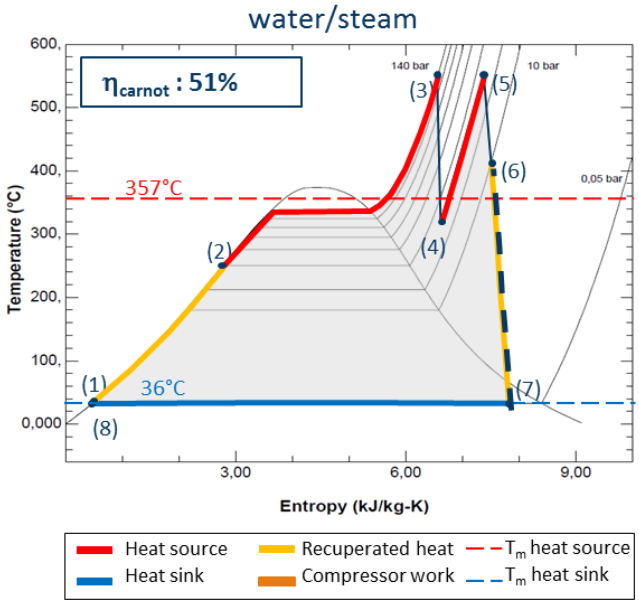

Figure 3: 150MW CSP, molten salt solar tower plant with water/steam

Figure 4 shows the temperature entropy diagram for the cycle with sCO_2 as working fluid and therefore higher pressure levels, but the maximum cycle temperature is also 550°C. Application of sCO_2 as working fluid leads to a higher average temperature of the heat source and resulting higher Carnot efficiency of 56%.

These basic comparisons illustrate already the potential of supercritical carbon dioxide for the target applications addressed by the authors. The research project CARBOSOLA (supercritical carbon dioxide as alternative working fluid for bottoming cycle and thermal application) has been initiated to conduct technology development for these target applications.

DOI: 10.17185/duepublico/46084

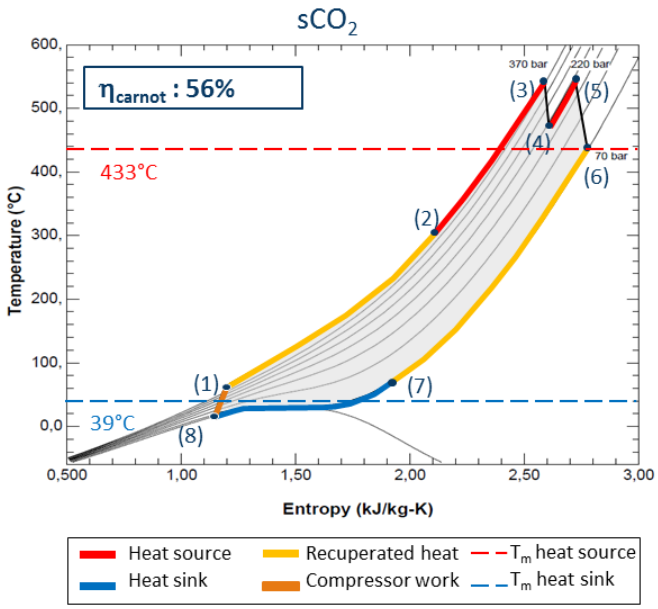

Figure 4: 150MW CSP, molten salt solar tower plant with sCO_2 as working fluid

The CARBOSOLA project comprises a consortium of industrial and scientific partners. Especially bottoming cycles behind gas turbines as well as gas and diesel engines with maximum temperatures between 350°C and 600°C for power generation and mechanical drive are in the focus of interest. Furthermore power generation based on waste heat of industrial processes will be considered. Primary heat sources will only be addressed for CSP and temperature range of 600°C to 700°C. The engineering and installation of a sCO2 test loop is part of the project.

TEST LOOP DEFINITION AND BASIC ARCHITECTURE

The sCO_2 test loop serves to contribute both to technology development by testing of singular modules or components and to basic research by generic experiments. Experiments regarding fluid mechanics, heat transfer, material behavior and damage mechanisms as a result of thermochemical and thermomechanical processes provide relevant information for development and advancement of design and evaluation methods. The sCO_2 loop will also be used for the development and testing of measurement technologies for sCO_2 cycles.

Based on the preliminary work, temperatures up to 600°C at a pressure level up to 300 bar have been specified as design parameters of the planned testing facility. The intended site for the sCO_2 test loop is on the premises of the Helmholtz-Zentrum Dresden-Rossendorf (HZDR). Existing infrastructure can be used. A power supply of maximum 3 MW can be utilized for an electrical heater and an existing heat removal system using a water-glycol mixture as heat transfer media provides a heat sink.

Basic flow scheme of the envisaged test loop is presented in Figure 6. The sCO_2 test loop concept is based on a modular approach in three expansion stages. The basic concept consists of a supply unit, recirculation blower, modular heater, component test section and a main cooler with a bypass. Later expansion stages, marked with a blue filling, will provide recuperator (stage 2) and turbine testing (stage 3) as well as the therefore necessary compressor and optional additional cooler. That allows to test different components in a complete cycle. The operating range of the final expansion stage is marked with a green area in the temperature entropy diagram presented in Figure 5.

Core of the first expansion stage is the horizontal component test section where certain flow conditions for experiments can be realized. Based on the 2.5 MW power input of the heater, a maximum mass flow of 3.5 kg/s for 600°C can be achieved. Of course, partial mass flow in the testing section will be possible.

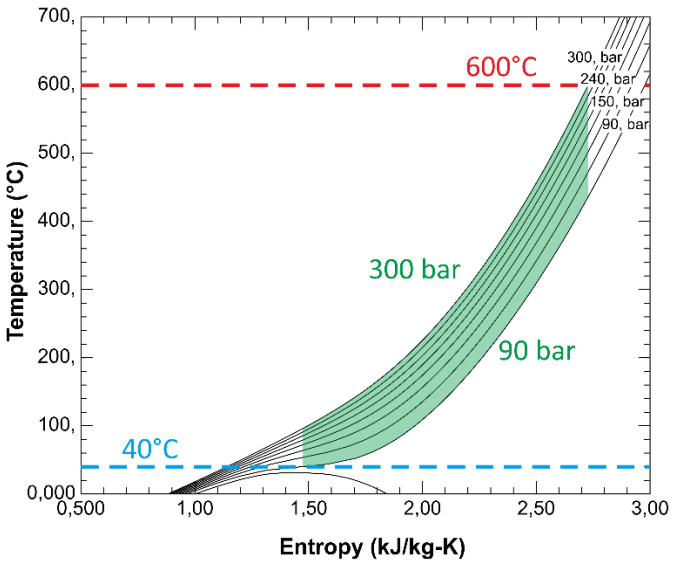

Figure 5: Operating range of the sCO_2 test loop in the final expansion stage

DOI: 10.17185/duepublico/46084

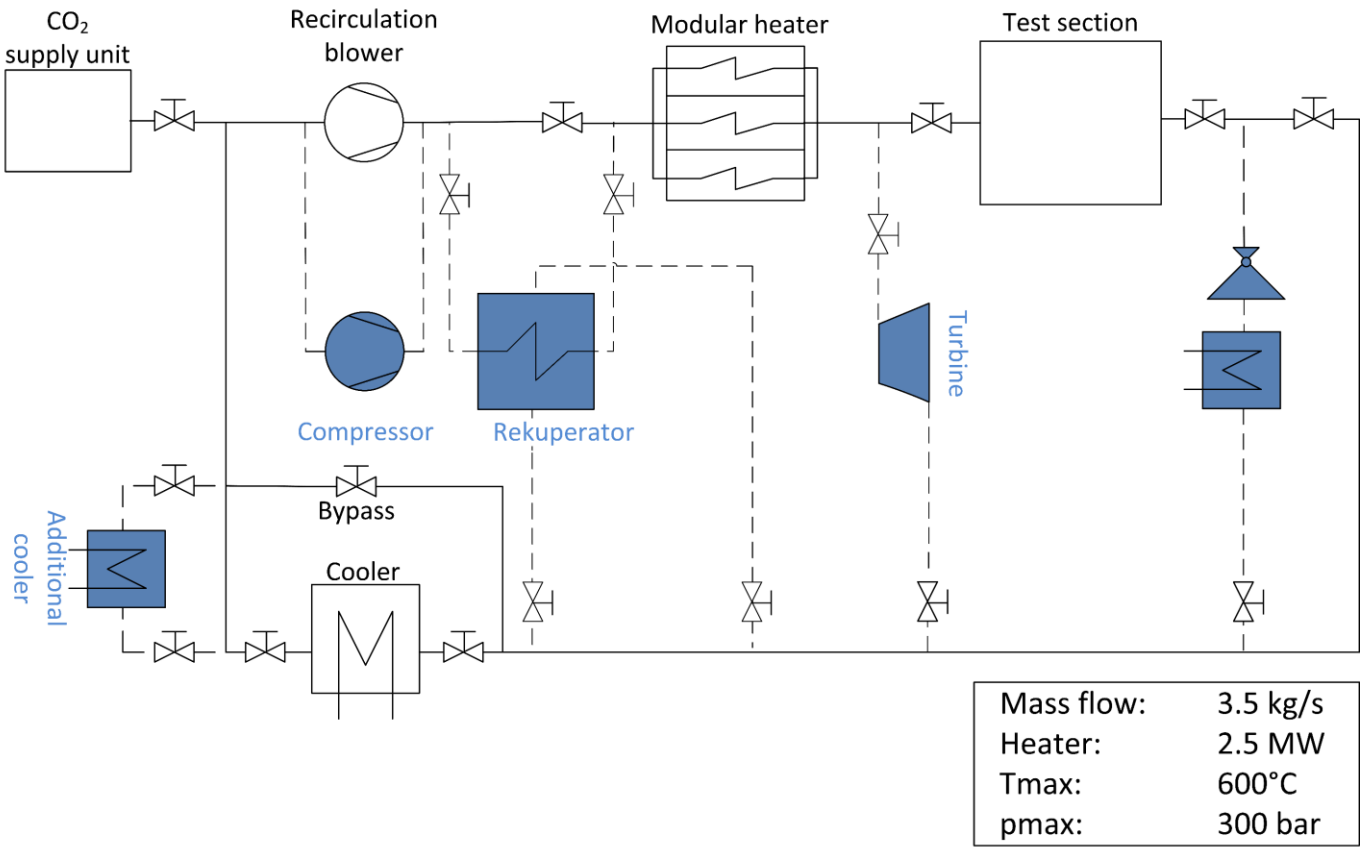

Figure 6: Basic test loop scheme (final expansion stages marked blue)

TEST LOOP DESIGN ASPECTS

In the current phase of preliminary design some substantial considerations were addressed containing the pre-sizing of interconnecting pipes and the basic instrumentation of the loop. Moreover, conceptual work on the first components namely the heater, the cooling system and the recirculation blower was done.

Piping and basic instrumentation

To determine a suitable size for the interconnecting pipes a comparative study on different nominal diameters (DN) was carried out. As a first guide value a maximum flow velocity of about 30 m/s (100 ft/s) was specified, which has been stated by Moore et al. [2] to be a good compromise between pipe size and pressure losses. In some cases, multiple pipe setups were considered to reduce the velocity splitting up the mass flow.
The minimum thickness of the pipes is calculated based on AD 2000 standard [3]. Related to a foregoing examination of suitable materials 347HFG stainless steel was chosen as a potential alternative to more expensive nickel alloys.

The results depicted in Table 1 show that especially the use of smaller diameters leads to solutions with inacceptable high pressure losses despite compliance with the set reference for flow velocity. Given that only single pipe configurations were chosen, the velocity criteria worked well for the low-pressure specification (p=90 bar) resulting in a specific loss of about 0.06 bar/m at DN 60. Regarding the selection of material all of the variants could be realized using preferred standard sizes according to DIN EN 10220 which confirms 347HFG stainless steel as an alternative to nickel alloys. For further investigations DN 60 was chosen as the preferred diameter equally for both of the pressure levels also in order to minimize the variety of accessory parts.

Table 1: Comparative Study of Pipe Specifications

	DN32			DN40		DN60		DN80	
	Dimensioning (T=600°C, p=300 bar), Material: 347HFG (1.4908)								
d_a [mm]	48.3			60.3		88.9		114.3	
s_b [mm]	8.8			11		16		20	
d_i [mm]	30.7			38.3		56.9		74.3	
	Pressure losses (**HP**: T=600°C, p=300 bar; **LP**: T=600°C, p=90 bar, Roughness = 0.04 mm)								
	HP	HP	LP	HP	LP	HP	LP	HP	LP
parallel pipes	1	2	3	1	2	1	1	1	1
v_{res} [m/s]	27.70	13.85	29.36	17.80	28.30	8.24	26.19	4.73	15.04
Δp [kPa/m]	44.85	11.25	15.93	14.07	11.23	1.88	5.97	0.44	1.41

DOI: 10.17185/duepublico/46084

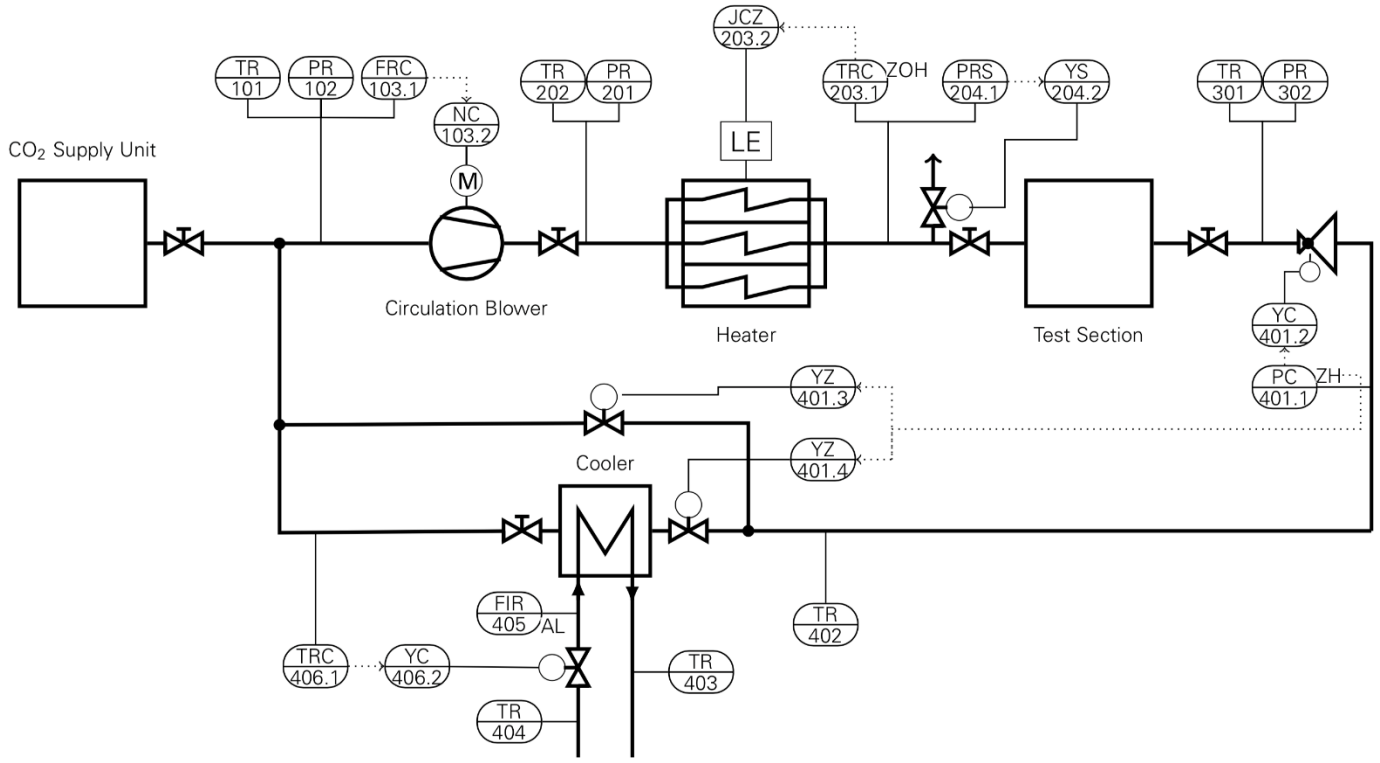

Figure 7: Basic instrumentation of the sCO2 test loop

As presented in Figure 7 the basic instrumentation should contain pressure and temperature sensors on every relevant point of state. The mass flow will be captured at the inlet of the recirculation blower. The monitoring for the whole loop is planned to take place from a central control room.

Modular heater

Fluid heating in similar test facilities is usually done by electric circulation heaters [4], waste heat boilers [5] [6] or indirect heating solutions [5] in different sizes and configurations which are mostly selected on the available energy sources or beneficial operating characteristics. Regarding the available infrastructure and power capacities on site the fluid heating for the present loop was decided to be based on electrical heating. To get a maximum of flexibility with respect to both the experimental parameters and future extensions a modular configuration was chosen. Like depicted in Figure 8 heating is assumed to take place in two stages, a main and a post heater in which the latter should provide a continuously variable heating power upon 250 kW. Furthermore, each stage should consist of several sections which enables the handling of lower mass flow rates. By connecting or disconnecting several of them a partial load behavior is enabled without changing the operational characteristics due to a change in the inner heat transfer coefficient.

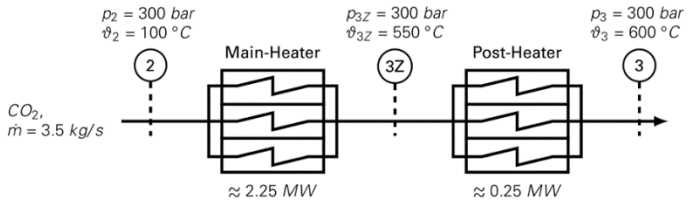

Figure 8: Modular heater concept

Since the aforementioned circulation heaters potentially resulting in high space requirements, as seen at the SANDIA rig [4], an own design approach has been developed to be compared later with a commercial circulation heater solution. In contrast to the latter where a set of heating rods immersing into the fluid at the alternative concept the tubing itself should generate the heat. Presented in Figure 9 this is expected to be done by splitting up the CO_2 to several small pipes which are operating as joule heating elements warming up the fluid flowing through.
A similar concept is already in use at another local test rig for the generation of saturated steam.

DOI: 10.17185/duepublico/46084

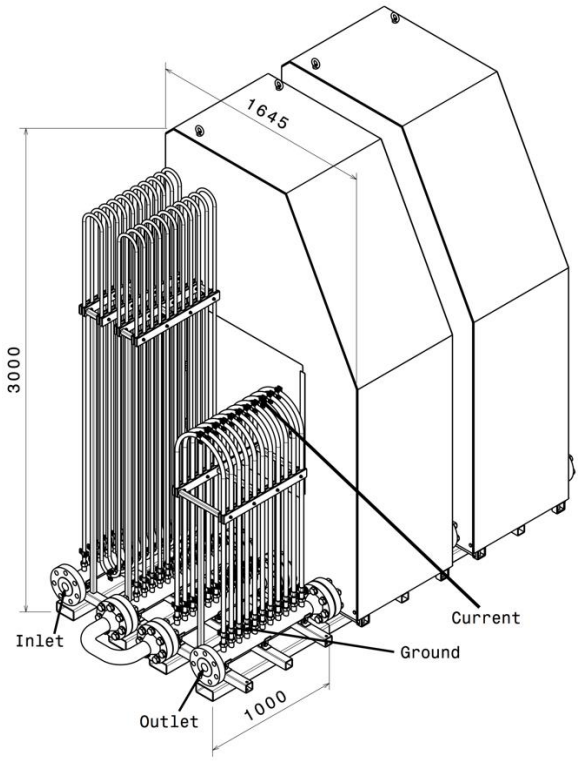

Figure 9: Heater design with 347HFG stainless steel

The limiting factor determining the size of the heating tubes is the maximum allowable wall temperature defined by strength limitations of the material. So, additional work was done comparing the created solution based on 347HFG stainless steel (Figure 9) with a second variant using IN 740H as tube material. With the latter the number of heater modules could be reduced from 3 to 2 containing the same number of pipes. Moreover, the resulting height decreases of about 50% regarding to the same base construction for both of the variants. Based hereon in ongoing work next steps will be addressed containing a fluid dynamical investigation plus the technical feasibility of the key components like the tube fittings and the electrical contacts.

Cooler

To serve existing test facilities a building near to the installation site is fitted with a powerful heat removal system using a water-glycol mixture as heat transfer media. Collected heat is dissipated by a roof mounted heat exchanger system to the ambient air with a 10 K temperature difference with reference to the ambient temperature. Circulation is done by an unregulated pump with a maximum mass flow rate of 51 kg/s splitting up to all simultaneous used fluid branches. Integration of new systems can be done by using existing pipe connections with a nominal diameter of DN 65 each. Regarding to the planned rig they are easily accessible from the expected location of erection through the buildings outer wall.

Thus, the choice of a suitable heat exchanger configuration was done against the background of integrating it in the existing system. Taking into account the fact that some of the rigs already attached to the system using carbon steel for their exchangers the priority was a reliable solution resistant to plugging and damages induced by oxide particles within the cooling media.

Given that the cooler is not object of the primary investigations neither a ``form follows function'' approach was chosen selecting the shell and tube architecture.

As presented in Figure 10 the final design resulted in a stack of three modules of two hairpin heat exchangers each. Regarding to the ambient dependency of the heat removal system the hairpin type design ensures a strict counter flow. By this means it is possible to get an optimal use of the remaining temperature difference between the primary outlet and the cooling media inlet temperature. The distribution in three modules was chosen equivalent to the heater concept giving the same modularity and moreover resulting in a construction using a variety of standardized components like pipe sections for the shell.

For calculation a cooling fluid inlet temperature of $T_{sec,in}$= 30°C has been used which has been stated as the most common inlet temperature during power operation of a similar test rig with 4 MW heater power. However, to make the cooling capacity less dependent from the ambient an additional cooling module is considered for later stages which adjusts the cooling water to a suitable inlet temperature before entering the cooler giving all time stable test conditions.

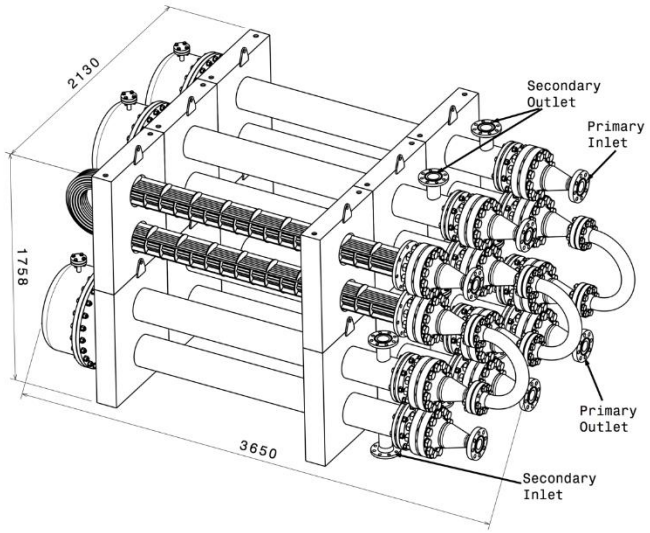

Figure 10: Cooler design

Recirculation blower

To cover all occurring pressure losses in the sCO_2 test loop, a recirculation blower is planned. A compressor to allow full cycle experiments will be part of the second expansion stage. The recirculation blower is supposed to cover a projected pressure drop of 15 bar, which leads to a pressure ratio of 1.05. The pressure drop is composed of estimated values for the heater, testing section and piping of the test loop. Due to the high temperatures (600°C), high pressure level (285 bar) at the

DOI: 10.17185/duepublico/46084

operating point and variable operating conditions, a custom designed centrifugal compressor is currently investigated. First preliminary design calculation show an outer impeller diameter of approximately 80 mm with a rotational speed of 30000 min^{-1} as shown in Figure 11 [7]. The electrical power requirement for the circulation blower are estimated to be 40 kW for a mass flow of 3.5 kg/s. The predesign and a numerical analysis will be presented at the conference.

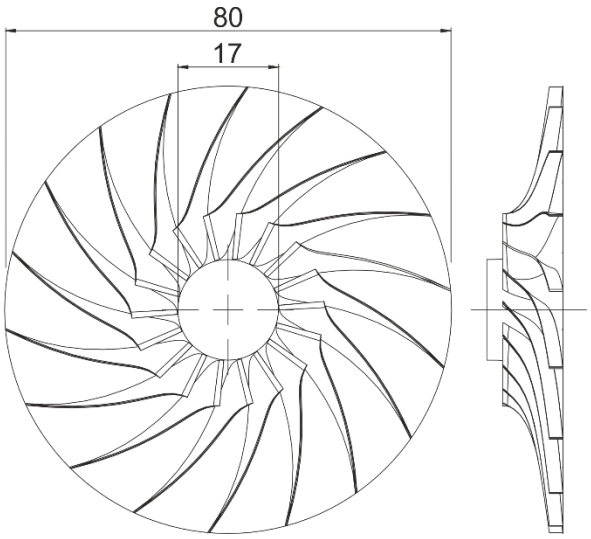

$\pi = 1.05 \quad n = 30000\ min^{-1} \quad \dot{m}_{CO2} = 3.5\ kg/s$

Figure 11: Recirculation blower predesign

SUMMARY AND TIME MANAGEMENT UNTIL COMMISSIONING

The aim of the sCO_2 test loop concept is to provide an experimental basis to test developed system components or singular modules as well as to conduct generic experiments. A motivation for the selection of the intended parameter range of maximum temperature of 600°C is presented. The test loop is planned at the site of the HZDR with a modular approach and three expansion stages. Some predesign aspects of selected components of the first expansion stage are discussed. With the start of the 3 year CARBOSOLA project the detailed engineering of the test loop components will be commenced. The erection of the test loop as well as the commissioning with the verification of the parameters is planned until the completion of the project.

NOMENCLATURE

CO_2	Carbon dioxide
CSP	Concentrated solar power
DN	Nominal diameter
d_a	Outer diameter
d_i	Inner diameter
$\dot{E}$	Exergetic flow
HP	High pressure pipe location
HSRG	Heat recovery steam generator
HZDR	Helmholtz-Zentrum Dresden-Rossendorf
LP	Low pressure pipe location
$\dot{m}$	Mass flow
n	Rotational speed
p	Pressure (bar, kPa)
Q	Heat (MW)
s	Wall thickness
sCO_2	Supercritical carbon dioxide
T	Temperature (°C, K)
v	Velocity (m/s)

η_{Carnot}	Carnot efficiency
η_{ex}	Exergetic efficiency
π	Total pressure ratio
ϑ	Temperature (°C, K)

REFERENCES

[1] Glos, Stefan, et al. (2018) Evaluation of sCO2 Power Cycles for Direct and Waste Heat Applications, 2nd European supercritical CO2 Conference, August 30-31, 2018, Essen, Germany

[2] Moore, Jeffrey, et al. (2014) Development of a 1MW Supercritical CO2 Brayton Cycle Test Loop. The 4th International Symposium - Supercritical CO 2 Power Cycles September 9-10, 2014, Pittsburgh, Pennsylvania.

[3] AD 2000 Regelwerk (2016). Verband der TÜV e.V., Berlin

[4] Pasch, Jim, et al. (2012) Supercritical CO 2 Recompression Brayton Cycle: Completed Assembly Description. Sandia Report - SAND2012-9546.

[5] Cho, Junhyun, et al. (2017) Development of the Supercritical Carbon Dioxide Power Cycle Experimental Loop with a Turbo-Generator. Proceedings of ASME Turbo Expo 2017: Turbomachinery Technical Conference and Exposition - GT2017, June 26-30, 2017, Charlotte, NC, USA.

[6] Eduardo Anselmi, Pavlos Zachos, Robert Collins, Mark Hassan. (2016) Development of an experimental S-CO 2 loop for bottoming cycle applications. 1st European Seminar on Supercritical CO2 (sCO2) Power Systems, 29.-30. September 2016 - Vienna - Austria.

[7] CFturbo GmbH (2018), CFturbo (10.2.7.717), Dresden – Munich, Germany

DOI: 10.17185/duepublico/46084

2nd European supercritical CO2 Conference
August 30-31, 2018, Essen, Germany

2018-sCO2.eu-119

COMPARISON OF CO_2 CRITICAL FLOW MODEL BASED ON HENRY-FAUSKE MODEL WITH TWO-PHASE FLOW

Min Seok Kim*
Department of Nuclear and Quantum Engineering,
Korea Advanced Institute of Science & Technology
Daejeon, South Korea
Email: minskim@kaist.ac.kr

Bong Seong Oh
Department of Nuclear and Quantum Engineering,
Korea Advanced Institute of Science & Technology
Daejeon, South Korea

Hwa-Young Jung
Department of Nuclear and Quantum Engineering, Korea Advanced Institute of Science & Technology
Daejeon, South Korea

Seong Jun Bae
Department of Nuclear and Quantum Engineering, Korea Advanced Institute of Science & Technology
Daejeon, South Korea

Jeong Ik Lee
Department of Nuclear and Quantum Engineering, Korea Advanced Institute of Science & Technology
Daejeon, South Korea

ABSTRACT

Understanding flows and predicting leakages past seals are important for designing supercritical CO_2 (S-CO_2) rotating machinery. Since the seal leakages can have a direct impact on the cycle efficiency. If pressure and temperature trends of leakage flow can be predicted analytically then recovery system can be optimized for better system's overall efficiency. Furthermore, the authors are interested in the transient behavior of seal leakage flow, since the supercritical CO_2 power system can loose inventory during part-load operation as well as during start-up and shut down sequences which was experienced in a few operating test facilities. Therefore, the off-design seal performance is also equally important while this is not dealt thoroughly yet. Thus, a transient simulation for estimating the critical flow in a turbo-machinery seal is essential to predict the leakage flow rate and to calculate the required total mass of working fluid in an S-CO_2 power system.

This paper describes the test data using a CO_2 critical flow experimental facility with three orifice configurations to model the flow resistance of a rotating shaft labyrinth seal. This data is used for validation of an existing transient analytical tool developed for transient hydraulic system analysis. Contained within this code is the analysis approach of Henry/Fauske from 1971 for two phase critical flow of one-component mixtures. The predictions of transient pressure, temperature, and flow profiles for critical and sub-critical flows of CO_2 relative to blowdown test data are presented to show that reasonable results can be generated from the code.

INTRODUCTION

A S-CO_2 Brayton cycle can improve safety of a Sodium-cooled Fast Reactor (SFR) by preventing the sodium-water reaction by changing the working fluid from water to CO_2. The major benefits are 1) relatively high efficiency under moderate turbine inlet temperature (450~750 ºC) which significantly reduces materials and maintenance related issues, 2) simple layout and physically compact power plant size due to smaller turbo-machinery and heat exchangers [1, 2]. These advantages are possible mainly because the S-CO_2 Brayton cycle has lower compressing work than other Brayton cycles due to its high density and low compressibility near the critical point [1]. Furthermore, the coolant chemistry control and component cooling systems are relatively simpler for the S-CO_2 cycle than the steam Rankine cycle, and therefore the total plant footprint can be greatly reduced further.

However, certain amount of leakage flow is inevitable in the rotating turbo-machinery via seals since the S-CO_2 power cycle is a highly pressurized system. Leakage can still occur at three points in the S-CO_2 power system for a Sodium-cooled fast reactor (SFR) application because turbo-machinery design layout of the innovative SFR is different from conventional gas turbine which has single shaft [3].

Figure 1 shows the triple shaft design. Three leakage points include turbine-main compressor, turbine-recompressing compressor, and turbine-generator. The parasitic loss caused by the leakage flow should be minimized since this greatly influences the cycle efficiency. The flow past labyrinth seals in a turbo-machinery will be choked (i.e. critical flow) due to high

DOI: 10.17185/duepublico/46092

pressure difference between supercritical CO_2 turbo-machinery and ambient conditions, while the fluid inside the seal should go through transition from supercritical phase to gaseous phase. Since the leakage flow of turbo-machinery is directly related to the S-CO_2 power cycle efficiency, a computational model of critical flow for a larger power system turbo-machinery seals is essential to predict the amount of leakage flow. From the calculation results, the total required mass of working fluid and the charging rate of the S-CO_2 power system can be determined.

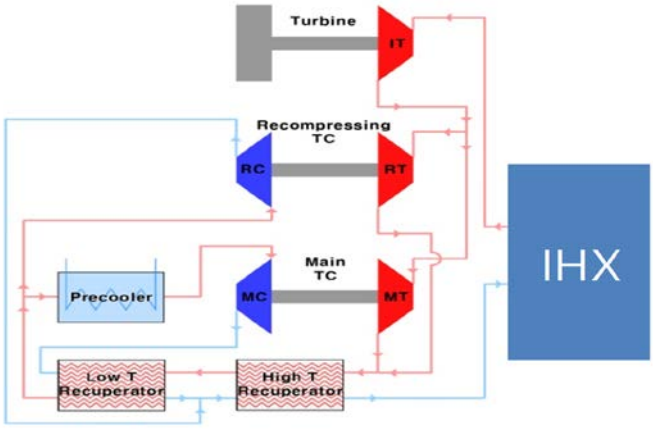

Figure 1: Triple-shaft design of S-CO_2 recompression cycle

Studies on CO_2 leak in a S-CO_2 power cycle were conducted previously. Mignot et al. [4] described the results of an experiment to measure the critical mass flux for numerous stagnation thermodynamic conditions, geometry and outlet tube roughness. 1D homogeneous equilibrium model showed relatively good (less than 10 % error) prediction of the test data but it is not directly related to the critical flow in an S-CO_2 turbo-machinery because the data were used for characterizing the behavior of supercritical fluids during a blowdown or rapid depressurization to validate certain aspects of safety analyses. Hylla et al. [5] gave an overview of numerical and experimental investigations on super-critical CO_2 flow through carbon floating ring seals. Simulation model considers the real gas effect, temperature deformation and the shaft rotation. However, the data were not disclosed since it is proprietary information of MAN Diesel & Turbo SE Inc. and there is a limitation to retrieve the key information for developing a numerical model. For instance, mass flow rate of the leakage flow cannot be obtained from this research as the dynamic behavior of lower pressure stage was not shown in this study. The mass flow rate of leakage flow should be reported for designing an inventory control system. A recent study by Yuan et al. [6] presents a numerical study of S-CO_2 flow using the computational fluid dynamic (CFD) simulation in see-through labyrinth seals. Various designs and conditions have been tested to study the flow characteristic and provide validation data for the numerical model. However, the upstream conditions (10MPa, 45ºC) were fixed and it is only for lower temperature CO_2, which more data for CO_2 leak flow are necessary to understand the full range of critical flow.

This paper presents both numerical and experimental studies of S-CO_2 critical flow while special attention is given to the turbo-machinery seal design. The thermal-hydraulic system transient analysis code MARS and the selected critical flow model are described. Experiments with a simple nozzle geometry were conducted to validate the code first. The comparison of numerical and experimental results of S-CO_2 critical flow will be presented. Furthermore, the validation of the MARS code will be carried out by utilizing the experimental data of CO_2 critical flow facility. In addition, experimental and numerical analysis of two-phase critical flow are conducted while special attention is given to the turbo-machinery seal design. Experimental data obtained from simple nozzle with two-phase condition are reported to study the flow characteristics and provide validation data for the numerical model. Also, comparison with MARS code based on Henry-Fauske model is performed by utilizing the experimental data of CO_2 critical flow facility.

CO_2 CRITICAL FLOW EXPERIMENT

Kim et al. constructed a critical flow test facility to validate the S-CO_2 critical flow model [7]. Figure 2 shows the designed experimental facility for the CO_2 critical flow simulation. The content of the experiment is that CO_2 flows from high-pressure tank (left) to low-pressure tank (right) through the designed nozzle, and pressure and temperature of each position are measured every second. Two tanks are connected by a 1090mm pipe and designed labyrinth seal geometry nozzle is installed between the ball valve and low-pressure tank.

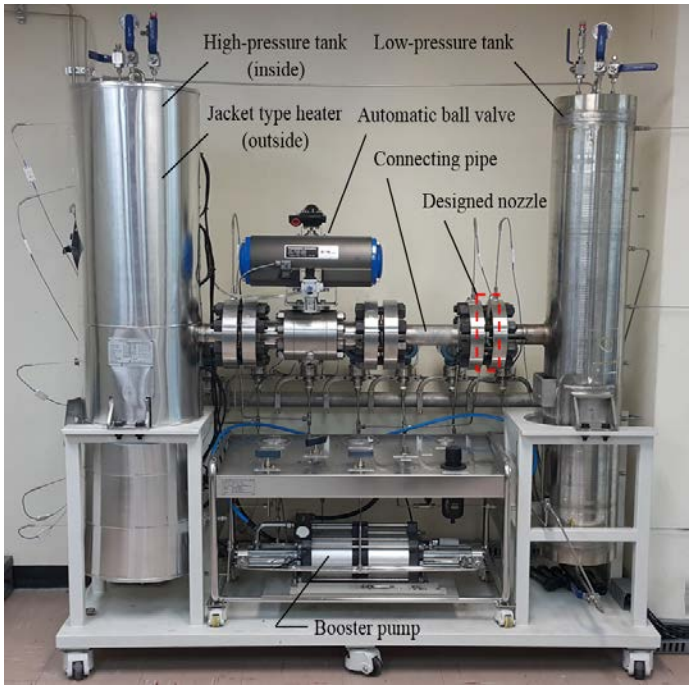

Figure 2: S-CO_2 critical flow experimental facility

DOI: 10.17185/duepublico/46092

Table 1: Design specifications of the experimental facility

	Design Parameters	
High/Low-pressure tank	Pressure (MPa)	22
	Temperature (ºC)	150
	Volume (L)	47 (I.D.:200 mm, H: 1600mm)
Pipe connecting two tanks	Internal diameter (mm)	57
	Length (mm)	1090
Heater (Jacket-type)	Electric capacity (kW)	5
Valve type	Ball valve	

Table 2: Known constant values and uncertainties for calculation

	Known value	Uncertainty		Uncertainty
D_{nozzle} (mm)	1.5/0.5	±0.02	P (kPa)	±(0.00025P)
D_{tank} (mm)	200	±0.5		
H_{tank} (mm)	1600	±1.2	T (ºC)	±(0.15+0.002T)
△Time (sec)	1	±0.03		

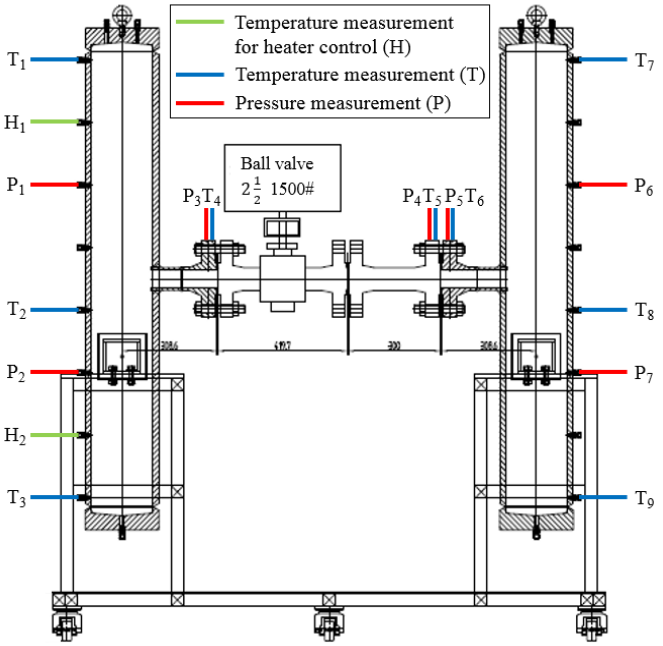

Figure 3: The location of measurements in the experimental facility

Each tank has 200mm of inner diameter, 1600mm of height, and 47 liters of volume and temperature and pressure limits are 150ºC and 22MPa. To control the initial temperature of the high-pressure tank, the heater covers the external surface of the high-pressure tank. The pressure of the high-pressure tank can be controlled by injecting the CO_2 gas through a booster pump. The ball valve is automatically opened and driven by hydraulic pressure (1MPa) from an air compressor to minimize the valve opening time.

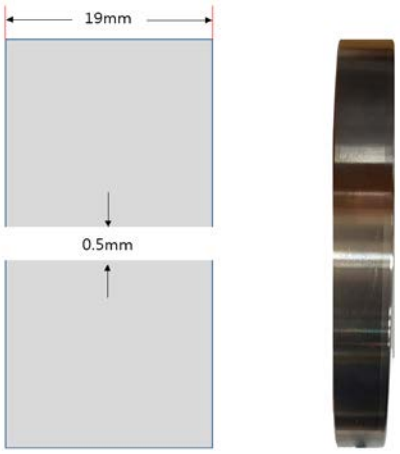

Figure 4: Internal and external geometry of simple nozzle

The nozzle geometry can be modified later to test for different flow conditions. The detail design specifications are shown in Table 1. For accurate measurements, total nine RTDs (Resistance Temperature Detectors) and seven pressure gauges are installed on the critical flow facility as shown in Figure 3. Three RTDs and two pressure gauges are installed on the high-pressure tank (left) and the low-pressure tank (right), respectively. They are located at top, middle, and bottom sections of each tank. One RTD and one pressure gauge are installed at the inlet and the outlet of the nozzle as well as between high-pressure tank and a valve, respectively. Moreover, one RTD and one pressure gauge are installed between high pressure tank and a ball valve. The known constant values and the uncertainties are summarized in Table 2.

Initial conditions of the low-pressure tank is maintained at room condition (about 15ºC, 0.101MPa) to maximize the pressure difference and have a long depressurization time for stable measurement of the CO_2 critical flow. The initial pressure and temperature of the high pressure tank were set to 15.5MPa and 120ºC. The temperature is high enough to maintain the gaseous state after the expansion.

The Barber-Nichols Inc. which is the first mover of turbo-machinery in S-CO_2 Brayton cycle suggested two applicable mechanical seals [8]: 1) Labyrinth seal, 2) Dry gas seal. Two seals are most widely used mechanical seals in high speed rotating machines. The labyrinth seal is non-contact sealing action and it is composed of many grooves, so that the fluid has to pass through a long and difficult path to escape. Leakage amount is proportional to the gap area and inversely proportional to the tooth number.

The dry gas seal or dry lift off seal is non-contacting, and dry-running mechanical face seal which consists of a mating (rotating) ring and a primary (stationary) ring. Although the dry gas seal is preferred over the labyrinth seal in larger supercritical CO_2 power systems, this paper focused on the labyrinth seal. This is because the authors believe that supercritical CO_2 turbomachinery should be hermetic type to make the system more compact and simpler, thus the labyrinth

DOI: 10.17185/duepublico/46092

seal is more likely to be selected for such machinery. The internal and external geometry of simple nozzle is shown in Figure 4.

The experimental procedure is as follows. Firstly, the ball valve was initially closed to separate the high and low pressure tanks before pressurizing the high pressure tank to the target pressure. To pressurize the high pressure tank with CO_2, the air compressor and the booster pump were used. With the hydraulic power of compressed air, the high pressure tank was filled with CO_2 from a storage tank until the pressure reaches the maximum (~13 MPa) pressure. After reaching the pressure, the temperature of the high pressure tank was set to meet the target point by controlling the heater. A venting process is needed during heating stage because the pressure of high pressure tank is increased during the heating of CO_2. By controlling the heater and the vent valve, the target initial conditions can be obtained. After setting the initial conditions, the heater was turned off and the ball valve was opened by hydraulic power of compressed air. The high pressure CO_2 started to flow to the low pressure tank through the nozzle as soon as the ball valve was opened. All temperatures and pressures in each point were measured every second until both tanks reach equilibrium.

NUMERICAL MODEL

To perform a transient simulation for estimating the critical flow in a turbo-machinery seal, we conducted analysis with the Multi-dimensional Analysis of Reactor Safety (MARS) code which is a thermal-hydraulic system transient analysis code developed by Korea Atomic Energy Research Institute (KAERI). MARS code has been developed for the realistic thermal-hydraulic system analysis of light water reactor transients. The bases of MARS are the RELAP5/MOD3.2.1.2 (Reactor Excursion and Leak Analysis Program) and the COBRA-TF (Coolant Boiling in Rod Arrays – Two Fluid) codes of USNRC (United States Nuclear Regulatory Commission). The RELAP5 code is a versatile and robust system analysis code based on one-dimensional two-fluid model for two-phase flows whereas the COBRA-TF code is based on a three-dimensional, two-fluid, three-field model. The two codes were consolidated into a single code by integrating the hydrodynamic solution schemes, and unifying various thermal-hydraulic models, EOS and I/O features. The one-dimensional conservation equations for mass, energy, and momentum of the flow are solved in MARS. The numerical solution method for the MARS hydrodynamic model is semi-implicit scheme. The flow model for two-phase flow is two-fluid model (1D module), and two-fluid, three-field model (3D Vessel module). The sources of the code were fully restructured using the modular data structure and a new dynamic memory allocation scheme of FORTRAN (Formula translation). In addition, a new multidimensional fluid model has been developed and implemented to the RELAP5 system analysis module in order to overcome some limitations of COBRA-TF 3D vessel module. Now MARS became currently a popular thermal-hydraulic tool in use for the analyses of nuclear reactor transients, experimental facility simulations and various safety research purposes in Korea.

To analyze the behavior of S-CO_2 critical flow at the nozzle, Henry-Fauske critical flow model [9] which is the default critical flow model in MARS was applied. It was developed for "nozzles, orifices, and short pipes" and includes an effect of thermal non-equilibrium upon the critical flow rate. By combining the mass flux at the throat for high velocities (1) and boundary condition at critical flow (2), the critical mass flux for an isentropic homogeneous mixture with flashing can be written as Eq. (3).

$$G_t^{-1} = -\left[\frac{d\{xu_v + (1-x)u_l\}}{dP}\right]_t \tag{1}$$

$$\left.\frac{dG_c}{dP}\right|_t = 0 \tag{2}$$

$$G_c^{\,2} = \frac{-1}{\left\{x\frac{\partial v_v}{\partial P} + (1-x)\frac{\partial v_l}{\partial P} + (v_v - v_l)\left.\frac{\partial x}{\partial P}\right|_s\right\}_t} \tag{3}$$

G_t is mass flux at the throat, x is quality, $u_{v,l}$ is velocity of vapor and liquid, P is pressure, G_c is mass flux of critical flow, and $v_{v,l}$ is vapor and liquid specific volume. Embedded in Eq. (3) is the assumption that the two phases move with the same velocity, that is, the slip ratio is unity. The amount of thermal non-equilibrium at the throat is more important in determining the critical flow rate than the amount of mechanical non-equilibrium. Thus, it is assumed that the phase velocities are equal. Henry-Fauske then argued that for normal nozzle configurations, there is little time for mass transfer to take place, and it is reasonable to assume that the amount of mass transferred during the expansion is negligible. Similarly, the amount of heat transferred between the phases during the expansion is also negligible, so that the liquid temperature is essentially constant. Since wall shear, heat transfer with the environment, and interfacial viscous terms were neglected, the system entropy during the expansion was assumed constant. This result along with the assumptions of negligible amounts of interphase heat and mass transfer imply that each phase expands isentropically.

The above assumptions eliminate the need to calculate the liquid specific volume and the quality at the throat, and also provide a relation for the vapor specific volume in terms of the throat pressure and the upstream conditions. Putting all of the above assumptions into Eq. (6), the final expression for the critical flow value of the mass flux is:

DOI: 10.17185/duepublico/46092

$$G_c^{\,2} = \left[\frac{x_0 v_v}{nP} + (v_v - v_{l,0}) \left\{ \frac{(1-x_0)N}{(s_{v,eq} - s_{l,eq})} \frac{ds_{l,eq}}{dP} - \frac{x_0 C_{p,v} (1/n - 1/\gamma)}{P(s_{v,0} - s_{l,0})} \right\} \right]_t^{-1} \quad (4)$$

If the thermal non-equilibrium factor, N, is taken to be unity, the prediction of Eq. (4) is close to that of the homogeneous equilibrium model, and if equals zero the solution is approximately the homogeneous frozen model. As noted by Henry & Fauske, the experimental results of Starkman et al. indicate that the critical flow rates are in relatively good agreement with the homogeneous equilibrium model for stagnation qualities greater than 0.10 [10].

Before the transient simulation for estimating the critical flow in a turbo-machinery seal, the validation of MARS results by comparing to experimental data from a simple nozzle was performed. The simple nozzle has the diameter of 1.5mm and length of 5.0mm and initial conditions of high-pressure tank is 13.5MPa and 160ºC.

In the MARS analysis, the authors assumed that the actual mass flow rate is the same as the theoretical mass flow rate. Also the homogeneous equilibrium model was utilized. For this reason, discharge coefficient was set to unity and throat equilibrium quality was set to 0.14 [9, 11]. Figure 5 shows the geometry modeled in MARS, and it consists of five pipes, one valve and one nozzle. Each tank is divided to three parts, so it has total nine volumes. The heat structures with initial temperature were added to model the thermal inertia effect.

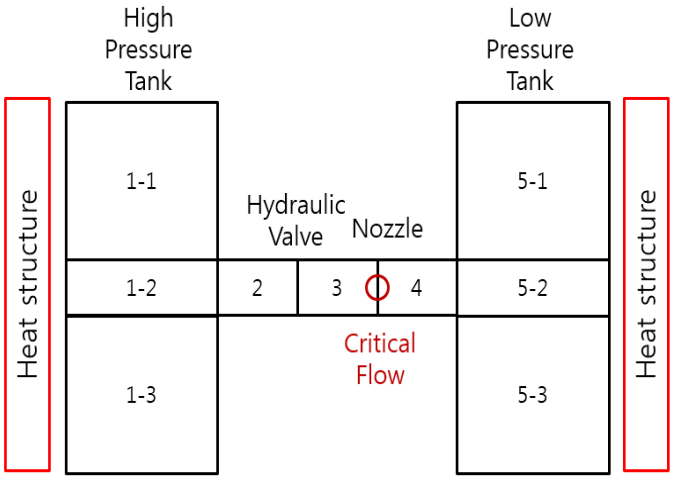

Figure 5: Input geometry and nodalization of MARS code

As shown in Figure 6, it is shown that the MARS results are within 4.7% of experiments and have a good accuracy for predicting the S-CO_2 critical and subcritical flows. Thus, it is reasonable to conclude that the MARS code is sufficient to predict the critical and subcritical flows of S-CO_2.

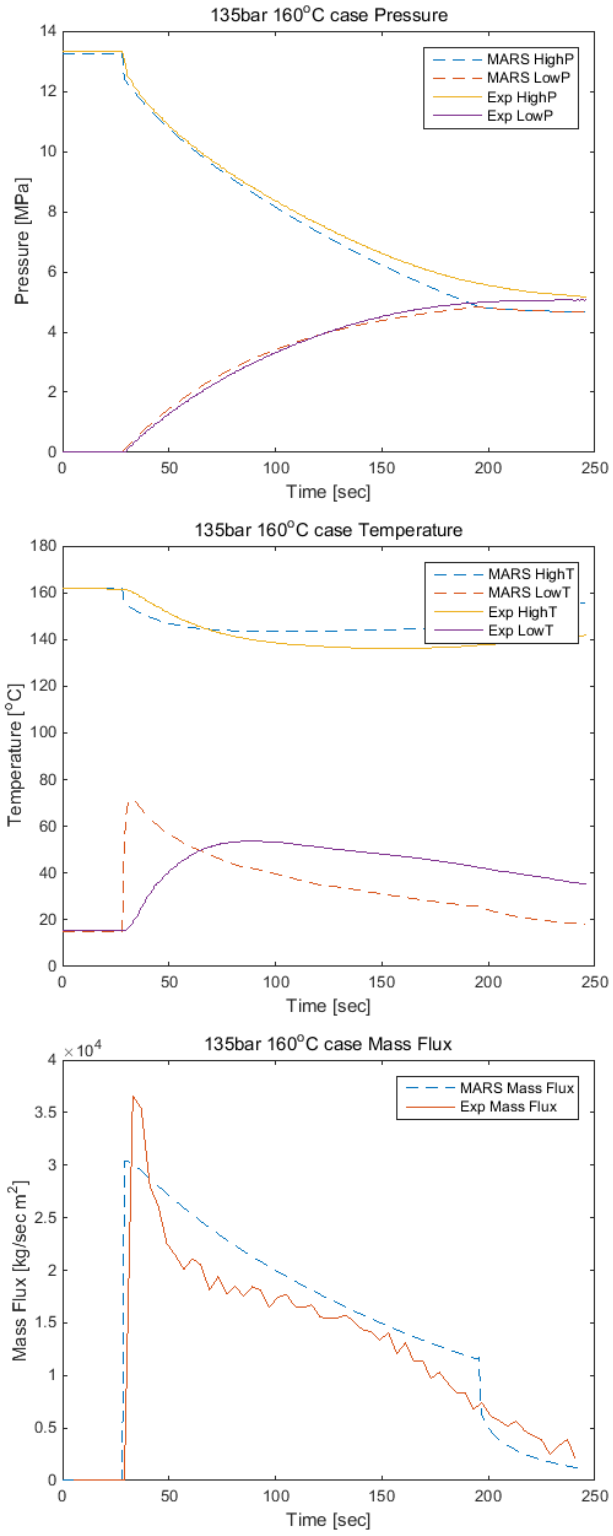

Figure 6: Pressure, temperature and mass flux plots between the experimental results and the MARS results (with simple nozzle)

DOI: 10.17185/duepublico/46092

EXPERIMENTAL RESULTS

To further evaluate if the MARS code can estimate the dynamic behavior under two-phase condition as well, more experiment was conducted. The initial temperature and pressure of the high pressure tank were set to 120ºC and 15.5MPa, respectively, to maintain the gaseous state of the high-pressure tank after the expansion. The CO_2 phase of low- pressure tank will be changed from gaseous state to liquid state after the expansion, which infers that during the critical flow experiment two phase conditions can be obtained. The quality of CO_2 in the low-pressure tank was calculated by using pressure and temperature in each time step. By maintaining the high-pressure tank in supercritical or gaseous state, mass difference can be calculated with the properties of high-pressure tank. Then, the quality of CO_2 in low-pressure tank is calculated with equation (8) since the volume of each tank is already known value, which is 47 liters.

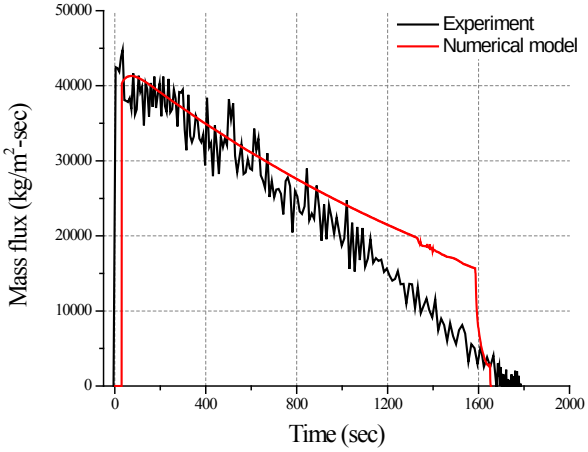

Figure 7: Comparison of mass flux between the experimental and numerical results

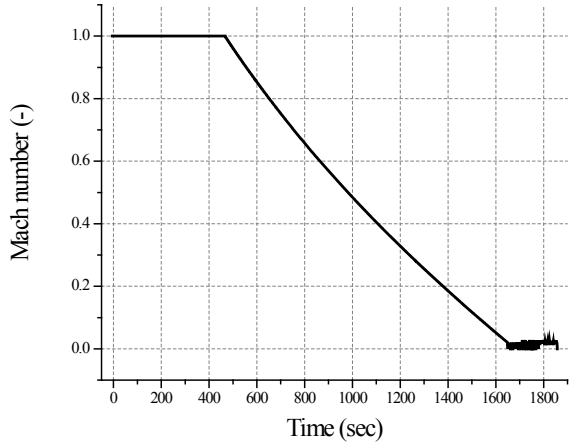

Figure 8: Mach number of experimental result

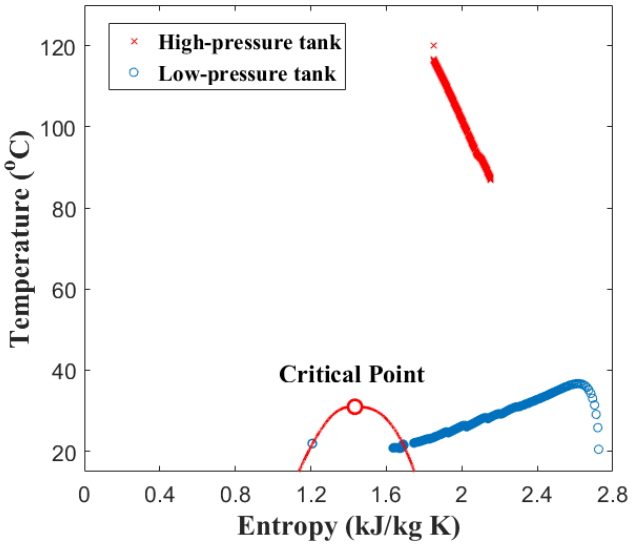

Figure 9: T-s diagram of two-phase flow experimental result

$$x = \frac{v_l(t) - v(t)}{v_l(t) - v_v(t)} \tag{8}$$

where, x is quality of CO_2 in low-pressure tank, and $v_{l,v}$ is specific volume of liquid and vapor.

Figure 7 shows the comparison of mass flux between the experimental data and numerical results, Figure 8 shows the Mach number of experimental result, and Figure 9 shows the T-s diagram of the two-phase flow experimental data. As shown in Figure 7, the difference of equilibrium reaching time between numerical and experimental results is within 1.45%. This indirectly confirms that Henry-Fauske model can estimate the equilibrium reaching time of CO_2 critical flow experimental result quite well. However, the deviation of mass flux is bigger from the experiment around the equilibrium as it can be observed from Figure 7. The main reason of this deviation is may come from the error of property database.

The temperature and pressure of the two tanks were measured during the experiment and the CO_2 properties can be obtained from the NIST reference fluid thermodynamic and transport properties database (REFPROP) after the experiment [13]. The NIST database was also examined in the previous study [14] for the loopback error which was determined to be below 10^{-7} order. However, the fluid thermodynamic and transport property tables use linear interpolation for segments between table search argument values in the MARS code.

Due to the characteristics of thermodynamic property variation of CO_2 near the critical point as shown in Figure 10, the design and analysis methodologies of the CO_2 power cycle components which operate near the critical point should be precise.

DOI: 10.17185/duepublico/46092

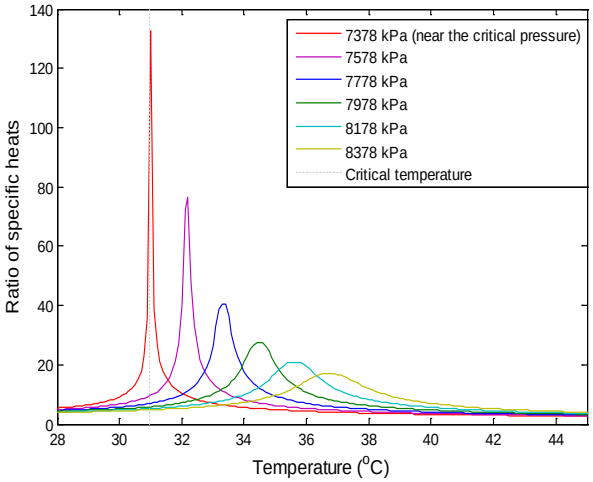

Figure 10: Specific heat ratio variation of S-CO_2 near the critical point [12]

As mentioned above, MARS code especially focus on the steam tables since it has been developed for the realistic thermal-hydraulic system analysis of light water reactor transients. Therefore, correlations and models for CO_2 two-phase flow should be re-examined, which will be the next step of this research.

CONCLUSIONS AND FURTHER WORKS

Predicting the leak flow rate is imperative to sustain the high performance of S-CO_2 power cycle. Thus, transient simulation of S-CO_2 critical flow with MARS code which is a thermal-hydraulic system transient analysis code for the realistic thermal-hydraulic system analysis of light water reactor transients was performed to identify the mass flow rate of CO_2 leakage in turbo-machinery.

The one-dimensional conservation equations for mass, energy, and momentum of the flow are solved in MARS. The numerical solution method for the MARS hydrodynamic model is semi-implicit scheme. The flow model for two-phase flow is two-fluid model (1D module), and two-fluid, three-field model (3D Vessel module). To analyze the behavior of S-CO_2 critical flow at the nozzle, Henry-Fauske critical flow model was applied. This study does not immediately contribute for reducing the leakage flow, but it gives useful information for further understanding of labyrinth seal leakage performance and eventually design optimization.

To validate the MARS code with experimental results, experiments of CO_2 critical flow with simple geometry nozzle were performed. The temperature, pressure, and mass flux of MARS code has similar trend with the result of experimental results in all cases. It was identified that the MARS code can simulate the critical and subcritical flow behavior of S-CO_2 reasonably.

Lastly the two phase flow conditions were experimented and compared to the model. The results shows that the MARS code based on Henry-Fauske model can estimate the equilibrium reaching time of CO_2 critical flow experimental result quite well. However, the deviation of the model is bigger from the experiment around the equilibrium due to the different property database. Due to the characteristics of thermodynamic property variation of CO_2 near the critical point, the design and analysis methodologies of the CO_2 power cycle components which operate near the critical point should be precise. Since the MARS code especially focus on the steam tables, the correlations and models for CO_2 two-phase flow should be re-examined, which will be the next step of this research.

NOMENCLATURE

SFR	Sodium-cooled fast reactor
S-CO_2	Supercritical CO_2
SWR	Sodium-water reaction
IT	Individual turbine
TC	Turbine-compressor
RC	Recompression compressor
RT	Recompression turbine
MC	Main compressor
MT	Main turbine
IHX	Intermediate heat exchanger
SNL	Sandia National Laboratory
1D	One-dimentional
Eq.	Equation
ID	Internal diameter
MARS	Multi-dimensional Analysis of Reactor Safety
RELAP5	Reactor Excursion and Leak Analysis Program
COBRA-TF	Coolant Boiling in Rod Arrays – Two Fluid
USNRC	United States Nuclear Regulatory Commission
KAERI	Korea Atomic Energy Research Institute
EOS	Equation of state
I/O	Input/output
FORTRAN	Formula translation
CFD	Computational Fluid Dynamics

SUBSCRIPTS

C_d	Discharge coefficient
ρ	Density of fluid
r	Rotor radius
ω	Rotor angular frequency
L_r	Rotor cylinder length
Re	Reynolds number
t	Air gap length
υ	Kinematic viscosity
μ	Dynamic viscosity
L_{tooth}	Tooth length
L_{cavity}	Cavity length
N	Tooth number
A	Cross section
P	Pressure
$\dot{m}_{v,l}$	Mass flow rate of vapor and liquid
$u_{v,l}$	Velocity of vapor and liquid

DOI: 10.17185/duepublico/46092

F_w	Wall shear stress
G	Mass flux
x	Quality
$v_{v.l}$	Specific volume of vapor and liquid
n	Thermal equilibrium polytropic exponent
γ	Ratio of specific heats
M	Mach number
R	Gas constant
H	Height
T	Temperature
N	Thermal non-equilibrium factor
x_0	Stagnation quality
h	Enthalpy
s	Entropy

ACKNOWLEDGEMENTS

This study was conducted with the support of Civil-Military Technology Cooperation Program (Project No.: 17-CM-EN-04, Development of the supercritical CO_2 power generation system for the exhaust heat recovery of surface ships) as part of the core industrial technology development project supported by the Ministry of Trade, Industry and Energy, which is gracious acknowledged.

REFERENCES

[1] V. Dostal, M.J. Driscoll, P. Hejzlar, A Supercritical Carbon Dioxide Cycle for Next Generation Nuclear Reactors, Thesis, MIT-ANP-TR-100 (2004).

[2] H. J. Yoon, Y. Ahn, J. I. Lee, Y. Addad, Potential advantages of coupling supercritical CO_2 Brayton cycle to water cooled small and medium size reactor, Nuclear Engineering and Designing, 245 (2012), pp. 223-232 (2012).

[3] Ahn, Y., Lee, J.I., 2014. Study of various Brayton cycle design for small modular sodium-cooled fast reactor. Nucl. Eng. Des. 276, 128–141.

[4] G.P. Mignot, M.H. Anderson, M.L. Corradini, Measurement of supercritical CO_2 critical flow: effects of L/D and surface roughness, Nucl. Eng. Des. 239 (2009) 949–955.

[5] Hylla, E., Schildhauer, M., Bussow, R., Metz, K., Klawes, R., 2015, "Investigations on Transonic Flow of Super-critical CO_2 Through Carbon Ring Seals". ASME Turbo Expo (2015).

[6] Yuan, H., Pidaparti, Wolf, M., Edlebeck, J., Anderson, M., 2015. Numerical modeling of supercritical carbon dioxide flow in see-through labyrinth seals. Nucl. Eng. Des. 293, 436–446

[7] M. S. Kim, B. S. Oh, J. S. Kwon, H. Jung, J. I. Lee, Transient Simulation of Critical Flow With Thermal-Hydraulic System Analysis Code for Supercritical CO_2 Applications, ASME Turbo Expo 2017: Turbomachinery Technical Conference and Exposition

[8] Robert Fuller, et al., 2012, Turbomahinery for Supercritical CO_2 Power Cycles, Proceedings of ASME Turbo Expo 2012

[9] R. E. Henry and H. K. Fauske. "The Two-Phase Critical Flow of One-Component Mixtures in Nozzles, Orifices, and Short Tubes." Transactions of ASME, Journal of Heat Transfer. 93. 1971. pp. 179-187.

[10] E. S. Starkman, et al. "Expansion of Very Low Quality Two Phase Fluid through a Convergent-Divergent Nozzle." Journal of Basic Engineering, Trans. ASME, Series D. Vol. 86. No. 2. June 1964. pp. 247-256.

[11] Thermal-Hydraulic Safety Research Division of the KAERI, MARS Code Manual (2009)

[12] Lee J, Cho SK, Cha JE, et al. Sensitivity study of S-CO_2 compressor design for different real gas approximations. In: ASME Turbo Expo 2016: turbomachinery technical conference and exposition. American Society of Mechanical Engineers; 2016: V009T36A010-V009T36A010.

[13] Lemmon, E.W., Huber, M.L., McLinden, M.O., 2013. NIST Standard Reference Database 23: NIST Reference Fluid Thermodynamic and Transport Properties-REFPROP, Version 9.1, National Institute of Standards and Technology. National Institute of Standards and Technology, Standard Reference Data Program, Gaithersburg.

[14] J. Lee, et al., 2014, Supercritical Carbon Dioxide turbomachinery design for water-cooled Small Modular Reactor application, Nuclear Engineering and Design, Vol. 270, pp. 76-89

DOI: 10.17185/duepublico/46092

2nd European supercritical CO2 Conference
August 30-31, 2018, Essen, Germany

2018-sCO2.eu-124

START UP MODELING OF S-CO_2 COOLED KAIST MICRO MODULAR REACTOR USING EXTENDED TURBOMACHINERY PERFORMANCE MAP

Bong Seong Oh*
Department of Nuclear and Quantum Engineering, Korea Advanced Institute of Science & Technology
Daejeon, Republic of Korea
Email: bongseongoh@kaist.ac.kr

Seong Gu Kim
Department of Nuclear and Quantum Engineering, Korea Advanced Institute of Science & Technology
Daejeon, Republic of Korea
Email: skim07@kaist.ac.kr

Seong Kuk Cho
Department of Nuclear and Quantum Engineering, Korea Advanced Institute of Science & Technology
Daejeon, Republic of Korea
Email: skcho89@kaist.ac.kr

Jeong Ik Lee*
Department of Nuclear and Quantum Engineering, Korea Advanced Institute of Science & Technology
Daejeon, Republic of Korea
Email: jeongiklee@kaist.ac.kr

ABSTRACT

KAIST research team has developed a direct cycle supercritical carbon dioxide cooled Micro Modular Reactor (MMR). It is designed to be an integral type modular reactor and a transportable system via road. In the previous work, components of MMR such as reactor core, power conversion system were designed and selected transients such as design basis accidents and load following operation were modeled. In this work, startup modeling of MMR will be presented. The system starts from near zero rotational speed in turbomachinery and slowly the mass flow rate reaches the on-design point. The beta line method which uses extended performance maps is introduced to the simulation code.

INTRODUCTION

A supercritical CO_2 (S-CO_2) cycle has high thermal efficiency at moderate temperature ranges and can be realized in physically compact size. This is because S-CO_2 is compressed near the critical point in the cycle where fluid become near incompressible but viscosity stays small [1]. The advantages of S-CO_2 cycles on the design point are well known in terms of efficiency and size. Based on these characteristics of the S-CO_2 cycle, KAIST research team has developed an S-CO_2 cooled fully integral modular reactor whose reactor system, power conversion system and safety systems are all contained in a single steel containment. This newly developed nuclear system is called as KAIST-MMR. is the whole module is designed to be transported via truck, ship and trailer to remote regions while minimizing on-site construction [2]. Until now, components were designed in concept level and selected transient conditions such as load following operations and postulated accident modeling were modeled with the modified GAMMA+ code which is revised to simulate transient condition of S-CO_2 systems [3]. Similarly, transient modeling of S-CO_2 cooled nuclear system has been studied by a few institutions [4-6] but startup modeling from near-zero rotational speed of turbomachinery to nominal state is rarely done. This is because S-CO_2 turbomachinery's performance data at low speed is hardly obtained due to the unsteady nature of low rotational speed conditions [7]. To resolve this problem Zhao et al. introduced extended performance map but they did not explain the detail procedure of how to extend the compressor performance map in the low speed region [8]. One extended method for air compressor and turbine is proposed by Sexton et al [7]. According to his work, similarity laws for pump (i.e. incompressible fluid) was introduced [9] and, the both efficiency and pressure ratio of air compressor and turbine are calculated by methods suggested by Agrawal and Yunis with ideal gas characteristics [10]. However, S-CO_2 has non-ideal gas properties especially at the compressor inlet condition so that some modification is essential to apply this method. In this work the modified method based on real gas properties will be proposed to obtain performance of S-CO_2 turbomachinery at low speed region. After the extended performance map is acquired,

DOI: 10.17185/duepublico/46096

the beta line method is implemented to GAMMA+ code. Another benefit of the beta line method is the code calculation becomes independent from the shape of performance map. After the turbomachinery modeling platform is set up, startup of the whole MMR system is simulated with the modified GAMMA+ code with automatic PID controllers.

PERFORMANCE MAP EXTENSION

Equations (1)~(2) show similarity laws of mass flow rate and work about given two speed lines for pump [9].

$$\frac{\dot{}}{\dot{}_2} = \left(\frac{N_1}{N_2}\right) \tag{1}$$

$$\frac{}{_2} = \left(\frac{N_1}{N_2}\right)^3 \tag{2}$$

Agrawal and Yunis [10] directly applied the similarity laws of pumps to the air turbomachinery because it is considered that compressible fluids like air act like incompressible fluid when pressure rise or expansion is small at low speed region. Based on the extended mass flow rate and work from reference point, the extended efficiency and pressure ratio of air turbomachinery could be obtained from ideal gas assumption. Similarly, Sexton also used similarity law of pumps but slightly modified exponent of the non-dimensional numbers to reflect the compressible effect of gas [7]. To obtain the modified exponent from the similarity laws of pump, properties at the two lowest lines of the original performance map were used. From the two lowest mass flow rate and work, the new exponents could be obtained as the following equations (3)~(4).

$$\frac{\dot{\mathrm{m}}_{lowest,1}}{\dot{\mathrm{m}}_{lowest,2}} = \left(\frac{\mathrm{N}_{lowest,1}}{\mathrm{N}_{lowest,2}}\right)^n \rightarrow n = \frac{\ln(\dot{\mathrm{m}}_{lowest,1}/\dot{\mathrm{m}}_{lowest,2})}{\ln(\mathrm{N}_{lowest,1}/\mathrm{N}_{lowest,2})} \tag{3}$$

$$\frac{\mathrm{W}_{lowest,1}}{\mathrm{W}_{lowest,2}} = \left(\frac{\mathrm{N}_{lowest,1}}{\mathrm{N}_{lowest,2}}\right)^m \rightarrow m = \frac{\ln(\mathrm{W}_{lowest,1}/\mathrm{W}_{lowest,2})}{\ln(\mathrm{N}_{lowest,1}/\mathrm{N}_{lowest,2})} \tag{4}$$

From the new exponent and performance data on reference speed line which is the lowest speed line of the original performance map, the performance information at very low speed can be generated. It is shown in equations (5)~(6).

$$\dot{m}_{new} = \dot{m}_{ref}\left(\frac{N_{new}}{N_{ref}}\right)^n \tag{5}$$

$$W_{new,actual} = W_{ref\ actual}\left(\frac{N_{new}}{N_{ref}}\right)^m \tag{6}$$

In the case of the extended efficiency and pressure ratio, it could be calculated from using the ideal gas assumption as shown in equation (7) for the turbine and equation (8) for the compressor.

$$\mathrm{Pr}_{new} = \left(1 - \frac{W_{new}}{C_P T_{in} \eta_{turb,ref}}\right)^{\frac{\gamma-1}{\gamma}} \tag{7}$$

$$\mathrm{Pr}_{new} = \left(1 - \frac{W_{new}\eta_{comp,\mathrm{ref}}}{C_P T_{in}}\right)^{\frac{\gamma-1}{\gamma}} \tag{8}$$

The efficiencies used in equations (7)~(8) are the values of the efficiencies on the lowest reference speed line of the original performance map. This is because a pressure ratio or an efficiency has to be inferred when both values are unknown. Thus, a constant efficiency from the reference speed line is used to calculate the extended pressure ratios. The reason why constant efficiency is used to predict extended pressure ratio instead of constant pressure ratio is because holding the efficiencies constant satisfy the criteria of similarity laws for similar operating points for each speed line. Moreover, the performances of turbomachinery at very low speed are similar to the original performance at the lowest speed line, so that using the constant efficiency is reasonable to obtain the extended pressure ratio. However, the constant efficiency is only used to predict the extended pressure. The extended efficiencies in the performance map should be calculated from the extended pressure ratios. For an ideal gas, equations for the extended efficiencies are written in equation (9) for the turbine and (10) for the compressor.

$$\eta_{new,turb} = \frac{N_{\max} \cdot W_{new,actual}}{\dot{m}_{new} \cdot C_p \cdot T_{in} \cdot \left(1 - \left(\frac{1}{\mathrm{Pr}_{new}}\right)^{\frac{\gamma-1}{\gamma}}\right)} \tag{9}$$

$$\eta_{new,\mathrm{comp}} = \frac{\dot{m}_{new} \cdot C_p \cdot T_{in} \cdot \left(1 - \left(\mathrm{Pr}_{new}\right)^{\frac{\gamma-1}{\gamma}}\right)}{N_{\max} \cdot W_{new,actual}} \tag{10}$$

Based on the previous work, an extension method for S-CO_2 turbomachinery should be differently applied while reflecting the characteristics of S-CO_2. Exponents for S-CO_2 turbomachinery can be calculated from equation (3) for the extended mass flow rate and (4) for the extended actual work. Nevertheless, equations (7)~(8) are not used to obtain S-CO_2 turbomachinery pressure ratio. This is because S-CO_2 turbomachinery experiences abrupt isobaric heat capacity change during compression or expansion process. Therefore, REFPROP data are referred to get outlet pressure of the S-CO_2 turbomachinery with using the inlet entropy and the ideal enthalpy at the outlet as independent variables [11]. In Figure.1, the procedure to get the outlet pressure of S-CO_2 turbomachinery is shown. With this outlet pressure, the pressure

DOI: 10.17185/duepublico/46096

ratio of S-CO_2 compressor can be obtained. Similarly, a constant efficiency from the reference speed line is also used in S-CO_2 case when the ideal enthalpy is evaluated.

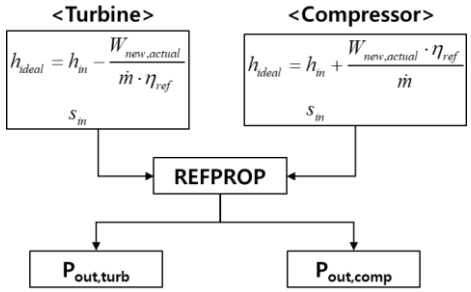

Figure 1: Procedure to get outlet pressure of S-CO_2 turbomachineries based on inlet entropy and extended actual work

Even though the efficiencies which were used to get the extended pressure ratio are the data on the reference map, efficiencies that will be newly drawn on the extended speed line have to be newly evaluated with slightly modified equations (9) ~(10). Since equations (9)~(10) was also derived from the ideal gas assumption, it is better to remove constant isobaric heat capacity and inlet temperature assumptions for the S-CO_2 turbomachinery. The way to cancel out the properties is dividing the extended efficiencies with the reference efficiencies as shown in equation (11) for the turbine and equation (12) for the compressor.

$$\eta_{new,turb} = \eta_{ref\ turb} \frac{W_{new,actual} \cdot \dot{m}_{ref} \cdot \left(1 - \left|\frac{1}{\mathrm{Pr}_{ref}}\right)^{\frac{\gamma-1}{\gamma}}\right)}{W_{ref,actual} \cdot \dot{m}_{new} \cdot \left(1 - \left(\frac{1}{\mathrm{Pr}_{new}}\right)^{\frac{\gamma-1}{\gamma}}\right)} \quad (11)$$

$$\eta_{new,\mathrm{comp}} = \eta_{ref,\mathrm{comp}} \frac{W_{ref,actual} \cdot \dot{m}_{new} \cdot \left(1 - \left(\mathrm{Pr}_{new}\right)^{\frac{\gamma-1}{\gamma}}\right)}{W_{new,actual} \cdot \dot{m}_{ref} \cdot \left(1 - \left(\mathrm{Pr}_{ref}\right)^{\frac{\gamma-1}{\gamma}}\right)} \quad (12)$$

The newly plotted pressure ratio map and efficiency map of MMR turbomachinery including the extended pressure ratios and efficiencies are shown in Figures 2-5.

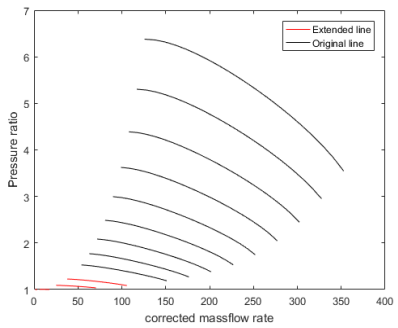

Figure 2: Extended compressor pressure ratio map

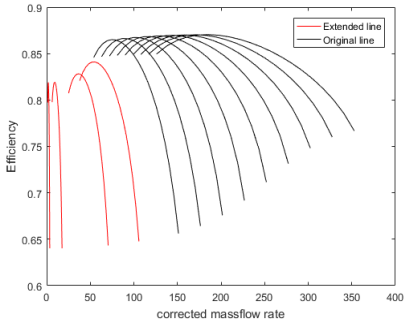

Figure 3: Extended compressor efficiency map

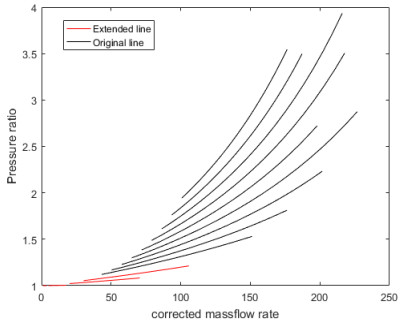

Figure 4: Extended turbine pressure ratio map

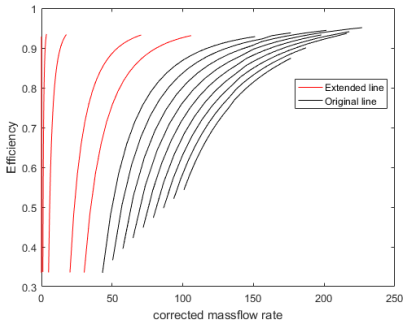

Figure 5: Extended turbine efficiency map

APPLICATION OF BETA LINE METHOD

Fortunately, the pressure ratio maps of the MMR compressor and turbine do not have a steep slope as shown in Figures 2 and 4. Each mass flow rate point has a single pressure

DOI: 10.17185/duepublico/46096

ratio at given speed line. However, if the pressure ratio has a steep slope with the mass flow rates, each mass flow rate can have numerous pressure ratio values at given speed line. This can make a situation that one can have modeling problems when a pressure ratio value is interpolated for a given mass flow rate. To resolve the problem Kurzke et al. proposed the beta line method which is an auxiliary coordinate to resolve dependence on the shape of the performance curve. It introduces a way of mapping the performance map in the system analysis code [12]. The beta lines can be drawn by equally spaced parabolas with parameter values of beta=0…1. The beta lines can be chosen arbitrarily as long as there are no unambiguous intersections of the beta lines with the speed lines. When the beta line method is adopted, the independent parameters to interpolate pressure ratio and isentropic efficiency become compressor speed and beta value as in the following equation (13). The performance map in which beta line is applied is shown in Figure 6.

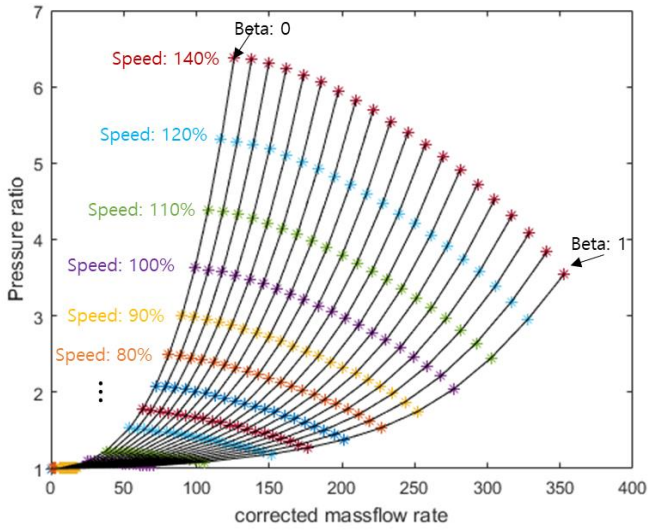

Figure 6: Compressor PR map in which beta line is applied

$$\mathrm{Pr} = f(N,\beta), \quad \eta = f(N,\beta) \qquad (13)$$

According to Kurzke, it is stated that there is no map reading problem when the corrected speed and pressure ratio or corrected mass flow rate are used as interpolation variables for turbine performance map [12]. This is because there are a lot of different map formats in use and usually turbine pressure ratio map has monotonically increasing pressure ratio with respect to the corrected mass flow rate. As a result, turbine performance map is directly used in GAMMA+ code without any additional auxiliary coordinate such as beta line.

MMR STARTUP MODELING

The modeling tool used in this work is the modified GAMMA+ code that has been originally developed for modeling a gas cooled nuclear reactor but it is revised for analyzing S-CO_2 cycles [3]. With this system code, MMR startup is simulated from very slow rotational speed to the nominal value. Figure 7 shows the diagram of MMR which is a transportable and integrally modularized nuclear power system to supply energy at remote regions. When the startup modeling of MMR is implemented, it is assumed that the procedure from vacuum to filling pipe line with CO_2 inventory is skipped so that it is regarded that whole system is filled with S-CO_2 fluid at 7.56MPa and 50°C at initial state. The next assumption is that inventory tank continuously provides the MMR system to fill it up with 8.00MPa and 60°C CO_2 fluid during the startup because the compressor inlet point of MMR is 8.00MPa and 60°C. Another benefit of the inventory supply assumption is that the mass inventory of the initial state could be naturally fitted to the nominal mass inventory by connecting constant pressure and temperature boundary during startup. Another bold assumption is linear increase of reactor power. Absolutely, reactor point kinetics should be applied to the startup modeling, which might not lead to a linear increase of reactor heat generation. However, this work focuses on only thermal hydraulic performance of S-CO_2 cycle during startup and more detail simulation including point kinetics of the nuclear reactor will be added in the further works.

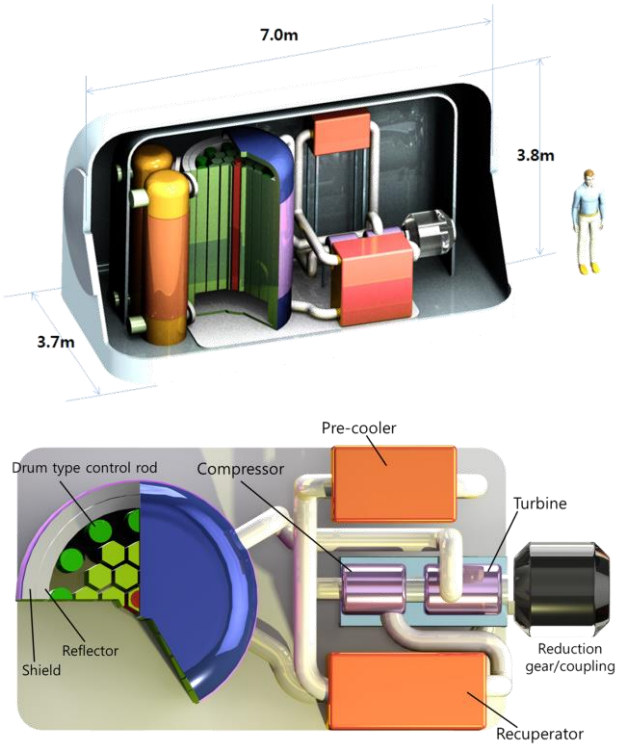

Figure 7: Configuration of MMR

The boundary condition of startup is the compressor rotational speed that linearly increase for 20 seconds. This boundary condition can be realized as connecting high speed motor to the shaft of MMR turbomachinery that makes compressor and turbine share rotational speed. Figure 8 shows the rotational

DOI: 10.17185/duepublico/46096

speed of MMR turbomachinery during startup and Figure 9 shows another boundary condition that is the reactor power. As shown in the figure reactor power also has linear trend with respect to simulation time.

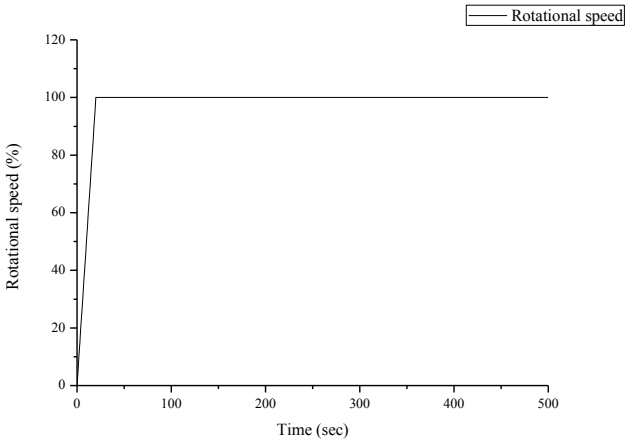

Figure 8: Rotational speed during startup

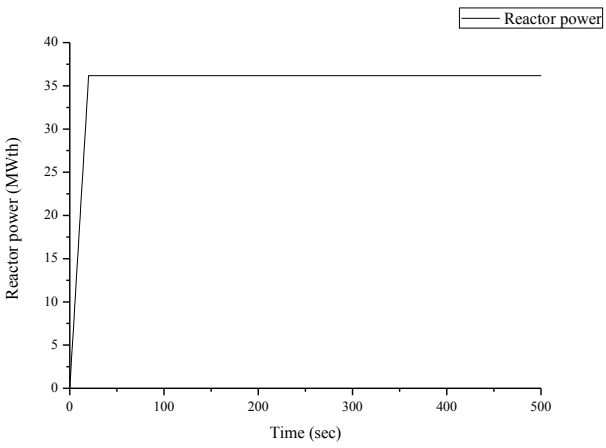

Figure 9: Reactor power increase during startup

Even though the required time for rotational speed was 20 seconds, the total needed time for settling down whole system is roughly estimated for 1500 seconds due to thermal inertia. Figures 10-13 show the pressures, temperatures, mass flow rate and turbomachinery's work of MMR. When MMR begins its operation, the mass flow rate from the air fan which is to keep the compressor inlet temperature at 60^{o}C is controlled by PID controller. Table 1 contains the differences between steady state results of startup and design parameters. The results prove that startup results are very similar to the design parameters.

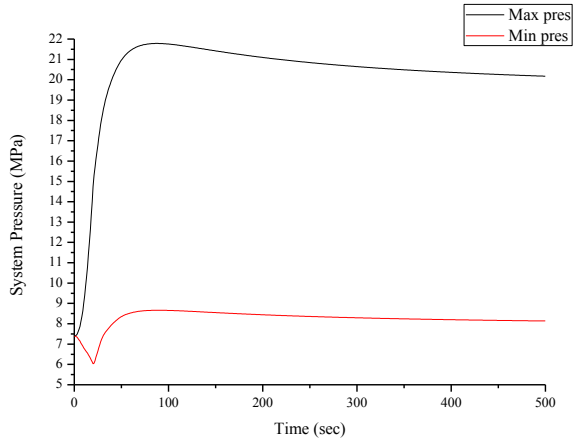

Figure 10: Pressure increase during startup

Since the minimum pressure is decreased during startup (i.e. for 20 sec), the rotational speed of turbomachinery is fixed to the startup motor rotational speed. This means rotational speed, pressure ratio and mass flow rate are unbalanced. However, of the startup motor is disengaged, the minimum pressure is increased back to the nominal value.

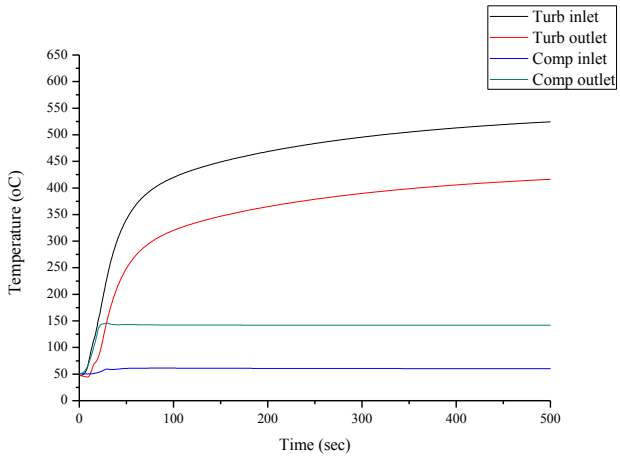

Figure 11: Temperature increase during startup

The reason behind the compressor outlet temperature being higher than the turbine outlet temperature for 20sec is due to the startup motor operation. In other words, the turbomachinery is spinning not due to the turbine power but due to the external force. Conversely, after the startup sequence is terminated the turbine outlet temperature becomes higher than the compressor outlet temperature.

DOI: 10.17185/duepublico/46096

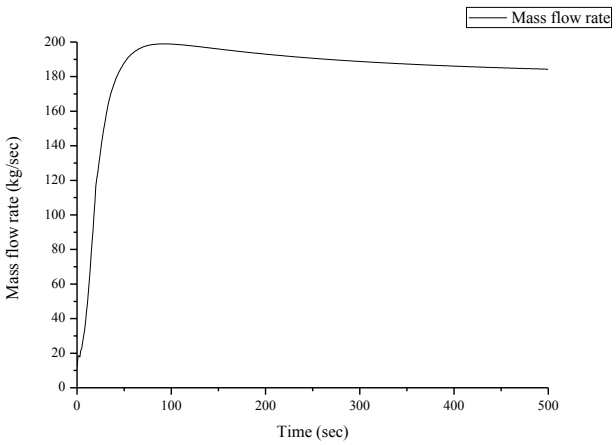

Figure 12: Mass flow rate increase during startup

Mass flow rate of the system is smoothly increased during the startup, which was the intention of the control.

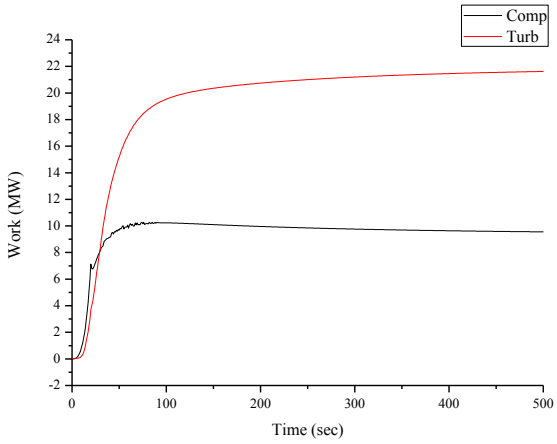

Figure 13: Turbomachinery's work increase during startup

Since startup motor engages for 20sec, the compressor work is larger than the turbine work. Finally, the turbine work is greater than the compressor work when the system is operating without the external motor.

Table 1. Difference between steady state of startup result and design parameters of MMR

	Startup results	Design parameters
Rotational speed [RPM]	19,300	19,300
Reactor power [MWth]	36.18	36.18
Generated work [MW] (W_{turb}-W_{comp})	12.67	12.46
$Temp_{turb,in}$ [°C]	555.9	550.0
$Temp_{turb,outlet}$ [°C]	445.4	440.5
$Temp_{comp,in}$ [°C]	59.97	60.5
$Temp_{comp,outlet}$ [°C]	141.6	142.0
$Press_{max}$ [MPa]	7.97	7.99
$Press_{min}$ [MPa]	19.7	19.7
Mass flow rate [kg/sec]	179.4	180.2

In table I, steady state results and design parameters are compared. As a result, steady state results after modeling the startup shows reasonable agreement with the original design parameters.

CONCLUSION

KAIST research team has developed an S-CO_2 cooled micro modular reactor called MMR. The system has been designed to be transported by ships, trailers and other transportations and it can be operated in remote regions to provide energy reliably for long time. Since the system has to have ability to operate in the isolated region, the number of operators has to be kept minimal. Because of this reason normal transient operations of MMR such as startup, load following and shutdown should be fast and simple. In this study, the startup from near zero rotational speed is analyzed by referring to an extension method of the turbomachinery performance map to the low speed regime using beta line method. This method is robust due to its independence from the performance map shape. After the original performance map of MMR is extended, system startup can be simulated in system analysis code GAMMA+. It is assumed that the startup rate of rotational speed is 5%/sec and the torque is delivered by an external startup motor. After 20sec, the rotational speed of turbomachinery and reactor power approaches to the nominal value but other properties such as mass flow rate, temperature, and pressure reach the steady state values in 1500sec. During the system startup sequence there is no abrupt change in system properties. In this paper, it is shown that the performance map extension method can be a useful method to model the system startup when the original map cannot be utilized directly. For further works, the startup modeling will be compared to the real experimental data to validate the extension method.

ACKNOWLEGEMENT

This work was supported by the National Research Foundation of Korea (NRF) grant funded by the Korea government (MSIP) (2017M2B2B1071971)

DOI: 10.17185/duepublico/46096

NOMENCLATURE

$\dot{m}$: Mass flow rate.
N : Turbomachinery rotational speed.
W : Turbomachinery power.
Pr : Turbomachinery Pressure ratio.
η : Turbomachinery Efficiency.
h : Enthalpy.
β : Beta value.
C_p : Isobaric heat capacity.
T : Temperature.
γ : Isobaric heat capacity to isochoric heat capacity ratio.

Subscript

lowest,1: The first lowest value.
lowest,2: The second lowest value.
new: Newly extended value.
ref: Reference value.
turb: Turbine.
comp: Compressor.
in: Inlet condition.

REFERENCE

[1] V. Dostal, M. J. Driscoll, and P. Hejzlar, "A supercritical carbon dioxide cycle for next generation nuclear reactors," *USA: Massachusetts Institute of Technology,* vol. MIT-ANP-TR-100, 2004.

[2] S. G. Kim, H. Yu, J. Moon, S. Baik, Y. Kim, Y. H. Jeong*, et al.*, "A concept design of supercritical CO2 cooled SMR operating at isolated microgrid region," *International Journal of Energy Research,* pp. n/a-n/a, 2016.

[3] B. S. Oh, Y. H. Ahn, H. Yu, J. Moon, S. G. Kim, S. K. Cho*, et al.*, "Safety evaluation of supercritical CO2 cooled micro modular reactor," *Annals of Nuclear Energy,* vol. 110, pp. 1202-1216, 2017/12/01/ 2017.

[4] A. Moisseytsev and J. J. Sienicki, "Development of a plant dynamics computer code for analysis of a supercritical carbon dioxide Brayton cycle energy converter coupled to a natural circulation lead-cooled fast reactor," ANL-06/27; TRN: US0704255 United States10.2172/910536TRN: US0704255Tue Feb 05 05:30:08 EST 2008ANLEnglish, 2007.

[5] M. A. Pope, J. I. Lee, P. Hejzlar, and M. J. Driscoll, "Thermal hydraulic challenges of Gas Cooled Fast Reactors with passive safety features," *Nuclear Engineering and Design,* vol. 239, pp. 840-854, 5// 2009.

[6] N. A. Carstens, D. M. Driscoll, D. P. Hejzlar, and D. j. Coderre, "Control Strategies for Supercritical Carbon Dioxide Power Conversion Systems," *USA: Massachusetts Institute of Technology,* vol. 213502891-MIT, 2007.

[7] W. R. Sexton, "A method to control turbofan engine starting by varying compressor surge valve bleed," 2001.

[8] H. Zhao, L. Zou, H. Zhang, and Y. Zhu, "DEVELOPMENT OF A FULLY IMPLICIT COMPRESSOR MODEL WITH JFNK FRAMEWORK," *NURETH 17,* September 3-8, 2017.

[9] B. R. Munson, D. F. Young, and T. H. Okiishi, "Fundamentals of fluid mechanics," *New York,* vol. 3, 1990.

[10] R. Agrawal and M. Yunis, "A generalized mathematical model to estimate gas turbine starting characteristics," in *ASME 1981 International Gas Turbine Conference and Products Show*, 1981, pp. V001T01A011-V001T01A011.

[11] E. W. Lemmon, M. L. Huber, and M. O. McLinden, "NIST Standard Reference Database 23," *NIST Reference Fluid Thermodynamic and Transport Properties—REFPROP, version,* vol. 9, p. 55, 2010.

[12] J. Kurzke, "How to get component maps for aircraft gas turbine performance calculations," *ASME paper,* p. 164, 1996.

DOI: 10.17185/duepublico/46096

2nd European supercritical CO2 Conference
August 30-31, 2018, Essen, Germany

2018-sCO2.eu-149

DESIGN AND DYNAMIC SIMULATION OF A 200 kW$_{th}$ LABORATORY sCO$_2$-TEST RIG

Gregor Klemencic
BERTSCHenergy
Bludenz, Austria

Andreas Werner*
Vienna University of Technology Vienna,
Austria
Email: Andreas.werner@tuwien.ac.at

Markus Haider
Vienna University of Technology
Vienna, Austria

Helmut Leibinger
Rohrdorfer Gruppe
Gmunden, Austria

Thomas Fellner
Scheuch GmbH
Aurolzmünster, Austria

Norbert Steinschaden
Zauner Anlagentechnik GmbH
Wallern, Austria

Thomas Bergthaller
Salzburg AG
Salzburg, Austria

Tim Nowack
Maschinenfabrik Liezen
Liezen, Austria

ABSTRACT

The paper describes the development of an sCO$_2$-test rig, which enables to investigate the behaviour of sCO$_2$ as a heat transfer medium as well as a working fluid for power cycles. The system can be operated in transcritical and supercritical mode. Maximum operating pressure is 240 bara, max. temperature is 400 °C in phase 1. In a second project phase (phase 2) maximum temperatures of 650 °C are intended to be achieved.

A dynamic simulation of the whole cycle was performed based on the software APROS (Advanced Process Simulator, edited by VTT) in order to evaluate the behaviour of the cycle under transient conditions. The time dependent behaviour of pressure and temperature levels, as well as the trend of the liquid level in the CO$_2$-tank have been simulated.

INTRODUCTION

Heat recovery from industrial processes is of rising interest due to the Energy Efficiency Directive of the EU and the latest United Nations Framework Convention on Climate Change in Paris (France 2015). Therefore the Institute for Energy Systems and Thermodynamics of TU Wien is currently working on a project that deals with the matter of using supercritical carbon dioxide (sCO$_2$) as a working fluid for different cycle processes, see [1]. The main aim for the first step of the sCO$_2$ project is to plan, construct and take into operation an sCO$_2$ test rig to gain operational expertise of component and process behaviour. In this paper the basic and detail engineering of the test rig and the functionality of the process control system for the different sCO$_2$ cycles is presented. A dynamic simulation of the test rig was performed to verify the process control system and the general dynamic behaviour of the complete test rig during operation. The current status of the project has the internal title ‘phase 1’. In phase 1 of the project no sCO$_2$ turbo machinery is available, instead a high pressure CO$_2$ pump and an expansion valve are used. The other main components are a CO$_2$ heater (tube bundle heat exchanger, thermal oil as heat source), a cooler (tube bundle heat exchanger, water as coolant), a buffer tank and a double pipe heat exchanger (heated with thermal oil). The main scientific objective of phase 1 is to investigate the heat transfer to sCO$_2$ in the vicinity of the critical point. The test rig can reach pressures and temperatures up to 240 bar and 450 °C at a nominal mass flow of 0.4 kg/s. The maximum thermal heat input is roughly 200 kW. Currently several approaches for a potential ‘phase 2’ are under evaluation and/or have been/will be submitted for public funding. The extension approaches are:

(a) installation of a gas fired heater in parallel to the thermo-oil heater. Such a heating source will allow to raise the maximum cycle temperature up to 650 °C and to raise nominal sCO2-mass flow from 0.4 into the range of 0.8 kg/s
(b) installation of an sCO$_2$/sCO$_2$ recuperator: this will allow to analyse realistic cycle arrangements for high temperature heat sources
(c) installation of turbo-expander and turbo-pump/compressor: this feature will allow to operate the test rig with full range industrial equipment.
(d) Operation of mixtures of CO$_2$ with other fluids (in the frame of a European research consortium), see [2].
(e) Extension to heat pump operation (flow reversal and

DOI: 10.17185/duepublico/46099

installation of a high temperature compressor).
The main objective of the phase 1 test rig was to install a flexible tool which allows analysing various questions related to the power cycle, to system operation, to control systems and to heat transfer, see [3], [4] and [5]. Also practical questions such as filling as well as transient operating conditions should be investigated. The test rig is currently (July 2018) in the hot commissioning phase. The next targets are to operate the system under stable conditions for all design cases and to start heat transfer experiments.

TEST RIG DESIGN – PHASE 1:

The set up to be designed should fulfil maximum requirements of flexibility within the financial boundary conditions, see [6]. The basic version of a trans-critical power cycle without expander (using a throttle valve instead) has been realized, in order to analyse heat transfer, start up and shutdown of the cycle and to collect expertise of the transient behaviour of the system. Heat input is performed by a thermal oil/sCO_2 heat exchanger with a maximum temperature level of ϑ_{TO}=380 °C. Heat rejection is realized in a condenser/cooler connected to a refrigeration cycle with cooling temperatures of ϑ_{COOL}=6 °C.
A double pipe heat exchanger allows to investigate heat transfer behaviour under conditions close to the critical point. Besides investigations related to power cycles, the potential of sCO_2 as a heat transfer medium, compared e. g. to pressurized water or thermal oil cycles will be investigated.

Table 1: Phase 1 Design Parameters:

	Supercritical operation			Transcritical operation		
	max.	min.	design	max.	min.	design
p_{High} [bar$_a$]	240	100	220	240	100	220
P_{Low} [bar$_a$]	120	75	80	70	50	60
$\vartheta_{T\text{-}V\_In}$ [°C]	400	150	380	400	150	380
ϑ_{Low} [°C]	50	35	40	28.7	14.3	22.0
m_{Dot} [kg/s]	0.7	0.1	0.4	0.7	0.1	0.4

A scheme of the test rig is shown in **Figure 12**, see annex A.

Heater for Phase 1:
The heater for phase 1 is of shell and tube construction (Figure 1).

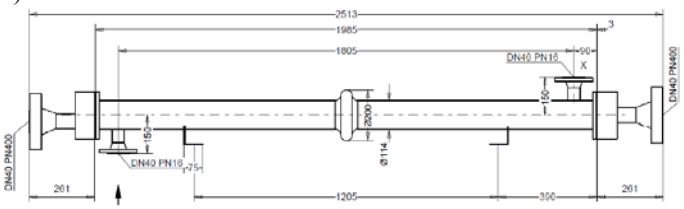

Figure 1: Drawing of Thermo-oil heater.

Pump:
The pump has to fulfil two tasks:

- the pressure increase during supercritical and transcritical operation
- the circulation of CO_2 in the heat displacement mode

The major task of the pump is the high pressure increase during the transcritical mode. Thus the pump design was based on this operation mode. The pump is a TRIPLEX-piston-pump which is able to supply the mass flow over the operating range. The mass flow is measured by using a Coriolis flow meter and controlled via a frequency converter. The inlet temperature for the CO_2 is in the range of 20-25 °C; within this operating range stable operation should be possible.

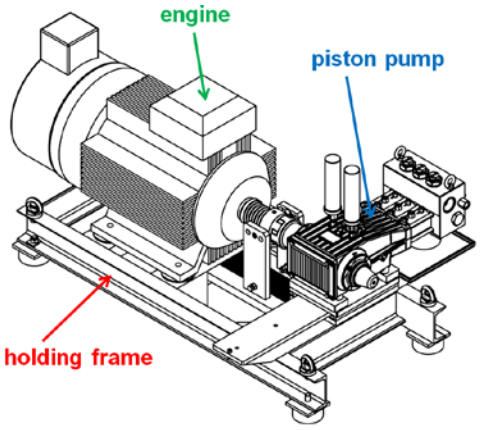

Figure 2: Piston Pump

Table 2: Phase 1 Operating parameters of pump

p_{Out_Max} [bar]	280.0	V_{Dot} [l/min]	50
p_{In_Min} [bar]	11.0	ϑ_{In_Min} [°C]	-40
p_{In_Max} [bar]	220.0	ϑ_{In_Max} [°C]	50
P_{el} [kW]	29.5	f [Hz]	50

Condenser/Cooler:
Whether the tube bundle heat exchanger is working as a cooler or condenser depends on the operational mode. There are two design cases, at the first the heat exchanger works as cooler and condenser at transcritical mode and in the second case as a cooler at supercritical operation mode.

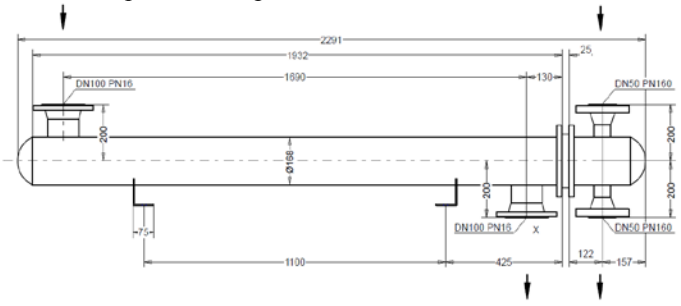

Figure 3: Condenser / Cooler

DOI: 10.17185/duepublico/46099

Figure 4: Picture of the test rig

OUTLOOK TO PHASE 2

Figure 14 (see annex A) gives a process flow diagram of the intended arrangement for phase 2 (funding is yet pending).

Heater for Phase 2:

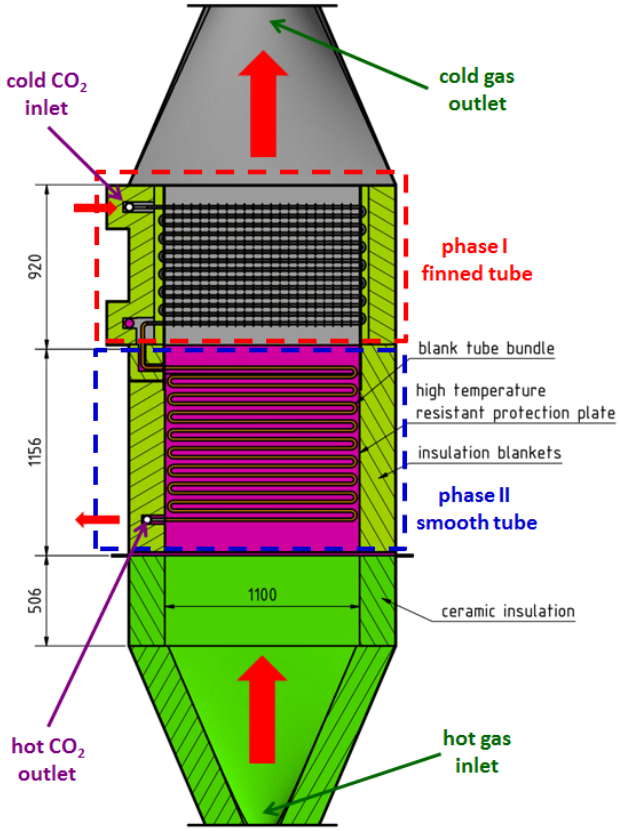

Figure 5: Hot gas heat exchanger

RESULTS AND DISCUSSION

Dynamic simulation of the sCO_2 test rig:

To test the process control system and the general dynamic behavior of the complete test rig during operation of the different CO_2 cycles (transcritical and supercritical), a dynamic simulation by using the process simulation tool APROS (Advanced Process Simulator, VTT) was performed. In **Figure 13** the APROS model of the sCO_2 test rig can be seen.

The basic stationary design of the test rig was done by using IpsePro based on selected and planned operating parameters. The two operating modes power cycle operation and heat transfer mode have been considered. The dynamic simulation is based on data returned from the detail engineering of the test rig. The CO_2-properties were calculated according to Span, R. and Wagner, W.: "A New Equation of State for Carbon Dioxide covering the Fluid Region from Triple Point Temperature to 1100 K at Pressures up to 800 MPa", see [7].

In **Figure 6**, **Figure** 7 and **Figure 8** the results for the transcritical CO_2 cycle are shown.
The simulation starts after filling the test rig at around 6 MPa and 21 °C and switching on the CO_2 pump. The mass flow is constantly held at 0.4 kg/s for the whole test cycle. In case of the TC-cycle the cooler constantly cools down the CO_2 to 21 °C. After 900 seconds the heating is activated and the CO_2 heats up to approximately 360 °C after 3600 seconds (see Fig 8). While heating up, the pressure rises slowly and the tank is completely filled (see Fig 8 and 10). After heating the system up, the high pressure control is activated at 2700 seconds (the expansion valve closes slowly) and the pressure rises up to 22 MPa after 4500 seconds, what is the desired high pressure level for the operation. During the rise of the high CO_2 pressure, the tank level drops a little bit, because more CO_2 mass is kept in the high pressure part of the test rig. In case of the TC cycle the low pressure level is controlled by the cooler. At the desired 21 °C a pressure of around 5.9 MPa is adjusted (see **Figure 7**) between 4500 and 7200 seconds).

To bring the system back to the starting point, first the high pressure level is reduced after 7200 seconds (the expansion valve opens slowly until it is completely open) and then the heating is constantly switched off (from 9000 to 10800 seconds). Finally the system returns to the starting conditions.

DOI: 10.17185/duepublico/46099

Simulation of the transcritical sCO₂ cycle:

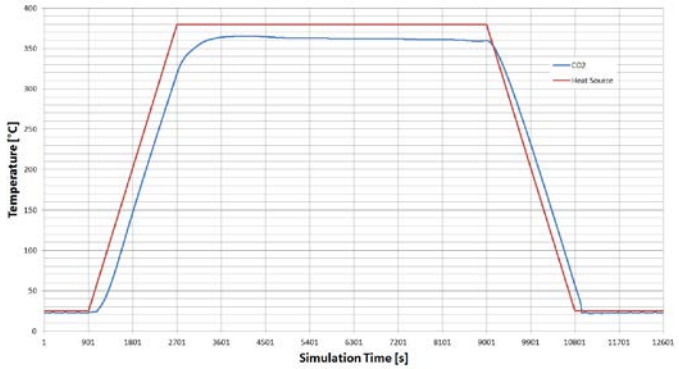

Figure 6: Trend of the temperatures of CO_2 (hot side) and the heat source (TC cycle)

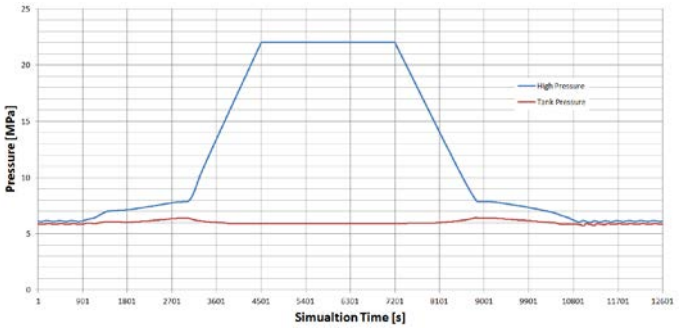

Figure 7: CO_2 pressure trends of the high pressure side and the tank (TC cycle)

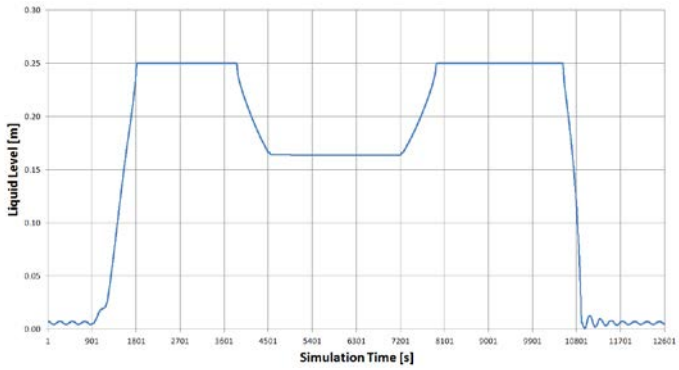

Figure 8: Trend of the liquid CO_2 level in the tank (TC cycle)

Simulation of the supercritical CO_2 cycle (SC cycle):

In **Figure 9, Figure 10** and **Figure 11** the results for the supercritical CO_2 cycle are shown. The simulation starts again after filling the test rig at around 6 MPa and 21 °C and switching on the CO_2 pump. The mass flow is constantly held at 0.4 kg/s for the whole cycle time. Now the starting value of the CO_2 cooling temperature is again 21 °C, but will be changed during the test cycle. This will be described later. In case of the SC cycle, the start up process to reach the supercritical state is a little bit more complex than before. First of all heating is activated after 900 seconds and the CO_2 reaches temperatures of approximately 360 °C after 3600 seconds.

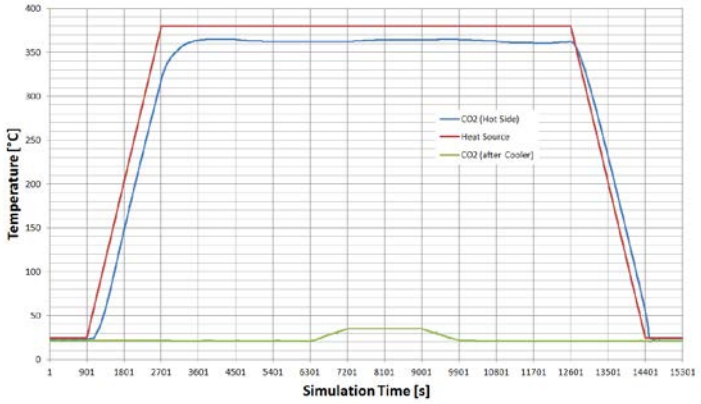

Figure 9: Trend of the temperatures of CO_2 (hot side and after cooler) and the heat source (SC cycle)

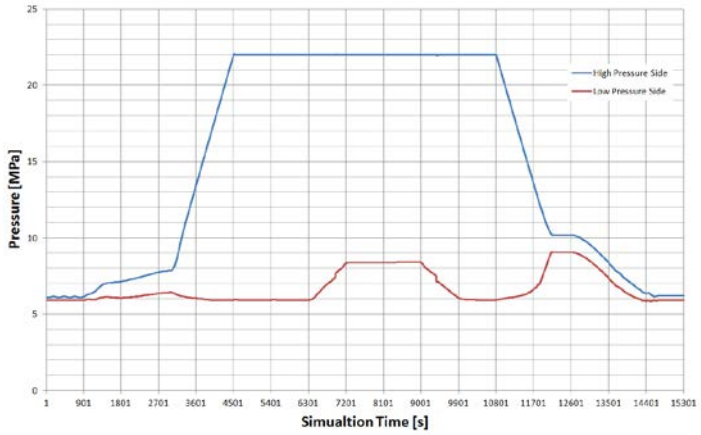

Figure 10: CO_2 pressure trends of the high pressure side and the low pressure (SC cycle)

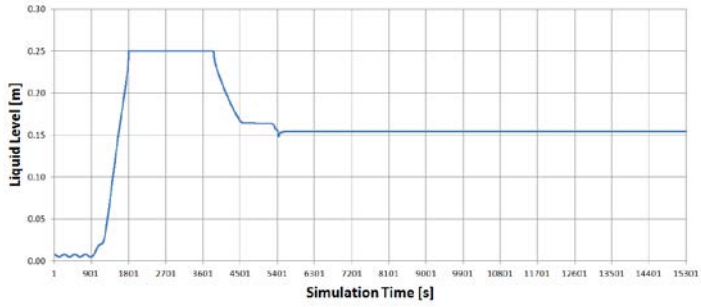

Figure 11: Trend of the liquid CO_2 level in the tank (SC cycle)

While heating up, the pressure rises slowly and the tank is completely filled. After heating the system up, the high pressure control is activated at 2700 seconds (the expansion valve closes slowly) and the pressure rises up to 22 MPa after 4500 seconds, what is again the desired high pressure level for the operation. During the rise of the high CO_2 pressure, the

DOI: 10.17185/duepublico/46099

tank level drops a little bit (like before for the TC cycle). In the next step, the bypass of the test rig is opened and the tank is decoupled by closing the appropriate valves. Now the total CO_2 flow is directed through the bypass. To reach the supercritical state, the CO_2 cooling temperature is raised to 35 °C to exceed the critical temperature of the CO_2 (T_{crit}=30.98 °C). This is shown in Fig 12 (green curve). Along with the temperature also the pressure rises in the low pressure part of the system. The resulting low pressure level depends now on the total CO_2 mass contained in the system (without the decoupled tank). In this case a pressure of around 8.4 MPa is obtained, what is also above the critical pressure of CO_2 (p_{crit}=7.38 MPa). The system now is completely under supercritical state. In the figures, this state accords to the time span between 7200 and 9000 seconds.

To bring the system back to the starting point, first of all the CO_2 cooling temperature is reduced to 21 °C again (between 9000 and 9900 seconds). The system returns to a TC state. Then the high pressure level is reduced after 10800 seconds (the expansion valve opens slowly until it is completely open) and the heating is constantly switched off (from 12600 to 14400 seconds). Finally the system returns to the starting conditions.
The dynamic simulations showed that the planned control system should work fine with the designed test rig. Nevertheless it will be very interesting to compare these simulation results with experimental data and see how the real system (with all the various components) reacts on dynamic changes.

NOMENCLATURE
f frequency [1/s]
m_{Dot} mass flow (kg/s)
p pressure [bar]
P power [kW]
V_{Dot} volumetric flow (l/min)
ϑ temperature (°C)

ACKNOWLEDGEMENTS
The authors gratefully thank FFG (Austrian Research Promotion Agency) for funding the current project "CO_2 as a working medium for heat recovery", Proj. No.: 853568.

REFERENCES
[1] Klemencic, et al.: Comparison of conventional and CO_2 power generation cycles for waste heat recovery. 5th Int. Power Cycle Symp. March 29-31, 2016, San Antonio, TX, USA.
[2] Yang, M.-H.: The performance analysis of the transcritical Rankine cycle using carbon dioxide mixtures as the working fluids for waste heat recovery. J. of Energy Conversion and Management 151, (2017), pp. 86-97.
[3] Rieberer, R.: CO_2 as Working Fluid for Heat Pumps, PhD-Thesis, (1998), TU Graz.
[4] Schoonbroodt, A.: Unterstützung der Entwicklung eines mit CO_2 als Kältemittel betriebenen HVAC-Systems für mobile Anwendungen. MS-Thesis, (2015), TU Wien.
[5] Baldinger, A.: Stillstandsdruckbegrenzung von Klimaanlagen mit dem Kältemittel R-744 in Schienen-fahrzeugen, MS-Thesis, (2018), TU Wien.
[6] Benda, L.: Design of a supercritical CO_2 test rig. MS-Thesis, (2017), TU Wien.
[7] Span, R., Wagner, W.: A New Equation of State for Carbon Dioxide Covering the Fluid Region from the Triple-Point Temperature to 1100 K at Pressures up to 800 MPa. J. of Physical and Chemical Reference Data 25, 1509 (1996).

DOI: 10.17185/duepublico/46099

ANNEX A

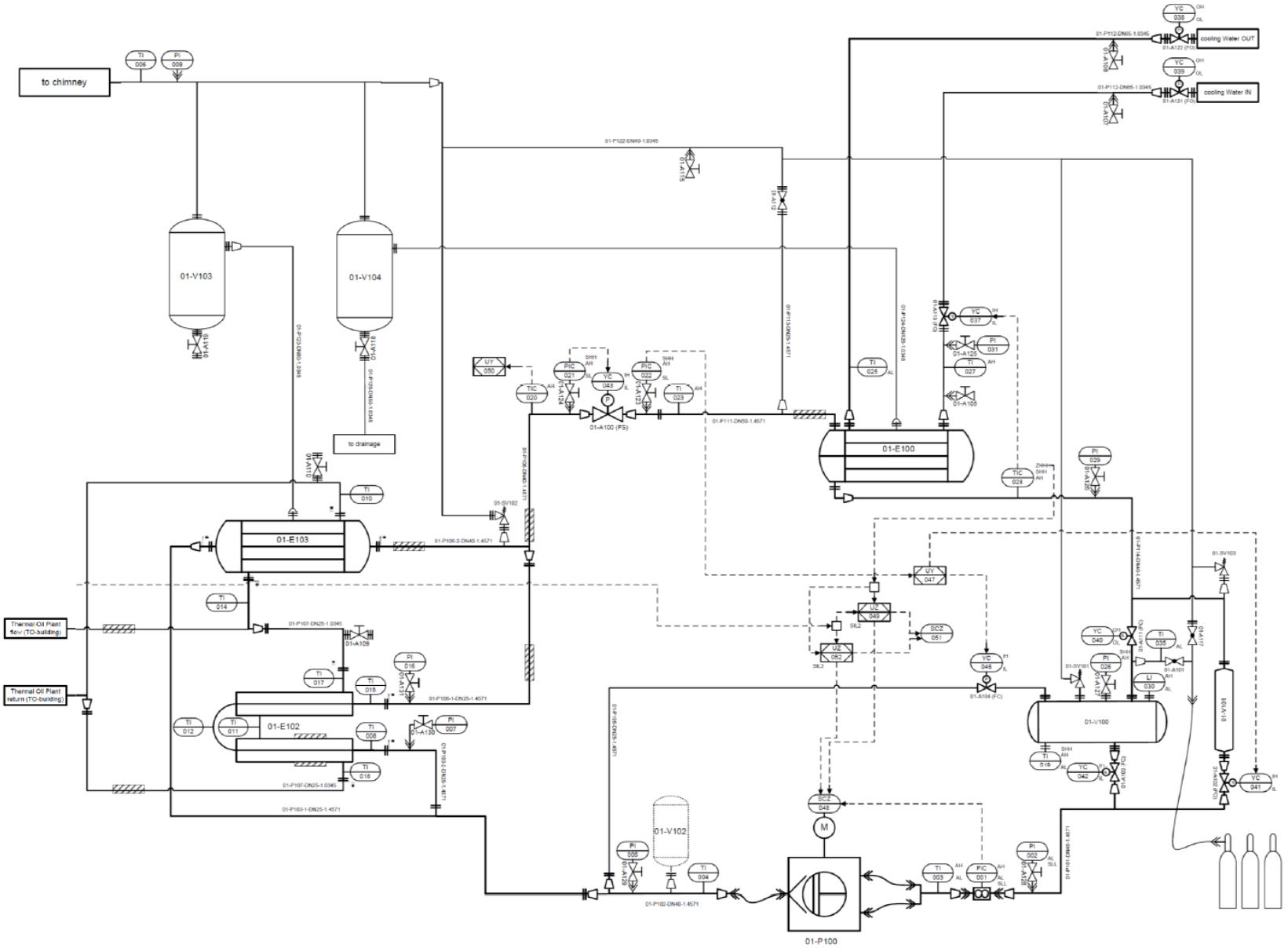

Figure 12: PID of the test rig- Phase1

DOI: 10.17185/duepublico/46099

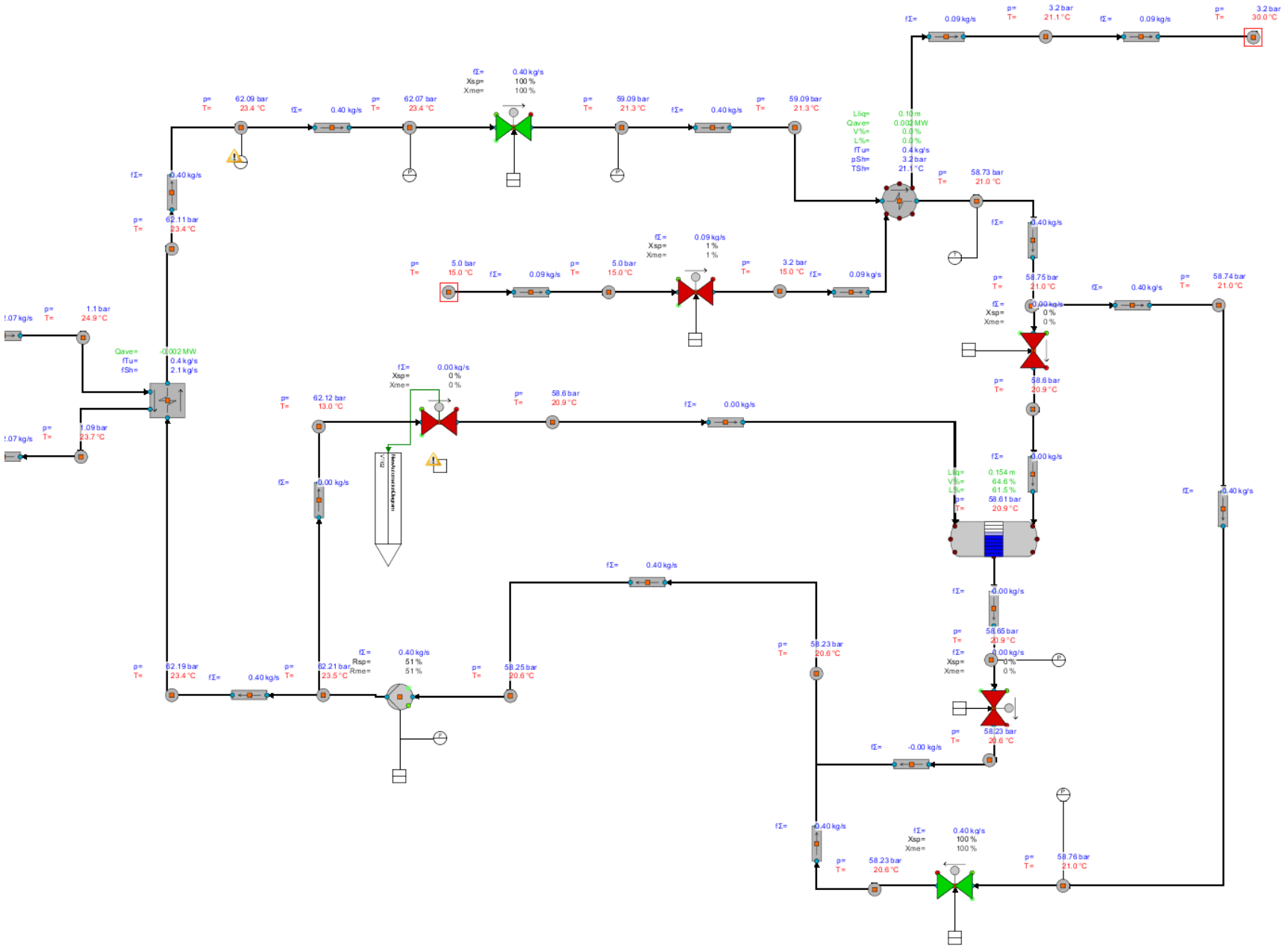

Figure 13: Dynamic model of the sCO_2 test rig in Apros

DOI: 10.17185/duepublico/46099

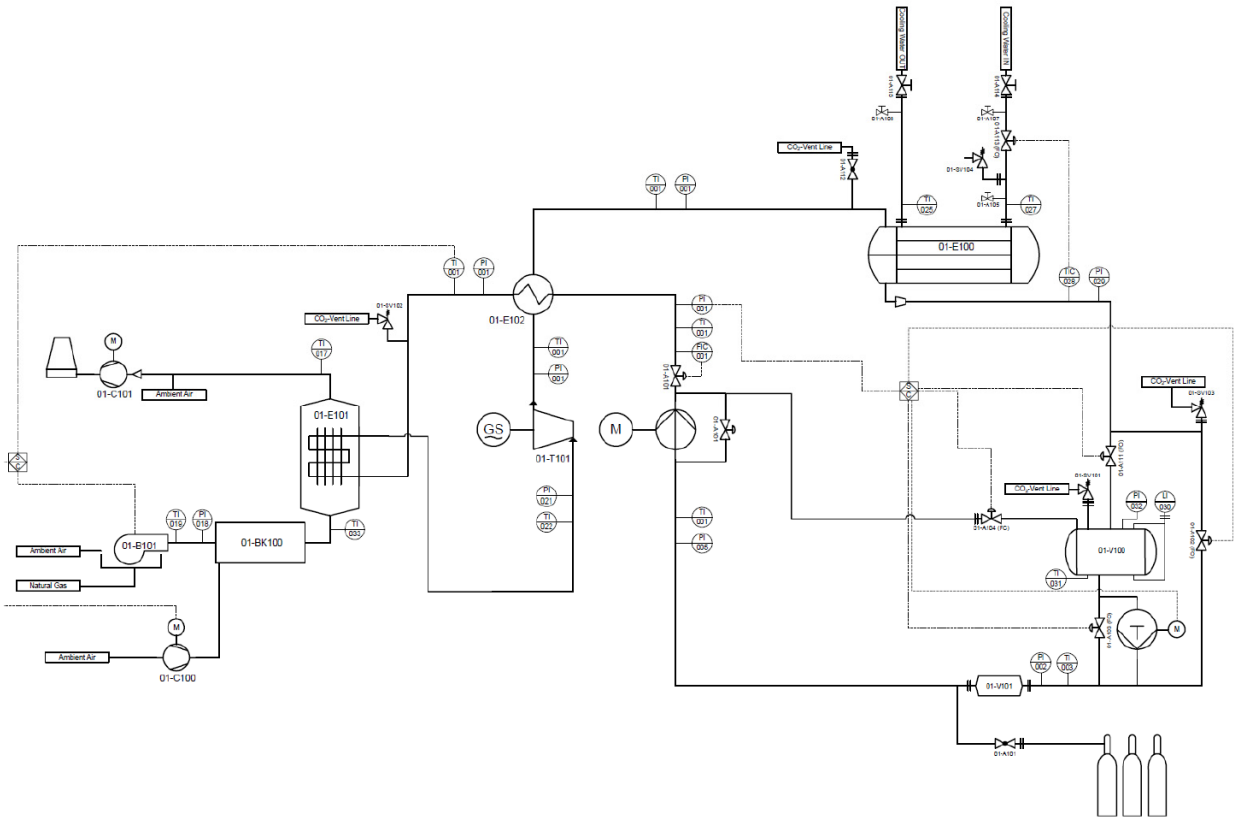

Figure 14: PFD for Phase 2

DOI: 10.17185/duepublico/46099

2nd European Supercritical CO2 Conference
August 30-31, 2018, Essen, Germany

2018-sCO2.eu-111

EFFECTS OF COLD TEMPERATURE AND MAIN COMPRESSOR INTERCOOLING ON RECUPERATOR AND RECOMPRESSION CYCLE PERFORMANCE

Nathan T. Weiland*
National Energy Technology Laboratory
Pittsburgh, PA, U.S.A.
Email: Nathan.weiland@netl.doe.gov

Charles W. White
KeyLogic
Fairfax, VA, U.S.A.

Andrew C. O'Connell
KeyLogic
Pittsburgh, PA, U.S.A.

ABSTRACT

The performance of supercritical CO_2 (sCO_2) power cycles in general can be improved by reducing the cold sCO_2 temperature in order to increase the sCO_2 density at the inlet to the compressor. This reduces the specific power required for compression and increases the net power and thermal efficiency of the sCO_2 cycle. For similar reasons, the addition of main compressor intercooling typically improves the specific power of a recompression cycle, reducing the sCO_2 mass flow, and thus the required cycle size and cost, for a given power output. The effects of intercooling on cycle efficiency are more complex and require consideration of temperature distributions along the recuperator train.

The present study investigates the effects of cold sCO_2 temperatures, compressor inlet pressures, and number of main compressor intercooling stages, on the efficiency and specific power of recompression Brayton cycles. In particular, it is shown that the addition of main compressor intercooling typically leads to an internal temperature pinch point within the low temperature recuperator. Cycle operation strategies for handling this internal pinch point are discussed, and apply to recompression cycles for all applications, as well as other split-flow cycle types, including partial cooling cycles. Further, internal pinch points and their remediation strategies are also considered for the main CO_2 cooler, as well as for the flue gas heat exchanger, as may be employed in economized recompression cycles for fossil energy applications and cascade-style cycles for waste heat recovery applications. Upfront consideration of these remediation strategies is essential in order to determine attainable cycle operating conditions and component sizing requirements for the sCO_2 cycle.

INTRODUCTION

Much work has been completed in recent years on closed sCO_2 power cycles for a variety of applications, including nuclear, concentrated solar, and fossil-fueled power generation. In most of these studies, the supercritical CO_2 recompression Brayton cycle (sRBC) is employed due to its inherently high efficiency, resulting from both an effective thermal recuperation scheme, and a high average temperature of heat addition at the primary heater. This leads to cycle and plant efficiencies that are typically higher than steam Rankine cycles at comparable operating conditions, as well as the possibility of smaller turbomachinery due to the high overall pressure and low pressure ratio relative to steam cycles.

Figure 1 shows a simplified diagram of the sCO_2 recompression Brayton power cycle. In this diagram, heat enters the cycle from a generic heat source through a primary heat exchanger (PHX) and is delivered to the turbine (T). The partially expanded sCO_2 then cools as it heats the cold high-pressure CO_2 in the high temperature recuperator (HTR) and low temperature recuperator (LTR). On exiting the LTR a portion of the cooled expanded CO_2 is diverted to the recycle compressor (RC) before joining the high-pressure CO_2 exiting the hot end of the LTR and then entering the cold end of the HTR. The non-bypass portion of the cooled CO_2 exiting the hot side of the LTR is then cooled in the primary CO_2 cooler and compressed in the main compressor (MC) before entering the cold end of the LTR. The high-pressure CO_2 is heated in the LTR and HTR before entering the PHX, completing the cycle.

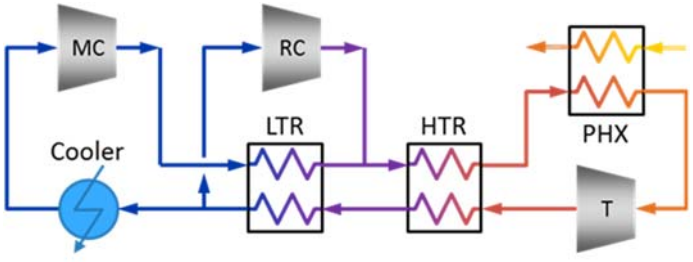

Figure 1: Recompression sCO_2 power cycle

DOI: 10.17185/duepublico/46085

Background

As with any power cycle, the efficiency of the cycle can be increased by either increasing the hot source temperature or decreasing the cold source temperature. A significant feature of these power cycles is their operation in the vicinity of the CO_2 critical point (31 °C, 7.37 MPa) at the cold side of the cycle. For the sRBC, the benefits of reducing the cold sCO_2 temperature are particularly advantageous. Typically, the sRBC efficiency is maximized when the CO_2 entering the main compressor is at or just above its saturation pressure, as shown below. In this regime, lowering the CO_2 temperature increases its density and reduces the specific power required for compression.

Lowering the cooler CO_2 temperature has two additional benefits for the sRBC performance. It allows for an increase in the LTR effectiveness and it makes low temperature heat recovery from process sources or the low temperature region of the heat source a more attractive option. Both of these effects can improve the efficiency of a power plant based on the sRBC: the former by directly increasing the power cycle efficiency and the latter by increasing the quantity of heat harvested by the cycle.

For similar reasons, the addition of main compressor intercooling typically improves the specific power of a recompression cycle, reducing the sCO_2 mass flow, and thus the required cycle size and cost, for a given power output. [1] However, the effects of intercooling on cycle efficiency are more complex and require consideration of temperature distributions along the recuperator train.

Several studies have explored the benefits of reducing the sCO_2 temperature at the cooler. An early study by Wright et al. [2] projected a 4-5 percentage point increase in plant efficiency for a nuclear light water reactor with an sCO_2 power cycle, by moving to condensing cycle operation. An experimental portion of this study proved the feasibility of this concept by demonstrating condensed CO_2 operation of a radial compressor and gas cooler that were designed for gas phase operation near the CO_2 critical point. A later study on sCO_2 power cycles for air-cooled sodium fast reactor nuclear applications shows improvement in cycle performance as the compressor inlet temperature is decreased, as well as variability in performance with compressor inlet pressure. [3]. Similar studies in the nuclear application space have shown that an optimal compressor inlet pressure exists for maximizing efficiency as the compressor inlet temperature is varied. This optimal pressure is typically at [4] or slightly above the pseudo-critical pressure for CO_2 [5].

A recent NETL report examined the cost and performance of a baseline coal-fired oxy-CFB power plant with carbon capture, incorporating the sRBC [1]. The results showed that the CO_2 plant offered a significantly higher efficiency and lower COE than a plant employing a Rankine cycles at operating conditions similar to the sCO_2 plant. The results also showed that a single stage of intercooling for the main compressor offered both higher overall plant efficiency (0.4 – 0.6 percentage points) and a lower cost of electricity (COE, 2.2–3.5 $/MWh) compared to the baseline configuration. More significant improvements in efficiency (0.6 – 1.6 percentage points) are reported in cases where the pressure ratio between intercooled main compressor stages is optimized [6].

Study Objectives

The present study investigates the effects of cold sCO_2 temperatures, compressor inlet pressures, and number of main compressor intercooling stages on the efficiency and specific power of indirect sCO_2 power cycles. In cases where colder sCO_2 temperatures or main compressor intercooling cause temperature pinch point problems in the heat exchangers, options for resolution of these issues are explored, as well as their impact on efficiency and other cycle parameters.

This study is novel in its approach to resolution of internal temperature pinch points in the LTR, which are shown to result from main compressor intercooling. Further, the effect of cold sCO_2 temperature on heat exchanger performance, plant efficiency and specific power is included in this study for both condensing and non-condensing CO_2 cycle operation.

The recompression Brayton cycle is studied in this work, although portions of the analysis apply to partial cooling and cascade cycles as well. Thus the work is relevant to a wide variety of sCO_2 power applications, including nuclear, concentrated solar, fossil, and waste heat sources.

METHODOLOGY

Modeling Approach

The thermodynamic performance of the plant concepts described in this paper are based primarily on the output from a steady-state system model developed using Aspen Plus® (Aspen). The individual unit operations models are the same as those used in the NETL oxy-coal indirect sCO_2 cycle study [1], which included a circulating fluidized bed (CFB) boiler and carbon capture enabled by oxycombustion. Details on the design basis, assumed feed compositions, and state point tables can be found in the NETL oxy-CFB indirect sCO_2 cycle study [1]. This study includes component capital cost estimations, total plant cost calculations, and cost of electricity analyses [1], although these are not considered in this work.

For the boiler and flue gas components of the process, the Aspen Physical Property Method PENG-ROB was used, which is based on the Peng-Robinson equation of state (EOS) with the standard alpha function [7]. This is consistent with the property methods used in other NETL systems studies of power plants with CFB or pulverized coal combustion heat sources.

Accurate modeling of sCO_2 power cycles requires high accuracy in determining the physical properties of CO_2, particularly near its critical point of 31 °C and 7.37 MPa. The Span-Wagner EOS [8] is the most accurate property method available for processes consisting of pure CO_2. Nevertheless, the greatest uncertainty in calculated properties using the Span-Wagner EOS occurs in the region of the critical point [9].

The Span-Wagner EOS is incorporated into the REFPROP (Reference Fluid Thermodynamic and Transport Properties Database) physical property method developed by the National Institute of Standards and Technology (NIST) and is

DOI: 10.17185/duepublico/46085

implemented in Aspen as the Physical Property Method REFPROP [10]. This method was used for all physical property estimates within the sCO_2 power cycle. The power cycle working fluid was assumed to be pure CO_2. Leakage and make-up flows were not modeled.

Modeling of the partial cooling cycle, investigation of solutions to LTR internal pinch points, and other cycle analyses were examined using the REFPROP add-in for Excel [10], which allows for the rapid development of simple cycle models and parametric sensitivity analyses. Analyses using this modeling tool investigate a simple sRBC cycle similar to that of Figure 1, with modifications to include main compressor intercooling and one stage of reheat, but with turbine inlet conditions identical to the more detailed Aspen model. Recuperator temperature profiles are determined in this model by dividing the recuperator into 20 segments of equal heat duty and pressure drop on each side of the recuperator and calculating the resulting sCO_2 temperatures via REFPROP.

Power Cycle: Design, Assumptions, and Operating Point

This study assumes a cycle design that includes a flue gas cooler in parallel with the LTR for the purpose of transferring additional thermal energy from the low quality combustion flue gas to the sCO_2 cycle, as shown in Figure 2. This Figure shows that additional process heat is also recovered from the flue gas in the oxidant preheater and in a nitrogen heater used to regenerate the air separation unit pre-purifier adsorbent. [1] These last integrations aside, this study's analysis of the flue gas cooler is also applicable to the waste heat recovery sCO_2 application, which typically seeks to maximize heat extraction from a low-quality gas turbine exhaust or other combustion flue gas source.

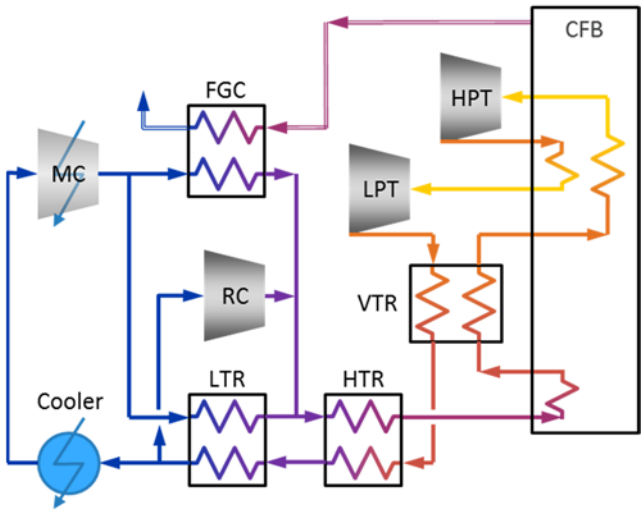

Figure 2: BFD for power cycle used in oxy-CFB power plant

Compared to Figure 1, Figure 2 shows the complete cycle heat integration scheme, a 2-stage turbine with reheat, an intercooled main CO_2 compressor, and a third recuperator stage (VTR) that supplements the HTR by exchanging heat from the relatively high-temperature low pressure turbine (LPT) exhaust with the effluent from an economizer within the CFB. A more detailed process flow diagram depicting all of the major plant components as well as a state point table is provided in Reference [1]. As the present work is primarily focused on process sensitivities around the low temperature components of the cycle, the presence or operation of these other cycle components affects the study results only in that they establish a baseline plant efficiency against which these sensitivities are compared.

In modeling the sCO_2 cycle, the exit temperatures in the recuperators are determined using design specifications within the Aspen model that target a minimum temperature approach at one or both ends of the recuperator of 5.6 °C (10 °F). Similar design specifications are applied to the flue gas and CO_2 coolers.

Second law validation of the heat integration scheme is accomplished from a pinch analysis performed on each heat exchanger in the process. This is done by using multi-stream heat exchanger blocks in Aspen model to represent the heat exchangers and performing granular zone analyses to generate temperature-heat duty (T-Q) and temperature approach-heat duty (ΔT-Q) diagrams for each exchanger.

As a default, the main CO_2 compressor has a single stage of intercooling, although the Aspen model allows a greater number of intercooling stages so that the optimal number of intercooling stages can be determined. In all cases where main compressor intercooling is used, the intercooler outlet temperature is set equal to the main CO_2 cooler outlet temperature, T_{cooler}, and the intercooler pressure drop was set to 0.014 MPa (2 psid). The isentropic efficiencies for each compression stage were equal and the pressure ratios for each compression stage were approximately equal. No attempts were made to optimize the stage pressure ratios in this work, though this may result in additional cycle efficiency gains. [6]

The PHX for the cycle comprises the upper heaters within the CFB in Figure 2, with each heating the high-pressure sCO_2 stream to the turbine inlet temperature of 760 °C. In addition to the economizer in the CFB between the HTR and VTR, a flue gas cooler (FGC) is arranged in parallel to the LTR to recover additional heat from the flue gas, as shown in Figure 2.

Table 1 lists the major assumptions and specifications applied to the sRBC.

Table 1: sCO_2 Brayton cycle parameters

Parameter	Value
Turbine inlet temperature (°C)	760
Compressor outlet pressure (MPa)	34.6
Intercooler pressure drop (MPa)	0.014
Turbine exit pressure (MPa)	7.9
Nominal compressor pressure ratio	3.8
Turbine isentropic efficiency	0.927
Compressor isentropic efficiency	0.85
Cycle pressure drop (MPa)	0.41
Minimum temperature approach (°C)	5.6

In addition to the cycle parameters shown in Table 1, several design variables were adjusted in sensitivity analyses to

DOI: 10.17185/duepublico/46085

thoroughly explore their impact on cycle performance and feasible heat integration. The most important of these was the cooler CO_2 exit temperature, $T_{cooler,}$ investigated for values of 20, 25, 30, 35, and 40°C. Note that the results for a CO_2 cooler exit temperature of 30 °C will be the least accurate due to the limitations of the Span-Wagner EOS near the CO_2 critical temperature of 31 °C. Additional sensitivity design variables were the number of intercooler stages and the intercooler pressure drop, which showed no significant difference in the plant performance when a single stage of intercooling was used.

RESULTS AND DISCUSSION

General Effects of Main Compressor Inlet Conditions

For each cooler CO_2 exit temperature, T_{cooler} examined, a sensitivity analysis was performed on the process (plant) efficiency as a function of the compressor inlet pressure (CIP). The results of these sensitivity analyses are shown in Figure 3.

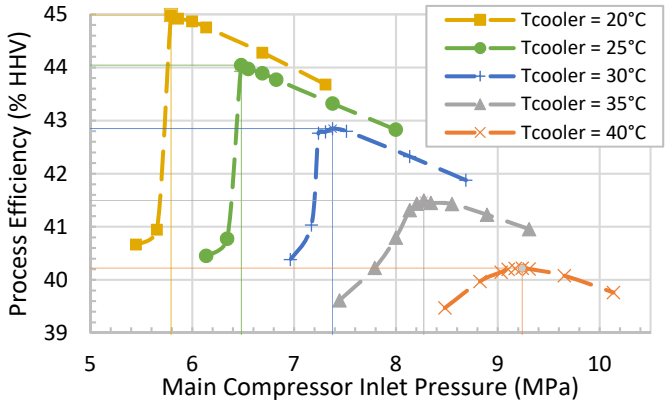

Figure 3: Process efficiency vs. main compressor inlet pressure with one intercooling stage

For each T_{cooler}, a maximum exists in the process efficiency at a particular CIP value. Note that for T_{cooler} below the critical temperature, the plant efficiency is particularly sensitive as the CIP falls below its optimal value. Therefore, in the Aspen model, the actual CIP used was 0.069 MPa greater than the calculated optimal CIP to avoid any convergence difficulties that could occur due to the high sensitivity of the process efficiency at compressor inlet pressures below the optimal value.

Figure 4 shows the points of maximum process efficiency (optimal CIP) as a function of T_{cooler}, as well as the CO_2 saturation line and pseudo-critical line. The optimal CIP for any T_{cooler} is shown to be slightly higher than the saturation pressure or pseudo-critical pressure, consistent with the results of Ref. [5].

A major benefit to reducing T_{cooler}, also the main compressor inlet temperature, is in the significant increase in cycle specific power, defined as the net cycle power output divided by the turbine mass flow. This is depicted in Figure 5 for the sRBC cycle with one main compressor intercooling stage and optimal CIP values per Figure 4. The reduction in T_{cooler} from 40 °C to 20 °C is shown to yield a 35% increase specific power, or viewed another way, a reduction in cycle mass flow by 26% for a fixed cycle power output, which should in turn reduce the capital cost of the sCO_2 power cycle.

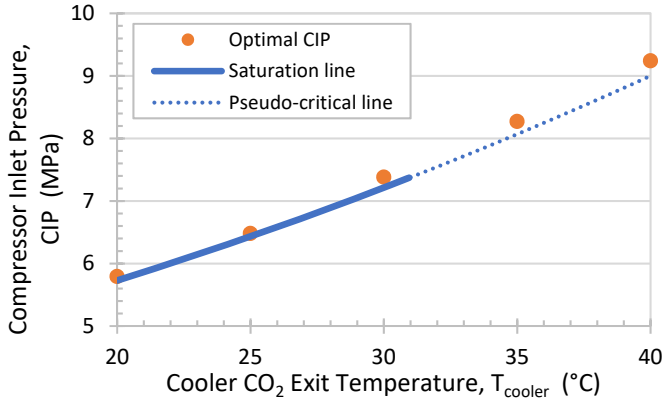

Figure 4: Optimal CIP versus cooler CO_2 exit temperature

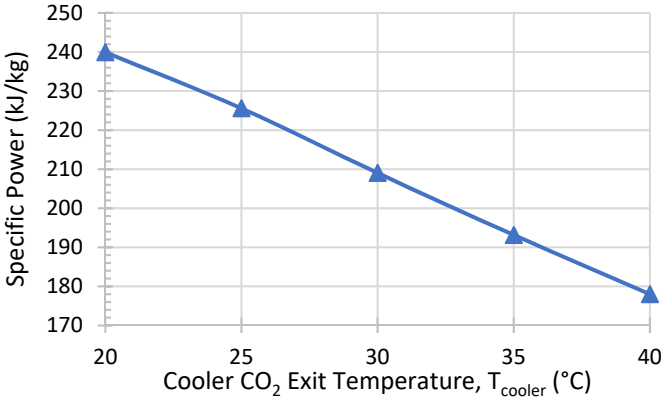

Figure 5: sRBC specific power vs. T_{cooler} for main compressor with one intercooler stage

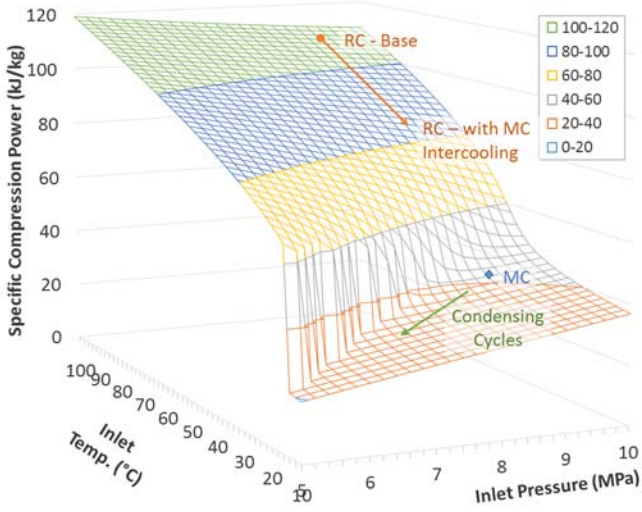

Figure 6: sCO_2 specific compression power for a constant pressure ratio of 4 and η_c = 85%. Compressor inlet conditions are marked for the T_{cooler} = 35 °C case.

DOI: 10.17185/duepublico/46085

The cause of this change is largely a result of reductions in compressor power requirements with increases in sCO_2 density at lower temperatures. This is illustrated in Figure 6, which shows specific compression power (power divided by flow rate) as a function of compressor inlet pressure and temperature. The results are shown for a constant pressure ratio compression process, which gives a sense for the auxiliary load of a recompression cycle with a comparable turbine pressure ratio. Specific compression power is shown to always decrease with compressor inlet temperature. More importantly, it is shown that one of the most significant effects of main compressor intercooling on sRBC performance is to reduce the recycle compressor inlet temperature and specific power consumption (in this case, by about 20%), assuming a constant LTR cold end approach temperature.

Identification of Anomalies in Low Temperature Heat Exchangers

While lowering the cold end CO_2 temperature offers multiple opportunities to increase cycle, and hence, plant efficiency, there are potential disadvantages as well. Low CO_2 temperatures generally require much lower temperature approaches and larger heat transfer areas and costs to attain a desired state point. In addition, low CO_2 temperatures impose limits on the feasible operating point for any given cooling technology. Finally, attaining low CO_2 temperatures on the high-pressure side may require many intercooling stages which may introduce an unacceptable pressure drop in the cycle.

Related to these disadvantages, a sufficiently low CO_2 cooling temperature will create condensation in the CO_2 cooler introducing an internal pinch point into this exchanger. A similar effect can be observed on the hot side of the flue gas cooler if the flue gas temperature falls below the dew point. This latter consideration constrains the maximum amount of heat that can be recovered in the flue gas cooler and diminishes the benefit of intercooling in the main CO_2 compressor.

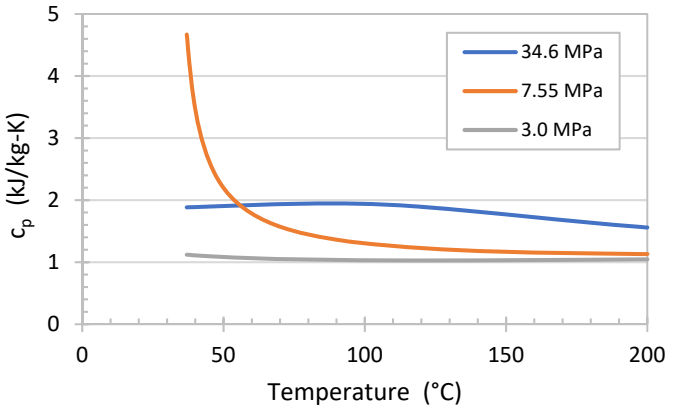

Figure 7: CO_2 constant pressure specific heat (c_p) versus temperature using REFPROP

A final consideration that is unique to sCO_2 power cycles is the rapid and non-linear variation in physical properties, particularly heat capacity (c_p), that occurs in the low temperature end of the cycle. Figure 7 shows the CO_2 c_p over the range of approximately 37 °C to 200 °C, at pressures of 3.0 MPa, 7.5 MPa and 34.6 MPa, typical pressures for the low-pressure side of a partial cooling sCO_2 cycle, low pressure side of a sRBC, and high-pressure side of either a sRBC or partial cooling sCO_2 cycle, respectively.

At the lowest temperatures shown in Figure 7, for the sRBC, the low pressure (hot side) c_p exceeds that for the high pressure (cold side) but this is reversed at temperatures above 56 °C. Further, the high-pressure side c_p has a maximum at a temperature of 88 °C while the low-pressure side shows a near singularity near the CO_2 critical temperature. These phenomena can lead to an internal pinch point and internal minimum temperature approach (below the target specification) in the LTR, even if the minimum temperature approach specification is satisfied at the ends of the LTR.

The use of the recompression configuration is itself an attempt to ameliorate one of the inherent weaknesses of the sCO_2 power cycle, namely that high recuperator effectiveness, which is needed to achieve the highest cycle efficiencies, is hampered by the large thermal capacitance of the cold end high pressure CO_2 compared to the cold end low pressure CO_2 in the cycle.

Note that the nonlinear c_p variation of CO_2 is significantly diminished for the low-pressure side of the partial cooling cycle. Nevertheless, as the temperature increases above 37 °C, the CO_2 c_p for the high-pressure and low-pressure sides diverge, then converge for temperatures above 93 °C. This can also lead to an internal pinch point in the LTR for this cycle, though the problem is generally not as severe as for recompression cycles.

Each of these potential disadvantages were found to impact one or more of the cold end heat exchangers at one or more sets of sensitivity variable values. The following sections describe the impacts to the low temperature flue gas cooler, LTR, and main CO_2 cooler.

Flue Gas Cooler

The flue gas exiting the oxy-CFB has a higher moisture content than would appear in the flue gas for a conventional pulverized coal combustor heat source or an air-fired CFB because a substantial portion of the flue gas is recycled. For the baseline power plant, the recycle fraction was 45% leading to a flue gas moisture content of 20.1% and a dew point temperature of 61.9 °C. Using T_{cooler} = 35 °C and a single main CO_2 compressor intercooler stage, also at 35 °C, the temperature of the CO_2 exiting the main CO_2 compressor is 52.8 °C. Under these conditions, it is infeasible to attain a 5.6 °C minimum temperature approach at the cold end of the low temperature flue gas cooler. Figure 8 shows the T-Q diagram for a flue gas cooler in which the minimum temperature approach specification of 5.6 °C is imposed on both ends of the heat exchanger. The solid lines correspond to the case where a single stage of intercooling is used while the dashed lines correspond to the case where intercooling is not used.

The internal pinch point and temperature cross are clearly evident with a single intercooler. A series of runs on the sensitivity variables showed that condensation occurred in the

DOI: 10.17185/duepublico/46085

low temperature economizer at all T_{cooler} between 20 °C and 40 °C if even a single stage of intercooling is used. If intercooling is not used, condensation in the exchanger did not occur until T_{cooler} fell below 25 °C.

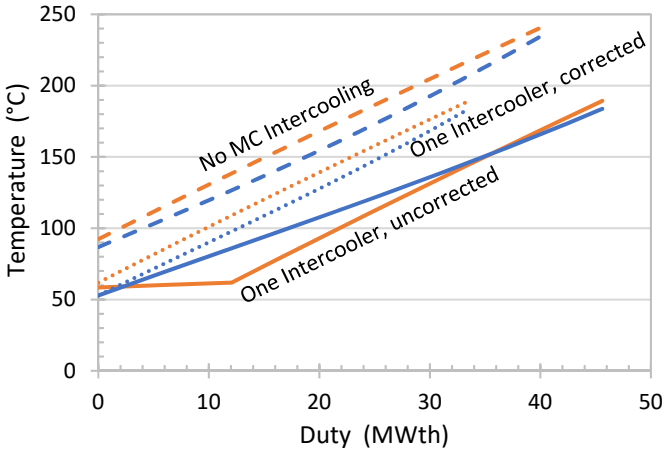

Figure 8: T-Q diagram for flue gas cooler at T_{cooler} = 35 °C. Flue gas on the hot side is in orange, while sCO_2 on the cold side is in blue.

To correct the internal temperature approach arising from condensation within the low temperature recuperator, the hot side (flue gas) exit temperature is limited to its dew point temperature (T_{dew}). This correction is plotted in Figure 8 as well, in which the mass flow rate of the cold sCO_2 is reduced to that required to bring the flue gas to its dew point, reducing the recoverable heat from this heat exchanger.

One alternative to this conservative approach would be to make process changes in the flue gas heat recovery train to remove moisture from the flue gas upstream of the recycle point. This would lower the moisture content of the flue gas and lower T_{dew} which would allow more heat to be recovered from the flue gas. A second alternative approach would allow the flue gas to partially condense up to the point where the minimum approach temperature was achieved.

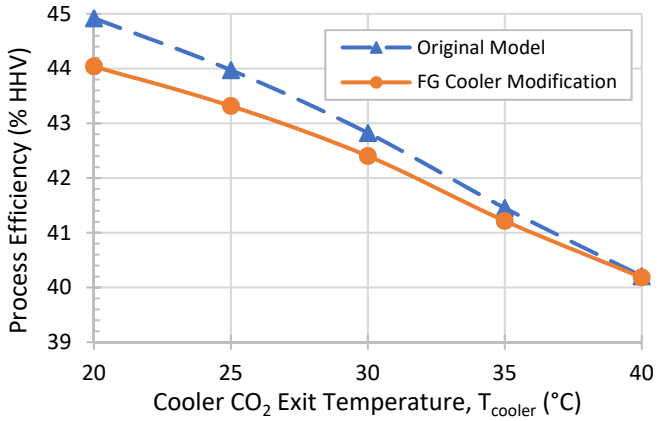

Figure 9: Process efficiency versus T_{cooler}

Figure 9 is a plot of process (plant) efficiency versus T_{cooler} for the baseline plant with one intercooling stage in the main CO_2 compressor. Results are shown for an uncorrected flue gas cooler design in which condensation is occurring and an internal minimum temperature approach exists. Results are also shown for the corrected flue gas cooler design in which the hot side temperature is always maintained at or above T_{dew}.

The results for the corrected flue gas cooler show the same qualitative trend as was observed in the original sensitivity analysis; i.e., the process efficiency increases monotonically with decreasing T_{cooler}. However, the absolute efficiency estimate for the corrected case is approximately 0-2% lower than for the original sensitivity analysis.

Figure 10 shows the sensitivity analysis of process efficiency to the number of intercooler stages in the main CO_2 compressor for T_{cooler} = 35 °C. The results show a similar qualitative behavior to those in Figure 9. The introduction of the design correction lowers the magnitude of the estimated process efficiency by 0-1%, but the qualitative trend in the sensitivity analysis is unaffected. There is a large increase in process efficiency with the introduction of one intercooler stage and a rapid drop-off in the efficiency increase as subsequent intercooler stages are used. Note that there is no impact on the overall efficiency from the flue gas cooler modification when main compressor intercooling is not used.

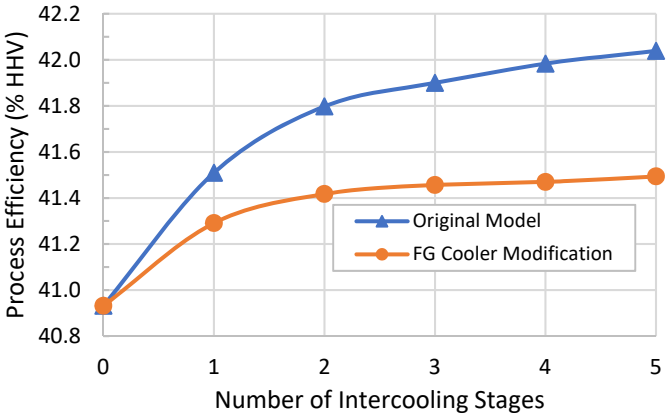

Figure 10: Process efficiency versus number of intercooler stages for T_{cooler} = 35 °C

Figure 11 shows the boiler efficiency (heat transferred to the cycle divided by fuel thermal input to the boiler/heat source) as a function of T_{cooler} when a single stage of main CO_2 compressor intercooling is used. Prior to the design modification to the flue gas cooler, the boiler efficiency increased monotonically with decreasing T_{cooler}, although this was the result of allowing ever larger amounts of water to condense in the flue gas cooler as the CO_2 high-pressure cold end temperature decreased. After the design modification to the flue gas cooler, the flue gas cold end temperature becomes fixed at the dew point temperature so the amount of heat that can be recovered from the flue gas cooler remains constant regardless of the cooler CO_2 exit temperature.

DOI: 10.17185/duepublico/46085

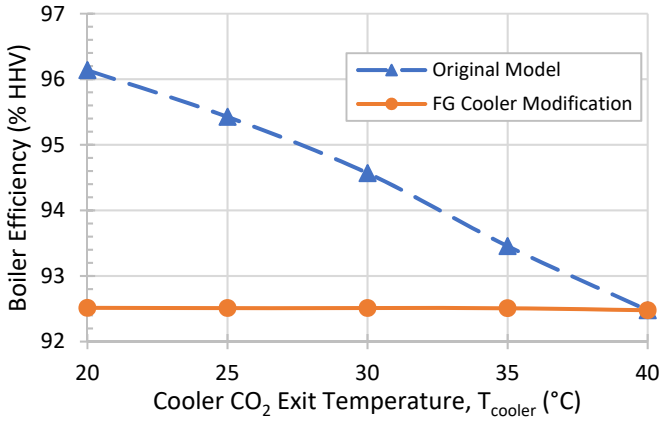

Figure 11: Boiler efficiency vs. T_{cooler}

A similar effect was noted in a sensitivity analysis of the boiler efficiency to the number of intercooling stages. After the flue gas cooler design modification, the cold end temperature was limited to the flue gas dew point temperature whenever intercooling was used, and hence the boiler efficiency remains constant regardless of the number of intercoolers used.

Low Temperature Recuperator

As noted above, the large and non-linear variations in c_p for CO_2 at the low temperature end of the cycle can limit the effectiveness of the LTR. The LTR pinch analysis was conducted for the full range of sensitivity variables and it was found that the addition of main compressor intercooling typically leads to an internal temperature pinch point within the LTR of recompression cycle. Figure 12 shows the LTR temperature profiles for T_{cooler} = 30 °C with a fixed approach temperature of 5.6 °C enforced at either end of the LTR, where the addition of a single stage of main compressor intercooling yields a very close approach temperature near its cold end.

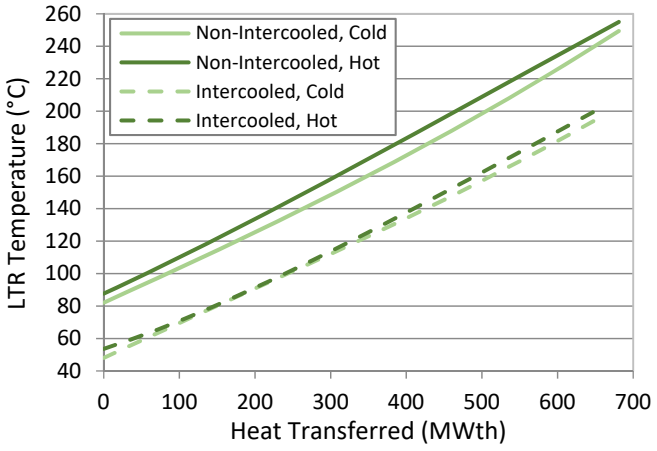

Figure 12: LTR temperature profiles for T_{cooler} = 30 °C as a function of main compressor intercooling

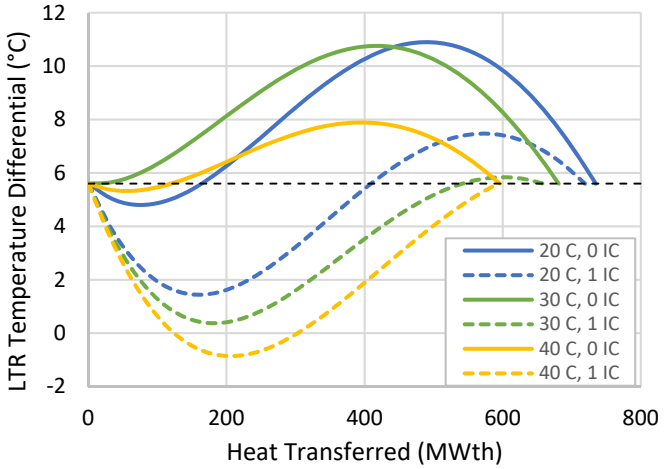

Figure 13: ΔT versus Q for LTR as a function of T_{cooler} and number of main compressor intercooler stages.

This is more readily seen in Figure 13, which plots the temperature difference, ΔT, between the hot and cold sides of the LTR, and also includes data for T_{cooler} values of 20 °C and 40 °C with and without intercooling. For fixed endpoint temperature approaches at 5.6 °C, the addition of intercooling results in very close internal temperature approaches, and even a temperature cross for the 40 °C case, within the LTR, with small internal temperature approaches also occurring without main compressor intercooling in some cases. Similar effects occur, but with a lower temperature differential, for main compressor intercooling in the partial cooling cycle.

Figure 14 shows the ΔT-Q diagram for the LTR for the baseline sRBC plant (T_{cooler} = 30 °C) under various temperature approach specification scenarios. The horizontal dashed line in Figure 14 denotes the target temperature approach of 5.6 °C.

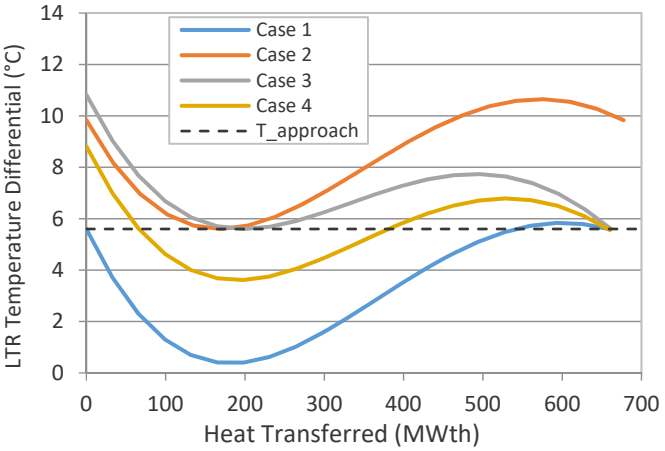

Figure 14: ΔT versus Q for LTR with T_{cooler} = 30 °C

The Case 1 scenario corresponds to the problematic temperature approach specification applied at both the hot and cold ends of the LTR, as shown in Figures 12 and 13, which yields a minimum temperature approach of approximately 0.4 °C

DOI: 10.17185/duepublico/46085

internal to the LTR at the point where approximately 200 MWth of heat has been exchanged. While this scenario leads to the highest cycle efficiency, it clearly violates the intent of the minimum temperature approach specification and is likely infeasible.

For the Case 2 scenario, both the hot end and cold end temperature approaches were increased until the internal temperature approach attained the target minimum of 5.6 °C. This was the most conservative scenario leading to the lowest cycle efficiency.

In the Case 3 scenario, the hot end temperature approach was set to the target value and the cold end temperature approach was adjusted until the internal minimum temperature approach reached the target value. This scenario yielded the maximum cycle efficiency while maintaining the minimum temperature approach specification throughout the exchanger. This is accomplished by increasing the bypass fraction, thereby reducing the cold side sCO_2 flow through the LTR and hence its thermal duty, effectively increasing the hot side exit temperature to increase the cold side ΔT. Note that fixing the LTR's hot end approach temperature, rather than the cold end, decreases the overall temperature difference in the HTR, thus increasing its effectiveness and the overall cycle efficiency. The higher LTR hot end approach temperature for Case 2 is a significant reason for the reduced performance relative to Case 3.

An alternative and less conservative approach is depicted in the Case 4 scenario in which the hot end temperature approach was set to the target value and the cold end temperature approach was adjusted until the average temperature approach throughout the LTR equaled the target value.

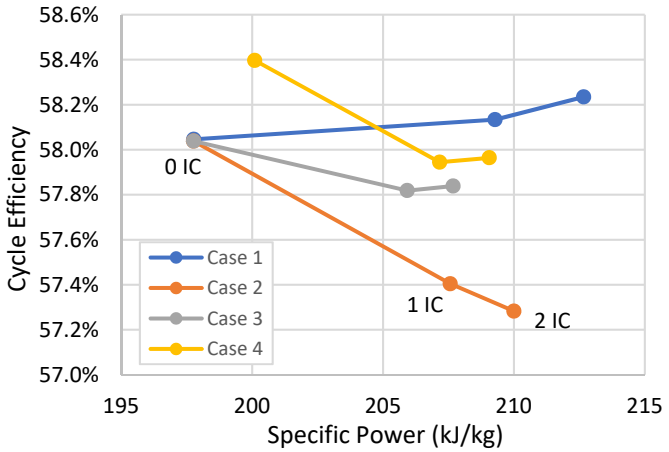

Figure 15: Cycle efficiency and specific power for each Case at T_{cooler} = 30 °C, with number of intercoolers increasing with specific power.

The effects of each LTR temperature approach design strategy on cycle efficiency and specific power is shown in Figure 15. While the Case 1 results show increased efficiency with main compressor intercooling, the internal temperature pinch renders this design infeasible. The remaining strategies generally result in slightly decreased cycle efficiency with main compressor intercooling, though specific power increases in all cases. The preferred strategy is for Case 3, where the minimum LTR temperature approach is strictly adhered to throughout the LTR, while maintaining a higher efficiency than the Case 2 strategy. For Case 3, the size and cost benefits of a 4% increase in specific power are expected to offset the slight reduction in efficiency, thus this design is chosen for most of the remaining analyses, with the expectation that some efficiency may be recovered once the stage pressure ratios are optimized [6].

The same sensitivity analyses as performed for the corrected flue gas cooler case were repeated for the corrected design specification for the LTR. Note that the heat exchanger design corrections were performed sequentially and hence the results for the corrected LTR case also include the correction to flue gas cooler design. Figure 16 shows the sensitivity analysis of process efficiency versus T_{cooler} for the case when one stage of main CO_2 compressor intercooling is used.

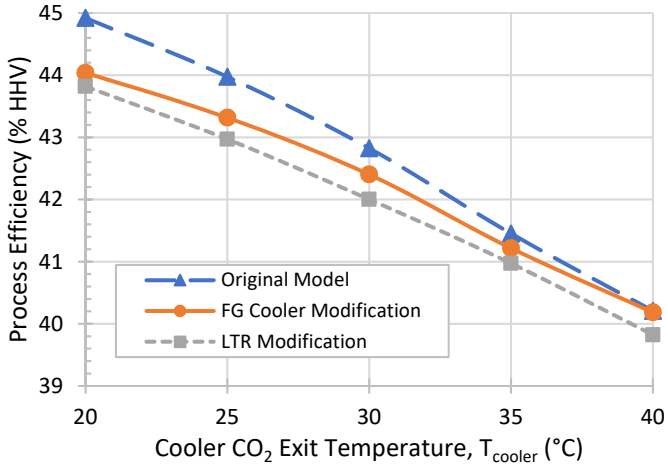

Figure 16: Process efficiency versus T_{cooler}

As with the correction to the low temperature economizer, the correction to the temperature approach specification for the LTR lowered the magnitude of the estimated process efficiency but did not change the qualitative trend of the sensitivity analysis. It appears that the impact of the LTR modification is somewhat less in magnitude than the efficiency change observed after the low temperature economizer modification.

Figure 17 shows the sensitivity analysis of process efficiency versus number of intercoolers at T_{cooler} = 30 °C. The results suggest that applying the design corrections to the low temperature and LTR renders the baseline plant process efficiency relatively insensitive to main CO_2 compressor intercooling.

DOI: 10.17185/duepublico/46085

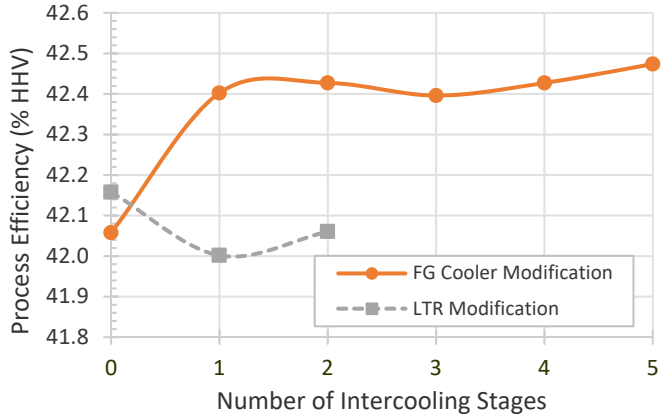

Figure 17: Process efficiency versus number of intercooler stages

Figure 18 shows the specific power as a function of the number of intercooler stages at T_{cooler} = 30 °C. The solid line shows the results after the flue gas cooler design modification and the dashed line shows the results after the flue gas cooler and LTR design modifications. The results show that the LTR modification lowers the absolute value of the specific power when intercooling is used but it does not alter the qualitative dependence of the specific power to the number of intercoolers. As the number of intercooling stages increases, the specific power rises monotonically. However, the most significant increase occurs with just a single stage of intercooling. The increase in specific power with intercooling suggests that intercooling will be economically advantageous as specific power is a surrogate for power cycle size and cost.

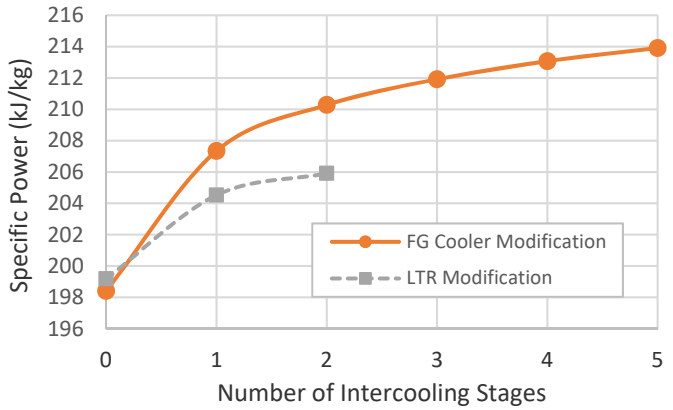

Figure 18: Specific power versus number of intercooler stages

Figure 19 shows the sensitivity analysis for specific power as a function of T_{cooler}. The blue dashed line corresponds to the original heat exchanger configuration, the orange solid line corresponds to the results after the flue gas cooler modification, and the gray dashed line corresponds to the results after the flue gas cooler and LTR design modifications.

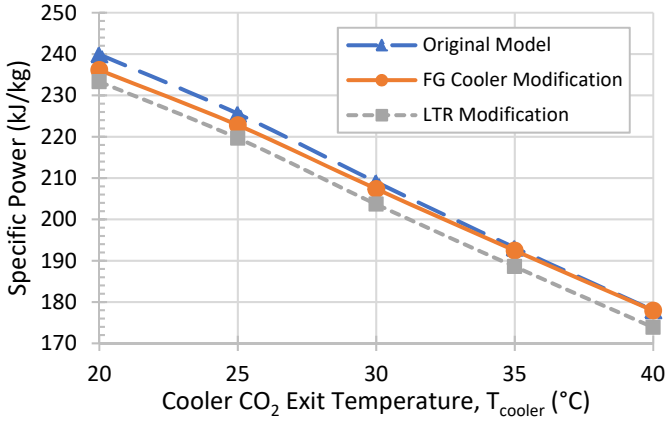

Figure 19: Specific power versus T_{cooler}

The results show that the specific power is strongly dependent on the cooler CO_2 exit temperature and increases monotonically as T_{cooler} decreases. Neither the flue gas cooler modification nor the LTR modification impacted this trend. The net impact of the flue gas cooler modification was to lower the specific power 0-2% while the LTR modification lowers the specific power an additional 1-2%.

Main CO_2 Cooler

This is a straightforward situation in which an internal pinch point can occur in an exchanger when phase change occurs on either the hot or cold side. For the sCO_2 power cycle, this issue is limited to condensing cycles where the cooler CO_2 exit temperature is below the CO_2 critical temperature.

Figure 20 shows the T-Q diagram for the CO_2 cooler in the baseline plant with T_{cooler} values of 25 °C and 20 °C. For both situations, the cooling medium is water with a temperature range from 15.6 °C to 26.7 °C. For T_{cooler} = 25 °C, the CO_2 cooler demonstrates an internal pinch point at the point where the CO_2 begins to condense. The minimum internal temperature approach is 3.7 °C. For T_{cooler} = 20 °C, this shows that the proposed heat exchanger configuration is infeasible due to a temperature crossover.

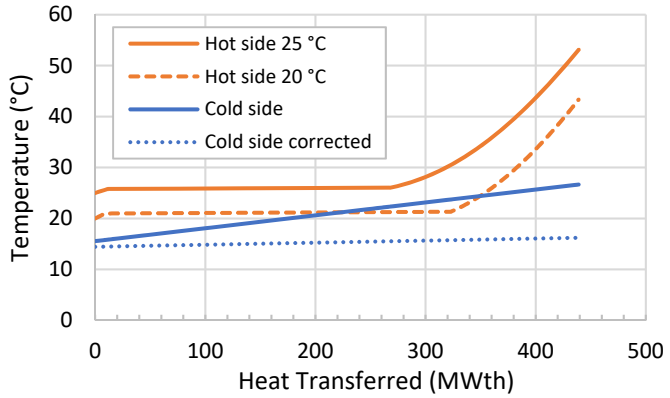

Figure 20: T-Q diagram for the CO_2 cooler, T_{cooler} = 25 °C & 20 °C

DOI: 10.17185/duepublico/46085

A number of strategies exist for addressing an internal minimum temperature approach or potential temperature cross in the CO_2 cooler. One approach would be to reduce the cooling water temperature range by increasing the cooling water flow rate. Another approach would be to reduce the cooling water inlet temperature by altering the cooling tower design. Finally, the target minimum approach temperature in the cooler could be lowered.

The blue dotted line in Figure 20 corresponds to a corrected cooling water configuration that is feasible for the T_{cooler} = 20 °C case. The cooling water inlet temperature was lowered from 15.6 °C to 14.4 °C by lowering the air-water temperature approach in the cooling tower from 4.7 °C to 3.6 °C. This raised the cold end temperature approach to the target value of 5.6 °C. To attain a minimum internal temperature approach or 5.6 °C, the cooling water temperature range was lowered from 11.1 °C to 1.8 °C. While this resulted in a thermodynamically feasible solution, the corrections increased the circulating water flow rate, circulating pump power requirement, and cooling tower fan power requirement by a factor 6. Future work under this study will identify the approach that leads to the lowest COE.

CONCLUSIONS & FUTURE WORK

This study highlights the importance of reducing or minimizing the cold sCO_2 temperature in the recompression Brayton cycle, as a means to increase plant efficiency and specific power, which reduces sCO_2 cycle size and cost. The specific power can also be increased by intercooling the main compressor, though this is shown to cause internal temperature pinch problems in the low temperature recuperator. Several strategies for avoiding these problems are presented, and generally show that maintaining the LTR hot side approach temperature is essential for maintaining cycle performance, while the bypass flow fraction can be increased slightly to reduce or eliminate the internal temperature pinch.

In addition, the effect of flue gas condensation is considered in the flue gas cooler, which can either be in parallel with the LTR in a fossil-fueled recompression cycle, or serve as the primary heat exchanger in a waste heat recovery application. It is shown that main compressor intercooling also increases the likelihood of water condensing out of the flue gas in this heat exchanger, though this is dependent on the water content of the flue gas.

Finally, temperature pinch issues are considered for the CO_2 cooler for cases in which condensation of CO_2 occurs. Several strategies for addressing this problem are considered, but involve a more detailed consideration of the specific cooling system employed, the flow rates and approach temperatures used, and consideration of the overall size and cost of the cooling system.

Future work in this study will focus on performance and cost modeling for direct dry cooling of the sCO_2, indirect dry cooling via water or another heat exchange fluid, and wet cooling towers. These models will be used with existing cost and performance models for the plant, as well as the remediation strategies discussed in this study for handling internal temperature pinches in low temperature heat exchangers as cold sCO_2 temperatures are reduced, in order to optimize the plant's cost of electricity through optimization of the capacity and operation of each type of cooling system.

NOMENCLATURE

ASPEN	-	Aspen Plus
ASU	-	Air separation unit
CFB	-	Circulating fluidized bed
CIP	-	Compressor inlet pressure
CO_2	-	Carbon dioxide
COE	-	Cost of electricity
Compr	-	Compressor
corr	-	Corrected
c_p	-	Heat capacity
CPU	-	CO_2 purification unit
DOE	-	Department of Energy
EOS	-	Equation of state
FG	-	Flue gas
FGC	-	Flue gas cooler
HHV	-	Higher heating value
HPT	-	High pressure turbine
HTR	-	High temperature recuperator
IC	-	Intercooler
LPT	-	Low pressure turbine
LTR	-	Low temperature recuperator
MC	-	Main compressor
NETL	-	National Energy Technology Laboratory
NIST	-	National Institute of Standards and Technology
PENG-ROB	-	Peng-Robinson physical property method
PHX	-	Primary heat exchanger
Q	-	Heat duty
RC	-	Recompression (bypass) compressor, Recompression cycle
REFPROP	-	Reference Fluid Thermodynamic and Transport Properties Database
sCO_2	-	Supercritical carbon dioxide
sRBC	-	Supercritical CO_2 Recompression Brayton Cycle
T	-	Temperature, Turbine
Tapp	-	Temperature approach
T_{cooler}	-	Cooler CO_2 exit temperature
T_{dew}	-	Dew point temperature
TIT	-	Turbine inlet temperature
T-Q	-	Temperature-heat duty
VTR	-	Very high temperature recuperator
ΔT	-	Temperature difference between hot and cold sides within a heat exchanger
η_c	-	Compressor isentropic efficiency

DOI: 10.17185/duepublico/46085

ACKNOWLEDGEMENTS

The authors wish to thank Richard Dennis (NETL) for his support for this project. This work was completed under DOE NETL Contract Number DE-FE0004001. The authors also wish to thank Wally Shelton, Travis Shultz (NETL), Mark Woods, Eric Lewis (KeyLogic) and Dale Keairns (Deloitte Consulting, LLP) for their technical assistance and input.

REFERENCES

[1] National Energy Technology Laboratory (NETL), "Techno-economic Evaluation of Utility-Scale Power Plants Based on the Indirect sCO2 Brayton Cycle," DOE/NETL- 2017/1836, Pittsburgh, PA, September 2017.

[2] S. A. Wright, R. F. Radel, T. M. Conboy and G. E. Rochau, "Modeling and Experimental Results for Condensing Supercritical CO2 Power Cycles," Sandia National Laboratories, Albuquerque, 2011.

[3] T. M. Conboy, M. D. Carlson and G. E. Rochau, "Dry-Cooled Supercritical CO2 Power for Advanced Nuclear Reactors," *Journal of Engineering for Gas Turbines and Power,* vol. 137, pp. 012901-1, 2015.

[4] J. J. Sienicki, A. Moisseytsev and Q. Lv, "Dry Air Cooling and the sCO2 Brayton Cycle," in *Proceedings of the ASME Turbo Expo 2017*, Charlotte, NC, 2017.

[5] S. R. Pidaparti, P. J. Hruska, A. Moisseytsev, J. J. Sienicki and D. Ranjan, "Technical and Economic Feasibility of Dry Air Cooling for the Supercritical CO2 Brayton Cycle Using Existing Technology," in *The 5th International Symposium - Supercritical CO2 Power Cycles*, San Antonio, Texas, 2016.

[6] Y. Ma, M. Liu, J. Yan and J. Liu, "Thermodynamic study of main compression intercooling effects on supercritical CO2 recompression Brayton cycle," *Energy,* vol. 140, pp. 746-756, 2017.

[7] D.-Y. Peng and D. B. Robinson, "A New Two-Constant Equation-of-state," *Ind. Eng. Chem. Fundam.,* vol. 15, pp. 59-64, 1976.

[8] R. Span and W. Wagner, "A New Equation of State for Carbon Dioxide Covering the Fluid Region from the Triple-Point Temperature to 1100 K at Pressures up to 800 MPa," *J. Phys. Chem. Ref. Data,* vol. 25, no. 6, pp. 1509-1596, 1996.

[9] C. W. White and N. T. Weiland, "Evaluation of Property Methods for Modeling Direct-Supercritical CO2 Power Cycles," *J Eng Gas Turb Power,* pp. 140(1):011701-011701-9. doi:10.1115/1.4037665, GTP-17-1264 2018.

[10] E. W. Lemmon, M. L. Huber and M. O. McLinden, "NIST Standard Reference Database 23: Reference Fluid Thermodynamic and Transport Properties-REFPROP, Version 9.1, National Institute of Standards and Technology," National Institute of Standards and Technology, Gaithersburg, 2013.

[11] Q. Zhao, M. Mecheri, T. Neveux, R. Privat and J.-N. and Jaubert, "Thermodynamic Model Investigation for Supercritical CO2 Brayton Cycle for Coal-fired Power Plant Application," in *5th International Supercritical CO2 Power Cycles Symposium*, San Antonio, Texas, March 29-31, 2016.

DOI: 10.17185/duepublico/46085

2nd European supercritical CO2 Conference
August 30-31, 2018, Essen, Germany

2018-sCO2.eu-118

sCO_2 CLOSED BRAYTON CYCLE FOR COAL-FIRED POWER PLANT: AN ECONOMIC ANALYSIS OF A TECHNICAL OPTIMIZATION

Mounir MECHERI
EDF
Chatou, FRANCE
Email: mounir.mecheri@edf.fr

ABSTRACT & NOMENCLATURE

The analysis of supercritical CO_2 Brayton cycle architectures has been performed by many scientific researchers over the years. These studied cycle architectures have advantages and drawbacks that depend on the context (application field, maximum and minimum parameter values, available heat…). In 2016, a preliminary study based on a sensitivity analysis of a supercritical CO_2 for coal-fired power plant has been performed to assess the impact of the cycle configurations on its performance. This publication was dealing with several ways to improve the sCO_2 Brayton cycle performances by using convenient cycle layout for coal power plant applications. However, the study only focused on cycle performance improvements and did not take into account the economic aspects.

This paper intends to complete this previous technical analysis by comparing the economic results with the technical optimization results. The economic analysis is done by using the combination of literature and "internally built" cost correlations.

The present work is one of the studies that can further feed the "sCO_2-Flex" European Project that involves 10 European academic and industrial partners aiming at designing a highly flexible "25 MW electrical" sCO_2 Brayton cycle for coal-fired power plant.

Abbreviation	Meaning
CAPEX	CAPital EXpenditure
COP	Compressor Outlet Pressure
L (or H) TR	Low (or High) Temperature Recuperator
LCOE	Levelized Cost of Electricity
MPa	MegaPascal
MW	MegaWatt
OPEX	OPerational EXpenditure
PFD	Process Flow Diagram
sCO_2	supercricitcal carbon dioxide
TIT	Turbine Inlet Temperature
UA	Product of U coefficient (Heat transfer coefficient) and A (exchange surface) for heat exchangers

CONTEXT

The main conclusions concerning the previous technical sensitivity analysis [1] are the following: a recompression cycle is highly recommended because the secondary compressor "partial flow" stream enables significant efficiency gains (+4.5%pt compared to basic Brayton cycle layout without recompression stage). Furthermore, "double reheat" architecture offers interesting efficiency improvement at "moderate" turbine inlet temperature (about +1.5%pt at 620°C turbine inlet temperature). In this context, the proposed power cycle architecture in [1] offers good performances with realistic maximal temperature and similar capital investment expectations than for existing "water-steam" coal power plants. This cycle architecture is illustrated in Figure 1. The operating conditions of this cycle are details in Table 1.

Table 1: Parameters of suggested sCO_2 coal-fired power cycle [1]

Variable/parameter	Value(s)	Unit
Main compressor inlet temperature	32	°C
Main compressor inlet pressure	7.9	MPa
Main compressor outlet pressure	30	MPa
Turbine inlet temperature	620	°C
Pressure drop (every component)	0.1	MPa
LTR and HTR pinch	6	K
Air-gas heat exchanger pinch	30	K
Compressors isentropic efficiency	89	%
Turbine isentropic efficiency	93	%
Alternator/Motor electrical efficiency	99.6	%
Mechanical efficiency	98.5	%
Air preheating configuration	Case C	–
Number of recompression stages	1	–
Number of reheat stages	2	–

DOI: 10.17185/duepublico/46091

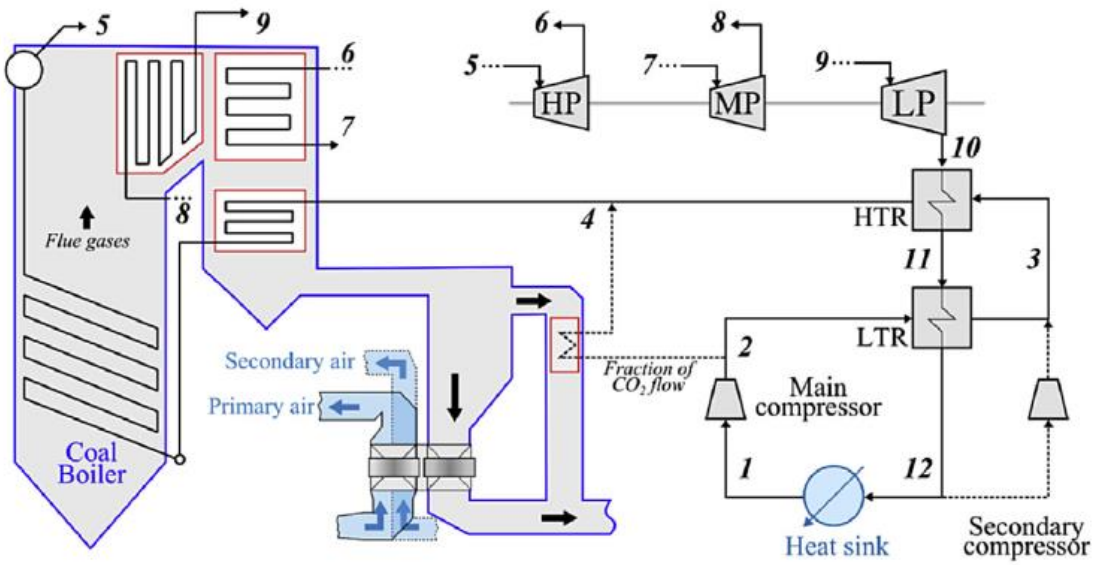

Figure 1: Process Flow Diagram (PFD) of suggested coal-fired power plant configuration in [1]

The pressure ratio of this cycle has been optimized to maximize the net cycle efficiency with a fixed maximum pressure of 30 MPa. Then, in this case, the cycle optimal minimum pressure is 7.9 MPa [1].

Improving the cycle performances logically leads to the maximization of the cycle temperature and pressure ratios. At fixed low temperature and pressure, it means that the cycle performance rise is related to the maximization of the cycle maximal temperature and pressure. However, increasing the cycle maximal temperature and pressure requires the use of specific high-grade and expensive materials to withstand corrosion and thermal stresses. Also, high performance cycles require very efficient recuperators in order to maximize the cycle heat integration. However, efficient recuperators have larger footprint and thus, are more expensive. In this context, the search for high performances is expected to have a large economic impact. The question is "how much does it cost to achieve higher efficiency"?

OBJECTIVES

This paper intends to complete the technical analysis done in 2016 [1] by achieving an economic evaluation of the proposed sCO_2 Brayton cycle architecture in order to observe if the technical conclusion matches with the economic conclusion. The economic analysis is done by using "equipment cost" correlations found in literature or internally built (see details in the methodology section below).

The present work is one of the studies that can further feed the future European Project "sCO_2 Flex". 10 European academic and industrial partners are involved is this project that aims at designing a highly flexible "25 MW net electrical" sCO_2 Brayton cycle for coal-fired power plants.

METHODOLOGY

The aim of this paper is to challenge the technical optimization results obtained in the study [1] by assessing the cost of the suggested sCO_2 Brayton cycle configurations in [1].

The work is divided in 4 parts:

1. Assessing the economic impact of the cycle configuration (number of reheat from 0 to 2).
2. Assessing the economic impact of the turbine inlet temperature (TIT) [600°C – 700°C – 800°C].
3. Assessing the economic impact of the recuperators' "pinch temperature" value (3K – 6K – 10K).
   (these first steps enable to find the best cycle configuration from the economic point of view).
4. Economic sensitivity analysis: observing the impact of a main component cost increment (+30%) and discount (-30%) on the total specific costs (see "Economic sensitivity analysis" description below).

Economic model

The cost analysis of this study does not intend to give accurate and absolute costs. The aim of the economic analysis is to compare the cost of different technical configurations. The economic evaluation method is based on the cost calculation of the main cycle components (boiler, turbomachineries, recuperators, coolers). As a first economic assessment, this study only focuses on the Capital Expenditure (CAPEX).

The CAPEX is composed of direct costs (purchased equipment, piping, electrical, civil work, transport, direct installation, auxiliary services, instrumentation and control, site preparation) and indirect costs (mainly engineering, supervision, start-up) [2; 3]. These direct and indirect costs can be expressed as a function of the "total component cost".

DOI: 10.17185/duepublico/46091

In this context, the CAPEX can be defined as in equations 1

$$\begin{aligned} CAPEX(\$) &= direct + indirect\ costs \quad and \quad indirect\ cost = x_1 \times direct\ costs \\ &= (1 + x_1) \times direct\ costs \quad and \quad direct\ costs = (1 + x_2) \times \sum component\ cost \\ &= (1 + x_1) \times (1 + x_2) \times \sum component\ cost \end{aligned} \tag{1}$$

where x_1 and x_2 are coefficients respectively fixed at 8% and 26% [2; 3], which means that the CAPEX can be expressed as a function of the total component cost as shown in equation 2.

$$CAPEX\ (\$) = 1.3608 \times \sum component\ cost\ (\$) \tag{2}$$

In this study, the component cost functions are assumed to be "power function" [4] with the global expression shown in equation 3

$$component\ cost(\$) = a \times (Parameter)^b \times f_p \times f_t \tag{3}$$

(where: "a" and "b" are empirical coefficients that depend on each considered components (turbomachinery, heat exchangers, boiler), "Parameter" represents characteristic variables i.e.: the heat duty for the boiler, the UA factor for heat exchangers (recuperators and coolers) and the electrical power for turbomachineries, f_p and f_t are pressure and temperature factors that simulate the rise of material cost with temperature and pressure.).

The f_p and f_t factors are defined as shown in equations 4

$$f_p = \begin{cases} 1 \ if\ P_{max} < 100\ bar \\ \alpha \times P_{max}\ (\text{in bar}) + \beta \end{cases} \quad and$$

$$f_T = \begin{cases} 1 \ if\ T_{max} < 400\ °C \\ \gamma \times T_{max}^2 (\text{in °C}) + \delta \times T_{max}\ (\text{in°C}) + \varepsilon \end{cases} \tag{4}$$

where α, β, γ, δ and ε are empirical parameters.

Also, the specific cost defined as the ratio of the "CAPEX" over the "net power electrical power output" is used as the criterion to find the best economic solution (equation 5).

$$specific\ cost\ (\$/kW_e) = CAPEX\ (\$)/Net\ electrical\ power\ output\ (kW_e) \tag{5}$$

This economic simplified model is used to complete the sensitivity analysis done within the study [1].

Assumptions

As for the study [1], the boiler design is assumed to be fixed for all analyzed cycle configurations in this paper. Also, CO_2 purity is assumed to be 100%. As a first simplification, the electricity consumption of auxiliaries is not considered.

CO_2 is assumed to be cooled by air (air inlet temperature of 20 °C) with a flow rate of about 13 000 m3/s. As said above, the auxiliary consumption is not taken into account in this study, as in [1].

Economic sensitivity analysis

An economic sensitivity analysis is done on one chosen sCO_2 Brayton cycle configuration. This analysis consists in modifying the cost of an equipment (first upward +30% and then downward -30%) to assess its impact on the total cycle specific costs (all other costs being fixed).

In this study, this cost increment (and reduction) is applied on the boiler, the turbomachinery and the recuperators' costs.

RESULTS

Impact of the cycle configuration (number of reheat from 0 to 2):

In the study [1], the sCO_2 Brayton cycle performance has been assessed regarding the number of reheat (from 0 to 2) for three different TIT (600/700/800°C) while the main compressor outlet pressure (COP) varies. In this paper, the economic model is applied on these cases, applying the same conditions/assumptions (see [1] for details).

Figure 2 illustrates both the net cycle efficiency (solid lines, left axis) and its corresponding specific cost (dashed lines, right axis) as a function of the main COP for 0, 1 and 2 reheats (for TIT of 600°C).

From the performance point of view, the logical conclusion is that, first, the efficiency rises with the number of reheat, and secondly, there is an optimal pressure ratio (for a given TIT) that depends on the number of reheat.

From the economic point of view, we can see that the best option depends on the COP and, contrarily to the technical results, is not linked to the highest number of reheat. This observation makes sense because 1) reheats involve higher averaged temperature in the turbines, 2) the maximum temperature in the High Temperature Recuperator (HTR) is also higher, 3) and the number of pipes that go from the boiler to the power block increase).

For low pressure ratio (COP from 20 to ~26 MPa), the "0 reheat" configuration has the lowest specific cost. Above a COP of 26 MPa, the "1 reheat" configuration offers the lowest specific cost.

DOI: 10.17185/duepublico/46091

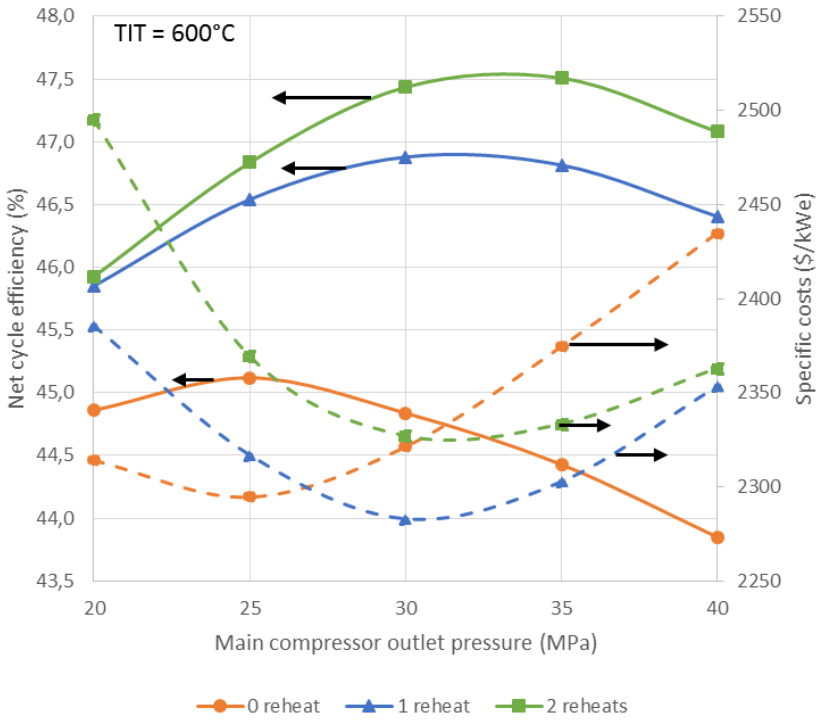

Figure 2: Net cycle efficiency (solid lines, left axis) and specific costs (dashed lines, right axis) as a function of the main compressor outlet pressure for TIT = 600°C for 0, 1 and 2 reheats

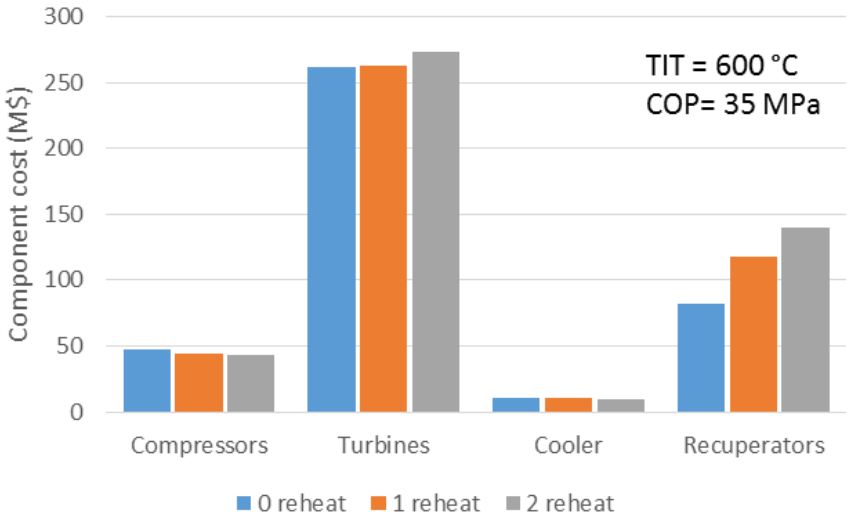

Figure 3: Component costs (except boiler) for TIT = 600°C and main compressor outlet pressure of 35 MPa for the three cycle configurations

Figure 3 shows the component cost breakdown for the 3 studied configurations (for TIT = 600°C and COP = 35 MPa). It can be observed that when the number of reheat rises:

- the cost of recuperators increases. This is due to higher temperature at the HTR hot side inlet and thus, higher exchange surfaces and more expensive materials.
- The cost of turbine rises. This is due to higher average CO2 temperature in the turbines.
- The costs of compressors and cooler decrease. Indeed, given that the boiler heat duty is fixed, the CO2 flow rate in the cycle decreases while the cycle efficiency increases (i.e. when the number of reheat rises). Lower CO2 flow rate

DOI: 10.17185/duepublico/46091

leads to lower "compressor power" consumption and lower "cooler duty".

When the TIT rises to 700°C, the specific cost increase with the number of reheat as depicted in Figure 4 below. Indeed, the COP where the specific cost of "0 reheat" and "1 reheat" configurations are crossing is above 40 MPa.

In the study [1], the sCO_2 Brayton cycle performance has been assessed regarding three TIT values (600°C – 700°C – 800°C) while the main COP varies. In this paper, the economic assessment is done in these same conditions.

From the economic point of view, it can be observed that the best option depends on the pressure ratio. But, contrarily to the "efficiency" best result, the "economic" best case is not related to the highest TIT. Indeed:

- for COP ≤ 26 MPa, it can be observed that the less expensive cycle is the "no reheat" configuration with a TIT of 600°C,
- for COP > 26 MPa, the "one reheat" configuration (TIT = 600°C) offers the best option.

The global lowest specific cost in the given conditions is observed for a "one reheat" cycle with TIT = 600°C and COP = 30 MPa.

Impact of the recuperators' pinch value:

In this section, the impact of the recuperator performance on the specific cost is analyzed. Indeed, performant heat exchangers with small pinch temperature are required to obtain efficient cycles but they have larger exchange surfaces and thus, larger volumes and material mass. In these conditions, the costs of a heat exchanger can drastically increase with its performance, especially while using high grade materials to prevent corrosion or thermal stresses.

In this section, three "pinch temperature" values are considered (respectively, 10, 6 and 3 K) for a "double reheat" cycle configuration and a 600°C TIT.

In these conditions, Figure 6 shows that the lowest specific cost can be obtained with "6K pinch" recuperators when the COP stays below ~22 MPa. For higher COP, the "10K pinch" case offers the lowest specific cost. Indeed, as explained above, performant heat exchangers are bigger and thus, they require more material to be built. As they are made of expensive materials, their cost are highly impacted by the chosen "pinch temperature" value. To conclude on the impact of the heat exchanger performance, a compromise must be found between high cycle performances and low specific costs, as for the TIT or the number of reheat.

It can also be observed on the Figure 6 that the "economic" optimal COP is different than the "technical" optimal COP for each case.

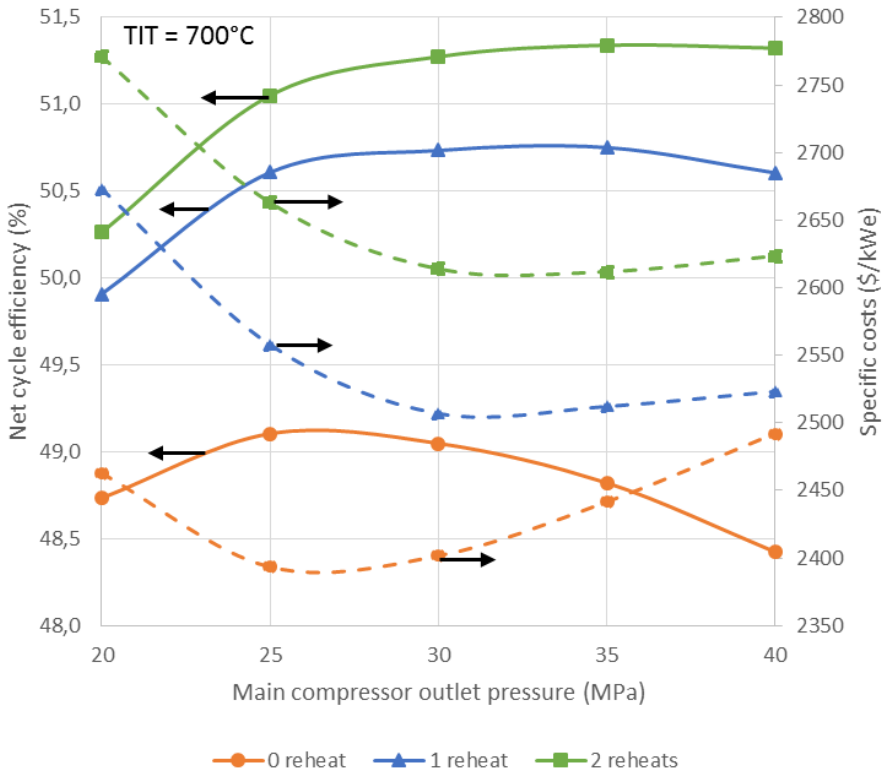

Figure 4: Net cycle efficiency (solid lines, left axis) and specific costs (dashed lines, right axis) as a function of the main compressor outlet pressure for TIT = 700°C for 0, 1 and 2 reheats

DOI: 10.17185/duepublico/46091

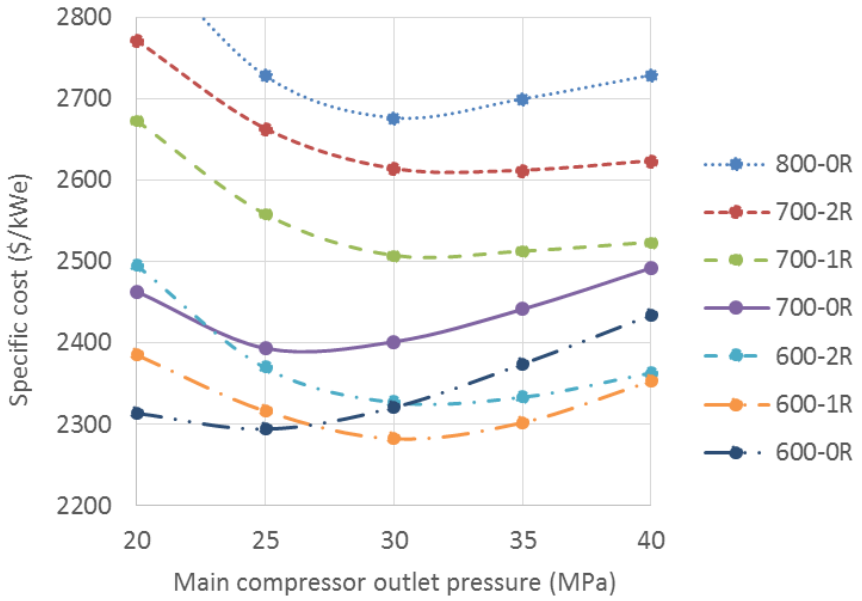

Figure 5: Specific costs (in $/kWe) as a function of the main compressor outlet pressure (in MPa) for several cycle configurations (legend: xxx-yR: "xxx" being the temperature in °C and "y" the number of reheat)

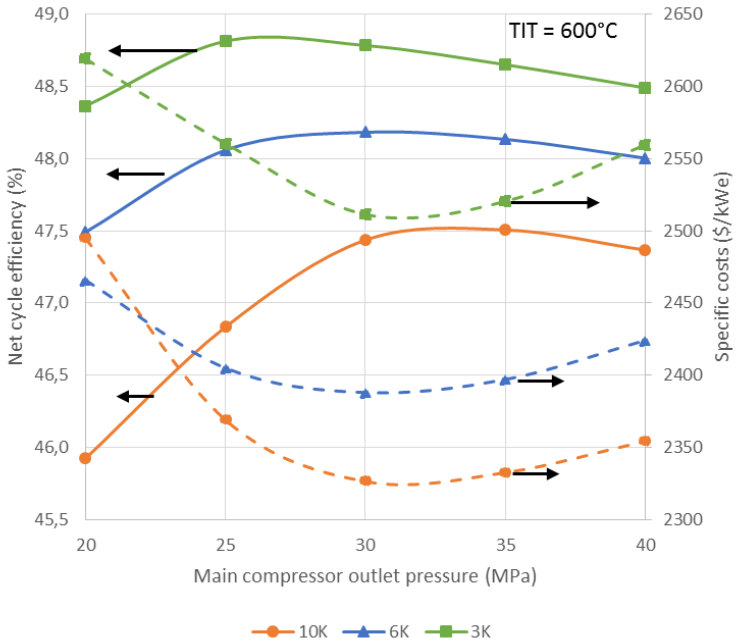

Figure 6: Net cycle efficiency (solid lines, left axis) and specific costs (dashed lines, right axis) as a function of the main compressor outlet pressure for TIT = 600°C for three "temperature pinch" values (10K, 6K and 3K)

DOI: 10.17185/duepublico/46091

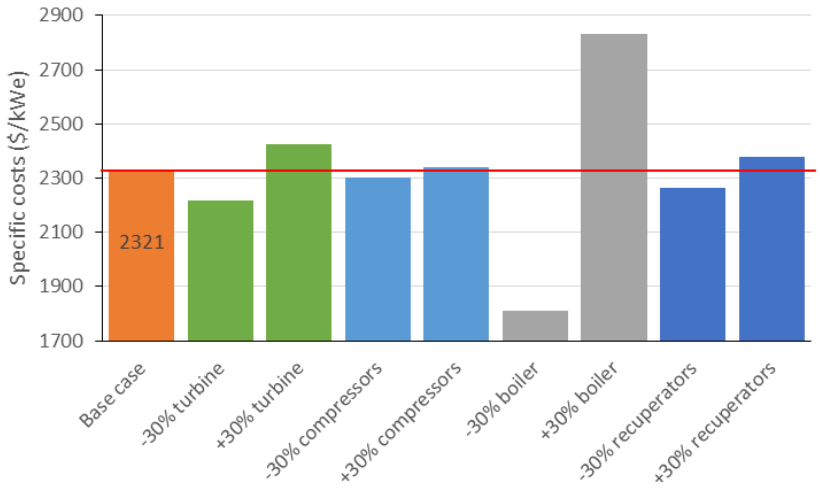

Figure 7: Specific costs variations as a function of main component cost increment (+30%) and discount (-30%) for a "no reheat cycle configuration, TIT = 600°C, COP = 30 MPa, recuperators pinch value=10K.

Economic sensitivity analysis:

The aim of this section is to assess the sensitivity of the economic model used in this study. To do so, a fixed configuration is chosen ("one reheat", TIT = 600°C, COP = 30 MPa, recuperators' pinch value = 10K) while the economic model is modified: a cost increment of +30% (and respectively a discount of -30%) is applied for each main component, one at a time.

Figure 7 shows the results of the "economic sensitivity analysis". Logically, the economic impact of the main components depends on their share in the global cost balance. Thus, these results show that the boiler cost modification has the biggest impact on the specific cost (all other parameters being fixed), followed by the turbine, the recuperators and the compressors. Then, it is more interesting to focus research and development effort to reduce costs of the boiler to maximize de cost reduction of such cycles.

CONCLUSION AND DISCUSSIONS

This paper deals with a preliminary economic analysis applied on a previous technical survey [1] that have been made to assess the sCO_2 Brayton cycle performance in a coal power plant with different cycle configurations. The cost analysis of this study does not intend to give accurate and absolute costs. This economic analysis enables to compare different technical cycle configurations. The economic evaluation method is based on the calculation of the main components' costs (boiler, turbomachineries, recuperators, coolers). As a first economic assessment, this study only focuses on the Capital Expenditure (CAPEX).

The technical results obtained in [1] led to the conclusion that the recommended cycle for such application is a "double reheat" cycle configuration with a 620°C turbine inlet temperature and using recuperators with a "6K temperature pinch" value. Indeed, looking for the best performances leads to maximize the turbine inlet temperature while reducing the heat exchanger "temperature pinch" value and pressure drops. However, these actions requires the use of expensive components.

The economic analysis shows that (within the studied framework and the given assumptions) the cycle configuration that offers the lowest specific cost (Capital expenditure over the net power production) is a "one reheat" configuration with a 600°C turbine inlet temperature. Also, the optimal cycle pressure ratio is different while considering the cycle efficiency or the specific cost. Finally, the sensitivity analysis show that the boiler is the critical component with the highest impact on the specific cost. Thus, cost reduction efforts must be focused on the boiler to have the highest impact on the global power plant specific cost.

PERSPECTIVES

As explained, this economic model only stands on the CAPEX and specific costs of the considered cycle configurations. Also, this model undergoes some limitations due to assumptions and hypotheses (this model has not been benchmarked on real cases because there are few available economic data of sCO_2 Brayton cycles or sCO_2 boilers). In this context, the economic model is still under construction and some perspectives can be expected to improve it as detailed in the following paragraph.

The simplified economic model used in this paper relies on the power plant CAPEX regarding its main components. Further work is then required to include the Operational Expenditure (OPEX) to then be able to calculate the Levelized Cost Of Electricity (LCOE) which is an appropriate criteria to compare different electricity production solutions. This perspective requires additional data concerning the boiler

DOI: 10.17185/duepublico/46091

(because OPEX includes costs such as combustible costs, salaries…) and about the power plant itself (number of hour of production at full load, availability factor…).

Secondly, further work is required to adapt the methodology for flexible power plant (part load conditions) given that performances and electricity production rate depend on the operating conditions.

ACKNOWLEDGEMENTS

This project has received funding from the European Union's Horizon 2020 research and innovation programme under grant agreement No 764690.

REFERENCES

[1] Mounir Mecheri and Yann Le Moullec, Supercritical CO_2 Brayton cycles for coal-fired power plants, Energy, Volume 103, 2016, Pages 758-771, ISSN 0360-5442 https://doi.org/10.1016/j.energy.2016.02.111

[2] Antonio C. Caputo, Mario Palumbo, Pacifico M. Pelagagge, Federica Scacchia, Economics of biomass energy utilization in combustion and gasification plants: effects of logistic variables, Biomass & Energy, 28, pp 35-51 http://dx.doi.org/10.1016/j.biombioe.2004.04.009

[3] SungHo Park, JoonYoung Kim, MunKyu Yoon, DongRyul Rhim, ChoongSub Yeom, Thermodynamic and economic investigation of coal-fired power plant combined with various supercritical CO_2 Brayton power cycle, Applied Thermal Engineering 130, pp 611-623, https://doi.org/10.1016/j.applthermaleng.2017.10.145

[4] Ravinder Kumar, Avdhesh Kr. Sharma, P. C. Tewari, Cost analysis of a coal-fired power plant using the NPV method, Journal of Industrial Engineering International, 11(4), 495-504. https://doi.org/10.1007/s40092-015-0116-8

DOI: 10.17185/duepublico/46091

2nd European supercritical CO2 Conference
August 30-31, 2018, Essen, Germany

2018-sCO2.eu-104

EXPERIMENTAL INVESTIGATION ON THE HEAT TRANSFER BETWEEN CONDENSING STEAM AND SCO2 IN A COMPACT HEAT EXCHANGER

Marcel Straetz*
University of Stuttgart
Stuttgart, Germany
marcel.straetz@ike.uni-stuttgart.de

Rainer Mertz
University of Stuttgart
Stuttgart, Germany
rainer.mertz@ike.uni-stuttgart.de

Joerg Starflinger
University of Stuttgart
Stuttgart, Germany
joerg.starflinger@ike.uni-stuttgart.de

ABSTRACT

In the frame of the "sCO2-HeRo" project (supercritical carbon-dioxide heat removal system) a self-launching and self-sustaining decay heat removal system for retrofitting into nuclear power plants is investigated. The system should be able to transfer the decay heat from the reactor core to the ultimate heat sink, e.g. the ambient air, in case of a station-blackout and loss-of-ultimate-heat-sink accident scenario. The system, in fact a Brayton cycle, consists of a compressor, a compact heat exchanger, a turbine, a sink heat exchanger and a generator. Since the turbine of the cycle produces more power than it is used in the compressor, the system is self-sustaining and excess electricity of the generator can be used e.g. for auxiliary devices in the power plant or for recharging batteries. Due to its convenient fluid properties near the critical point, for instance the heat capacity and the fluid density, supercritical carbon dioxide is used as working fluid.

Within the project a two-scale approach is applied. This means, that in the first part of the project a small-scale demonstrator unit of the sCO2-HeRo system is designed, manufactured and retrofitted into the pressurized water reactor glass model at Gesellschaft für Simulatorschulung (GfS), Essen. In the second part the received experimental results at the demonstrator will be used for validation of models e.g. for heat transfer and pressure drop. Afterwards, they will be transferred to component models on power plant size to be implemented into the thermal-hydraulic code ATHLET.

The Institute of Nuclear Technology and Energy Systems (IKE), University of Stuttgart, is responsible for the experimental investigation on the heat transfer between condensing steam and supercritical carbon-dioxide in the compact heat exchanger. Thereby, low pressure (glass model application) and high pressure (power plant application) investigations on the heat transfer between condensing steam and supercritical carbon-dioxide were carried out. This paper starts with an overview of the sCO2-HeRo system, retrofitted into a PWR, followed by a description of the investigated two-plate CHX test configuration. Afterwards, the test facility for the high pressure steam experiments is shown and the measurement parameter as well as the position of each measurement device is described. The analyzed experimental results, for example the sCO_2 pressure drop as a function of the sCO_2 mass flow rate, the heat transfer ratio between the steam side and the sCO_2 side or the surface temperature distribution on the sCO_2 side of the CHX, and the calculated measurement errors are discussed. Finally, the received results are summarized and a conclusion is given.

INTRODUCTION

In case of a station-blackout (SBO) and loss-of-ultimate-heat-sink (LUHS) accident scenario in a light water reactor, plant accident measures depend on the availability of external power. If this is not guaranteed, the core will be violated if no other cooling measures will be successful. Such scenarios lead to the development of self-launching, self-propelling and self-sustaining decay heat removal systems which are independent from external energy, but fulfilling the safety function transferring the decay heat from the reactor core to an ultimate heat sink, e.g. the ambient air. The supercritical carbon-dioxide (sCO_2) heat removal system "sCO2-HeRo" is

DOI: 10.17185/duepublico/46078

such a system. It is a Brayton cycle, using sCO_2 as working fluid due to his convenient fluid properties near the critical point. The main components of the cycle are a turbo-compressor-system (TCS) with integrated generator, a compact heat exchanger (CHX) and an air-cooled heat exchanger. Since the turbine of the cycle produces more power than it is used for the compression work, excess electricity can be generated in the generator for any kind of auxiliary devices. Supercritical CO_2 is chosen as working fluid because it is not toxic, not combustible and abundantly available. Furthermore, the convenient fluid properties near the critical point, e.g. the fluid density and the specific heat capacity, allows the design of compact components. This is especially important for the compact heat exchanger, connecting the steam generator of the power plant with the sCO2-HeRo cycle, because of space limitations in the containment.

Venker et al. [1-6] have studied the feasibility of such a decay heat removal system using the German thermal-hydraulic code ATHLET "Analysis of Thermal-hydraulic of Leaks and Transients" for a boiling water reactor (BWR). The simulation results have shown that the sCO2-HeRo system has the potential to enlarge the grace time for interaction to more than 72 h. However, the results are based upon the implemented heat transfer and pressure drop models in ATHLET and these must be validated for the working fluid sCO_2.

Therefore, partners from three European countries are working in the first part of sCO2-HeRo project on the design, manufacturing and assessment of a small-scale demonstrator unit into the pressure water reactor (PWR) glass model at Gesellschaft für Simulatorschulung (GfS), Essen, Germany. This is the step towards technology readiness level 3 (TRL3) [7]. By means of the small-scale demonstrator unit, experiments will be carried out and the received results will be used for validation of heat transfer and pressure drop correlations. In the second part the results will be transferred to component models on power plant scale to be implemented into the German thermal-hydraulic code ATHLET.

In the early stage of the project thermodynamic cycle calculations were performed for the small-scale demonstrator unit and for the power plant system. The optimum cycle parameters were determined with respect to maximum generator excess electricity. The received results as well as the determined optimum cycle parameters for the small-scale demonstrator unit of the glass model are summarized by Straetz et al. [8] and for the power plant scale by Hajek [9].

A scheme of the sCO2-HeRo setup, attached to the steam generator of a pressure water reactor, is shown in Figure 1.

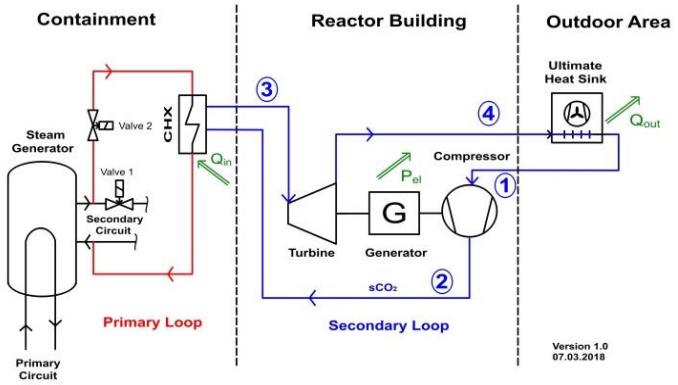

Figure 1: sCO2-HeRo retrofitted into a PWR

In case of a combined SBO and LUHS accident scenario in the PWR power plant the main coolant pumps as well as the turbine are switched off, solenoid valve 1 is closed and solenoid valve 2 is opened automatically, establishing a natural circulation driven cooling loop in the primary loop. The decay heat power in the reactor core generates steam in the secondary circuit of the steam generator with a pressure of about 70 bar and a corresponding saturated steam temperature of about 286 °C. Driven by natural convection the steam flows into a compact heat exchanger (CHX), located above the steam generator, where the heat is transferred to the sCO_2 and the steam is condensed. The condensate flows downwards driven by gravity and re-enters the steam generator through the liquid line. The transferred condensing power of the steam is heating up the sCO_2 on the secondary side of the CHX (2-3), located in the containment. After heating up the sCO_2 it enters the turbine in the reactor building where it is expanded (3-4) followed by cooling down in an ultimate heat sink (4-1) to a defined temperature. Air-fans are intended to improve the heat transfer between the gas-coolers and the ultimate heat sink, the ambient air. If the turbine (3-4) of the sCO2-HeRo system produces more power than it is used in the compressor (1-2), the system is self-sustaining and the generated excess electricity at the generator can be used for the air-fans.

TWO-PLATE CHX TEST CONFIGURATION

The experimental investigations on the heat transfer between condensing steam and sCO_2 are carried out with a two-plate CHX. The manufactured plates as well as a technical drawing are depicted in Figure 2 and Figure 3 and described.

DOI: 10.17185/duepublico/46078

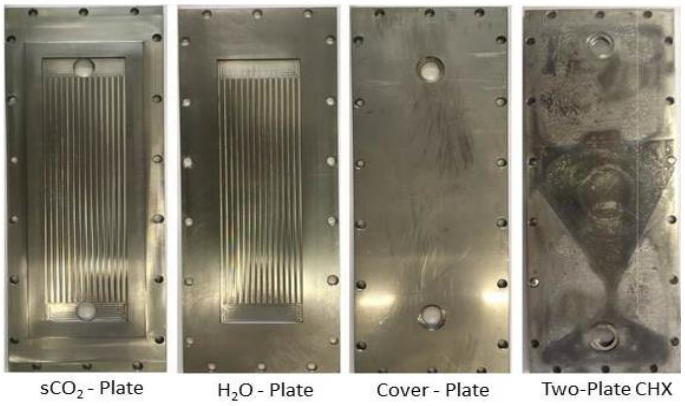

Figure 2: CHX plates with 2x1 mm channels

A rectangular channel dimension with a width of 2 mm and a height of 1 mm (2x1 mm) is used on both sides (sCO_2 Plate and H_2O Plate) of the two-plate CHX. This dimension was chosen with respect to recommendations for CHX`s from the literature, e.g. according to Hesselgreaves [13]. The design of the plates was determined after the selection of the channel dimension with respect to boundary conditions like the pressure, temperature, mass flow rate as well as from restrictions of the diffusion bonding machine.

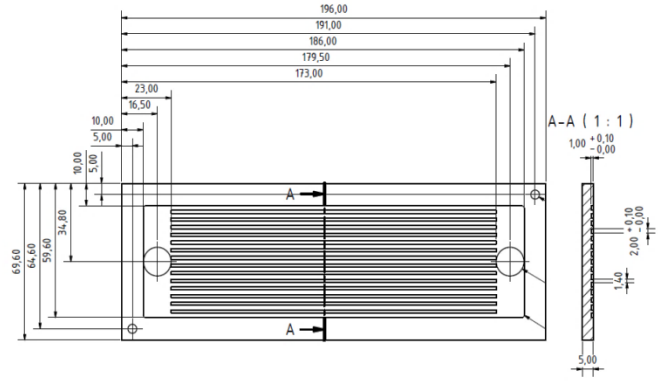

sCO_2-Plate

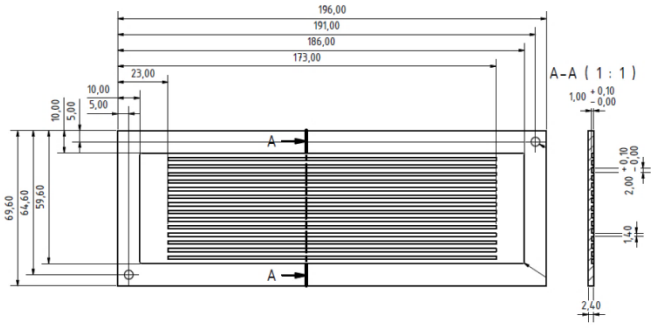

H_2O-Plate

Figure 3: Technical drawing of sCO_2-Plate and H_2O-Plate

The manufactured sCO_2 plate with 15 straight rectangular channels and a channel length of 150 mm is shown on the left hand side of Figure 2. The technical drawing of the sCO_2 plate is depicted in the upper picture in Figure 3. The wall thickness between two channels was determined according to the Barlow's formula to 1.4 mm, which was additionally verified by a finite-element-method simulation with the software COMSOL to ensure that the CHX will be able to withstand all operation conditions. The plate thickness was determined conservatively to 5 mm. During operation the sCO_2 enters the CHX plate at the bottom through a ½" pipe connection, flows upwards into the channels and is heated. Afterwards it leaves the CHX at the top through a second ½" pipe connection. Both plenums have a length of 49.6 mm, a width of 13 mm and a height of 1 mm (Figure 3). The second picture shows the H_2O plate with 15 straight channels, a channel length of 150 mm and a plate thickness of 2.4 mm. The steam inlet plenum is shown at the top and the outlet plenum at the bottom. Both have a length of 49.6 mm, a width of 13 mm and a height of 1 mm. The steam cover plate has a plate thickness of 4 mm and is depicted in the third picture in Figure 2. Two drillings with a diameter of 13 mm are included in the plate, the upper one for the steam inlet and one for the outlet of the condensate at the bottom. The last picture shows the diffusion bonded two-plate CHX with 2x1 mm channels. After welding the pipe connections onto the CHX, it will be ready for the installation into the test section.

TEST FACILITIES

Within the sCO2-HeRo project IKE, University of Stuttgart (USTUTT) is responsible for the experimental investigation on the heat transfer between condensing steam and sCO_2 in the CHX. During the project, low-pressure and high-pressure steam experiments are carried. They correspond to the small-scale demonstrator unit for the glass model and for power plant application. The investigations for the power plant application take place in the laboratory of IKE using two test facilities. The first one is the SCARLETT test loop which provides sCO_2 under defined conditions and the second one is the steam cycle which provides high-pressure steam. The piping and instrumentation (P&I) diagram of the SCARLETT test loop [10] is depicted in Figure 4.

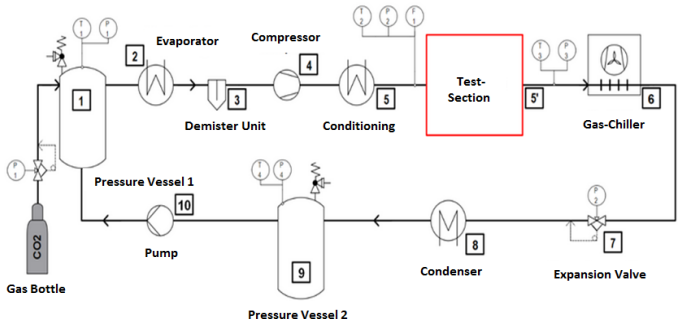

Figure 4: P&I diagram of the SCARLETT test loop

DOI: 10.17185/duepublico/46078

At the start the pressure vessels (1, 9) are filled with CO_2 by a gas bottle after evacuating the loop with a vacuum pump. During operation, liquid CO_2 flows from the pressure vessel 1 into an electrical heated evaporator (2) where it is slightly superheated. In a demister unit (3) remaining liquid CO_2 is separated from the flow before it enters a compressor (4) where it is compressed to a defined pressure and simultaneously compression-heated. After the compressor the sCO_2 is conditioned before it enters the test section, which means that a defined temperature can be adjusted via heating or cooling the sCO_2 mass flow rate. In a test-section (red box) different kind of experiments can be performed, e.g. the heat transfer in CHX with condensing steam and sCO_2 or electrically heated plates. The installed measurement devices, for instance resistance thermometers (Pt-100), pressure gauges and mass flow meters, at the inlet (5) and outlet (5') of the test section measures relevant parameters of the experiments. The sCO_2 is cooled down in a gas chiller (6) after leaving the test section and before entering an expansion valve (7). In a condenser (8) the CO_2 can be cooled down again before it flows into the pressure vessel 2 (9). From there it is pumped back into vessel 1.

The sCO_2 mass flow rate $\dot{m}_{sCO2}$ can be varied in the SCARLETT test loop from about 30 to 110 g/s. The achievable mass flow rate depends on the compressor performance map, which leads to less mass flow rate at higher pressures and vice versa. The sCO_2 temperature at the inlet of the test section T06 can be varied by conditioning from about 0 °C to 40 °C and the pressure P04 can be adjusted from about 75 bar to 110 bar.

The P&I diagram of the high-pressure steam cycle is depicted in Figure 5 and described as follows.

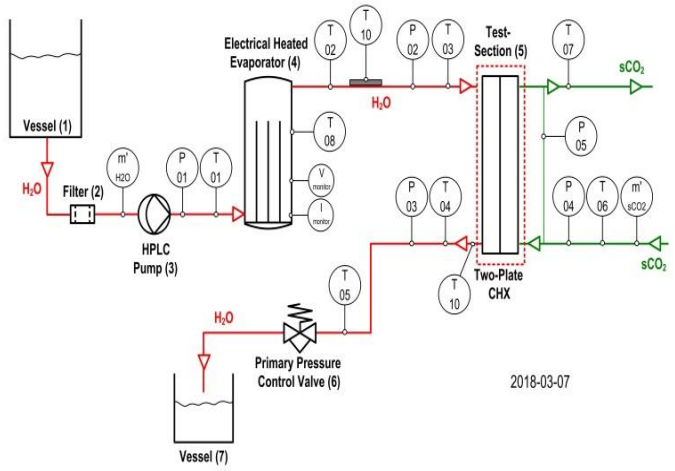

Figure 5: P&I diagram of the high-pressure steam cycle

At first a storage vessel (1) is filled with deionized water. During operation the water is pumped from the storage vessel by a high performance liquid chromatography pump (3) (HPLC) through a filter (2) into an electrical heated evaporator (4). There the water is evaporated and slightly superheated before the steam flows into a test section (5). In the test section any kind of component can be installed, e.g. a diffusion bonded two-plate CHX. The pressure in the high-pressure steam cycle can be adjusted by the mechanical primary pressure control valve (6). After the expansion in the pressure control valve the condensate flows into the storage vessel (7). For monitoring the fluid and steam properties in the cycle, measurement devices like resistance thermometers Pt-100 (T), pressure gauges (P) and a mass flow meter (m') are installed. The position and nomenclature of each measurement device is shown in the P&I diagram in Figure 5. For example, T01 is the resistance thermometer at the inlet of the electrical heated evaporator and P03 is the pressure gauge at the outlet of the two-plate CHX test section.

The pressure in the steam cycle can be adjusted from about 1 bar to 105 bar and the corresponding steam temperature is rising from about 100 °C to 315 °C. The water volume flow rate can be varied by the HPLC pump (3) from 0.05 l/h to 2.5 l/h. The installed electrical heating power of the evaporator (4) with 1.6 kW is high enough for evaporation and superheating the adjusted water volume flow rates.

MEASUREMENT PARAMETERS AND POSITION OF SURFACE PT-100

Table 1: Measurement campaigns of the two-plate CHX

Campaign	*$P_{sCO2\ in}$ - P04 [bar]*	*$T_{sCO2\ in}$ - T06 [°C]*	*Status*
1	110	40 (44.5)	Design Point **"DP"**
2	100	40 (41.3)	
3	95	39.5	
4	110	40 (44.5)	Out of Design Point "**ODP**"
5	100	40 (41.3)	
6	95	39.5	

$\dot{m}_{sCO2}$ [g/s]	*$\dot{m}_{H2O}$ [l/h]*	*Q_{Evap} [W]*	*Status*
46	0.65	460	**DP**
56	0.80	560	**DP**
68	0.97	680	**DP**
37	0.65	460	**ODP**
37	0.80	560	**ODP**
37	0.97	680	**ODP**
37	1.17	830	**ODP**
37	1.43	1010	**ODP**
37	1.74	1230	**ODP**

The measurement parameters for the investigation on the heat transfer between the high-pressure steam side (70 bar) and the sCO_2 side in the two-plate CHX were determined under consideration of the carried out low-pressure steam cycle (0.3 bar) experiments for the glass model application [14]. According to the low-pressure experiments, six measurement

DOI: 10.17185/duepublico/46078

campaigns were carried out in which different inlet conditions on both sides (H_2O and sCO_2) of the two-plate CHX were used to obtain experimental results of the heat transfer performance under "design point" (DP) and "Out of the design point" (ODP) conditions. It should be mentioned, that the measurement parameters for the DP and ODP experiments were derived from investigations at the glass model [11] and from internal restrictions at the test facilities. To be able to compare the results of both, the low-pressure and high-pressure steam cycle, the same measurement campaigns were used (Table 1).

In the DP experiments according to campaign 1, 2 and 3 the sCO_2 mass flow rates $\dot{m}_{sCO2}$ from 46 g/s to 68 g/s correspond to the water volume flow rates $\dot{m}_{H2O}$ from 0.65 l/h to 0.97 l/h. The power of the electrical heated evaporator Q_{Evap} was adjusted according to the water volume flow rates from 460 W to 680 W. To investigate the heat transfer capacity also ODP, measurement campaign 4, 5 and 6 were done. Therefore, a constant sCO_2 mass flow rate $\dot{m}_{sCO2}$ of 37 g/s and gradually increasing water volume flow rates $\dot{m}_{H2O}$ from 0.65 l/h to 1.74 l/h were used. The power of the electrical heated evaporator Q_{Evap} was adjusted according to the water volume flow rates from 460 W to 1230 W. To investigate the heat transfer behavior additionally with different sCO_2 inlet pressures P04, new thermodynamic cycle calculations were carried out for the sCO2-HeRo system to determine the sCO_2 inlet temperatures T06 into the CHX. The results have led to a temperature of T06 = 39.5 °C for P04 = 95 bar, T06 = 41.3 °C for P04 = 100 bar and T06 = 44.5 °C for P04 = 110 bar. Considering the internal restrictions of the SCARLETT test facility, the maximum sCO_2 inlet pressure was determined to P04 = 110 bar and the inlet temperature to T06 = 40 °C.

For monitoring the temperatures on the surface of the CHX during the investigation, nine resistance thermometers (Pt-100) are mounted on the sCO_2 plate. The position of each Pt-100 is shown in the CAD drawing (Figure 6).

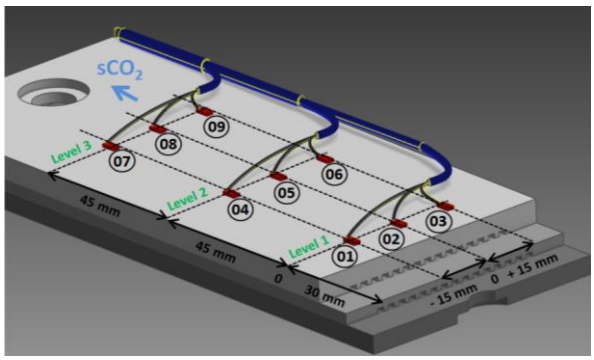

Figure 6: Pt-100 position on the sCO_2 plate surface

The resistance thermometers are mounted symmetrically in three levels on the surface of the sCO_2 plate. Level 1 is located 30 mm above the sCO_2 inlet plenum, level 2 is 45 mm above level 1 and level 3 is 45 mm above level 2. The Pt-100 02, 05 and 08 are mounted in the center line of the sCO_2 plate. Pt-100 01, 04 and 07 are located 15 mm on the left hand side of the center line and Pt-100 03, 06 and 09 15 mm on the right hand side of the center line.

EXPERIMENTAL RESULTS AND MEASUREMENT ERRORS

The experimental results of the sCO_2 pressure drop △P05 in the two-plate CHX with 15 straight channels and a channel dimension of 2x1 mm is shown in Figure 7 for the DP experiments as a function of the sCO_2 mass flow rate $\dot{m}_{sCO2}$.

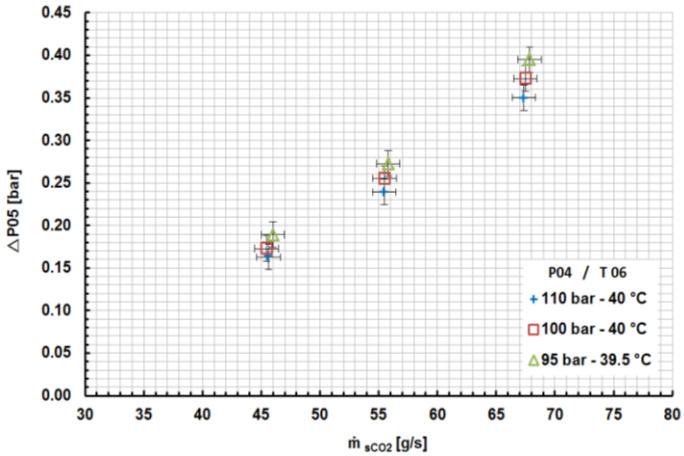

Figure 7: Results of △P05 and $\dot{m}_{sCO2}$ - DP

The results show, that an increased sCO_2 mass flow rate $\dot{m}_{sCO2}$ leads to an increased pressure drop △P05, for a constant inlet pressure P04 and inlet temperature T06. For example, that is shown by the 100 bar results, where a sCO_2 mass flow rate $\dot{m}_{sCO2}$ = 45 g/s leads to a sCO_2 pressure drop △P05 = 0.17 bar, 55 g/s leads to 0.26 bar and 67 g/s leads to 0.37 bar. The results additionally show that an increased inlet pressure P04 leads to decreased sCO_2 pressure drops △P05 - for a constant mass flow rate $\dot{m}_{sCO2}$ and inlet temperature T06. This can be explained by the equation of continuity and the fluid density. The fluid density of sCO_2 depends on the pressure and the lower the pressure, the closer the pressure is to the critical point, the lower is the density and due to that the higher is the pressure drop for a given sCO_2 mass flow rate because of higher flow velocities in the channels. According to the results depicted in Figure 7 a sCO_2 inlet pressure P04 = 95 bar, combined with an inlet temperature T06 = 40 °C and a mass flow rate $\dot{m}_{sCO2}$ = 56 g/s, leads to a pressure drop △P05 = 0.27 bar, P04 = 100 bar leads to △P05 = 0.26 bar and P04 = 110 bar leads to △P05 = 0.24 bar.

The results of the heat input into the sCO_2 Q_{sCO2} are depicted in Figure 8 as a function of the condensing power of the steam Q_{H2O} for the ODP experiments (Table 1). Q_{H2O} and

DOI: 10.17185/duepublico/46078

Q_{sCO2} were calculated in general according to Eq. 1, using the measured mass flow rates $\dot{m}$ and the enthalpy differences between the inlet h_{in} and outlet h_{out} of the fluids at the two-plate CHX. The enthalpies were calculated with NIST REFPROP, using the measured fluid temperatures and pressures.

$$Q = \dot{m} \cdot (h_{in} - h_{out}) \quad (1)$$

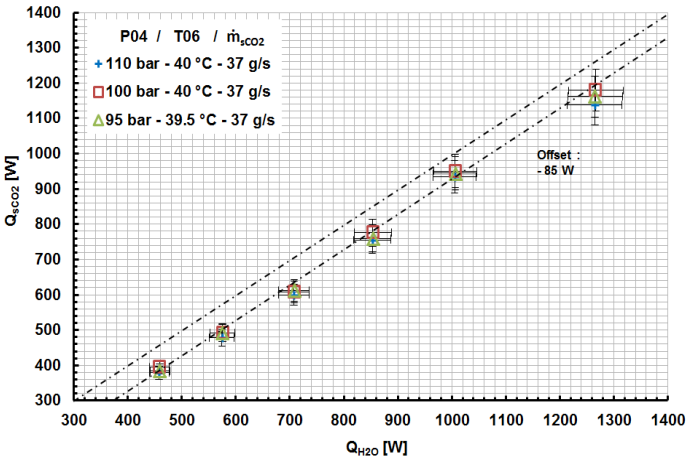

Figure 8: Results of Q_{sCO2} and Q_{H2O} - ODP

The received results of the 100 bar experiments (Figure 8) are described as example in more detail. A calculated condensing power of the steam Q_{H2O} = 458 W leads to a calculated sCO_2 heat input Q_{sCO2} = 395 W, Q_{H2O} = 708 W leads to Q_{sCO2} = 607 W and Q_{H2O} = 1267 W leads to Q_{sCO2} = 1179 W. Furthermore it can be seen, that on the one hand side the graphs have a similar tendency for all investigated inlet pressures P04 and on the other hand side that there is a schematically offset between the condensing power of the steam Q_{H2O} and the sCO_2 heat input Q_{sCO2}. This offset can be explained by thermal losses in the test section due to high temperatures of about 290 °C. Taken into account the results, the offset Q_{H2O_offset} can be calculated by the energy balance according to Eq. 2:

$$Q_{H2O\_offset} = Q_{H2O} - Q_{sCO2} \quad (2)$$

with the calculated condensing power of the steam Q_{H2O} and the calculated heat input into the sCO_2 Q_{sCO2}. The average offset, for the ODP measurement campaigns 4, 5 and 6, was determined by Eq. 2 to Q_{H2O_offset} = 85 W, which is shown by the lower black dashed line in Figure 8. Neglecting thermal losses, the heat transfer ratio R = $Q_{sCO2}/(Q_{H2O} - Q_{H2O\_offset})$ is more than 95 %. The theoretical heat transfer ratio R of 100 % is additionally visualized by the upper black dashed line. Furthermore, the results of the steam temperature measurements T04 at the outlet of the CHX verify that the steam was completely condensed and subcooled, for all measurement campaigns.

The calculated results of the sCO_2 temperature increase T07-T06 are summarized in Figure 9 as a function of the sCO_2 heat input Q_{sCO2} for the ODP measurement campaign 4, 5 and 6.

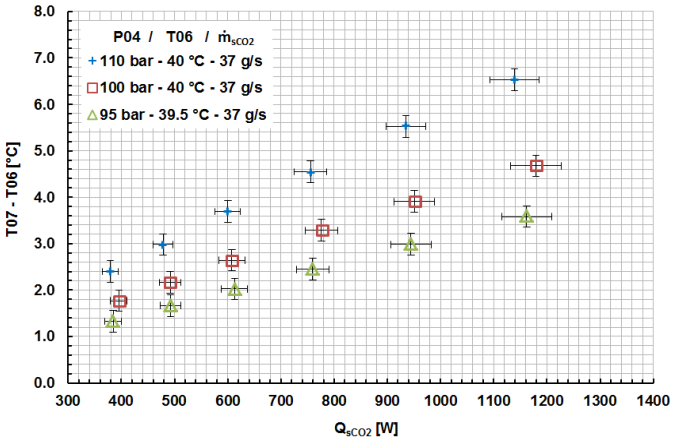

Figure 9: Results of T07-T06 and Q_{sCO2} - ODP

The results of the 110 bar measurement campaign are described in more detail at the beginning. A sCO_2 heat input Q_{sCO2} = 379 W leads to a sCO_2 temperature increase T07-T06 = 2.4 °C, Q_{sCO2} = 600 W leads to T07-T06 = 3.7 °C, Q_{sCO2} = 756 W leads to T07-T06 = 4.6 °C and Q_{sCO2} = 1139 W leads to T07-T06 = 6.5 °C. In addition, the other results depicted in Figure 9 have a similar linear tendency only with different gradients because of different specific heat capacities. Moreover, a lower inlet pressure P04 leads to lower sCO_2 temperature increases T07-T06 because of higher specific heat capacities near the critical point. A sCO_2 heat input Q_{sCO2} = 1150 W, combined with a sCO_2 mass flow rate $\dot{m}_{sCO2}$ = 37 g/s and a sCO_2 inlet temperature T06 = 40 °C, leads to a sCO_2 temperature increase T07-T06 = 6.5 °C for P04 = 110 bar, to T07-T06 = 4.7 °C for P04 = 100 bar and T07-T06 = 3.6 °C for P04 = 95 bar. The specific heat capacity c_p can be calculated in general for each measurement parameter according to Eq. 3:

$$c_p = \frac{Q_{sCO2}}{\dot{m}_{sCO2} * (T07 - T06)} \quad (3)$$

with the sCO_2 heat input Q_{sCO2}, the sCO_2 mass flow rate $\dot{m}_{sCO2}$ and the sCO_2 temperature increase T07-T06. For the 110 bar measurement campaign (Figure 9) the specific heat capacity c_p is in the range of 4.3 kJ/kg K to 4.8 kJ/kg K, for the 100 bar campaign from 6.1 kJ/kg K to 6.9 kJ/kg K and for the 95 bar campaign between 7.9 kJ/kg K and 8.8 kJ/kg K.

The experimental results of the surface temperatures T on the sCO_2 side of the CHX are depicted in Figure 10 as a function of the position X of the Pt-100 (Figure 6). The results are received from the ODP measurement campaign 4 with a

DOI: 10.17185/duepublico/46078

sCO_2 heat input of Q_{sCO2} = 755 W, an inlet temperature T06 = 40 °C and a sCO_2 mass flow rate $\dot{m}_{sCO2}$ = 37 g/s.

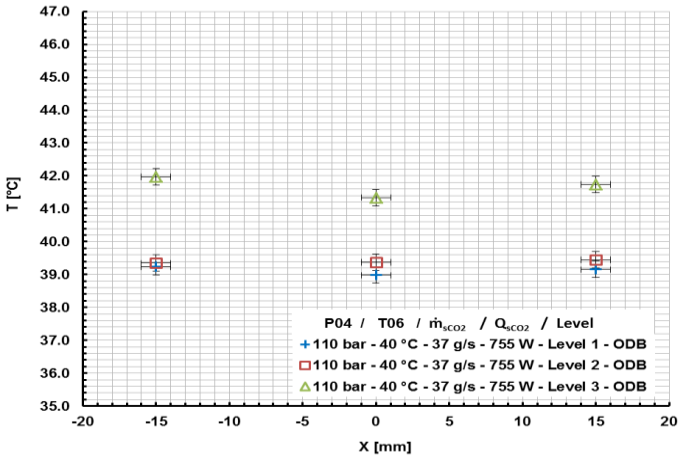

Figure 10: Results of T and X - ODP and Q_{sCO2} = 755 W

The depicted results of the surface temperatures have a symmetrical profile with lower temperatures in the center and higher temperatures at the outer area of the two-plate CHX, which can be explained by inhomogeneous mass flow distributions over all channels. As example, the temperature profile at level 3 shows, that the temperatures T07 = 42.0 °C (left hand side) and T09 = 41.8 °C (right hand side) are similar. The temperature T08 = 41.3 °C in the central axis of the CHX is about 0.5 °C lower than T07 and T09. The gradually increasing surface temperatures from level 1 to level 3 are described in the following at position X = 0 mm. The sCO_2 enters the CHX with a temperature of 40 °C and flows upwards into the channels. Level 1 is located 30 mm above the plenum and the measured surface temperature is T02 = 39.0 °C. Flowing upward, the sCO_2 is heated in the CHX due to the heat transfer of condensing steam. This leads to a surface temperature of T05 = 39.4 °C on level 2 and T08 = 41.3 °C on level 3. In addition, the measured surface temperatures correspond to the results of the sCO_2 temperature increases T07-T06 according to Figure 9. There, a sCO_2 mass flow rate $\dot{m}_{sCO2}$ = 37 g/s, an inlet pressure P04 = 110 bar, an inlet temperature T06 = 40 °C and a heat input Q_{sCO2} = 755 W leads to a temperature increase of about T07-T06 = 4.5 °C - which corresponds to the measured surface temperatures on level 3 of about 42.0 °C. But it should be mentioned, that the received surface temperatures are always lower than the sCO_2 fluid temperatures T07 at the outlet of the CHX due to thermal losses and the measurement position of level 3, which is 30 mm below the sCO_2 outlet.

Finally, the experimental results of the surface temperatures T on the sCO_2 side of the CHX are shown in Figure 11 as a function of the position X of the Pt-100. The results correspond to the ODP measurement campaign 4 with an sCO_2 heat input of Q_{sCO2} = 1140 W.

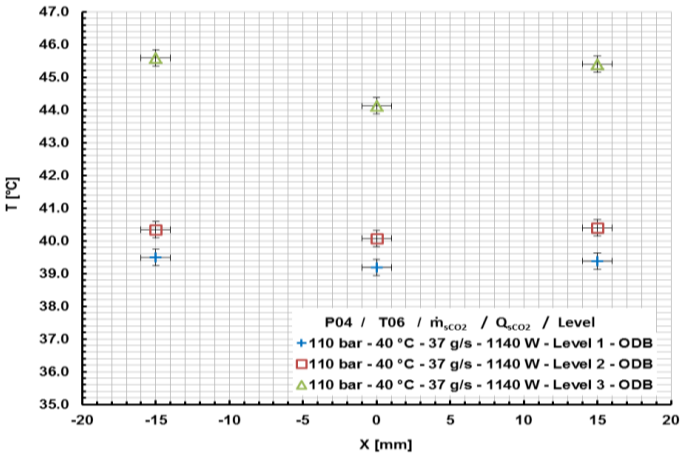

Figure 11: Results of T and X - ODP and Q_{sCO2} = 1140 W

The shown results in Figure 11 have similar symmetrical tendencies, compared to the depicted results in Figure 10. As example, the increase of the surface temperature at position X = 0 mm is described in more detail. A sCO_2 mass flow rate $\dot{m}_{sCO2}$ = 37 g/s, a sCO_2 inlet pressure P04 = 110 bar and a sCO_2 inlet temperature T06 = 40 °C leads to a surface temperature of T02 = 39.2 °C on level 1. Flowing upward, the sCO_2 is heated in the CHX due to the heat transfer of condensing steam, which leads to a surface temperature of T05 = 40.1 °C on level 2 and T08 = 44.1 °C on level 3. Comparing the results of both campaigns (Figure 10 and Figure 11) they show, that the surface temperatures on level 1 are quite similar with a temperature of about T02 = 39.2 °C. On level 2 there is a discrepancy of 0.7 °C between the surface temperature T05 = 39.4 °C (755 W) and the surface temperature T05 = 40.1 °C (1140 W). On level 3 there is a discrepancy of 2.8 °C between the surface temperature T05 = 41.3 °C (755 W) and the surface temperature T05 = 44.1 °C (1140 W). The temperature discrepancies on level 2 and especially on level 3 can be explained by the way of the heat input into the sCO_2 from the condensing power of the steam Q_{H2O}. A higher heat input Q_{sCO2} into the sCO_2 corresponds to a higher steam condensing power Q_{H2O} and this lead to increased steam mass flow rates. Increased steam mass flow rates need more heat transfer area and this leads to a forced steam mass flow downwards the CHX in the direction of level 3 and level 2.

The error bars, shown in Figure 7 - Figure 11, were derived from manufacturer's instructions and from calculated measurement error propagations.

The temperature measurement uncertainty of a Pt-100 is given as a function of the measured temperature T according to +/- (0.15°C+0.002*T). The pressure measurement uncertainty depends on the pressure measurement type and on the

DOI: 10.17185/duepublico/46078

measurement range. The sCO_2 inlet pressure P04 into the CHX was measured with an uncertainty of +/- (0.5%*200bar) and the sCO_2 pressure drop P05 with an error of +/- (0.15%*10bar). The sCO_2 mass flow rate $\dot{m}_{sCO2}$ was measured with an accuracy of +/- 0.8 g/s. The water volume flow rate $\dot{m}_{H2O}$ on the steam side has an uncertainty of +/- (5%*$\dot{m}_{H2O}$) and the H_2O inlet and outlet pressures P02 and P03 were measured with an accuracy of +/- (0.5%*100bar).

The error propagations for the calculated enthalpies σ_h and for the calculated sCO_2 heat input $\sigma_{Q_{sCO2}}$ as well as steam condensing power $\sigma_{Q_{H2O}}$ are described more in detail. Eq. 4 shows the equation for the statistical error propagation

$$\sigma = \sqrt{\sigma_1^2 + \sigma_2^2 + \cdots} \tag{4}$$

with σ_1: measurement uncertainty of the first independent parameter and σ_2: measurement uncertainty of the second independent parameter, which implies the uncertainties to be not correlated.

For the calculation of the sCO_2 enthalpy uncertainty at the inlet of the CHX $\sigma_{h_{sCO2-in}}$(Eq. 5) four enthalpies were used. The first one was $h_{sCO2-in}|_{T06/P04_{max}}$, which was a function of the measured sCO_2 inlet temperature T06 and the maximum possible inlet pressure $P04_{max}$ according to pressure measurement uncertainties. The second one was $h_{sCO2-in}|_{T06/P04_{min}}$, which was calculated with the measured sCO_2 inlet temperature T06 and the minimum possible inlet pressure $P04_{min}$. The third one was $h_{sCO2-in}|_{P04/T06_{max}}$, which was a function of the measured sCO_2 inlet pressure P04 and the maximum possible inlet temperature $T06_{max}$. The fourth one was $h_{sCO2-in}|_{P04/T06_{min}}$, which was calculated with the measured sCO_2 inlet pressure P04 and the minimum possible inlet temperature $T06_{min}$. The propagated sCO_2 enthalpy uncertainty at the outlet of the CHX $\sigma_{h_{sCO2-out}}$ was calculated in the same way as for $\sigma_{h_{sCO2-in}}$, only with the sCO_2 outlet temperature T07 and sCO_2 outlet pressure p_{sCO2_out}.

$$\sigma_{h_{sCO2-in}} = \frac{\sqrt{\left(h_{sCO2-in}|_{T06/P04_{max}} - h_{sCO2-in}|_{T06/P04_{min}}\right)^2 + \left(h_{sCO2-in}|_{P04/T06_{max}} - h_{sCO2-in}|_{P04/T06_{min}}\right)^2}}{2} \tag{5}$$

The heat input into the sCO_2 was calculated according to $Q_{sCO2} = \dot{m}_{sCO2} * (h_{sCO2-in} - h_{sCO2-out})$. It can be seen, that Q_{sCO2} is a function of three independent parameters. According to the linearized Taylor-series and the propagation of uncertainty, for independent parameters, the error propagation $\sigma_{Q_{sCO2}}$ was calculated after rewriting according to Eq. 6:

$$\sigma_{Q_{sCO2}} = \sqrt{\left((h_{sCO2-out} - h_{sCO2-in}) * \sigma_{\dot{m}_{sCO2}}\right)^2 + \left(\dot{m}_{sCO2} * (\sigma_{h_{sCO2-out}} - \sigma_{h_{sCO2-in}})\right)^2} \tag{6}$$

The error propagation $\sigma_{Q_{sCO2}}$ includes the calculated sCO_2 enthalpies at the inlet $h_{sCO2-in}$ and outlet $h_{sCO2-out}$ of the CHX, the measurement error of the sCO_2 mass flow rate $\sigma_{\dot{m}_{sCO2}}$ = +/- (0.8 g/s), the measurement results of the sCO_2 mass flow rate $\dot{m}_{sCO2}$ and the calculated enthalpy uncertainties $\sigma_{h_{sCO2-out}}$ and $\sigma_{h_{sCO2-in}}$. The error propagation was repeated in the same way for the steam side.

The results have shown an error propagation of less than 6 % for the calculated measurements values for the sCO_2 heat input Q_{sCO2} and the steam condensing power Q_{H2O}.

CONCLUSION

An advanced heat removal system, a Brayton cycle with supercritical sCO_2 as working fluid, is currently investigated within the EU-funded sCO2-HeRo project. The system consists of a turbine, a compressor, a generator, a compact heat exchanger, gas-coolers and auxiliary devices. In the design point of the system it is assumed, that the turbine provides more power than it is used for the compression work, which leads to a self-launching, self-propelling and self-sustaining decay heat removal system. In the EU-funded project a two-scale approach is applied. Showing the feasibility in the first part of the project a small-scale demonstrator unit of the sCO2-HeRo system is designed, manufactured and attached into the PWR glass model at GfS, Essen. In the second part the received experimental results at the demonstrator will be used for validation of models e.g. for heat transfer and pressure drop. Afterwards, they will be transferred to component models on power plant size to be implemented into the German code ATHLET.

The Institute of Nuclear Technology and Energy Systems (IKE) is responsible for the investigation of the compact heat exchanger, which connects the steam side of the power plant with the sCO_2 side of the sCO2-HeRo system. Using two test facilities, the sCO_2 SCARLETT test loop and the high-pressure steam cycle, experimental investigations on the heat transfer between condensing steam (70 bar, 286 °C) and sCO_2 were performed in the CHX with 15 straight rectangular channels, a channel length of 150 mm an a channel dimension of 2x1 mm.

The results of the sCO_2 pressure drop $\triangle$P05 in the CHX show a typical parabolic profile with an increasing pressure drop for increasing sCO_2 mass flow rates. The depicted results of the heat input Q_{sCO2} into the sCO_2 verify that the condensing power of the steam was reliably transferred to the sCO_2 side for all measurement campaigns, under consideration of thermal losses and measurement uncertainties. The sCO_2 temperature increase T07-T06 shows for all measurement campaigns a nearly linear profile, which can be explained by the specific heat capacity. Additionally, the plate surface temperatures were measured during the measurement campaigns on the sCO_2 side of the CHX with nine Pt-100. The results show lower plate surface temperatures T in the center axis of the CHX and higher temperatures at the outer area, which can be explained by inhomogeneous mass flow distributions over all channels.

DOI: 10.17185/duepublico/46078

NOMENCLATURE

Variable	Description	Unit
c_p	Heat Capacity	kJ/kg K
h	Enthalpy	kJ/kg K
$\dot{m}$	Mass Flow	kg/s
P	Pressure	bar
ΔP	Pressure Drop	bar
Q	Heat Power	W
R	Heat Transfer Ratio	%
T	Temperature	°C
TO	Temperature Surface	°C
X	Position	mm
σ	Measurement uncertainty	-

Subscripts	Description	Unit
H20	Steam / Water	-
H20_offset	Thermal Losses	-
in	Inlet	-
Evap	Evaporator	-
out	Outlet	-
sCO2	Supercritical Carbon Dioxide	-

ABBREVIATIONS

Variable	Description	Unit
ATHLET	Analysis of Thermal-hydraulic of Leaks and Transients	-
BWR	Boiling Water Reactor	-
CHX	Compact Heat Exchanger	-
COMSOL	Comsol Multiphysics	-
DP	Design Point	-
EU	European Union	-
GfS	Gesellschaft für Simulatorschulung mbH	-
HeRo	Heat Removal	-
HPLC	High Performance Liquid Chromatography	-
IKE	Institute of Nuclear Technology and Energy Systems	-
LUHS	Loss of Ultimate Heat Sink	-
ODP	Out of Design Point	-
P&I	Piping and Instrumentation	-
PWR	Pressurized Water Reactor	-
SCARLETT	Supercritical Carbon Dioxide Loop at IKE Stuttgart	-
SBO	Station Black Out	-
sCO_2	Supercritical Carbon Dioxide	-
TCS	Turbo-Compressor-System	-
TRL	Technology Readiness Level	-
USTUTT	University of Stuttgart	-

ACKNOWLEDGEMENTS

The project leading to this application has received funding from the Euratom research and training programme 2014-2018 under grant agreement No 662116.

REFERENCES

[1] J. VENKER, “Development and Validation of Models for Simulation of Supercritical Carbon Dioxide Brayton Cycle and Application to Self-Propelling Heat Removal Systems in Boiling Water Reactors”, University of Stuttgart, IKE2-156, ISSN-0173-6892 (2015).

[2] J. VENKER, “A passive heat removal retrofit for BWRs”, Nuclear Engineering International, 58, 711, 14-17 (2013).

[3] J. VENKER, J. STARFLINGER and A. SCHAFFRATH, “Code Development and Simulation of the supercritical CO2 Heat Removal System”, Proceedings of the European Nuclear Conference, Warsaw, Poland, October 9-13 (2016).

[4] J. VENKER, D. VON LAVANTE, M. BUCK, D. GITZEL and J. STARFLINGER, "Interaction between Retrofittable and Existing Emergency Cooling Systems in BWRs”, Proceedings of the 10th International Topical Meeting on Nuclear Thermal-Hydraulics, Operation and Safety, NUTHOS-10, Okinawa, Japan (2014).

[5] J. VENKER, D. VON LAVANTE, M. BUCK, D. GITZEL, and J. STARFLINGER, "Transient Analysis of an Autarkic Heat Removal System", Proceedings of the 2014 International Congress on Advances in Nuclear Power Plants, ICAPP 2014, Charlotte, USA (2014).

[6] J. VENKER, D. VON LAVANTE, M. BUCK, D. GITZEL, J. STARFLINGER, "Concept of a Passive Cooling System to Retrofit Existing Boiling Water Reactors", Proceedings of the 2013 International Congress on Advances in Nuclear Power Plants, ICAPP 2013, Jeju, South Korea (2013).

[7] K-F. BENRA, D. BRILLERT, O. FRYBORT, P. HAJEK, M. ROHDE, S. SCHUSTER, M. SEEWALD and J. STARFLINGER, “A Supercritical CO2 Low Temperature Brayton-Cycle for Residual Heat Removal”, Proceedings of the 5th International sCO2 Power Cycles Symposium, San Antonio, Texas (2016).

[8] M. STRAETZ, R. MERTZ and J. STARFLINGER, “Power cycle calculations and preliminary design of a compact heat exchanger of a scaled down sCO2-HeRo-system for a PWR glass model at KSG/GfS”, 1st European Seminar on Supercritical CO2 (sCO2) Power Systems, 29-30 September 2016, Vienna, Austria (2016).

DOI: 10.17185/duepublico/46078

[9] P. HAJEK, “Advantages Analysis of Supercritical Power CO2 Cycles”, 1st European Seminar on Supercritical CO2 (sCO2) Power Systems, 29-30 September 2016, Vienna, Austria (2016).

[10] W. FLAIG, R. MERTZ, and J. STARFLINGER, “Setup of the supercritical CO2 test-facility „SCARLETT“ for basic experimental investigations of a compact heat exchanger for an innovative decay heat removal system”, Proceedings of the 25th international conference on nuclear engineering, ICONE25, 02-06 July 2017, Shanghai, China (2017).

[11] M. SEEWALD and M. STRAETZ, “Deliverable No. 1.1 - Release thermodynamic cycle parameter”, sCO2-HeRo Project (2015).

[12] M. STRAETZ and S. SCHUSTER, “Milestone No. 1.1 - Review control characteristics/ strategy/ number of sCO2-HeRo turbo-machine sets for parallel use”, sCO2-HeRo Project (2016).

[13] J. E. HESSELGREAVES, “Compact Heat Exchangers - Selection, Design and Operation”, Pergamon, Amsterdam – London – New York – Oxford – Paris – Shannon – Tokyo (2001).

[14] M. STRAETZ, R. MERTZ and J. STARFLINGER, “’Design of a compact heat exchanger and heat transfer investigations of a scaled down sCO2-HeRo system”, Proceedings of the 2018 International Congress on Advances in Nuclear Power Plants, ICAPP 2018, 08-11 April 2018, Charlotte, USA (2018).

DOI: 10.17185/duepublico/46078

2nd European supercritical CO2 Conference
August 30-31, 2018, Essen, Germany

2018-sCO2.eu-105

FLOW AND HEAT TRANSFER CHARACTERIZATION FOR SUPERCRITICAL CO2 DURING HEAT REJECTION

Sandeep Pandey*, Eckart Laurien
Institute of Nuclear Technology and Energy Systems
University of Stuttgart
Stuttgart, Germany
*Email: sandeep.pandey@ike.uni-stuttgart.de

Xu Chu
Institute of Aerospace Thermodynamics
University of Stuttgart
Stuttgart, Germany

ABSTRACT

Supercritical carbon dioxide (sCO2) has a wide spectrum of application in different fields such as working fluid in energy production and conversion industries. Most of the applications employ sCO2 in the near-critical region to gain maximum efficiency; however, it creates a problem in heat transfer prediction because of drastic change in thermophysical properties. Heat transfer to supercritical CO2 gets affected by the buoyancy and thermal contraction during the heat rejection process in pre-cooler section of the power cycle based on recompression-Brayton power cycle. Thus, direct numerical simulations were conducted to simulate the cooling process in the near-critical region with a relatively moderate bulk Reynolds number of 5400 at two different heat fluxes. The simulation results show the impaired heat transfer during downward flow and an enhanced heat transfer during the upward flow, contrary to the heating of CO2. In the downward flow, heat transfer is deteriorated initially but soon enough a heat transfer recovery was observed. The decomposition of skin friction factor and the Nusselt number was performed to understand the role of individual terms viz. laminar, turbulent and inhomogeneous contribution. The major contribution on skin friction factor was brought by the body force due to the gravity. While the turbulent and inhomogeneous part equally affects the Nusselt number in supercritical flows. The turbulence statistics such as Reynolds shear stress, turbulent kinetic energy, and turbulent heat flux typically shows an increasing trend for upward flow and decreasing trend for the downward flow. All these turbulence quantities show a recovery in downward flow case near to the outlet. To investigate this recovery, quadrant analysis was conducted to examine the role of sweep (Quadrant-4) and ejection (Quadrant-2) events. During the heat transfer deterioration, sweep and ejection events reduced greatly, this triggers the reduction in turbulence. The recovery in heat transfer is brought by the Quadrant-1 and 3 commonly known as outward and wall-ward interaction events. After the recovery, these interaction events dominate the flow and it is completely opposite to the normal turbulence in which sweep and ejection events are significant. In addition to this, the turbulent heat flux in radial and streamwise direction became weaker along with a lesser number of frequencies during the buoyancy-favored flow. Turbulence anisotropy of Reynolds stress tensor is quantified by using the second and third invariants and it showed that the turbulence structure becomes rod-like during the deteriorated heat transfer regime in the downward flow.

INTRODUCTION

The lower critical pressure and temperature of carbon dioxide (p_c=7.38 MPa, T_c= 304.25 K) as compared to water (p_c=22.06 MPa, T_c= 674.09 K) provide an opportunity to generate power in the reduced operating range. The supercritical carbon dioxide (sCO2) Brayton cycle takes the advantage of lower fluid density in the near-critical region to reduce the compression work and also circumvent the problem of dry-out, which occurs in sub-critical power cycles. There exist several plant layouts with carbon dioxide as the working fluid, including single and split flow layouts with the options of precompression, recuperation, intercooling, and reheating [1]. Among all these layouts, the recompression layouts have shown a great potential in terms of higher efficiency [2]. In a typical recompression Brayton cycle, isobaric heat addition takes place at high pressure as shown by process 2-3-4-5 in *T-s* diagram in Figure 1, which is far away from the critical point (in the range of 20 to 25 MPa) and heat rejection takes place in the near-critical pressure (7.5 to 10 MPa) as depicted by process 6-7-8-1. The flow is split at Point 8, and the major part of the fluid is cooled down in the reject heat exchanger (i.e. pre-cooler) in process 8-1. The fluid is compressed isentropically in the compressor (process 1-2) and recompressor (process 8-3). During process 2-3, the major part of the split fluid is heated in the low-temperature recuperator and at point-3; it is mixed up

DOI: 10.17185/duepublico/46079

with the fluid coming from the recompressor. Then the fluid is sent to the high-temperature recuperator (process 3-4), where it extracts the heat from the fluid at the low-pressure side (process 6-7). The remaining part of the heat is supplied via an external source such as nuclear during the process 4-5. The isentropic expansion from high-pressure to low-pressure takes place in the turbine in process 5-6 and fluid is passed through the high and low-temperature recuperator for the regeneration purpose. The overall cycle promises high efficiency theoretically, yet might severely suffer from poor heat transfer termed as heat transfer deterioration, which arises in the near-critical region due to significant variation in the thermophysical properties.

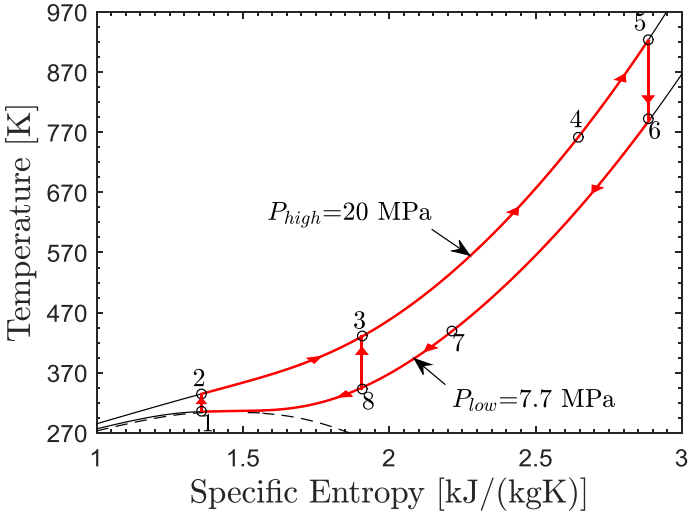

Figure 1: T-s diagram of the recompression Brayton cycle

At the high pressure of 20 MPa, thermophysical properties variation is smooth, thus commonly used correlation for constant properties can be applied to predict the heat transfer. The problem of an accurate and reliable prediction of heat transfer arises at the lower pressure, for e.g. at 7.7 MPa, where almost all thermophysical properties change abruptly. Heat transfer deterioration was observed in the near-critical region for heating of sCO2 in various experiments, in which the wall temperature increased significantly due to poor heat transfer between the wall and bulk fluid [4]. Along with experiments, computational fluid dynamics (CFD) studies are an important tool which provides insight information. Numerous attempts have been made in the past to model the heat transfer to sCO2 by means of turbulence modeling [5-7]. The turbulence models either over-predict or under-predict the heat transfer [5, 6]. Thus, direct numerical simulation (DNS) is an attractive alternative at low Reynolds numbers. Several DNS have been conducted specifically for CO2 [8-10, 19]. Most of these DNSs were conducted for the heating of CO2. Therefore, in this work, we made an attempt for DNS of cooling at different heat flux and direction of flow. We also examined few cases further by different turbulence techniques. The gained knowledge and DNS database can be used to develop analytical model or correlations [16-17]. The database also has a huge potential in machine learning based approach [18].

METHODOLOGY

In this DNS, the low-Mach Navier-Stokes (N-S) equations are used instead of the fully compressible N-S equations. This valid assumption was also employed by Bae et al. [8], Chu et al. [9, 11] and Nemati et al. [10]. Equations 1-3 represent the mass, momentum and energy conservation. In equations 1-3; ρ denotes the fluid density, u is the velocity vector, p is the pressure, μ represents the dynamic viscosity, h is the specific enthalpy, κ is the thermal conductivity and T denotes the temperature. The B_f is the body force due to gravity and its value is $[0, 0, \pm\rho g]^T$ and S represents the strain tensor.

$$\partial_t \rho + \boldsymbol{\nabla} \cdot (\rho \boldsymbol{u}) = 0 \quad (1)$$

$$\partial_t (\rho \boldsymbol{u}) + \boldsymbol{\nabla} \cdot (\rho \boldsymbol{u}\boldsymbol{u}) = -\boldsymbol{\nabla} \boldsymbol{p} + \boldsymbol{\nabla} \cdot (2\mu \boldsymbol{S}) \pm \boldsymbol{B}_f \quad (2)$$

$$\partial_t (\rho h) + \boldsymbol{\nabla} \cdot (\rho \boldsymbol{u} h) = \boldsymbol{\nabla} \cdot (\kappa \boldsymbol{\nabla} T) \quad (3)$$

While solving the equations, all thermophysical properties are a function of enthalpy only. They are implemented by spline functions. These properties were derived from NIST REFPROP [3]. An open-source CFD code, OpenFOAM, has been used for this work. The code is overall second order accurate in both space and time.

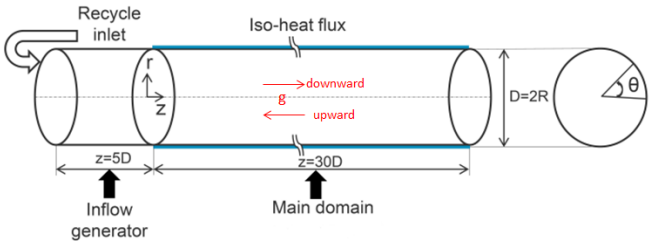

Figure 2: Computational domain

The simulation domain consists of a tube of 2 mm diameter with a total length of 35 diameters (35D) as depicted in Figure 2. The tube is divided into two parts: the inflow generator and the main domain. The inflow generator has a length of 5D. The objective of this section is to provide a fully developed turbulent flow to the main domain. For this purpose, a recycling procedure with the isothermal wall is adopted. A resolution of 120×360×300 was chosen for the inflow generator. The main domain is distinguished from the inflow generator by a uniform heat flux for the remaining length. In the main domain, the no-slip boundary condition is imposed on the wall and a convective outflow boundary condition is used for the velocity and other variables at the outlet. A resolution of 120×360×1800 was used in radial, circumferential and axial direction with structured hexahedral mesh for the main domain to resolve the small scales. Uniform grid spacing is used in the axial direction, while the radial grid is refined close to the wall. The non-dimensional grid resolution is given in wall units defined by $y^+ = y u_{\tau,0} / \nu_0$. Here, R is the radius of pipe, ν is the kinematic viscosity and u_τ is the friction velocity. The subscript '0' is for the conditions corresponding to the inlet (i.e. p_0= 8

DOI: 10.17185/duepublico/46079

MPa and T_0= 342.05 K). The distinction between upward, downward and zero gravity (i.e. forced) flow are made by changing the body force term (B_f) in the streamwise momentum equation. This numerical procedure has been validated with the experiments as well as with the DNS (refer [9, 12]), therefore, no further validation is discussed here. Table 1 shows the simulation parameters for this study. Total six cases were simulated with the variation of body force and heat flux.

Table 1: Simulation parameters, inlet temperature= 342.05 K, inlet pressure= 8 MPa

Sr. No.	Case	B_f (kg/m^{2}s^2)	q_w (kW/m^2)	q_w/G (kW/kg-s)
1	FC8q1	0	-30.87	-0.57
2	UC8q1	$-\rho g$		
3	DC8q1	ρg		
4	FC8q2	0	-61.74	-1.14
5	UC8q2	$-\rho g$		
6	DC8q2	ρg		

RESULTS AND DISCUSSION

Direct numerical simulations have been accomplished with the conditions of Table 1 and various results are discussed in this section. Here, all quantities are averaged by either Reynolds averaging or Favre averaging depending upon the variable. After obtaining the mean quantity by either of the methods, further averaging was done in the circumferential direction. Turbulent statistics were obtained by averaging in time for at least 10 flow through times, corresponding to the 300-fold characteristic turbulent timescale. For the DNS, 400-1400, computational cores has been used where parallel efficiency was 80-110%. Approximately 150,000 cpu-hours are needed for 10 flow through time with 1400 cores.

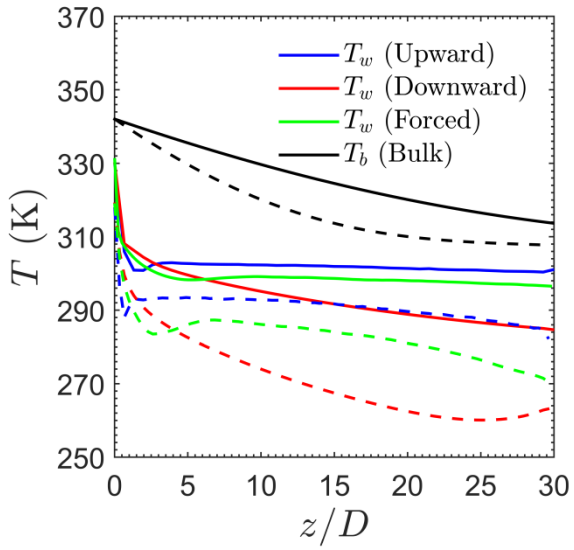

Figure 3: Variation of temperature along the axial direction; full lines: single heat flux (case 1-3); dashed lines: double heat flux (case 4-6)

Firstly, basic heat transfer characteristics are discussed. Figure 3 shows the variation of wall temperature for all six cases along with bulk temperature variation[1]. The 'z/D' represents the axial coordinates along the flow (i.e. streamwise) direction. The bulk enthalpy decreases linearly in the flow direction due to the negative uniform heat flux, and bulk temperature has a downward-concave profile due to the non-linear variation of the isobaric specific heat. Typically, the upward flow has the highest heat transfer coefficient indicated by the least difference between the bulk and wall temperature (see Figure 3), resulting in the highest Nusselt number. The flow with the downward direction suffers from the poor heat transfer. In the double heat flux case, a recovery can be observed near to the outlet. The density variation leads to a buoyancy effect, which gives rise to this dissimilar distribution of temperature in the forced and mixed convection. In upward flow cases, the wall temperature drops rapidly to the liquid-like region while the core fluid is still in the gas-like region. This sharp density gradient between the wall and core enhances the mixing of fluid radially, thereby promotes the heat transfer.

To analyze the hydraulic characteristics, skin friction factor ($C_f = \frac{2\tau_w}{\rho_b U_b^2}$) decomposition was performed, commonly known as FIK analysis [13-14]. We have re-derived this identity for supercritical carbon dioxide in this study. For the derivation, we first took the Favre-average of streamwise-momentum equation (i.e. Equation 3) and then integrate it two times. Following equation shows this relationship, the operator <> denotes fluctuations based on the cross-sectional area.

$$C_{f,FIK} = \underbrace{-\frac{64}{\rho_b U_b^2 D^3}\int_0^R r\overline{\mu}\overline{S_{rz}}rdr}_{C_1} + \underbrace{\frac{64}{\rho_b U_b^2 D^3}\int_0^R r\overline{\rho u_r'' u_z''}rdr}_{C_2} + \underbrace{\frac{32}{\rho_b U_b^2 D^3}\int_0^R (R^2-r^2)\left\langle\frac{\partial\overline{p}}{\partial z}\right\rangle rdr}_{C_3} + \underbrace{\frac{64}{\rho_b U_b^2 D^3}\int_0^R r\overline{\rho}\widetilde{u_r}\widetilde{u_z}rdr}_{C_4} + \underbrace{\frac{32}{\rho_b U_b^2 D^3}\int_0^R (R^2-r^2)\left\langle\frac{\partial\overline{\rho}\widetilde{u_z}\widetilde{u_z}}{\partial z}\right\rangle rdr}_{C_5} + \underbrace{\frac{32}{\rho_b U_b^2 D^3}\int_0^R (R^2-r^2)\left\langle\frac{\partial\overline{\rho u_z'' u_z''}}{\partial z}\right\rangle rdr}_{C_6} - \underbrace{\frac{32}{\rho_b U_b^2 D^3}\int_0^R (R^2-r^2)\left\langle\frac{1}{r}\frac{\partial r\overline{\mu' S_{rz}'}}{\partial r}\right\rangle rdr}_{C_7} - \underbrace{\frac{32}{\rho_b U_b^2 D^3}\int_0^R (R^2-r^2)\left\langle\frac{\partial\overline{\mu S_{zz}}}{\partial z}\right\rangle rdr}_{C_8} - \underbrace{\frac{32}{\rho_b U_b^2 D^3}\int_0^R (R^2-r^2)\left\langle\frac{\partial\overline{\mu' S_{zz}'}}{\partial z}\right\rangle rdr}_{C_9} \pm \underbrace{\frac{32}{\rho_b U_b^2 D^3}\int_0^R g(R^2-r^2)\langle\overline{\rho}\rangle rdr}_{C_{10}}$$

In this equation, $C_{f,FIK}$ is the skin friction factor computed by FIK identity using the above equation. In the equation, C_1 represents the laminar contribution, C_2 represents the turbulent contribution and C_{10} dennotes the buoyancy contribution and '-' sign is for upward flow and '+' sign is for downward flow. Remaining quantities (C_3-C_9) are for inhomogeneous contribution due to the variable properties. The quantity with overbar represents the Reynold averaged, with tilde shows the Favre averaged, with single prime represents the fluctuating part came out due to Reynolds averaging and double prime is the fluctuations based on Favre averaging. Figure 4 illustrates the implementation of this identity on Case UC8q2 and DC8q2.

[1] Corresponding DNS data are available at: https://www.ike.uni-stuttgart.de/forschung/sco2/dns/

DOI: 10.17185/duepublico/46079

The variation of C_1, C_2, C_4, C_5, and C_{10} can be seen; the remaining parts which are not shown here have negligible magnitude. The first observation is that the symbol ($C_{f,DNS}$) and line in black color ($C_{f,FIK}$) overlaps which suggests that accuracy of identity and its implementation on our cases. The downward flow case offers more hydraulic resistance to the fluid as compared to the upward flow. It is contributed by the buoyancy as shown later by means of term 'C_{10}'. In upward flow case, we observed a peculiarity in the skin friction factor (see Figure 4a). The value of C_f fluctuates around zero initially and then becomes negative. This is a result of the negative wall-normal gradient of streamwise velocity. It means that flow exhibits an annular type of flow in which the gradient in the near-wall region is negative but in the core region it turns to positive.

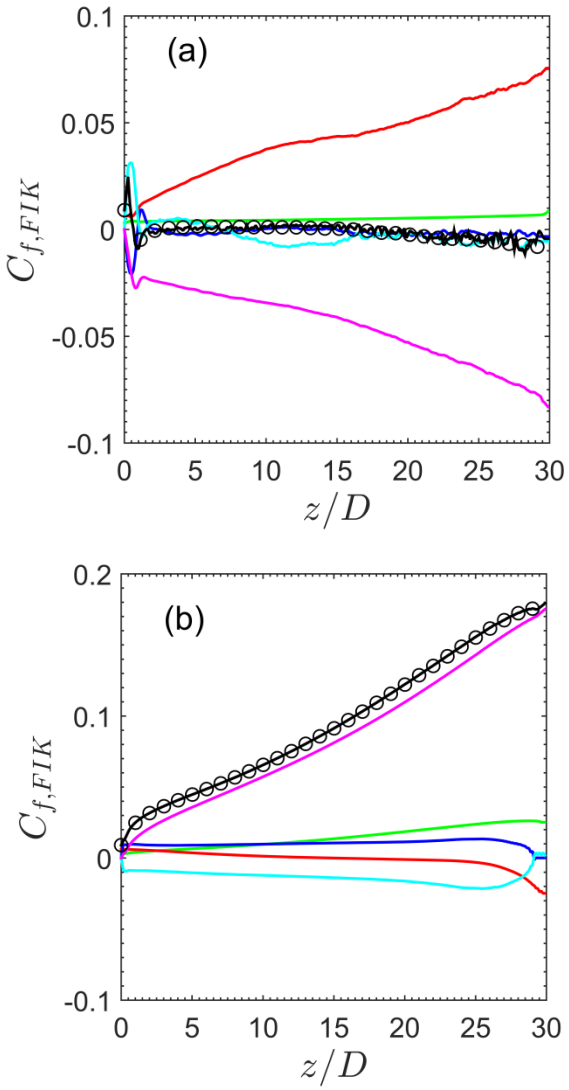

Figure 4: FIK analysis (a) Case UC8q2 and (b) DC8q2; green: C_1, red: C_2, blue: C_4, cyan: C_5, magenta: C_{10}, black: $C_{f,FIK}$, Symbols: C_f from DNS

In both the cases, the bulk Reynolds number decrease in the streamwise direction due to the cooling and it brings down the laminar contribution (C_1). The turbulent contribution (C_2) is decreasing due to the reduction in turbulent shear stress (not shown here). On the other hand, during the upward flow, turbulent shear stress increase and it contributes the comparatively higher magnitude of C_2. The term C_4 depends on the mean velocity profiles in radial and axial directions as well as on the mean density. Their profiles remain approximately constant in the axial direction in case DC8; therefore, we observe an almost constant value in Figure 4b. A similar trend was observed for the upward flow except for a peak in the inlet region, in Figure 4a. The evolution of the streamwise momentum flux directly affects C_5. Interestingly, the buoyancy contribution (C_{10}), has a notable contribution to the overall skin friction factor. For downward flow, C_{10} has a positive magnitude and is responsible for more than 90% of total hydraulic resistance (refer Figure 4b). The negative C_{10} is responsible for the very low skin friction in upward flow in Figure 4a. Though the decomposition of Nusselt number is not shown but a brief discussion is as follow. The results show a similar behavior i.e. enhanced heat transfer in upward flow is brought by the turbulent fraction while in downward flow turbulent contribution reduced significantly which caused ultimately the heat transfer deterioration. Through this analysis, one can deduce that upward flow should be preferred during the cooling of sCO2 in heat exchangers as it will result in higher heat transfer rate and lower pressure drop due to the lesser hydraulic resistance.

A heat transfer recovery was observed earlier in case DC8q2 near to the outlet in Figure 3. To examine it, we perform conditional averaging of the Reynolds shear stress. This method is known as "Quadrant analysis" and for it, data of Reynolds shear stress were sampled based on the sign of $\sqrt{\rho}u_r^{"}$ and $\sqrt{\rho}u_z^{"}$. Depending on their sign, quadrants are named after the possible events which can take place. For instance, the first ($\sqrt{\rho}u_r^{"}>0$, $\sqrt{\rho}u_z^{"}>0$) and third ($\sqrt{\rho}u_r^{"}<0$, $\sqrt{\rho}u_z^{"}<0$) quadrant are known as the wall-normal and wall-ward interaction events, respectively. While the second ($\sqrt{\rho}u_r^{"}>>0$, $\sqrt{\rho}u_z^{"}<0$) and the fourth ($\sqrt{\rho}u_r^{"}<0$, $\sqrt{\rho}u_z^{"}>0$) quadrants ($\sqrt{\rho}u_r^{"}<0$, $\sqrt{\rho}u_z^{"}<0$) are identified as ejection and sweep events, respectively. Ejection event indicates that low-streamwise velocity fluid is moving away from the wall with a high cross-stream velocity, and sweep event shows that high streamwise velocity fluid is moving towards the wall with a lower cross-stream velocity. (Here, high and low are with respect to the mean).

Figure 5 shows the analysis of downward flow case with double heat flux (i.e. case DC8q2) and these quadrants are normalized by the $\sqrt{\tau_w}$ at the inlet. The Quadrant-2 (ejection) and Quadrant-4 (sweep) have the major contribution to Reynolds shear stress at the inlet (at *z=0D*). At z=15D, all events suppress and this leads to the reduced turbulence in the flow. Ultimately, it will result in the deteriorated heat transfer in the downward flow. At z=27.5D, a growth in Quadrant-1 and 3

DOI: 10.17185/duepublico/46079

can be seen in Figure 5. This will recover the turbulence in the flow and results in the heat transfer recovery. An interesting point from this analysis is that heat transfer recovery is brought by the interaction events instead of the typical turbulence generation mechanism (ejection and sweep).

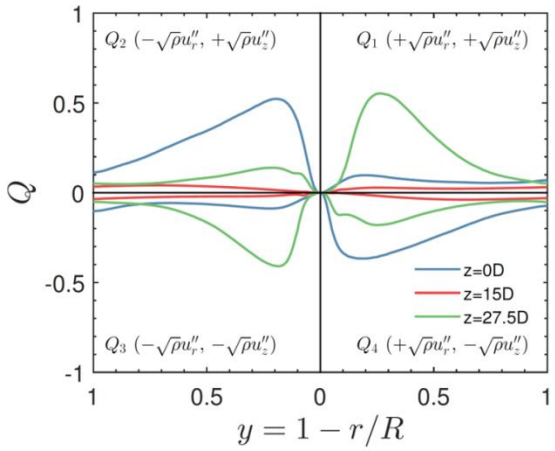

Figure 5: Quadrant analysis for Case DC8q2

The above-discussed quadrant analysis gives information regarding the time-averaged behavior of flow. To further analyze the heat transfer deterioration in the downward flow case (Case DC8q2), we investigate the frequencies of the events over time. We used a statistical technique known as weighted joint probability density function (JPDF), in which probabilities of events are multiplied by the corresponding magnitude. For this analysis, data were sampled at every 100^{th}-time step for 10 flows through times. These data were sampled at different axial locations and here we discuss the few of them in the near-wall area. The iso-contours of weighted JPFD of radial turbulent heat flux is shown in Figure 6 for two different axial locations at *r/R* of 0.8 (corresponding y^+*=36* based on inlet values). At *z=5D,* hot and cold wall-normal motions are responsible for the generation of turbulent heat flux in the wall normal direction. The contributions of existing quadrants become stronger downstream with increasing radial velocity.

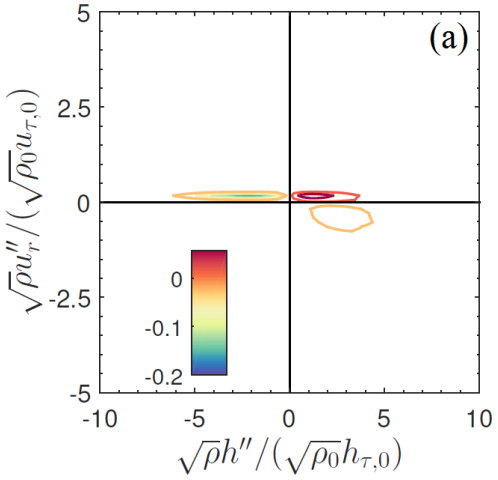

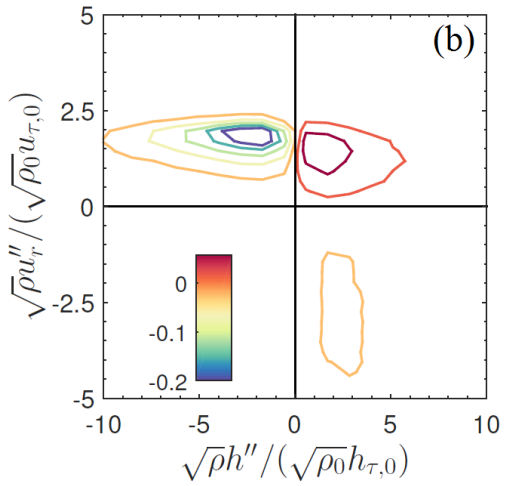

Figure 6: Iso-contours of weighted JPDF of radial turbulent heat flux for Case DC8q2; (a) *z=5D* and (b*) z=27.5D*

Now, we provide a brief discussion on the role of anisotropy in the deteriorated downward flow case (Case DC8q2). This kind of analysis provides the information for properly predicting the amount and type of anisotropy, which is critical for accurate numerical simulation using the conventional modeling approach. The anisotropy is quantified by Reynolds stresses. The Reynolds stress is second order tensor (say b_{ij}, with i,j= 1,2,3) in terms of a 3×3 matrix in which diagonal components are the normal stresses. Therefore, we remove the normal stress and only concentrate on the traceless part of this matrix (say b_{ij}'), and this is normalized by the turbulent kinetic energy. As a next step, the Eigenvalues (say λ_1, λ_2, and λ_3) of this normalized traceless matrix are calculated. Then two new variables are defined as; $\eta^2 = (\lambda_1^2 + \lambda_1\lambda_2 + \lambda_2^2)/3$ and $\xi^3 = -\lambda_1\lambda_2(\lambda_1 + \lambda_2)/2$. The degree of anisotropy is defined with the η and the characteristic shape described by the ξ. Figure 7a shows the mapping of η and ξ, the area bounded by the blue line is known as the Lumley triangle [15]. The vertex of this triangle at the origin is corresponding to the isotropic turbulence, the top right vertex is corresponding to the 1-dimensional turbulence and the left top vertex indicates the 2-dimensional axisymmetric turbulence. At the inlet, turbulence structure is 2-dimensional in near-wall region, while in the core region turbulence has prolate structure. Figure 7b shows the Lumely triangle for the deteriorated heat transfer at *z=15D*. We can see that turbulent structure become 1-component (or rod-like) in the near-wall while in the core region turbulence structure remains the same. This shift to 1-component turbulence structure indicates elongated streaks. The ejection events are responsible for breaking the streaks by 'turbulent burst' and allow the near-wall fluid to move away from the wall. But such events reduce greatly. This attenuates the near-wall turbulence and causes heat transfer deterioration. It suggests that modulation of near-wall turbulence leads to the poor heat transfer in the pipe.

DOI: 10.17185/duepublico/46079

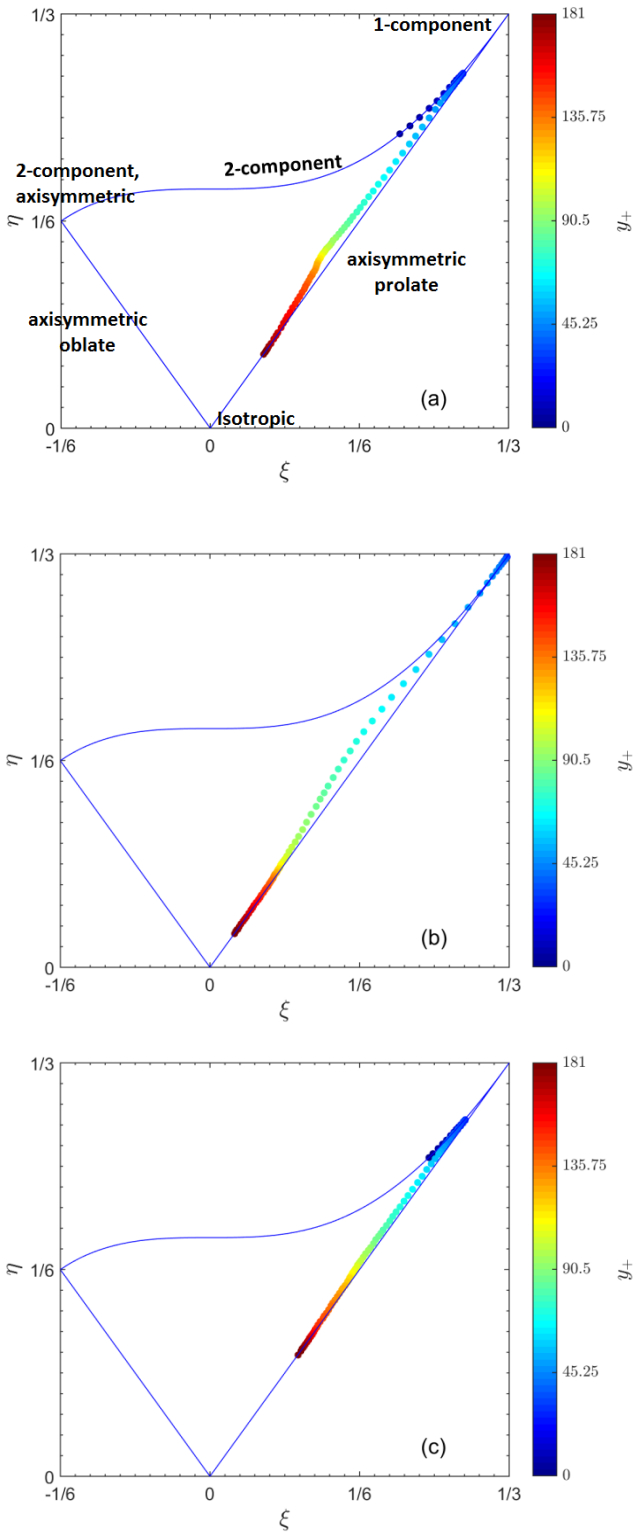

Figure 7: Lumely triangle to visualize the anisotropy of Reynolds stress tensor in the flow for Case DC8q2; (a) *z=0D*, (b) *z=15D* and (c) *z=27.5D*

As soon as the heat transfer recovers at *z=27.5D*, a transition back to the 2-component can be observed in the Figure 7c. As seen earlier in quadrant analysis, the recovery is brought by the interaction events. These interaction events promote the momentum transfer and result in recovery of turbulence thereby the increase in the heat transfer rate.

In the end, flow visualization is discussed with the help of low- and high-speed streak, and vortex. There are different ways by which one can identify the streaks in the flow. In this study, we used $\sqrt{\rho}u_z^{"}$ to take density fluctuation into account. These streaks are identified as the low- and high-speed depending upon their signs and the term low and high correspond to the mean flow. The vortex structures are also identified with the help of $\lambda 2$-criterion. The $\lambda 2$ is the second Eigenvalue of the symmetric tensor $s^2+\omega^2$ with, s and ω as the symmetric an antisymmetric part of velocity gradient tensor. In this study, we use instantaneous velocity fields.

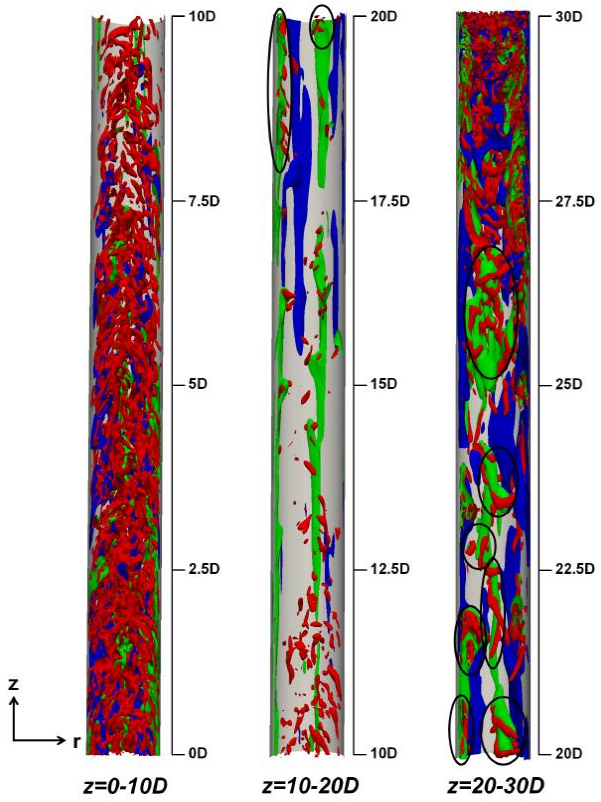

Figure 8: Iso-surfaces of streaks and vortex structure along the pipe for Case DC8q2; blue: low-speed streaks; green: high-speed streaks; red: $\lambda 2$.

Figure 8 shows the iso-surfaces of low- and high-speed streaks along with the iso-surface of $\lambda 2$ to visualize the coherent turbulent structure. The $\lambda 2$ vortex starts reducing in the downstream direction and coherent structures start shifting away from the wall. The low-speed streaks are suppressed and strength of the coherent structure also reduced significantly. Moreover, high-speed streak survives in the flow of the deteriorated heat transfer regime and it is stretched out in the streamwise direction in the near-wall region as observed earlier.

DOI: 10.17185/duepublico/46079

After the reappearance of low-speed streaks at *z=15D*, *λ2* vortex also starts increasing and interestingly the coherent structures are superimposed mainly on the high-speed streak as highlighted with black circles.

SUMMARY

This study was motivated by the wide application of cooling of supercritical CO2 especially in the pre-cooler section of the recompression-Brayton cycle. We carried out numerical experiments and these numerical experiments were conducted with an inlet temperature of 342.05 K and inlet pressure of 8 MPa, which are comparable with the reject heat exchanger in the proposed power cycle. Due to the computational limitations, a moderately low inlet Reynolds number was selected 5400. The results from 6 different DNS were presented here which include upward, downward flow along with the forced convection. The initial investigation shows heat transfer deterioration in downward flow and enhancement for the upward flow. The upward flow case shows a higher heat transfer rate and lower pressure drop due to the lesser hydraulic resistance, which promoted the upward flow orientation in the cooling. Further investigations were focused on the downward flow with double heat flux to understand the reason behind the heat transfer deterioration followed by recovery. We found out that sweep and ejection events which are responsible for the generation of turbulent stresses, decreased significantly and it triggers the attenuated heat transfer. In the deteriorated heat transfer regime, the streak elongates in the near-wall region and turbulence structure becomes rod-like. Near to the outlet section of the investigated domain, a heat transfer recovery was observed. The outward and wall-ward motions are responsible for this recovery, and it gives rise to the turbulent shear stress. In the recovery regime, we observed the streak breakdown and turbulence acquired 2-dimensional structure.

NOMENCLATURE

B_f	Body force (kg/m^{2}s^2)
C_1-C_{10}	Fractions of skin friction factor
C_f	Skin friction factor
D	Pipe diameter (m)
G	mass flux (kg/m^2-s)
h	Specific enthalpy (kJ/kg)
p	Pressure (Pa)
Q	Quadrant
r, θ, z	Radial, circumferential and axial coordinates
S	Strain rate (1/s)
s,	Symmetric of velocity gradient tensor (1/s)
T	Temperature (K)
u	Velocity (m/s)
y	Distance from the wall (m)
κ	Thermal conductivity (W/m^2.K)
λ	Eigenvalue
μ	Dynamic viscosity (Pa-s)
ρ	Density (kg/m^3)
ω	antisymmetric part of velocity gradient tensor (1/s)

ACKNOWLEDGEMENTS

We are thankful to the *Forschungsinstitut für Kerntechnik und Energiewandlung (KE) e.V. Stuttgart*, and *High Performance Computing Center (HLRS) Stuttgart*.

REFERENCES

1. V. Dostal, M. Driscoll, P. Hejzlar, A supercritical carbon dioxide cycle for next generation nuclear reactors. Tech. rep. MIT (2004).
2. Y. Ahn, S.J. Bae, M. Kim, S.K. Cho, S. Baik, J.I. Lee, J.E. Cha, Review of supercritical CO2 power cycle technology and current status of research and development, Nucl. Eng. Technol. 47 (6) (2015), 647–661.
3. E. Lemmon, M. Huber, M. McLinden, NIST standard reference database 23: reference fluid thermodynamic and transport properties-REFPROP, version 9.1 (2013).
4. H. Kim, Y. Bae, H. Kim, J. Soong, B. Cho, Experimental investigation on the heat transfer characteristics on a vertical upward flow of supercritical CO2, in: Proc. ICAPP, Reno, NV (2006).
5. S. He, W. Kim, J. Bae, Assessment of performance of turbulence models in predicting supercritical pressure heat transfer in a vertical tube, Int. J. Heat Mass Transfer 51 (19–20) (2008), 4659–4675.
6. M. Sharabi, W. Ambrosini, S. He, J. Jackson, Prediction of turbulent convective heat transfer to a fluid at supercritical pressure in square and triangular channels, Ann. Nucl. Energy 35 (6) (2008), 993–1005.
7. A. Pucciarelli, I. Borroni, M. Sharabi, W. Ambrosini, Results of 4-equation turbulence models in the prediction of heat transfer to supercritical pressure fluids, Nucl. Eng. Des. 281 (2015), 5–14.
8. J.H. Bae, J.Y. Yoo, H. Choi, Direct numerical simulation of turbulent supercritical flows with heat transfer, Phys. Fluids 17 (10) (2005).
9. X. Chu, E. Laurien, Flow stratification of supercritical CO2 in a heated horizontal pipe, J. Supercrit. Fluids 116 (2016), 172–189.
10. H. Nemati, A. Patel, B.J. Boersma, R. Pecnik, Mean statistics of a heated turbulent pipe flow at supercritical pressure, Int. J. Heat Mass Transfer 83 (2015), 741–752.
11. X. Chu, E. Laurien, D.M. McEligot, Direct numerical simulation of strongly heated air flow in a vertical pipe, Int. J. Heat Mass Transfer 101 (2016), 1163–1176.
12. X. Chu, E. Laurien, Direct numerical simulation of heated turbulent pipe flow at supercritical pressure, J. Nucl. Eng. Radiat. Sci. (2) (2016).

DOI: 10.17185/duepublico/46079

13. K. Fukagata, K. Iwamoto, and N. Kasagi, Contribution of Reynolds stress distribution to the skin friction in wall-bounded flows," Physics of Fluids 14 (2002).

14. H. Nemati, A. Patel, B. J. Boersma, and R. Pecnik, The effect of thermal boundary conditions on forced convection heat transfer to fluids at supercritical pressure," Journal of Fluid Mechanics 800 (2016), 531-556.

15. J. Lumley, and G. Newman, The return to isotropy of homogenous turbulence. J. Fluid Mech. 82 Lumley, J. & Newman, G. The return to isotropy of homogenous turbulence. J. Fluid Mech. 82 (1977), 161–178.

16. S. Pandey, E. Laurien, Heat transfer analysis at supercritical pressure using two layer theory, J Supercritical Fluids (2016), 80-86.

17. S. Pandey, E. Laurien, X. Chu, A modified convective heat transfer model for heated pipe flow of supercritical carbon dioxide, Int. J. Therm. Sci. 117 (2017), 227–238.

18. X. Chu, W. Chang, S. Pandey, J. Luo, B. Weigand, and E. Laurien, A computationally light data-driven approach for heat transfer and hydraulic characteristics modeling of supercritical fluids: From DNS to DNN, Int. J. Heat Mass Transfer 123 (2018), 629–636.

19. J. W. R. Peeters, R. Pecnik, M. Rohde, T. H. J. J. van der Hagen, and B. J. Boersma, Characteristics of turbulent heat transfer in an annulus at supercritical pressure, Physical Review Fluids 2 (2017), 024602.

DOI: 10.17185/duepublico/46079

2nd European supercritical CO2 Conference
August 30-31, 2018, Essen, Germany

2018-sCO2.eu-123

A NOVEL APPROACH TO ACCURATELY MODEL HEAT TRANSFER TO SUPERCRITICAL FLUIDS

Gustavo J. Otero R.
Process and Energy Department Mechanical Engineering Delft University of Technology
Delft, the Netherlands
Email: g.j.oterorodriguez@tudelft.nl

Ashish Patel
Process and Energy Department Mechanical Engineering Delft University of Technology
Delft, the Netherlands
Email: a.patel@tudelft.nl

Rene Pecnik*
Process and Energy Department
Mechanical Engineering Delft
University of Technology
Delft, the Netherlands
Email: r.pecnik@tudelft.nl

ABSTRACT

We propose to solve the standard turbulence models on their semi-locally scaled form to considerably increase their accuracy for predicting turbulent heat transfer to supercritical fluids. Many previous studies have shown that current turbulence models are unable to provide a reasonable result for heat transfer calculations [1], which leaves heat exchanger manufactures to rely on empirical correlations in their design process. Using simulations that are based on first principles, i.e. simulations that completely resolve turbulence without using turbulence models, we gained fundamental knowledge on turbulent heat transfer to supercritical fluids [14,19] that allowed us to considerably improve turbulence models.

INTRODUCTION

Research in the field of supercritical heat transfer has been active since the fifties to support the thermal design of fossil fueled power plants operating at supercritical pressures. The interest in this field regained momentum in the nineties [21] owing to its potential to improve the thermal efficiency in modern nuclear power plants. Several experiments were conducted during this period using water or CO_2 flowing in heated vertical tubes at supercritical pressures to collect data for heat transfer distributions and wall temperatures. Most of the experiments were conducted in the turbulent regime with high Reynolds numbers. Results from these experiments, especially in upward flows, showed peculiar features of turbulent heat transfer to supercritical fluids such as heat transfer enhancement and deterioration [1]. Peculiar characteristics of heat transfer were often observed when the bulk temperature (T_b) was less than the pseudo-critical temperature (T_{pc}) and the wall temperature (T_w) was higher than the pseudo-critical temperature, namely $T_b < T_{pc} < T_w$, relevant for the compression process of the supercritical CO_2 power cycle [26]. Several comprehensive reviews on heat transfer to supercritical fluids have been published by [20,6,10,9,22,21,3] and recently by [27].

More recently, detailed numerical simulations (direct numerical simulations, DNS) have been performed to study heat transfer to supercritical fluids in turbulent pipe flows by [1,14]. However, these accurate simulations are limited to simple geometries and low Reynolds numbers. Because of this fact, turbulence models rely on a limited number of accurate data, and their development is moreover hampered by the lack of knowledge on how turbulence is affected by strong variations of thermophysical properties, e.g. in the supercritical region. Since all turbulence models have been developed for incompressible flows, several extensions have been proposed in the past by [7,23,28] to include compressible effects, but their predictive capability for flows with strong thermophysical property variations is still low.

In this work, we propose to use turbulence models in their semi-locally scaled form to properly account for thermo-physical variations. The starting point of the derivation is the semi-locally scaled (SLS) turbulent kinetic energy (TKE) equation, which was derived by Pecnik and Patel [19]. The derivation is based on analytic scaling laws and is therefore applicable, as we will discuss later in this paper, to several eddy viscosity models. The results of the models are then compared to DNS data for a fully developed turbulent channel flow with

DOI:10.17185/duepublico/46095

varying thermo-physical properties [16], and a heated turbulent pipe flow with CO_2 at super-critical pressure [14].

SLS TURBULENCE MODELLING

Huang *et al.* [8] in 1995 proposed the semi-local scaling (SLS) to collapse turbulence statistics for compressible flows at high Mach numbers with turbulence statistic for incompressible flows. SLS is based on local mean quantities, like density and viscosity, and the wall shear stress τ_w to account for changes in viscous scales due to mean variations in thermophysical properties. The semi-locally scaled friction velocity is defined as $u_\tau^\star = \sqrt{\tau_w/\langle\rho^*\rangle}$, where $\langle\cdot\rangle$ indicated Reynolds averaging. Accordingly, the semi-local wall distance can be defined as

$$y^\star = \frac{u_\tau^\star \langle\rho^*\rangle\, y}{\langle\mu^*\rangle}$$

and the semi-local Reynolds number as,

$$Re_\tau^\star = \frac{u_\tau^\star \langle\rho^*\rangle\, h^*}{\langle\mu^*\rangle} = \sqrt{\frac{\langle\rho^*\rangle}{\rho_w^*}}\frac{\mu_w^*}{\langle\mu^*\rangle}Re_\tau$$

where h^* the characteristic length of the flow geometry, $Re_\tau = u_\tau\rho_w^* h^*/\mu_w^*$ is the friction Reynolds number and $u_\tau = \sqrt{\tau_w/\rho_w^*}$ is the friction velocity, both based on viscous wall units. Given the scaling based on wall units and semi-local units, any flow variable can be non-dimensionalized as outlined in table 1.

Pecnik and Patel [19] extended the use of the SLS to derive an alternative form of the TKE equation for wall-bounded flows with strong variations in thermophysical properties. The derived SLS TKE equation then reveals that effects of property variations on turbulence can be characterized by gradients of the semi-local Reynolds number $Re_\tau^\star$ only, and that the additional compressible terms in the TKE equation, such as the solenoidal dissipation, pressure -work, -diffusion and -dilatation, have a minor effect on the change in near-wall turbulence [8,19]. The SLS TKE reads,

$$t_\tau^\star\frac{\partial\hat{\rho}\hat{k}}{\partial t^*} + \frac{\partial\hat{\rho}\hat{k}\hat{u}_j}{\partial\hat{x}_j} = \hat{P}_k - \hat{\rho}\hat{\varepsilon} + \frac{\partial}{\partial\hat{x}_j}\left[\left(\frac{\hat{\mu}}{Re_\tau} + \frac{\hat{\mu}_t}{\sigma_k}\right)\frac{\partial\hat{k}}{\partial\hat{x}_j}\right]$$

with $\hat{P}_k$ as the turbulent production and $t_\tau^\star = h^*/u_\tau^\star$. The semi-locally scaled quantities are denoted with the accent "^", as $\hat{\phi}$. Note, for a fully developed turbulent channel flow the turbulent production can be written as $\hat{P}_k = \hat{\mu}_t(\partial\hat{u}/\partial y)^2$. If the equation above is used to determine the turbulent shear stress using the Boussinesq approximation, it was shown that the turbulence model (v^2-f model [4]) results significantly improve -- if compared to DNS -- for turbulent channel flows with strong variations in density and viscosity.

In this work, we investigate if other eddy viscosity turbulence models can be used in their semi-locally scaled form as well to improve their predictive capability for flows with large property variations. We chose five models

- an algebraic model developed by Cess in 1958 [2],
- the one-equation model of Spalart-Allmaras (SA) [24],
- the low Reynolds number $k-\varepsilon$ model of Myong and Kasagi (MK) [13],
- Menter's shear stress transport (SST) model [12],
- and the four-equations v^2-f model (V2F) [4].

In order to change a model into its semi-locally scaled form, it is necessary to set $\hat{\rho}=1$, replace $\hat{\mu}$ by $1/Re_\tau^\star$, replace $\partial\hat{u}$ in P_k by $\partial u^{vD} = \sqrt{\langle\rho^*\rangle/\rho_w^*}\,\partial(\{u^\star\}/u_\tau)$, and, if a model makes use of y^+ and/or Re_τ, replace them by $y^\star$ and $Re_\tau^\star$, respectively [19]. Note that $\{\cdot\}$ indicates Favre averaging.

TEST CASES

In order to test the proposed methods, two different test cases are investigated, first a fully developed channel flow for a fluid with varying thermo-physical properties, density and viscosity are only function of temperature, similar to those of CO_2, and second a heated turbulent pipe flow with carbon dioxide undergoing heat transfer at super-critical pressure. The second test case is a developing flow which crosses the supercritical temperature, therefore strong gradients in density, viscosity, and thermal conductivity are simulated. Tables 2 and 3 describe in more detail the fully developed channel flow case and heated turbulent pipe flow case, respectively.

1. FULLY DEVELOPED CHANNEL FLOW

The Favre-averaged Navier-Stokes equations, written in Cartesian coordinates, are used to simulate a fully developed channel flow. The conservation equations for streamwise momentum and energy are solved in non-dimensional form, normalized by values at the channel wall, and are given as,

$$0 = \langle\rho\rangle\langle f_x\rangle + \frac{\partial}{\partial y}\left[\left(\frac{\langle\mu\rangle}{Re_\tau} + \mu_t\right)\frac{\partial\{u\}}{\partial y}\right]$$

$$0 = \frac{\Phi}{Re_\tau\, Pr_w} + \frac{\partial}{\partial y}\left[\left(\frac{\lambda}{Re_\tau\, Pr_w} + \frac{Cp\mu_t}{Pr_t}\right)\frac{\partial\{T\}}{\partial y}\right]$$

where T and λ are the locally scaled temperature and thermal conductivity, respectively, all normalized with wall quantities, ϕ_w. The wall Prandtl number is defined as $Pr_w = \mu_w^* Cp_w^*/\lambda_w^*$, where Cp_w^* is the isobaric heat capacity. The flow is driven by an external body force, $\langle\rho\rangle\langle f_x\rangle$, set to 1 for the normalized momentum equation. The temperature at both channel walls is maintained constant. The uniform volumetric heat source increases the temperature within the channel, such that variation on density and viscosity occur. The Reynolds shear stress and turbulent heat flux, are modeled using the Boussinesq approximation and the gradient diffusion hypothesis, respectively. The turbulent Prandtl number is assumed constant as $Pr_t = 1$ [17]. As the normalized conservation equations are solved, the semi-locally scaled eddy viscosity $\hat{\mu}_t$, which is provided by the turbulence model, has to be transformed to the conventionally scaled form μ_t, see table 1.

DOI:10.17185/duepublico/46095

Table 1. Comparison of local ϕ and semi-local $\hat{\phi}$ scaling for most relevant quantities. The superscript $*$ denotes dimensional quantities, not to be confused with $\star$ which is used for SLS characteristic variables ($Re_\tau^\star, u_\tau^\star, y^\star$). The subscript w indicates a reference condition, most commonly the value at the wall is chosen.

Quantity			Local Scaling		Semi-local scaling	Units
Length	x_i^*	=	$x_i h^*$	=	$\hat{x}_i h^*$	$[m]$
Wall distance	y^*	=	$y^+ h^*/Re_\tau$	=	$y^\star h^*/Re_\tau^\star$	$[m]$
Velocity	u^*	=	$u\, u_\tau$	=	$\hat{u}\, u_\tau^\star$	$[m/s]$
Pressure	p^*	=	$p\, \rho_w^* u_\tau^2$	=	$\hat{p}\, \langle\rho^*\rangle u_\tau^{\star 2}$	$[(kg\ m/s^2)/m^2]$
Density	ρ^*	=	$\rho\rho_w^*$	=	$\hat{\rho}\langle\rho^*\rangle$	$[kg/m^3]$
Viscosity	μ^*	=	$\mu\mu_w^*$	=	$\hat{\mu}\langle\mu^*\rangle$	$[kg/(m\ s)]$
Eddy viscosity	μ_t^*	=	$\mu_t \rho_w^* h^* u_\tau$	=	$\hat{\mu}_t\langle\rho^*\rangle h^* u_\tau^\star$	$[kg/(m\ s)]$
Turbulent Kinetic energy	k^*	=	$k\, u_\tau^2$	=	$\hat{k}\, u_\tau^2$	$[m^2/s^2]$
Turbulent Dissipation	ε^*	=	$\varepsilon\, u_\tau^3/h^*$	=	$\hat{\varepsilon}\, u_\tau^{\star 3}/h^*$	$[m^2/s^3]$
Specific turbulent dissipation	ω^*	=	$\omega\, u_\tau/h^*$	=	$\hat{\omega}\, u_\tau^\star/h^*$	$[1/s]$

Table 2. Test case investigated for the fully developed channel flow: C $Re_\tau^\star$- refers to a variable property case with a fluid whose density and viscosity are proportional to $1/T$ and $\sqrt{1/T}$ respectively, such that $Re_\tau^\star$ remains constant across the channel. The DNS data were taken from Patel *et al.* 2016 [18]. $Re_{\tau_w}^\star$ and $Re_{\tau_c}^\star$ refer to the value of the semi-local Reynolds number at the wall and center of the channel, respectively, while Φ refers to the volumetric heat source. No-slip conditions and equal temperature at both channel walls are applied as boundary conditions.

Case	ρ/ρ_w	μ/μ_w	$Re_{\tau_w}^\star$	$Re_{\tau_c}^\star$	Φ
Constant $Re_\tau^\star$ (C $Re_\tau^\star$)	$(T/T_w)^{-1}$	$(T/T_w)^{-0.5}$	395	395	95

Table 3. Test cases investigated for the supercritical CO_2 pipe flow. A flow with forced convection flow and an upward flow with high buoyancy are considered. The DNS was taken from Nemati *et al.* [14]. The forced convection and the mixed flow are named case A and case C in [14], respectively. Re_τ is the Reynolds number based on the friction velocity at the pipe inlet, Ri_x is the Richardson number, while Q refers to the dimensionless wall heating. No-slip condition and a constant heat flux at the pipe wall are applied as boundary conditions.

Case	Type	Flow direction	Re_τ	Ri_x	Q
A	Forced	–	360	0.0	2.4
C	Mixed	Upward	360	-79.67	2.4

The result for all turbulence models are now compared with the results obtained by DNS, see figure 1. In all of the resulting plots, the DNS data are plotted using symbols, while the model results are depicted with lines. The results for the velocity are reported in terms of u/u_{max} figure 1(a), and $u^\star$, figure 1(b), whereby u_{max} is the maximum DNS velocity and $u^\star = \int_0^{u^{vd}} [1 + (y/Re_\tau^\star)\partial Re_\tau^\star/\partial y\,]\partial u^{vd}$ is the universal transformation as given in Patel *et al.* [18]. The Reynolds shear stresses are shown in figure 1(c). The modification clearly improves the performance of the turbulence models for flows with strong variations on the thermo-physical properties. For both profiles of $u^\star$ and $\{u''v''\}/\tau_w$, a good collapse is seen with the DNS data for most of the turbulence models solved in semi-local form, outperforming the conventional models.

2. SUPERCRITICAL CARBON DIOXIDE FLOW IN A PIPE

The Favre-averaged Navier-Stokes equations, written in cylindrical coordinates, are solved to investigate the heated turbulent pipe flow with a fluid undergoing heat transfer at super-critical pressure. The governing equations can be expressed in non-dimensional form, using the low-Mach number approxumation, assuming a two-dimensional axis-symmetric flow, without time derivative as:

- for momentum in streamwise direction,

$$\frac{\partial\langle\rho\rangle\{u\}^2}{\partial x} + \frac{1}{r}\frac{\partial\, r\langle\rho\rangle\{u\}\{u_r\}}{\partial r} = -\frac{\partial\langle p\rangle}{\partial x} + \langle\rho\rangle Ri_x + \frac{\partial}{\partial x}\left[\left(\frac{\langle\mu\rangle}{Re_\tau} + \mu_t\right)\left(2\frac{\partial\{u\}}{\partial x} - \frac{2}{3}\nabla.\{\boldsymbol{u}\}\right)\right] + \frac{1}{r}\frac{\partial}{\partial r}\left[r\left(\frac{\langle\mu\rangle}{Re_\tau} + \mu_t\right)\left(\frac{\partial\{u\}}{\partial r} + \frac{\partial\{u_r\}}{\partial x}\right)\right]$$

- for momentum in radial direction,

$$\frac{1}{r}\left[\frac{\partial r\langle\rho\rangle\{u\}\{u_r\}}{\partial x} + \frac{\partial\, r\langle\rho\rangle\{u_r\}^2}{\partial r}\right] = -\frac{\partial\langle p\rangle}{\partial r} + \frac{1}{r}\frac{\partial}{\partial r}\left[r\left(\frac{\langle\mu\rangle}{Re_\tau} + \mu_t\right)\left(2\frac{\partial\{u_r\}}{\partial r} - \frac{2}{3}\nabla.\{\boldsymbol{u}\}\right)\right] + \frac{\partial}{\partial x}\left[\left(\frac{\langle\mu\rangle}{Re_\tau} + \mu_t\right)\left(\frac{\partial\{u\}}{\partial r} + \frac{\partial\{u_r\}}{\partial x}\right)\right] - \frac{1}{r}\left(\frac{\langle\mu\rangle}{Re_\tau} + \mu_t\right)\left(2\frac{\{u_r\}}{r} - \frac{2}{3}\nabla.\{\boldsymbol{u}\}\right)$$

- and energy,

DOI:10.17185/duepublico/46095

$$\frac{\partial\langle\rho\rangle\{H\}\{u\}}{\partial x}+\frac{1}{r}\frac{\partial\, r\langle\rho\rangle\{H\}\{u_r\}}{\partial r}$$
$$=\frac{1}{r}\frac{\partial}{\partial r}\left[r\left(\frac{\langle\lambda\rangle/Cp}{Re_\tau Pr}+\frac{\mu_t}{Pr_t}\right)\frac{\partial\{H\}}{\partial r}\right]$$
$$+\frac{\partial}{\partial x}\left[\left(\frac{\langle\lambda\rangle/Cp}{Re_\tau Pr}+\frac{\mu_t}{Pr_t}\right)\frac{\partial\{H\}}{\partial x}\right]$$

Where H is the enthalpy, u_r is the radial velocity component, $\nabla.\{\boldsymbol{u}\}$ is the divergence of the velocity vector in cylindrical coordinates, and $Ri_x = g_x^* h^*/u_\tau$ is the Richardson number that takes into account the buoyancy effects with g_x^* the gravitational acceleration. Moreover, the turbulence models are solved in cylindrical coordinates with buoyancy production G_k in the $k-$, $\varepsilon-$ and $\omega-$ equation. In order to estimate the thermo-physical properties of the supercritical CO_2, a multi-parameter equation of state (Kunz and Wagner [11]) is used. The relations between the viscosity and thermal conductivity are given by Fenghour *et al* [5] and Vesovic *et al* [25], respectively. The turbulent heat flux is modelled with the turbulent Prandtl number, which is assumed constant ($Pr_t = 0.9$).

The simulation of the super-critical fluid in the heated pipe consists of two parts. First, a fully developed pipe flow with periodic inlet and outlet boundaries, and no heat transfer from the wall is used to generate the inflow for the developing simulation. Later, a developing pipe flow uniformly heated from the wall is simulated. Two cases are considered, which are reported in table 3. For all the simulations of the supercritical CO_2 flow in a pipe, the inflow conditions correspond to $p_0 = 80$ bar and $T_0 = 310$ K. Therefore by heating the pipe, the pseudo-critical conditions are achieved. In the supercritical the transport properties such as the density, viscosity, and thermal conductivity show strong gradients.

Figures 2 and 3 depict the comparison of the temperature along the pipe wall between DNS (Nemati *et al.*[15]) and the different turbulence models, solved in their conventional and semi-locally scaled form, respectively. For the case of forced convection (figure 2) it can be seen that the SST model shows the best agreement with DNS if it is solved in its conventional form. While for the SA, MK and V2F models, the results for the wall temperature is improved, if the turbulence model in SLS form is used. The largest improvement using the turbulence model in SLS form is achieved with the V2F model, whereas the conventional V2F significantly over-predicts the wall temperature. In general, it can be seen that using the semi-locally scaled form of the turbulence models, all results are more consistent.

For the case with high buoyancy, shown in figure 3 (Ri_x =-79.67), the flow experiences both heat transfer deterioration and recovery according to the DNS data. The heat transfer deterioration can be noticed by the increase of wall temperature at the beginning of the heated pipe (x/L<20), while afterwards, the wall temperature decreases, indicating a better heat transfer and thus a heat transfer recovery. We have estimated the deterioration and recovery using the turbulence models in their conventional and SLS forms. However, an over-prediction of the wall temperature is seen in all cases. Moreover, the V2F strongly overemphasizes the heat transfer deterioration and recovery. For this specific case, the SLS versions of SA, V2F, and MK are closer to the DNS data. The most likely reason for over predicted wall temperatures using the turbulence model is the crude approximation of the buoyancy production term (G_k) and turbulent heat flux. The buoyancy production term we used for the turbulence models is calibrated for a fluid that obeys the ideal gas law. Moreover, the turbulent heat flux was modelled with a constant Prandtl number, which is not valid for flows with high molecular Prandtl number, as is the case for a supercritical fluid. In order to improve the model results, it is thus necessary to develop better models for the buoyancy production and turbulent heat flux term that are based on DNS of supercritical fluid flows.

CONCLUSION

Solving the turbulent transport equations in semi-local scaled form make turbulence models more reliable for wall bounded flows with strong gradients in the thermo-physical properties. The methodology is based on the semi-local scaling of the turbulent transport equations, which has shown excellent agreement with DNS data in previous work. Even though, the semi-locally scaled turbulent equations do not take into account common compressibility terms, such as; pressure work term and pressure dilation, the compressibility effects are taken into account by the semi-locally scaled variables. In general, the semi-locally scaled turbulence models result in a better agreement with the DNS data in terms of the velocity profile and the heat transfer for the investigated cases herein. Interestingly, the original Spalart-Allmaras model, the one equation turbulence model originally developed for external flow, gives the most reliable results, if compared to other standard models, for the variable property cases investigated herein. However, we recommend using Myong and Kasagi's low Reynolds number model with the method of this study for supercritical CO_2 application as it is a simple model if compared to the SST and V2F model, and a better approximation of the buoyancy production G_k can be developed. The SA model has no $k-$equation and therefore has no buoyancy production term.

REFERENCES

[1] J. H. Bae, J. Y. Yoo, and H. Choi. Direct numerical simulation of turbulent supercritical with heat transfer, Journal of Physics of Fluids, (April), 2005.

[2] D. Cess, R. A Survey of the literature in heat transfer in turbulent tube Tech. Westinghouse Research Rept, Report 8-0529-R-24, 1958.

[3] R. B. Duey and I. L. Pioro. Experimental heat transfer of supercritical carbon dioxide inside channels (survey), Nuclear Engineering and Design, 235(8): 913-924, 2005.

[4] P. A. Durbin. Separated Flow Computations with the k-e-v2 Model. AIAA Journal, 33(4): 659-664, 1995.

DOI:10.17185/duepublico/46095

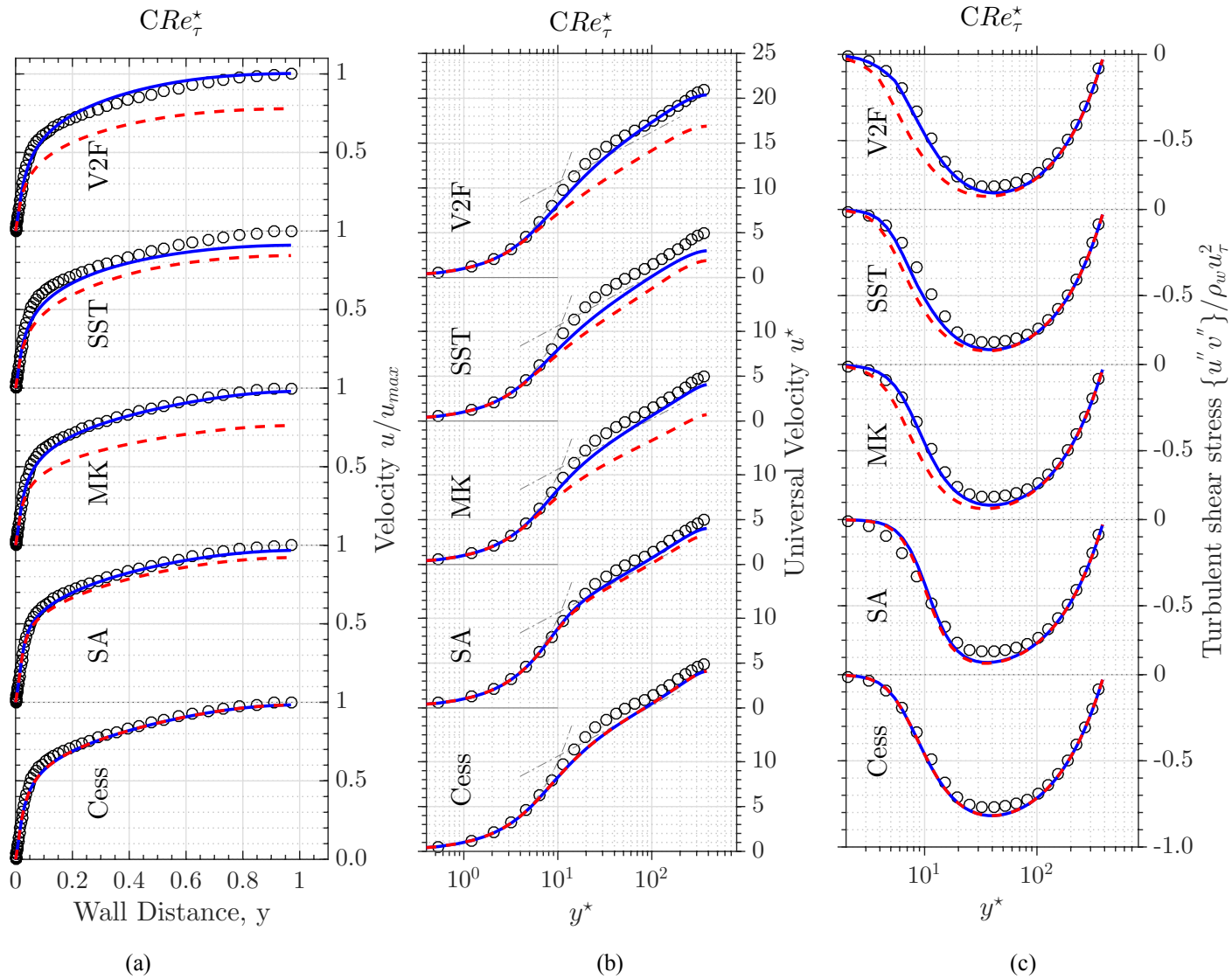

Figure 1. Fully developed turbulent channel flow results, DNS in symbols compared to conventional (dashed red line) and current study (solid blue line) turbulence model for five turbulence models: Cess, Spalart Allmaras, Myong and Kasagi, Menter's shear stress transport and Durban's $v^2 - f$. (a) Mean velocity by maximum DNS velocity u/u_{max} with respect to the wall-normal distance y, (b) Universal velocity transformation $u^\star$ with respect to the semi-locally scaled wall normal distance $y^\star$, and (c) Semi-locally scaled Reynolds stress $\{u''v''\}/\tau_w$ with respect to the semi-locally scaled wall normal distance $y^\star$. The grey dashed line in b) respresent $u^\star = y^\star$ and $u^\star = \frac{1}{\kappa}\ln(y^\star) + C^\star$ in the viscous sub-layer and log-law region, respectively, where $\kappa = 0.41$ and $C^\star = 5.5$.

DOI:10.17185/duepublico/46095

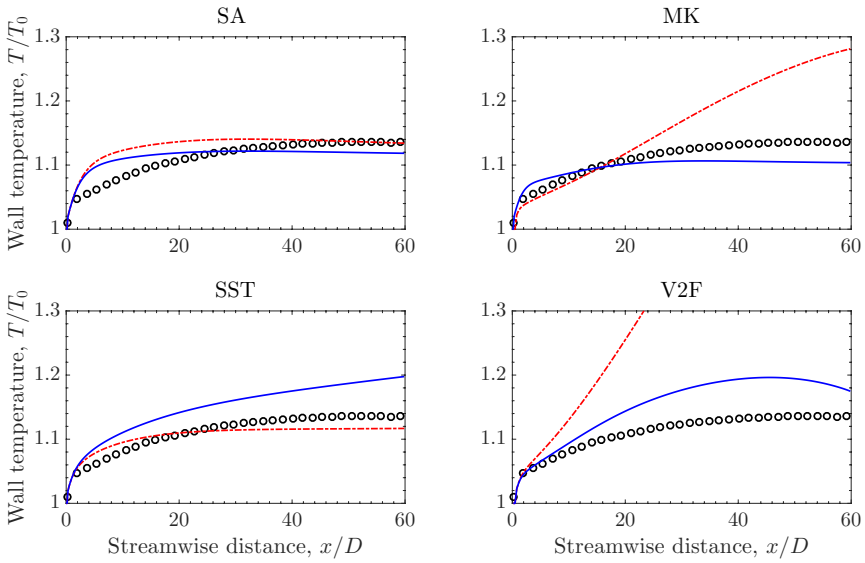

Figure 2. Case A: Wall temperature with respect to the streamwise distance for a heated pipe flow with CO_2 at supercritical pressure under forced convection. DNS results in symbols compared to conventional (dashed red line) and current study (solid blue line) turbulence model for four turbulence models: Spalart Allmaras, Myong and Kasagi, Menter's shear stress transport and Durban's $v^2 - f$.

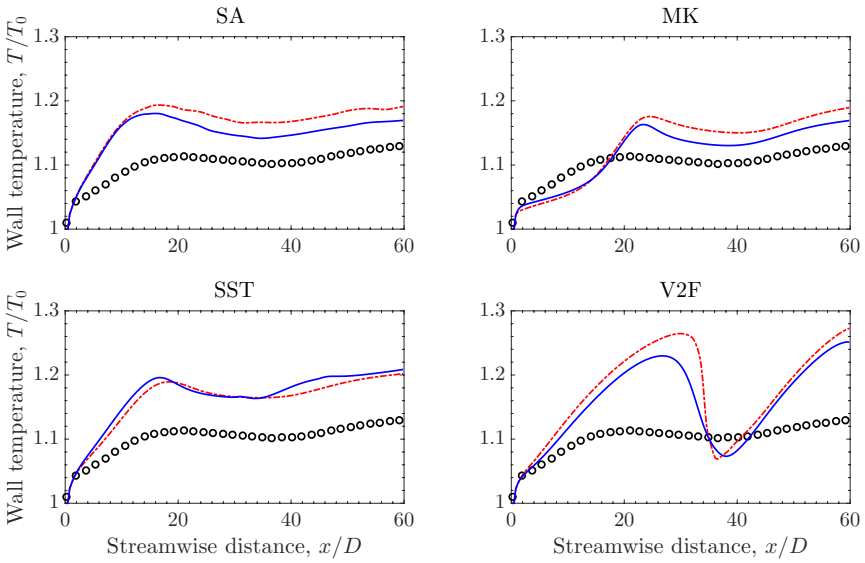

Figure 3. Case C: Wall temperature with respect to the streamwise distance for a heated pipe flow with CO_2 at supercritical pressure under mixed flow and upward flow with average buoyancy Ri_x =-79.67. DNS results in symbols compared to conventional (dashed red line) and current study (solid blue line) turbulence model for four turbulence models: Spalart Allmaras, Myong and Kasagi, Menter's shear stress transport and Durban's $v^2 - f$

[5] A. Fenghour, W. Wakeham, and V. Vesovic. The viscosity of carbon dioxide, Journal of Physical and Chemical Reference Data, (27):31-44, 1998.

[6] W. B. Hall. Heat transfer near the critical point. Advances in Heat Transfer, 7(1): 86, 1971.

[7] P. G. Huang, P. Bradshaw, and T. J. Coakely. Turbulence models for compressible boundary layers. AIAA Journal, 32(4):735-740, 1994. ISSN 0001-1452. doi: 10.2514/3.12046. URL http://arc.aiaa.org/doi/10.2514/3.12046.

[8] P. Huang, P. G., Coleman, G. N., Bradshaw. Compressible Turbulent channel flows, DNS results and modeling. JFM, (1995): 185-218, 1995.

[9] J. D. Jackson and W. B. Hall. Forced convection heat transfer to fluids at supercritical pressure. Turbulent Forced Convection in Channels and Bundles, 2:563-611, 1979.

[10] J. D. Jackson and W. B. Hall. Influences of buoyancy on heat transfer to fluids in vertical tubes under turbulent conditions. Turbulent Forced Convection in Channels and Bundles, 2:613{640, 1979.

[11] O. Kunz and W. Wagner. The gerg-2008 wide-range

DOI:10.17185/duepublico/46095

equation of state for natural gases and other mixtures: an expansion of gerg-2004. Journal of chemical & engineering data, 57(11): 3032-3091, 2012.
[12] F. R. Menter. Zonal Two Equation k-w, Turbulence Models for Aerodynamic Flows. AIAA paper, page 2906, 1993. doi: 10.2514/6.1993-2906.
[13] N. Myong, H.K. and Kasagi. A new Approach to the Improvement of k-e turbulence model for wall-bounded shear flows. JSME, 33(2), 1990.
[14] H. Nemati, A. Patel, B. J. Boersma, and R. Pecnik. Mean statistics of a heated turbulent pipe flow at supercritical pressure. International Journal of Heat and Mass Transfer, 83:741-752, 2015.
[15] H. Nemati, A. Patel, B. J. Boersma, and R. Pecnik. The effect of thermal boundary conditions on forced convection heat transfer to fluids at supercritical pressure. Journal of Fluid Mechanics, 800:531{556, 2016.
[16] A. Patel, J. W. R. Peeters, B. J. Boersma, and R. Pecnik. Semi-local scaling and turbulence modulation in variable property turbulent channel flows. 095101, 2015. doi: 10.1063/1.4929813. URL http://dx.doi.org/10.1063/1.4929813.
[17] A. Patel, B. J. Boersma, and R. Pecnik. Scalar statistics in variable property turbulent channel flows. Physical Review Fluids, 2(8):084604, 2017.
[18] R. Patel, A; Boersma, B; Pecnik. The influence of near-wall density and viscosity gradients on turbulence in channel flows. 2016.
[19] A. Pecnik, R., Patel. Scaling and Modelling of turbulence in variable property channel, Journal of fluid Mechanics 2017.
[20] B. S. Petukhov. Heat transfer and friction in turbulent pipe flow with variable physical properties. Advances in Heat Transfer, 6:503{564, 1970.
[21] I. L. Pioro, H. F. Khartabil, and R. B. Duffey. Heat transfer to supercritical fluids owing in channels-empirical correlations (survey). Nuclear Engineering and Design, 230(1):69{91, 2004.
[22] A. F. Polyakov. Heat transfer under supercritical pressures. Advances in Heat Transfer, 21:1-53, 1991.
[23] S. Sarkar, G. Erlebacher, M. Hussaini, and H. Kreiss. The analysis and modelling of dilatational terms in compressible turbulence. Journal of Fluid Mechanics, 227:473-493, 1991.
[24] A. Spalart, S, Allmaras. A One-Equatlon Turbulence model. doi: 10.2514/6.1992-439.
[25] V. Vesovic, W. Wakeham, G. Olchowy, J. Sengers, J. Watson, and J. Millat. The transport properties of carbon dioxide. Journal of physical and chemical reference data, 19(3):763-808,
1990.
[26] S. A. Wright, R. F. Radel, M. E. Vernon, G. E. Rochau, and P. S. Pickard. Operation and analysis of a supercritical co2 brayton cycle. Sandia Report, No. SAND2010-0171, 2010.
[27] J. Y. Yoo. The turbulent ows of supercritical uids with heat transfer. Annual Review of Fluid Mechanics, 45:495{525, 2013.
[28] O. Zeman. A new model for super/hypersonic turbulent boundary layers. In 31st Aerospace Sciences Meeting, page 897, 1993.

DOI:10.17185/duepublico/46095

2nd European supercritical CO2 Conference
August 30-31, 2018, Essen, Germany

2018-sCO2.eu-128

IMPACT OF SOLAR TOWER DESIGN PARAMETERS ON SCO2-BASED SOLAR TOWER PLANTS

Reiner Buck*
DLR, SF-STS
Stuttgart, Germany
reiner.buck@dlr.de

Stefano Giuliano
DLR
Stuttgart, Germany

ABSTRACT

Integrating high efficiency sCO_2 power cycles into solar tower plants is characterized by high upper temperature and low temperature spread of the cycle working fluid sCO_2. New heat transfer media (HTM) are required, enabling higher temperatures and low cost storage. The present study evaluates modular solar tower plants using solid particles as HTM, allowing temperatures up to 1000°C. In a parameter study the influence of HTM temperatures on levelized cost of electricity (LCoE) is evaluated.

The results show a significant impact of the HTM temperature selection, mainly governed by the HTM temperature difference. A high temperature difference results in reduced LCoE. The most important factors for this reduction are the reductions in particle inventory, storage containment, and particle-sCO_2 heat exchanger. This reduction is partially offset by an increase in heliostat field and tower cost.

The results indicate that the use of solid particles for solar high efficiency sCO_2 power cycles offers unique advantages due to the wide temperature range of the particles.

INTRODUCTION

Power cycles using supercritical (sCO_2) as working fluid promise to become a competitive solution for future power cycles. The turbomachinery of such cycles is significantly smaller than that of comparable steam power cycles, and there is a potential for higher thermal efficiencies at elevated temperatures. In addition, the smaller components might improve the operational flexibility as there is less thermal inertia in the turbomachinery. Furthermore, the smaller components promise to reduce the specific power cycle cost.

For the application with concentrating solar power (CSP) systems the high efficiency potential makes the sCO_2 cycles especially attractive, as the "expensive " solar energy input can be reduced accordingly. This would result in smaller heliostat fields, receivers and storage systems, thus reducing investment cost. The intended high efficiency sCO_2 cycles are characterized by two aspects:

- high upper temperature of the cycle working fluid sCO_2, typically above 600°C
- low temperature spread of the cycle working fluid sCO_2, typically in the range of 150K

State-of-the-art heat transfer media (HTM) like "solar salt", a mixture of 60% $NaNO_3$ and 40% KNO_3, are not suitable for such high temperatures. Therefore, new HTM are required. These new HTM should also provide cost-effective storage capabilities.

In the US study on the next generation of CSP plants ("Concentrating Solar Power Gen3 Demonstration Roadmap") [1] sCO_2 cycles are foreseen for solar power generation, operating at upper temperatures as high as 715°C. Three potential candidates for the HTM are identified: new molten salt mixtures, solid particles and pressurized gases. For the last option, solid particles are also favored as storage material.

All three candidate HTM offer flexibility in the selection of the lower and upper temperature levels, which influence the layout and operating conditions of the solar power plant. The selection of these temperatures influences mainly the following aspects: area of the primary heat exchanger of the sCO_2 cycle, receiver efficiency, HTM mass flow, storage mass and volume, thermal insulation. Some of these parameters have a significant impact on investment cost.

In the present analysis, solid particles are selected as HTM. The reason for this selection is the extremely wide acceptable temperature range, up to 1000°C and without a limitation at lower temperatures (e. g. no freezing issues). The low cost of the particles enables also direct use as storage material.

The objective of this paper is the evaluation of trends when a high efficiency sCO_2 cycle is combined with a CSP system using a new HTM. The analysis is based on several simplified assumptions, as many of the components are not developed yet and therefore detailed cost and performance are not available. The results should be understood as trend indicators, not as absolute numbers.

MODEL AND ASSUMPTIONS

For the analysis, a solar tower system with a power rating of 100 MW_e is considered. The plant consists of 14 solar tower modules (multi-tower design) delivering heat to a single central power station. Each solar tower module consists of a heliostat

DOI: 10.17185/duepublico/46098

field, a tower with a receiver on top, a hot and cold storage containment and the heat transfer medium loop. The components of the plant are described in the following sections.

Power Cycle

The power cycle is a sCO_2 cycle in recompression configuration, with reheat and intercooling. The cycle layout was developed by SIEMENS and is shown in Figure 1. Further characteristics of the cycle are discussed in [2] in more detail. The primary heat exchanger, where the solar heat is introduced, consists of the main heat exchanger (item 6 in Figure 1) and the reheater (item 11 in Figure 1). In the main heat exchanger, sCO_2 is heated from 454°C to 605°C, in the reheater sCO_2 is heated from 502°C to 605°C. The sophisticated cycle configuration results in an excellent cycle efficiency of 50%, without increasing the cycle temperatures too much. With this efficiency, a thermal input power of $200MW_{th}$ is required from the solar subsystem. For the layout and costing of the primary heat exchanger it is considered as a single heat exchanger. Then the average inlet temperature of the main and reheat section of 478°C is used.

Currently, no reliable cost data for such a large power cycle is available. In [3] the specific cost of several sCO_2 cycles is estimated. High efficiency configurations of the investigated sCO_2 cycles were estimated in the range from $1097\$/kW_e$ to $1392\$/kW_e$ For the shown complex sCO_2 power cycle configuration, only preliminary cost estimates can be made. For the present analysis, the primary (particle-to-sCO_2) heat exchanger is treated as a separate cost item, as the cost of this heat exchanger is strongly influenced by the selected temperature range. For the cost of the remainder of the sCO_2 cycle, a fixed specific cost of $C_{sp,cycle} = 1000€/kW_e$ is assumed. This results in a power cycle cost C_{pc} of 100 Mio € (excluding primary heat exchanger).

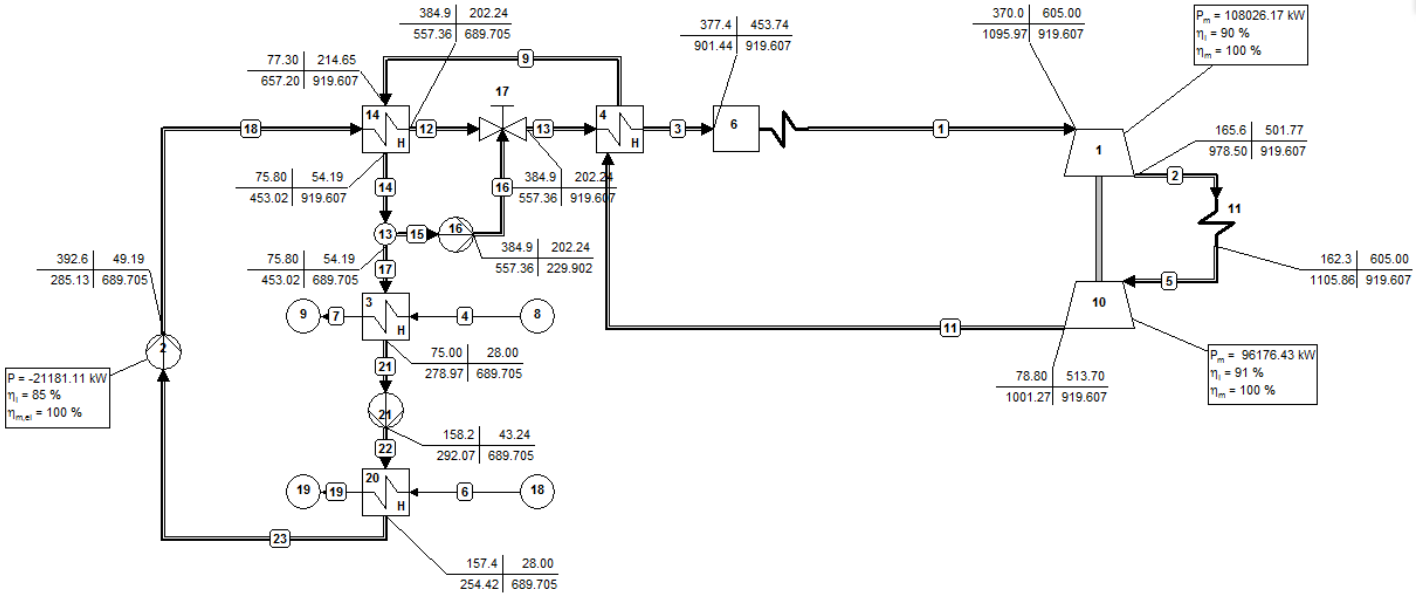

Figure 1: Configuration of the high efficiency / high temperature sCO_2 cycle

Solar Tower Module Description

Each of the 14 solar tower modules consists of a receiver with a design point (DP) power of $50MW_{th}$ and the corresponding heliostat field and thermal storage. A scheme of a module is shown in Figure 2.

The module power of $50MW_{th}$ at DP conditions results in a total thermal system power of $700MW_{th}$. With the power cycle demand of $200MW_{th}$ this represents a solar multiple of 3.5.

For the analysis, a site in Northern Chile with an annual direct normal insolation (DNI) of $3583kWh/m^2a$ is assumed. This is an extremely good solar site, however the trend results should be representative for other sites as well.

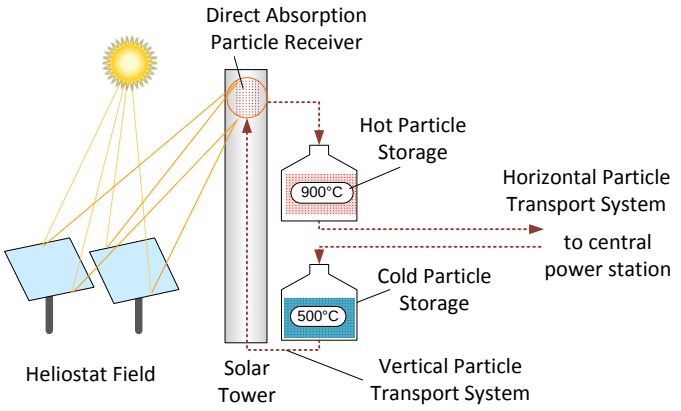

Figure 2: Solar tower module scheme

DOI: 10.17185/duepublico/46098

Heat Transfer and Storage Medium

Bauxite particles are assumed as heat transfer and storage medium, since these particles are relatively inexpensive and allow flexible selection of temperature ranges up to 1000°C. Above this temperature, sintering effects might create problems in particle handling. Also, a lower temperature limit does not exist, and therefore electrical heat tracing is not necessary to avoid HTM freezing. Simplified assumptions for the particle properties are:

heat capacity: $c_{p,part} = 1200\,J/kgK$

particle bulk density: $\rho_{part} = 2000\,\frac{kg}{m^3}$

Such bauxite particles are produced in huge quantities, e. g. for use in fracking or casting processes. A specific particle cost of $C_{sp,part}$ = *1€/kg* is assumed.

Figure 3: Solid bauxite particles used as HTM

Thermal Storage System

For the solar tower system, a thermal storage time of 12h full load operation was assumed, resulting in a total thermal storage capacity E_{st} of 2.4 GWh. This storage capacity is evenly distributed over all solar tower modules. The hot and cold storage containments are either installed inside the tower (eventually using the tower walls as containment walls, with inner insulation) or close to the tower.

Thermal losses through the thermal insulation are neglected. Such losses are usually relatively small. This simplification is also justified since the cost of the insulation is assumed temperature-dependent, i. e. for higher temperatures an improved quality insulation is foreseen.

The particle inventory per module is calculated as

$$m_{st} = \frac{E_{st}}{n_{mod} \cdot c_{p,part} \cdot \left(T_{r,ex} - T_{r,in}\right)}$$

Another 10% of this particle mass is added to account for particles in other components, e. g. the transport containments.

The cost of the particle inventory C_{part} is then calculated as

$$C_{part} = 1.1 \cdot m_{st} \cdot C_{sp,part}$$

The cost of the storage containment C_{stc} is calculated from the surface area A_{stc} of the containment. A cylindrical containment with the cylinder height being twice the cylinder diameter is assumed. From the particle inventory, the volume of a fully charged containment is calculated, and then the cylinder diameter and the surface area are derived. Then a temperature-dependent area-specific insulated structure cost $C_{sp,is}$ is calculated as follows:

$$C_{A,sp,is}(T_{st}) = 1000 + f_{ins} \cdot \frac{(T_{st} - 600)}{400}$$

The insulation factor f_{ins} describes the cost share of the thermal insulation. In the above formulation, the insulation cost is doubled when the storage temperature T_{st} (in K] is increased from 600°C to 1000°C. A value of f_{ins} = 0.3 is assumed for the insulation cost share. The storage containment cost is the sum of the cost of the hot and cold storage containments:

$$C_{stc} = A_{stc} \cdot C_{A,sp,is}\left(T_{r,ex}\right) + A_{stc} \cdot C_{A,sp,is}\left(T_{r,in}\right)$$

The total cost of the storage system C_{st} is then calculated as

$$C_{st} = C_{part} + C_{stc}$$

Solar Receiver

The receiver technology is based on the centrifugal particle receiver technology CentRec® [4] . This receiver technology is currently under development at DLR. The receiver is based on the direct absorption principle, meaning that the dark bauxite particles are irradiated directly by the concentrated solar power and get heated from the absorbed radiation.

A first demonstration receiver with about 2.5MW$_{th}$ peak power is installed at the DLR solar tower test facility in Jülich, Germany. Due to constraints of the test platform in the solar tower test facility, which is located about midway up the tower, a thermal power output of up to 500kW$_{th}$ is expected. More than 30h of solar testing has been carried out so far, and receiver outlet temperatures up to 775°C have been achieved [4] . Solar tests will continue in spring 2018 with the goal to demonstrate the design outlet temperature of 900°C.

The receiver is characterized by a circular aperture that is facing south, since the plant site is located in Chile on the southern hemisphere. The aperture area A_{ap} varies according to the selected temperature range and is determined during the solar system optimization. A simplified receiver model is considered, with the absorbed power $P_{r,abs}$ defined as a function of intercepted power $P_{r,int}$ and receiver exit temperature $T_{r,ex}$ by

$$P_{r,abs} = \alpha \cdot P_{r,int} - \varepsilon\sigma\, A_{ap}\, T_{r,ex}^4 - h\, A_{ap}\, (T_{r,ex} - T_{amb})$$

with

effective solar absorptivity: $\alpha = 0.95$

effective thermal emissivity: $\varepsilon = 0.9$

convective heat loss coefficient: $h = 30\,W/m^2K$

Note that in the above correlation all temperatures must be used in [K]. For the ambient temperature, a value of 300K is

DOI: 10.17185/duepublico/46098

taken. The receiver cost is described by two contributing factors: one depending only on the receiver aperture, another one depending on the surface area of the internal insulated structure and the receiver exit temperature. The surface area of the internal insulated structure is calculated for a cylindrical receiver chamber with a diameter of 1.3 times the aperture diameter and a depth of 2 times the aperture diameter. The area of the insulated structure $A_{r,is}$ is then composed of area of the cylinder wall and the area of the flat back wall of the cylinder. The total cost of the receiver system C_r is calculated as

$$C_r = 70000 \cdot A_{ap} + A_{r,is} \cdot C_{A,sp,is}(T_{r,ex})$$

Heliostat Field

The heliostat field consists of a large number of rectangular heliostats, tracked in two axes. The heliostat dimension is 12.84 m width and 9.45 m height. A reflectivity of 88% is assumed, accounting for the mirror reflectivity and an average dirt coverage of the mirrors. A specific cost $C_{sp,f}$ of 100 €/m² installed heliostat field is assumed.

For each temperature range, the heliostat field layout and the number of heliostats are optimized using the simulation tool HFLCAL [6] . A radially staggered field layout is selected. As a result, the total heliostat field area A_f is obtained.

The total cost of the heliostat field C_{field} is calculated as

$$C_f = A_f \cdot C_{sp,f}$$

Tower

A tower is required to locate the solar receiver at a suitable height above the heliostat field. The tower height is dominated by the heliostat field and receiver configuration, and is optimized together with other parameters.

The cost of the tower is assumed as

$$C_t = 128 \cdot H_t^{1.9174}$$

Heat Exchanger

A moving bed particle heat exchanger (Figure 4) is foreseen for the heating of the working fluid sCO_2 of the power cycle. In this heat exchanger type, the solid particles are moving slowly across the heat exchanger tubes, driven by gravity [6] . The mass flow is controlled by variable gate valves at the cold exit of the heat exchanger.

The required heat transfer area of this heat exchanger is calculated as

$$A_{HX} = \frac{P_{el}/\eta_{cycle}}{h_{HX} \cdot \Delta T_{log}}$$

In [6] convective heat transfer coefficients up to 240 W/m²K were measured for a tube bundle type heat exchanger with particle inlet temperatures ranging from 355°C to 470°C. Since the particle heat exchanger for a sCO_2 power cycle is operated at significantly higher temperatures, radiative heat transfer will be improving the heat transfer. Here, a constant heat transfer coefficient h_{HX} of 300 W/m²K is assumed. The logarithmic temperature difference ΔT_{log} for a heat exchanger in cross-flow configuration is calculated based on the solid particle temperature selection and the power cycle temperature levels. The primary heat exchanger temperatures of the power cycle are 605°C for the sCO_2 outlet and 478°C for the sCO_2 inlet.

The primary heat exchanger material temperatures are mainly defined by the sCO_2 cycle conditions, as the highest heat transfer resistance will be between particles and tube material, i. e. the tube material temperatures will be quite independent of particle temperatures. Thus, the heat exchanger cost is only a function of the heat transfer area.

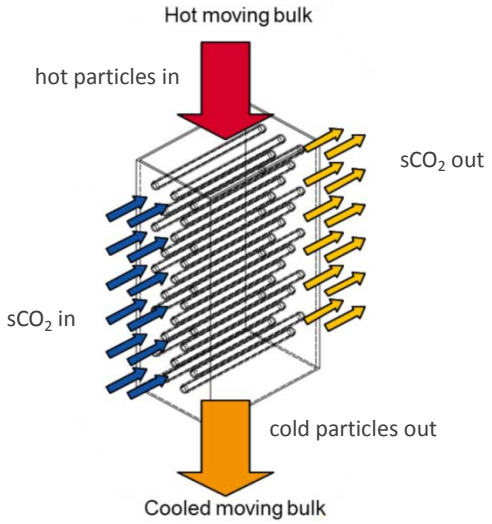

Figure 4: Moving bed particle heat exchanger

For the cost of the heat exchanger a correlation was derived using the MATCHE data base [8] assuming Inconel625 as tube material. With a correction factor the high pressure of the sCO_2 system, a translation from 2014 cost into actual cost and after converting from $ to € this resulted in the following correlation:

$$C_{HX} = 128122 \cdot A_{HX}^{0.66}$$

Particle Transport System

The multitower system needs particle transportation in two ways: lifting the "cold" particles up to the receiver inlet ("vertical" particle transport) and transporting the particles between a solar tower module and the central power station ("horizontal" particle transport). After being cooled down in the central particle-sCO_2 heat exchanger, the cold particles are transported back to the solar tower modules and are either lifted up to the receiver (when enough solar power is available to heat the particles) or lifted to the inlet of the cold storage container. When more solar power is available than the power cycle takes, particles from the cold storage are lifted up to the receiver and, after being heated up, put into the hot storage. Particle transport downwards is always accomplished by gravitational flow.

DOI: 10.17185/duepublico/46098

Vertical particle transport

For the vertical particle transport a mine hoist system is foreseen. Repole et al. [9] have made a conceptual design for a mine hoist system for a solar demonstration system with a thermal capacity of 60MW$_{th}$. Since the selected solar tower module size is close to this capacity, this mine hoist design was taken as base value for the calculation of the cost for the specific configuration. Scaling factors are applied for conditions differing from the original design values. The used correlation is

$$C_{tr} = C_{tr,0} \cdot \left\{1 + k_T \left(\frac{T_l - T_{l,0}}{T_{l,0}}\right)\right\} \cdot \left\{1 + k_m \left(\frac{\dot{m} - \dot{m}_0}{\dot{m}_0}\right)\right\} \cdot \left\{1 + k_H \left(\frac{H_l - H_{l,0}}{H_{l,0}}\right)\right\}$$

with

$C_{tr,0} = 425000€$ (converted from 523000$)

The original design values in [9] are:

$T_{l,0} = 300°C$ (assumed, not clearly stated in [9])

$\dot{m}_0 = 128\ kg/s$

$H_{l,0} = 70m$

The selected scaling factors are:

$k_T = 0.1$

$k_m = 0.5$

$k_H = 0.2$

Horizontal particle transport

For the transportation between the solar tower modules and the central power station a number of trucks are foreseen, each transporting insulated containers (one for hot and another for cold particles). One truck is serving one module. This is sufficient for the highest particle mass flows (i. e. the smallest temperature particle difference of 200K), for lower mass flows this is even oversized and might be reduced in further system optimization. The trucks are continuously operated whenever the power cycle is producing electricity, e. g. also during night time. As the paths between the solar tower modules and the central power block are clearly defined, fully autonomous trucks are foreseen. The cost of each truck system is estimated as $C_{tr,h}$ = 280000€ and includes the truck and 6 insulated containers (3 for cold particles and 3 for hot particles). This enables continuous operation of the horizontal particle transport system, with one container discharged, one container being transported, and one container being charged at the same time.

Other Performance Assumptions

For simplicity reasons, thermal losses through the insulation are neglected, as they are usually very small: Also, the parasitic power consumption of the various components (rotation drive of cylindrical receiver, vertical and horizontal particle transport system, power cycle parasitics) was excluded from the analysis. While thermal losses might slightly increase with higher temperatures, parasitic power will decrease as the particle mass flow will go down.

OPTIMIZATION OF SYSTEM CONFIGURATION

A number of system configurations are evaluated, with the levelized cost of electricity (*LCoE*) as the evaluation criteria.

The capital expenditures for a single tower module ($CAPEX_{mod}$) are calculated by

$$CAPEX_{mod} = C_f + C_t + C_r + C_{tr,v} + C_{tr,h} + C_{st}$$

For the calculation of the total capital expenditures (*CAPEX*) the cost of all modules is combined with the cost of the central power block (consisting of heat exchanger and power cycle), and contingencies of 30% are added to this sum:

$$CAPEX = 1.3 \cdot \left(n_{mod} \cdot CAPEX_{mod} + C_{HX} + C_{pc}\right)$$

Annual operational expenditures (*OPEX*) are assumed as 2% of the total *CAPEX*. The annual electric power production is then calculated from the annual thermal energy as obtained from the HFLCAL layout optimization:

$$E_{el,annual} = E_{th,annual} \cdot \eta_{cycle}$$

The evaluation of the *LCoE* is based on a simplified annuity approach as follows:

$$LCoE = \frac{CAPEX \cdot f_{annuity} + OPEX}{E_{el,annual}}$$

The annuity factor $f_{annuity}$ is based on the interest rate and the depreciation period [9] . With an interest rate of 5% and a depreciation period of 25a an annuity factor of 7.1% is obtained.

Each configuration is defined by a specific receiver inlet and outlet temperature. For each temperature set, the solar subsystem is optimized for minimal *LcoE*. The following parameters are varied during the optimization: receiver aperture area, receiver tilt angle, tower height and field layout. A radially staggered field layout is assumed. The simulation tool HFLCAL [6] was used to determine the optimal parameters for each temperature set.

RESULTS

The parameter study was carried out using receiver inlet temperatures of 500°, 600°C and 700°C. Temperature differences between receiver exit and inlet temperature were between 200°C and 500°C, with an upper limit for the receiver exit temperature of 1000°C.

Figure 5 shows the resulting LCoE for the selected parameter sets. It is obvious that the higher the receiver exit temperature the lower the LCoE is. For a given receiver exit temperature, lower receiver inlet temperatures result in lower LCoE. The LCoE difference between the best (500°C/1000°C) and the worst case (500°C/700°C) is about 9%.

DOI: 10.17185/duepublico/46098

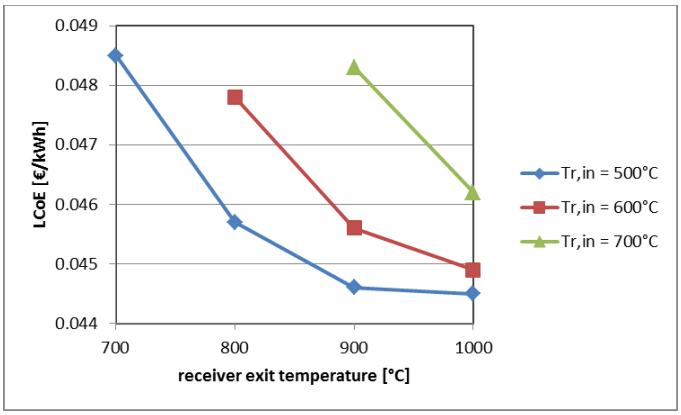

Figure 5: Levelized cost of electricity vs. temperature range

Showing the data in a different representation based on the temperature difference between receiver exit and inlet temperature (Figure 6) it is evident that this temperature difference is the dominant factor for the change in LCoE.

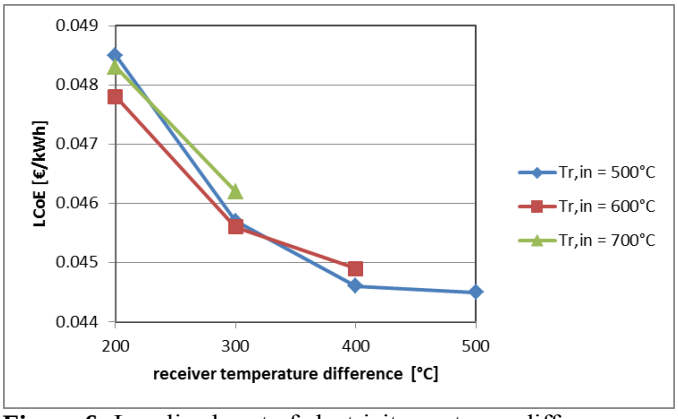

Figure 6: Levelized cost of electricity vs. temp. difference

Figure 7 shows the cost contributions of the most important factors for the LCoE change. The shown characteristic is mainly resulting from a significant cost decrease in the storage cost and in the heat exchanger cost, when the temperature difference is increased. A minor cost decrease occurs in the particle transport system, mainly due to reduced mass flow requirements.

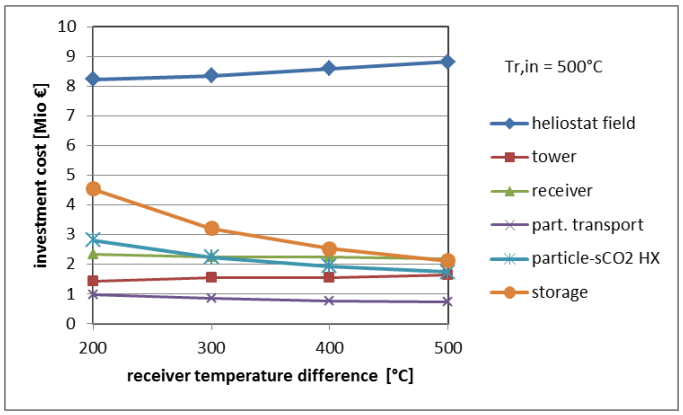

Figure 7: Component cost vs. temperature difference

On the other hand, the cost of heliostat field and tower increase with increasing receiver exit temperature. This is caused by decreasing receiver efficiency, requiring more heliostats and a higher tower to deliver the required thermal power. When the receiver exit temperature is increased, higher area-specific thermal losses occur in the receiver. In the solar system optimization this leads to smaller receivers, which is why the receiver cost decrease. More details on the component cost are given in Table 1.

Table 1: Detailed results of parameter study

receiver inlet temperature	**[°C]**	**500**	**500**	**500**	**500**	**600**	**600**	**600**	**700**	**700**
receiver exit temperature	**[°C]**	**700**	**800**	**900**	**1000**	**800**	**900**	**1000**	**900**	**1000**
component cost										
heliostat field	[Mio €]	115.2	116.9	120.3	123.3	118.6	121.6	124.2	120.9	124.0
tower	[Mio €]	19.9	21.6	21.8	23.0	19.8	20.7	22.1	20.5	22.5
receiver	[Mio €]	32.9	31.4	31.5	30.6	32.5	31.4	31.1	32.3	30.7
vertical particle transport	[Mio €]	9.7	7.8	6.8	6.3	10.0	8.0	7.1	10.4	8.4
horizontal particle transport	[Mio €]	3.9	3.9	3.9	3.9	3.9	3.9	3.9	3.9	3.9
particle-sCO2 heat exchanger	[Mio €]	39.4	31.4	27.2	24.4	26.5	23.2	21.0	20.8	18.9
sCO2 power cycle (excl. HX)	[Mio €]	100.0	100.0	100.0	100.0	100.0	100.0	100.0	100.0	100.0
particle inventory	[Mio €]	43.1	28.7	21.5	17.2	43.1	28.7	21.5	43.1	28.7
storage containments	[Mio €]	20.3	16.1	13.8	12.3	21.9	17.3	14.7	23.4	18.4
LCOE	**[€/kWh]**	**0.0485**	**0.0457**	**0.0446**	**0.0445**	**0.0478**	**0.0456**	**0.0449**	**0.0483**	**0.0462**

DOI: 10.17185/duepublico/46098

CONCLUSIONS

Integrating high efficiency sCO_2 power cycles into solar tower plants is characterized by high upper temperature of the cycle working fluid sCO_2 (typically above 600°C) and low temperature spread of the cycle working fluid sCO_2, typically in the range of 150K. This requires the use of new HTM, suitable for higher temperatures and featuring low cost storage. The present study evaluates modular solar tower plants using solid particles as HTM, allowing HTM temperatures up to 1000°C. In a parameter study the influence of the lower and upper HTM temperature on LCoE was evaluated.

The results show a significant impact of the HTM temperature selection, mainly governed by the HTM temperature difference. A high temperature difference results in reduced LCoE. The most important factors for this reduction are the reductions in particle inventory, storage containment, and particle-sCO_2 heat exchanger. This reduction is partially offset by an increase in heliostat field and tower cost.

The results indicate that the use of solid particles for solar high efficiency sCO_2 power cycles offers unique advantages due to the wide temperature range of the particles. In addition, the modular solar tower design will allow simple adaptation to other power levels and capacity factors.

It should be stated that several of the used cost correlations are "best guesses", as currently no sound database exists for many of the new components. These correlations should be refined by future work to improve the quality of the results.

NOMENCLATURE

Symbols:

Symbol	unit	description
A	$[m^2]$	area
C	[€]	cost
c_p	[J/kgK]	heat capacity
E	[J]	energy
H	[m]	tower height
n_{mod}	[-]	number of solar tower modules
$LCoE$	[€/MWh]	levelized cost of electricity
P	[W]	power
T	[°C]; [K]	temperature
ρ	$[kg/m^3]$	density
η	[-]	efficiency

Subscripts:

abs	absorbed
amb	ambient
annual	annual value
ap	aperture
cycle	sCO_2 power cycle
el	electric
ex	exit
f	field
h	horizontal
HX	(primary) heat exchanger
in	inlet
int	intercepted
is	insulated structure
mod	(solar tower) module
part	particle
pc	power cycle
r	receiver
st	storage
stc	storage containment
sp	specific
th	thermal
tr	transport
t	tower
v	vertical

ABBREVIATIONS

CAPEX: capital expenditures
CSP: concentrating solar power
DNI: direct normal insolation
DP: design point
HTM: heat transfer medium
OPEX: operational expenditures

ACKNOWLEDGEMENTS

The author would like to thank Stefano Giuliano and Lars Amsbeck for valuable discussions on the performance and cost assumptions.

REFERENCES

[1] Concentrating Solar Power Gen3 Demonstration Roadmap; Technical Report NREL/TP-5500-67464, January 2017. Available at www.nrel.gov/publications.

[2] Glos, S., Wechsung, M., Wagner, R., Heidenhof, A., Schlehuber, D. (2018). Evaluation of sCO_2 Power Cycles for Direct and Waste Heat Applications, 2nd European supercritical CO_2 Conference, August 30-31, 2018, Essen, Germany (to be published)

[3] Carlson, M. D., Middleton, B. M., Ho, C. K. (2017). Techno-economic Comparison of Solar-driven sCO_2 Brayton Cycles using Component Cost Models Baselined with Vendor Data and Estimates, PowerEnergy2017-3590, Proc. ASME PowerEnergy2017, June 26-30, 2017, Charlotte, NC, USA

[4] Ebert, M., Amsbeck, L., Jensch, A., Hertel, J., Rheinländer, J., Trebing, D., Uhlig, R., Buck, R. (2016). Upscaling, Manufacturing and Test of a Centrifugal Particle Receiver. PowerEnergy2016-59252, Proc. ASME Energy Sustainability Conference, 26.-30. June 2016, Charlotte, United States.

[5] Ebert, M., Amsbeck, L., Buck, R., Rheinländer, J., Schlögl-Knothe, B., Schmitz, S., Sibum, M., Stadler, S., Uhlig, R. (2018). First On-sun Tests of a Centrifugal Particle Receiver System, PowerEnergy2018-7166, Proc. ASME 2018 Power and Energy Conference (PowerEnergy2018), June 24-28, 2018, Lake Buena Vista, FL, USA (to be published)

[6] Schwarzbözl, P., Pitz-Paal, R. and Schmitz, M. (2009) Visual HFLCAL - A Software Tool for Layout and

DOI: 10.17185/duepublico/46098

Optimisation of Heliostat Fields. Proceedings SolarPACES 2009, Berlin.
[7] Baumann, T., Zunft, S. (2014). Experimental Investigation on a Moving Bed Heat Exchanger used for discharge of a particle-based TES for CSP. Eurotherm Seminar #99 - Advances in Thermal Energy Storage. Eurotherm Seminar #99, 28.05.-30.05.2014, Lleida, Spain. ISBN 978 84 697 0467 7
[8] http://matche.com/equipcost/Exchanger.html (last visited 22.06.2018)
[9] Repole, K. D., Jeter, S. M. (2016). Design and Analysis of a High Temperature Particulate Hoist for Proposed Particle Heating Concentrator Solar Power Systems. ASME Energy Sustainability 2016. doi:10.1115/ES2016-59619.
[10] Roy, A., Meinecke, W., Blanco, M. (1997). "Introductory Guidelines for Preparing Reports on Solar Thermal Power Systems", SolarPACES Rep. No. III-3/97.

DOI: 10.17185/duepublico/46098

2nd European supercritical CO2 Conference
August 30-31, 2018, Essen, Germany

2018-sCO2.eu-121

PRELIMINARY EXPERIMENTAL STUDY OF CO_2 BASED MIXTURE SUPERCRITICAL POWER CYCLE

Seungjoon Baik
Department of Nuclear and Quantum Engineering,
Korea Advanced Institute of Science and Technology
Daejeon, Republic of Korea
Email:bsj227@kaist.ac.kr

Jeong Ik Lee*
Department of Nuclear and Quantum Engineering,
Korea Advanced Institute of Science and Technology
Daejeon, Republic of Korea
Email: jeongiklee@kaist.ac.kr*

ABSTRACT

The supercritical carbon dioxide (sCO_2) Brayton power cycle has been receiving worldwide attention due to the high thermal efficiency and compact system configuration. Because of the incompressible liquid like characteristic (e.g. high density, low compressibility) of the CO_2 near the critical point (30.98℃, 7.38MPa), sCO_2 Brayton cycle can achieve high efficiency by reducing compression work. The system is sufficiently advanced, but has drawbacks in terms of minimum temperature and high operating pressure. These disadvantages can be improved by mixing working fluid with different materials. In this study, the authors evaluated the performance improvement by changing critical point and operating conditions. The higher molecular weight substances (SF_6, Organic refrigerants, Hydrocarbons…) can be utilized to increase the mixture critical temperature and lower the mixture critical pressure. In this study, thermodynamic evaluations of mixing CO_2 with difluoromethane (R-32) or toluene are considered. Also the preliminary experimental verification of the CO_2 + R-32 case is conducted to show the technical feasibility of the suggested ideas.

INTRODUCTION

In recent years, interests in research on high-efficiency energy conversion technology have increased substantially to resolve global warming problems and respond to the increase in energy demand. The supercritical carbon dioxide Brayton power cycle technology has been thought to be one of the promising technical solutions to these issues [1- 3].

The sCO_2 power conversion cycle can achieve high efficiency by reducing compression work due to the high density and low compressibility characteristics near the critical point (30.98℃, 7.38MPa). Moreover, the power cycle can be designed in compact size due to the high density of the working fluid. Moreover, the compact sCO_2 power system can be utilized as modularized distributed power generation or advanced marine propulsion technology.

However, the sCO_2 power cycle has intrinsic limitation on the minimum temperature which is at the critical temperature of the CO_2. Due to the small temperature difference between ultimate heat sink and system minimum temperature, the sCO_2 power system requires a large amount of cooling flow rate or massive heat exchanger to dissipate the waste heat especially via air-cooling in hot regions.

In order to improve the sCO_2 system regarding the minimum temperature limitation, a research on the CO_2 based gas mixture power cycle has been conducted previously. Jeong et al. mixed CO_2 with N_2, O_2, He or Ar gas to evaluate the performance of the binary mixture gas supercritical Brayton cycles [4]. Yin et al. suggested CO_2-SF_6 mixture for geothermal power plants [6-7]. Hu et al. and Wu et al. analyzed CO_2-based binary mixture with organic fluids (e.g., butane, cyclohexane, ethyl fluoride) [8-9]. Also the authors presented the thermodynamic analysis of CO_2 mixture with substances such as SF_6, R-123, R-134a, R-22, R-32 and toluene power cycle in supercritical state to improve the system efficiency and reduce the difficulty of air-cooled waste heat removal method [14].

In this study, thermodynamic evaluations of mixing CO_2 with difluoromethane (R-32) or toluene are considered to configure trans-critical power cycles at 150℃ and 300℃ of maximum temperature, respectively. Also the preliminary experimental verification of the CO_2 + R-32 case (12% of mass fraction) is conducted to show the technical feasibility of the suggested ideas.

CRITICAL POINT OF VARIOUS SUBSTANCES

According to the thermodynamic definition, the critical point is a temperature and pressure of a material beyond which there is no longer any difference between the liquid and gas phases. Pure substances have their unique critical point and it is known that the critical point can be changed by mixing with other substances.

The most basic mathematical model for estimating the mixture critical point is the W. B. Kay's equilibrium critical point model [10]. It is a mole fraction based linear interpolation method as shown in the following equations.

$$(P_c)_{\text{mix}} = \sum_i y_i P_{ci} \quad (1)$$

$$(T_c)_{\text{mix}} = \sum_i y_i T_{ci} \quad (2)$$

Where, y_i is mole fraction of the i^{th} component

It can be utilized for gas dynamics problem for ideal case but the real gas equilibrium critical point locus shows different locus compared to the suggested linear interpolation methods [11]. Furthermore, it is difficult to identify generalized formulation of critical locus because of the actual phenomenon differs depending on the substances and their combinations. There exist six different principal types, but the basic type of binary mixture critical locus is shown in the following figure. In Figure 1, the saturation line and critical point of each substance are marked as solid line with the empty circle. The dotted line shows the locus of mixture critical point depending on the mixing ratio of the two substances. At the certain mixing ratio, the two-phase region is shown through the bubble and dew lines in temperature-pressure (T-P) graph rather than a single curve.

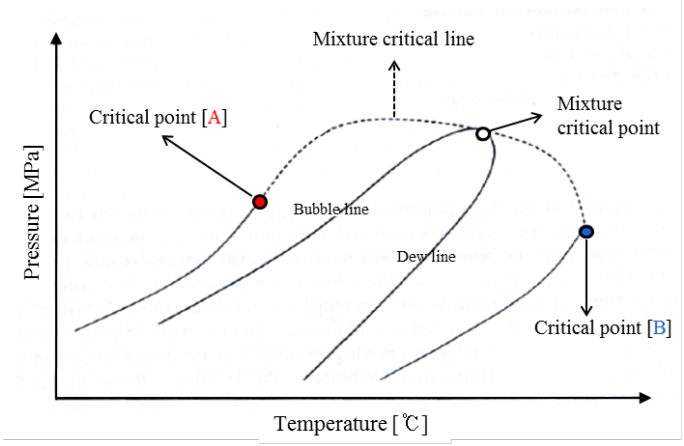

Figure 1: An example of critical locus of binary gas mixture [11]

In this study, the thermodynamic analysis is carried out based on the most reliable NIST REFPROP (ver. 10.0) property data base. The NIST data base is an international standard in thermal fluid engineering which is based on extensive experimental results [12, 13]. As examples of critical point change of CO_2 based mixtures, the critical loci are plotted in T-P graph while varying the mixing fraction.

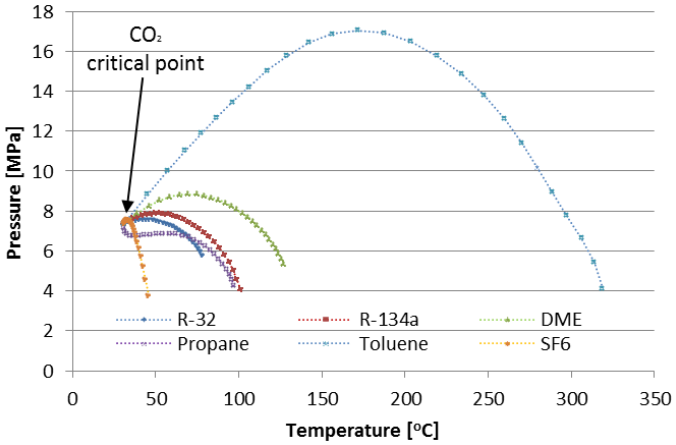

Figure 2: Critical locus of CO_2 based mixtures

Among the pure fluids available in NIST data base, the authors defined isentropic enthalpy difference index ($\left(\frac{\partial h}{\partial P}\right|_s$) and compared the values at compressor and turbine inlet conditions for the preliminary screening criteria on choosing substances [14]. The compressor and turbine inlet conditions are 7.41MPa, 31℃ and 20MPa, 300℃ respectively. Also the compressor inlet density is compared together to minimize the compression work at the compressor. The information of critical point, density and isentropic enthalpy difference index are tabulated in Annex A.

As shown in Annex A, high density and low isentropic enthalpy difference at compressor, high isentropic enthalpy difference at turbine, high critical temperature substances are highlighted in bold letters. Those substances were rearranged with basic information in Table 1.

Organic refrigerants, including R-32 and R-134a, have a critical temperature range of 50-200℃ and a critical pressure range of 3-5 MPa. Due to the suitable range for engineering purpose, those refrigerants are mainly used as a working fluid for refrigeration system or heat pump applications.

Dimethyl ether and propane are sometimes regarded as refrigerants, but they are mainly used as fuels or propellants due to the high flammability [15-16]. Toluene is an organic compound used primarily as a solvent, but recently it has been recommended as a suitable working fluid for high temperature organic Rankine cycle (ORC) applications. [17] The SF_6 is heavy gas which is mainly used in high voltage circuit breakers due to the small electric conductivity and stability in high temperature [18].

Table 1: Information of each substance

Substance	Molar mass [kg/kmol]	T_c [℃]	P_c [MPa]	D_c [kg/m^3]
CO_2	44.01	30.98	7.3773	467.6
R-32 (CH_2F_2)	52.02	78.11	5.7820	424.0
R-134a (CF_3CH_2F)	102.03	101.06	4.0593	511.9
Dimethyl ether (CH_3OCH_3)	46.07	127.23	5.3368	273.7
Propane ($CH_3CH_2CH_3$)	44.10	96.74	4.2512	220.5
Toluene ($C_6H_5CH_3$)	92.14	318.60	4.1263	292.0
SF_6	146.06	45.57	3.7550	742.3

MIXTURE PROPERTIES

In this study, thermodynamic studies of CO_2 power cycle mixing with R-32 or toluene are first considered. The preliminary screening results based on the existing mixture properties available in open literature are shown.

As mentioned above, estimation of the critical locus or thermodynamic properties of mixture is difficult to generalize. Microscopically, it is due to the differences of the physical characteristics from the molecular structure and intermolecular interactions between mixtures. However, the microscopic approach on the thermodynamic system such as establishing the equation of state or mixing rule is beyond the scope of the study. Therefore, the calculated mixture property results of the REFPROP software were verified by comparing with the existing experimental results.

Previously, the experimental studies on vapor-liquid equilibria data and critical locus of CO_2+R-32 and CO_2+Toluene cases were conducted by many chemical engineers [19-21]. Those studies are conducted in purpose of using mixtures for refrigeration system or extraction process by modifying their thermodynamic characteristics.

The authors aimed to increase the critical temperature of CO_2 by mixing additives to enable condensation at 31℃, it is important to predict accurately the bubble and dew pressure. Comparisons of REFPROP calculated data with experimental data were plotted. As shown in the figures, the mixture of CO_2+R32 showed reliable estimation on bubble and dew pressure. Also the critical locus showed reasonable agreement. On the other hand, the estimation of CO_2+Toluene mixture case showed unreliable results compare to the experimental data at high temperature regions and when CO_2 fraction is small (CO_2 mass fraction lower than 0.7). However, the estimation of critical locus with REFPROP was reliable when it is compared to the two experimental data sets.

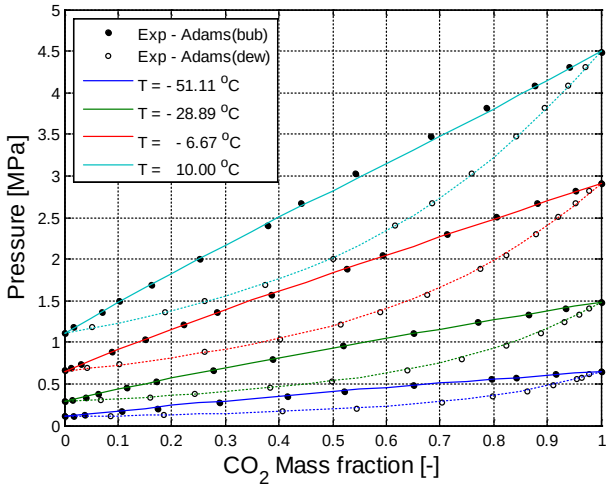

Figure 3: Comparison of calculated bubble pressure and dew pressure of CO_2+R-32 mixture from REFPROP with experimental data [19]

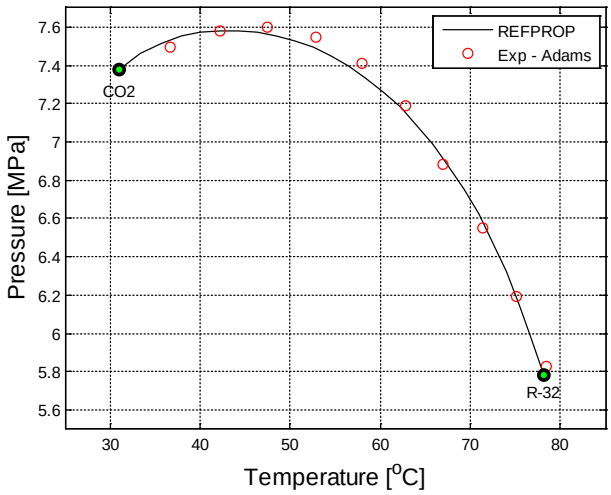

Figure 4: Comparison of calculated critical locus of CO_2+R-32 mixture from REFPROP with experimental data [19]

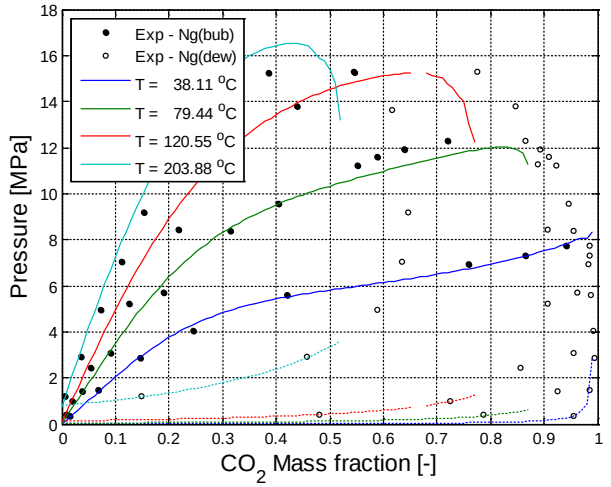

Figure 5: Comparison of calculated bubble pressure and dew pressure of CO_2+Toluene mixture from REFPROP with experimental data [20]

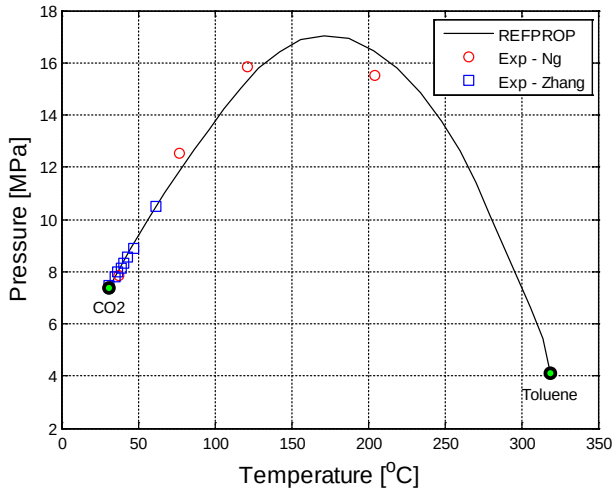

Figure 6: Comparison of calculated critical locus of CO_2+Toluene mixture from REFPROP with experimental data [21]

Through these verifications, the authors confirmed that the obtained data from the REFPROP package is reliable for CO_2+R-32 case and CO_2+Toluene at CO_2 rich region. In these regions, thermodynamic analysis of binary CO_2 mixture system is conducted.

THERMODYNAMIC ANALYSIS

In order to design and analyze the sCO_2 power cycle, KAIST research team developed an in-house code; namely KAIST_CCD. The developed code has been validated and verified through the previous studies [22, 23]. By utilizing the developed code, thermodynamic analyses of CO_2 based mixture are conducted and compared to the pure CO_2 system's performance.

To compare two thermodynamic systems in fair manner, the cycle was calculated while the lowest temperature was kept at 30℃ and the efficiency of each component was set identical as summarized in the table below. The efficiencies of components were selected as conservative values and the pressure drop was neglected in this study for simplification. Since the pressure losses can't be neglected in an actual system, the authors plan to consider it in the future study.

Table 2: Description of analysis

System type	Trans-critical cycle / Recuperated Trans-critical cycle
Working Fluid	CO_2 / CO_2+R-32 / CO_2+Toluene
Thermal input	1 MW_{th}
Mass flow rate	4-5 kg/s
Maximum Pressure	20.0 MPa
Maximum Temperature	150 ℃ / 300 ℃
Minimum Temperature	30 ℃
Compressor Efficiency	80 %
Turbine Efficiency	90 %
Recuperator effectiveness	90 %
Pressure Losses	0 % (Neglected)

The maximum temperatures of the system with addition of R-32 and toluene are selected 150℃ and 300℃ to ensure the thermal stability. In the CO_2 system mixing with toluene case, recuperator was needed to utilize the high turbine outlet temperature. The schematic diagram of each type is shown with T-s diagram in the following figures.

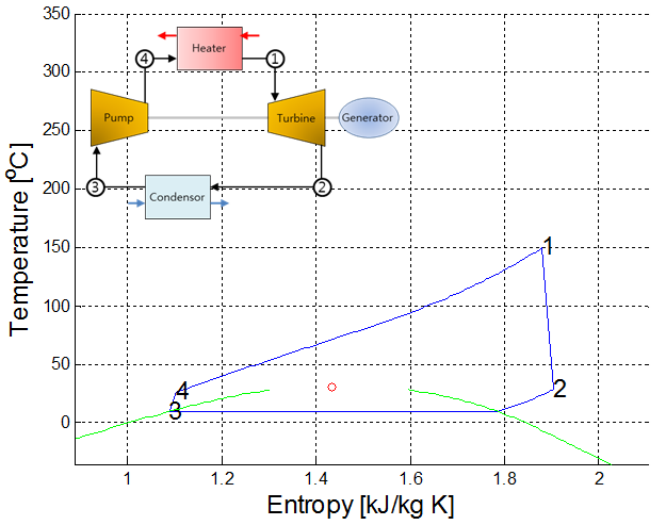

Figure 7: Schematic diagram and T-s diagram of simple trans-critical cycle

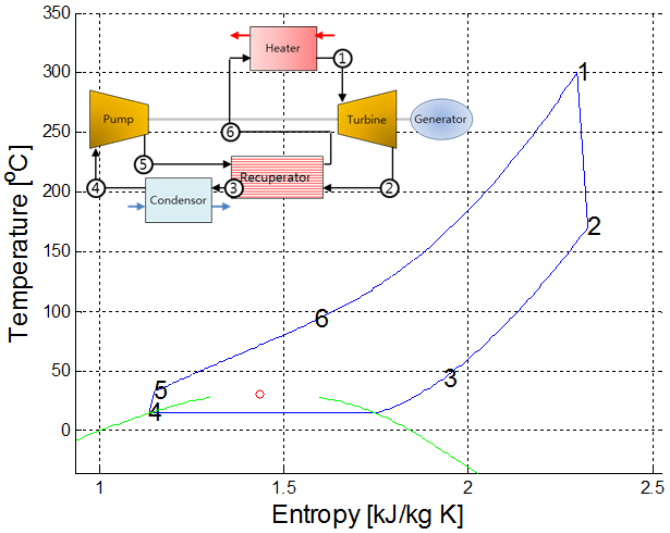

Figure 8: Schematic diagram and T-s diagram of recuperated trans-critical cycle

From thermodynamic calculations, variations of system efficiency with respect to different additive compositions are

plotted in the following figures. The system efficiency is 1st law thermal efficiency which is expressed by equation (3).

$$\text{Thermal efficiency } (\eta_{th}) = \frac{W_{net,out}}{Q_{in}} \qquad (3)$$

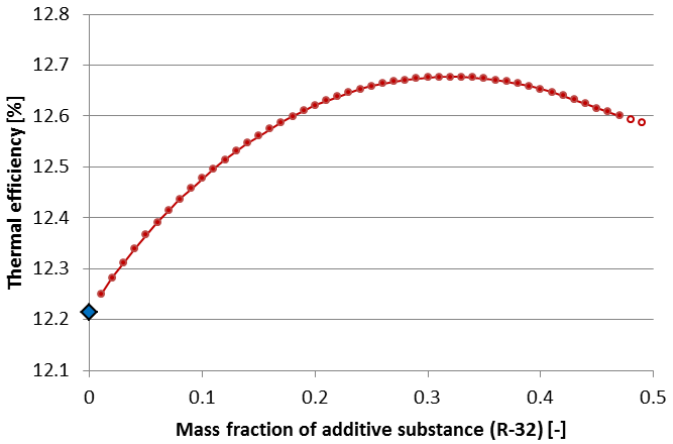

Figure 9: Efficiency change of CO_2+R-32 trans-critical cycle with respect to R-32 mass fraction

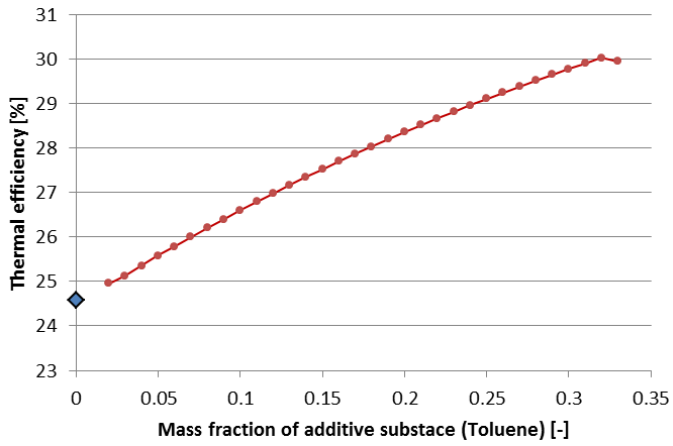

Figure 10: Efficiency change of CO_2+Toluene recuperated trans-critical cycle with respect to the toluene mass fraction

When R-32 is mixed with CO_2 and the maximum temperature is 150℃, the calculation showed an increase in efficiency over the pure CO_2 system. It was found that mixing up to 32% can increase the efficiency by 0.46% point. The results of adding R-32 more than 48% are excluded because the droplets may occur at the turbine outlet condition.

For the maximum temperature of 300℃ and when toluene is mixed, the calculation result also showed an increased efficiency compared with the pure CO_2 system. The calculated system efficiency at the maximum mixing ratio (32%) is 30.02%, which is 5.2%p higher than the reference pure CO_2 system. Adding toluene more than 44% are not recommended since the turbine outlet condition may exceed the dew point.

From the thermodynamic studies based on the REFPROP property database, R-32 and toluene showed improvement in the system efficiency compared to the pure CO_2 power cycle. In order to clarify the property uncertainties and confirm the feasibility of the suggested system, experimental tests are conducted with KAIST-S-CO_2PE facility.

EXPERIMENTAL STUDY

The authors conducted a compressor performance test with CO_2+R-32 (0.88:0.12 mass fractions) mixture by utilizing KAIST-S-CO_2PE facility. The experimental facility, which is shown in the following figure, is a sCO_2 power cycle demonstration facility. The test facility was configured to have a simple Brayton cycle layout [23] and it has been utilized for performance test of sCO_2 power cycle components such as centrifugal compressor, PCHE (Printed Circuit Heat Exchanger) and STHE (Shell and Tube Heat Exchanger) types of pre-cooler. The 26kW powered radial compressor was utilized to circulate and compress the working fluid. For the compressor performance test, 234mm diameter shrouded type impeller was operated at constant speed of 3600rpm.

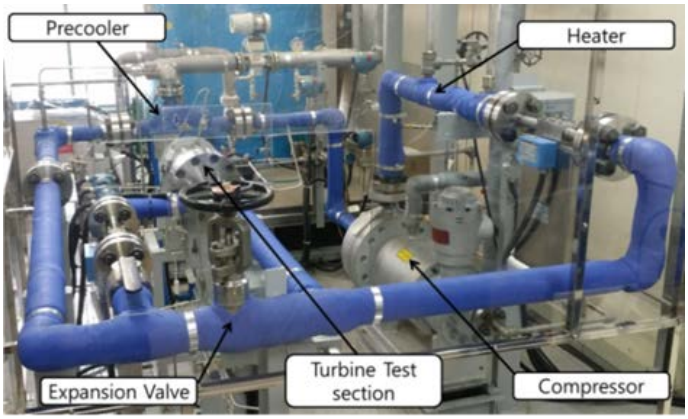

Figure 11: sCO_2 power cycle demonstration facility (KASIT S-CO_2PE facility)

From the previous study [24], pure CO_2 compressor performance test results were accumulated and used as the reference case. 16 different reference test cases are summarized with fluid property in Annex B.

In order to set the mixing ratio of the working fluid accurately, a highly accurate scale (CAS HB-150, Max 150kg, ±10g) was utilized to measure the charged weight of each fluid. Compressor test cases 4, 5, 7 and 10 were selected and re-evaluated using CO_2+R-32 (0.88:0.12 mass fractions) fluid. The largest enthalpy change in the experimental facility occurred in the compressor. Therefore, the authors checked the enthalpy rise by measuring the compressor inlet and outlet pressure and temperature to observe any inconsistencies in the property database.

EXPERIMENTAL RESULTS

As shown in Table 3, the CO_2+R-32 cases showed 1~2% higher pressure ratio than the pure CO_2 cases. For the pressure measurement, ±0.05% accuracy of pressure transmitter (Rosemount, 3051S1CG5A2) was utilized. Throughout the test range, maximum pressure measurement error is 4.7kPa and uncertainty of pressure ratio is ±0.2%. 1~2% of pressure ratio increase was measured. It seems small increase but it is still meaningful value since it is consistently outside the measurement uncertainty.

Table 3: Experimental results of CO_2 and CO_2+R-32 case

#	T [℃]	P [MPa]	CO_2		CO_2 + R-32 (0.88:0.12)		$\frac{PR_2}{PR_1}$
			Mass flow rate [kg/s]	PR_1 Pressure ratio [-]	Mass flow rate [kg/s]	PR_2 Pressure ratio [-]	
4-1	31	8.4	3.96	1.11	4.15	1.12	1.007
4-2			2.97	1.12	2.96	1.12	1.007
4-3			2.00	1.11	1.93	1.12	1.005
5-1	29.2	7.7	3.94	1.12	3.91	1.13	1.010
5-2			2.99	1.12	2.99	1.14	1.009
5-3			2.02	1.12	2.02	1.13	1.008
7-1	37	8.4	3.88	1.11	3.82	1.12	1.008
7-2			3.16	1.08	3.09	1.11	1.021
7-3			2.29	1.08	2.27	1.11	1.020
7-4			1.61	1.08	1.57	1.1	1.020
7-5			0.82	1.08	0.80	1.1	1.018
10-1	33	7.4	2.81	1.11	2.81	1.12	1.006
10-2			2.09	1.11	2.02	1.12	1.005
10-3			1.35	1.11	1.35	1.11	1.005
10-4			0.65	1.10	0.64	1.11	1.004

To clarify the increase of the pressure ratio, the pressure ratio and pressure difference of the compressor inlet and outlet are plotted in figures 12 and 13.

The red markers represent the test cases of the mixed fluid (CO_2+R-32, 0.88:0.12 mass fractions), and it can be confirmed that the result has a similar tendency to the result of the same high density case of previous pure CO_2 results. The authors concluded that the 1~2% increase of pressure ratio was caused by 10~40% increase of compressor inlet density.

The amount of the performance increase seemed relatively small due to the limitation of low speed compressor, but the difference can be larger in high performance, high speed compressor. Conversely, less work or less speed may be required to raise the same pressure if the CO_2 power system is designed with the mixture.

Moreover, mixing additive will allow CO_2 to liquefy even at temperatures above 31℃. It is expected that the CO_2 based mixture cycle system not only improves system efficiency but also can get around with mechanical issues due to using high-speed compressors for the Brayton cycle by simply replacing compressors with pumps.

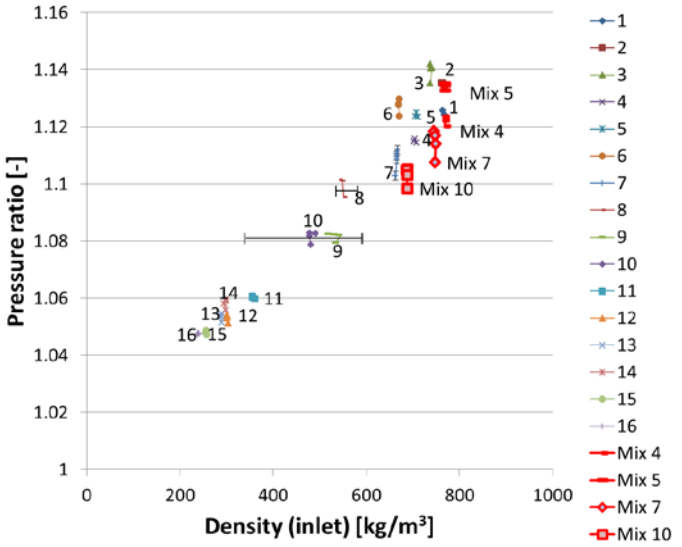

Figure 12: S-CO_2PE compressor performance test result (pressure ratio = P_{out}/P_{in}) in various inlet density conditions

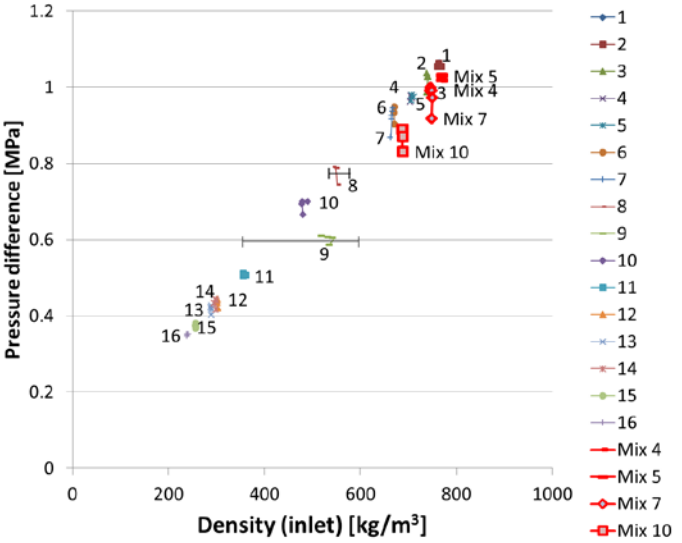

Figure 13: S-CO_2PE compressor performance test result (pressure difference = P_{out}-P_{in}) in various inlet density conditions

SUMMARY AND FUTURE WORKS

In order to improve the thermodynamic performance of the sCO_2 power cycle and reduce the limitation of the cycle minimum temperature, a study on the CO_2 based mixture is conducted. To increase the critical temperature, mixing higher molecular weight substances (such as R-32, R-134a, Toluene, Dimethyl ether…) is investigated. In this study, thermodynamic analyses of CO_2 system by adding R-32 and toluene are conducted. To ensure the thermal stability of additive substances, the maximum temperature of the system was restricted to 150℃, 300 ℃ respectively. At each maximum temperature condition, R-32 case showed 0.46%p increase in thermal efficiency and toluene case showed 5.2%p increase in efficiency compared to the pure CO_2 system.

Also the experimental test of R-32 case is conducted to show the technical feasibility of the suggested CO_2 based binary mixture power cycle. As expected, the compressor pressure ratio of mixture cases are increased while maintaining the same operating temperature, pressure and mass flowrate conditions to the pure CO_2 cases. The 1~2% increase of pressure ratio was caused by 10~40% increase of compressor inlet density. And it was confirmed that the result has a similar tendency to the results for the high density pure CO_2 cases.

Through a simple compressor performance test, uncertainties of the mixture property were indirectly evaluated near the mixture critical point. The authors concluded that the binary mixtures such as CO_2+R-32 and CO_2+toluene can potentially improve the cycle efficiency by moving critical point of the pure CO_2 system. Also it is expected that, the lowering minimum temperature can further increase the efficiency due to the liquid state compression and maximizing pressure ratio. However, it was noted that the optimum additive substances or composition of addition can be varied depending on the minimum temperature or operating conditions. The detailed study on designing binary mixture system will be conducted next.

Further studies will be carried out on the reduction of exergy destruction with temperature gliding in binary mixture condensation and improvement of cycle operation by utilizing equilibrium conditions. Furthermore, the economic analysis of binary mixture system application will be followed.

NOMENCLATURE

CO_2 : Carbon dioxide
N_2 : Nitrogen
O_2 : Oxygen
DME : Dimethyl ether
SF_6 : Sulfur hexafluoride
R-### : Refrigerant
ORC : Organic Rankine Cycle
NIST : National Institute of Standards and Technology
T_c [℃] : Critical temperature
P_c [MPa] : Critical pressure
D_c [kg/m^3] : Density at critical point
$\left.\frac{\partial h}{\partial P}\right|_s$ [kJ/kg MPa] : Isentropic enthalpy difference index
η_{th} [%] : The 1st law thermal efficiency

REFERENCES

[1] Dostál, V., M. J. Driscoll, and P. Hejzlar. "A Supercritical Carbon Dioxide Cycle for Next Generation Nuclear Reactors. 2004." Massachusetts Institute of Technology.

[2] Ahn, Yoonhan, et al. "The design study of supercritical carbon dioxide integral experiment loop." ASME Turbo Expo 2013: Turbine Technical Conference and Exposition. American Society of Mechanical Engineers, 2013.

[3] Sarkar, Jahar. "Second law analysis of supercritical CO2 recompression Brayton cycle." Energy 34.9 (2009): 1172-1178.

[4] Jeong, Woo Seok, Jeong Ik Lee, and Yong Hoon Jeong. "Potential improvements of supercritical recompression CO2 Brayton cycle by mixing other gases for power conversion system of a SFR." Nuclear Engineering and Design 241.6 (2011): 2128-2137.

[5] Vesely, Ladislav, and Vaclav Dostal. "Research on the Effect of the Pinch Point Shift in Cycles with Supercritical Carbon Dioxide." The 4th International Symposium-Supercritical CO2 Power Cycles. 2014.

[6] Yin, Hebi, et al. "Mixtures of SF6–CO2 as working fluids for geothermal power plants." Applied energy 106 (2013): 243-253.

[7] Sabau, Adrian S., et al. "Mixtures of CO2-SF6 as working fluids for geothermal plants." ASME 2011 International Mechanical Engineering Congress and Exposition. American Society of Mechanical Engineers, 2011.

[8] Hu, Lian, et al. "Investigation on the performance of the supercritical Brayton cycle with CO2-based binary mixture as working fluid for an energy transportation system of a nuclear reactor." Energy 89 (2015): 874-886.

[9] Wu, Chuang, et al. "Thermodynamic analysis and performance optimization of transcritical power cycles using CO2-based binary zeotropic mixtures as working fluids for geothermal power plants." Applied Thermal Engineering 115 (2017): 292-304.

[10] Cengel, Yunus A., and Michael A. Boles. "Thermodynamics: an engineering approach." Sea 1000 (2002): 8862.

[11] Papon, Pierre, Jacques Leblond, and Paul HE Meijer. Physics of Phase Transitions. Berlin Heidelberg, Germany: Springer-Verlag, 2002.

[12] Lemmon, Eric W., Marcia L. Huber, and Mark O. McLinden. "NIST reference fluid thermodynamic and transport properties—REFPROP." NIST standard reference database 23 (2002): v7.

[13] Lemmon, Eric W., and Richard T. Jacobsen. "Equations of state for mixtures of R-32, R-125, R-134a, R-143a, and R-152a." Journal of physical and chemical reference data 33.2 (2004): 593-620..

[14] Baik, Seungjoon, et al. "Preliminary study of supercritical CO2 mixed with gases for power cycle in worm environments." ASME Turbo Expo 2018: Turbine Technical Conference and Exposition. American Society of Mechanical Engineers, 2018.

[15] Afroz, Hasan MM, and Akio Miyara. "Binary mixtures of carbon dioxide and dimethyl ether as alternative refrigerants and their vapor-liquid equilibrium data predicti." International Journal of Engineering, Science and Technology 3.1 (2011).

[16] Lewis, Tom Goslee, Thomas M. Conboy, and Steven A. Wright. Supercritical CO2 mixture behavior for advanced power cycles and applications. No. SAND2011-2691C. Sandia National Lab.(SNL-NM), Albuquerque, NM (United States), 2011.

[17] Lai, Ngoc Anh, Martin Wendland, and Johann Fischer. "Working fluids for high-temperature organic Rankine cycles." Energy 36.1 (2011): 199-211.

[18] Wang, Weizong, et al. "Fundamental properties of high-temperature SF6 mixed with CO2 as a replacement for SF6 in

high-voltage circuit breakers." Journal of Physics D: Applied Physics 47.25 (2014): 255201.
[19] Stein, Fred Paul, and Robert A. Adams. "Vapor-liquid equilibriums for carbon dioxide-difluoromethane system." Journal of Chemical & Engineering Data 16.2 (1971): 146-149.
[20] Ng, Heng-Joo, and Donald B. Robinson. "Equilibrium-phase properties of the toluene-carbon dioxide system." Journal of Chemical and Engineering data 23.4 (1978): 325-327.
[21] Zhang, Haifei, Zhimin Liu, and Buxing Han. "Critical points and phase behavior of toluene-CO2 and toluene-H2-CO2 mixture in CO2-rich region." The Journal of Supercritical Fluids 18.3 (2000): 185-192.
[22] Ahn, Yoonhan, et al. "Review of supercritical CO2 power cycle technology and current status of research and development." Nuclear Engineering and Technology 47.6 (2015): 647-661.
[23] Baik, Seungjoon, et al. "Study on CO2dy on CO2O2 CO2ycle design and transient analysis for Sodium-cooled fast rea$_2$ phases for S-CO_2 power cycle application." Applied Thermal Engineering 113 (2017): 1536-1546.
[24] Baik, Seungjoon, et al. "Preliminary Experimental Study of Precooler in Supercritical CO2 Brayton Cycle." ASME Turbo Expo 2015: Turbine Technical Conference and Exposition. American Society of Mechanical Engineers, 2015.

ANNEX A

Substance	**Molar mass** [kg/kmol]	**T_c** [℃]	**P_c** [MPa]	**D_c** [kg/m^3]	**A Compressor inlet density** [kg/m^3]	**B Compressor inlet** $\left.\frac{\partial h}{\partial P}\right\|_s$ [kJ/kg MPa]	**C Turbine inlet** $\left.\frac{\partial h}{\partial P}\right\|_s$ [kJ/kg MPa]	**A ÷ B × C** [kg/m^3]
CO_2	44.0	31.0	7.377	467.6	573.2	1.74	5.21	1711.9
R-11	137.4	198.0	4.408	554.0	1481.6	0.675	1.191	2613.7
R-12	120.9	112.0	4.136	565.0	1328.6	0.753	1.662	2933.4
R-13	104.5	28.9	3.879	582.9	1003.5	0.997	2.296	2312.2
R-14	88.0	-45.6	3.750	625.7	335.3	2.983	2.976	334.5
R-21	102.9	178.3	5.181	526.0	1372.4	0.729	1.530	2881.9
R-22	86.5	96.1	4.990	523.8	1203.9	0.831	2.358	3417.3
R-23	70.0	26.1	4.832	526.5	844.1	1.185	3.316	2362.6
R-32	**52.0**	**78.1**	**5.782**	**424.0**	**970.4**	**1.031**	**3.949**	**3718.4**
R-41	34.0	44.1	5.897	316.5	588.8	1.698	6.295	2182.8
R-113	187.4	214.1	3.392	560.0	1569.1	0.637	1.006	2478.0
R-114	170.9	145.7	3.257	580.0	1468.0	0.681	1.240	2672.1
R-115	154.5	80.0	3.129	614.8	1325.7	0.754	1.547	2718.3
R-116	138.0	19.9	3.048	613.3	1047.3	0.955	1.897	2081.0
R-123	152.9	183.7	3.662	550.0	1469.6	0.680	1.203	2597.6
R-124	136.5	122.3	3.624	560.0	1370.3	0.730	1.542	2895.4
R-125	120.0	66.0	3.618	573.6	1230.5	0.813	1.963	2972.8
R-134a	**102.0**	**101.1**	**4.059**	**511.9**	**1222.0**	**0.818**	**2.071**	**3092.8**
R-141b	116.9	204.4	4.212	458.6	1237.5	0.808	1.398	2140.7
R-142b	100.5	137.1	4.055	446.0	1120.5	0.892	1.877	2356.4
R-143a	84.0	72.7	3.761	431.0	959.4	1.042	2.587	2382.0
R-152a	66.1	113.3	4.517	368.0	908.5	1.101	2.911	2402.6
R-218	188.0	71.9	2.640	628.0	1379.8	0.725	1.404	2673.1
R-227ea	170.0	101.8	2.925	594.3	1413.6	0.707	1.417	2830.9
R-236fa	152.0	124.9	3.200	551.3	1374.0	0.728	1.457	2750.2
R-245fa	134.0	154.0	3.651	516.1	1344.7	0.744	1.491	2695.8
R-365mfc	148.1	186.9	3.266	473.8	1262.3	0.792	1.371	2185.3
R-1216	150.0	85.8	3.150	583.4	1345.5	0.743	1.613	2919.7
R-1233zd	130.5	165.6	3.573	478.9	1269.7	0.788	1.481	2387.6
R-1234yf	114.0	94.7	3.382	475.6	1115.0	0.897	1.956	2431.3
R-1234ze	114.0	109.4	3.635	489.2	1177.6	0.849	1.912	2651.5
RC-318	200.0	115.2	2.778	620.0	1521.3	0.657	1.240	2869.0
RE-245cb2	150.0	133.7	2.886	499.5	1281.7	0.780	1.469	2413.9
RE-245fa2	150.0	171.7	3.433	515.0	1390.5	0.719	1.339	2588.8
RE-347mcc	200.1	164.6	2.476	524.1	1416.4	0.706	1.181	2369.1
DME	**46.1**	**127.2**	**5.337**	**273.6**	**665.4**	**1.503**	**3.973**	**1759.2**
Propane	**44.1**	**96.7**	**4.251**	**220.5**	**501.3**	**1.995**	**4.668**	**1173.1**
Benzene	78.1	288.9	4.907	304.7	873.5	1.145	1.682	1283.7
Toluene	**92.1**	**318.6**	**4.126**	**292.0**	**862.5**	**1.159**	**1.608**	**1196.4**
MM	162.4	245.5	1.939	304.4	766.4	1.305	1.738	1021.0
MDM	236.5	290.9	1.415	256.7	823.0	1.215	1.603	1085.5
SF_6	**146.1**	**45.6**	**3.755**	**742.3**	**1432.6**	**0.698**	**1.650**	**3386.5**

ANNEX B

Table B. S-CO_2PE pure CO_2 test cases and inlet fluid property

Test case	**Temperature** [℃]	**Pressure** [MPa]	**Density** [kg/m^3]	**Speed of sound** [m/s]	**Comp. Factor** [-]
1	27.0	8.44	765	361	0.19
2	25.6	7.84	765	355	0.18
3	26.0	7.30	739	320	0.17
4	31.1	8.44	705	302	0.21
5	29.2	7.84	708	297	0.19
6	29.0	7.30	671	253	0.19
7	33.0	8.44	665	269	0.22
8	33.0	7.80	548	189	0.25
9	31.0	7.38	533	144	0.24
10	37.0	8.45	482	193	0.30
11	39.3	8.44	358	197	0.40
12	40.1	8.20	302	203	0.46
13	37.0	7.80	289	199	0.46
14	33.0	7.45	299	191	0.43
15	40.1	7.80	257	208	0.51
16	37.3	7.39	239	208	0.53

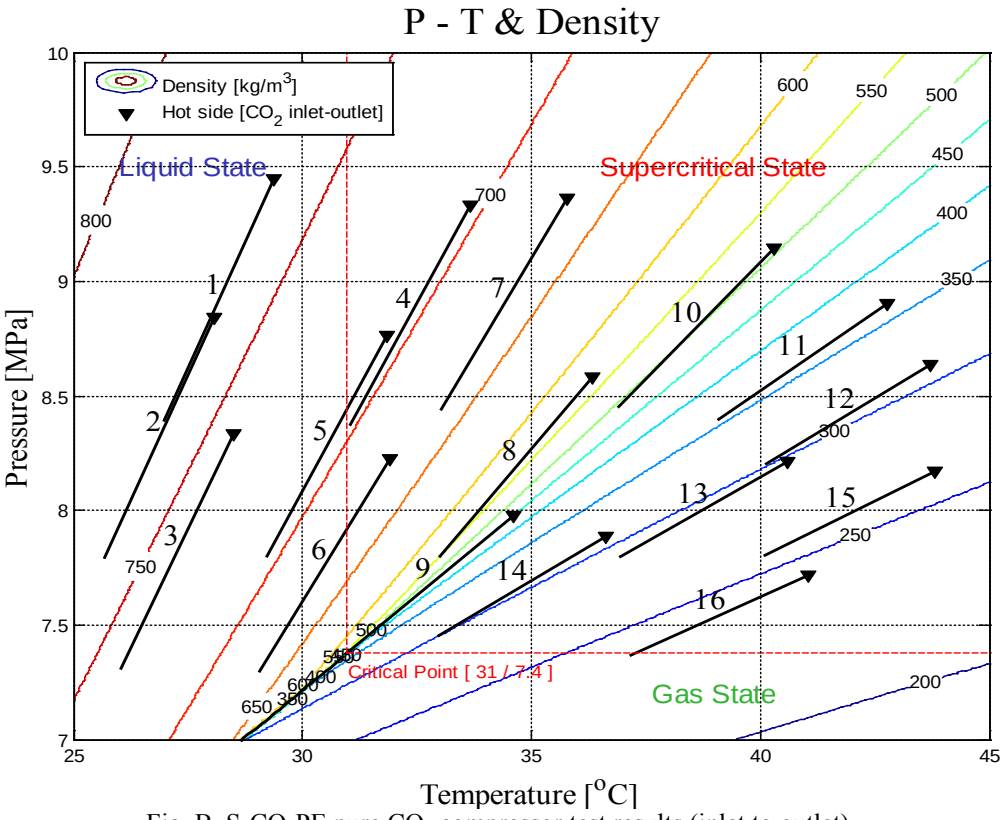

Fig. B. S-CO_2PE pure CO_2 compressor test results (inlet to outlet)

2nd European supercritical CO2 Conference
August 30-31, 2018, Essen, Germany

2018-sCO2.eu-126

INVESTIGATING THE HEAT TRANSFER CHARACTERISTICS OF SUPERCRITICAL HFC-125 IN LOW-TEMPERATURE ORGANIC RANKINE CYCLES

Marija Lazova*
Research fellow
Ghent, Belgium
Email: marija.lazova@ugent.be

Michel De Paepe
Professor, PhD
Ghent, Belgium

ABSTRACT

Investigating the heat transfer phenomena of fluids at supercritical pressures started in the first half of the 20th century, for either cooling or heating applications. Several fluids (water, CO_2, helium) were tested under various conditions and configurations. For instance, CO_2 was at first used as a model fluid due to its beneficial thermophysical properties and lower critical pressure and temperature (74 bar and 31°C) compared to water. Today, the supercritical CO_2 is used as working fluid in many applications. However, in the literature there is a lack of data related to heat transfer at supercritical pressures to organic fluids in large tube diameters conducted under organic Rankine cycle (ORC) conditions. Therefore, the aim of this study is experimentally to determine the heat transfer characteristics of the fluid HFC-125 in horizontal flow and inner tube diameter of 24.8 mm. The favorable thermophysical properties and the low critical pressure and temperature (36 bar and 66°C) make HFC-125 suitable working fluid for low-temperature (~100°C) transcritical ORC technology. During the measurements the pressure was in the range of 38-55 bar, the heat flux 8-30 kW/m^2 and the mass flow rate of the working fluid 0.2-0.3 kg/s. The test section has a counter-flow tube-in-tube configuration with a total length of 4 m. The results show that the effects of the flow acceleration during heating process have an influence to the heat transfer rate. Furthermore, the local wall temperatures vary non-linearly, which is considerably dominant in the vicinity of the critical point of HFC-125. For determining the buoyancy effect a criterion proposed in the literature was used. It was found out that at low heat flux the buoyancy effect is less dominant. In horizontal flow the impact of the buoyancy effect strongly influences the heat transfer rate and the heat transfer regime occurring at these conditions should be studied.

INTRODUCTION

Utilization of low-temperature heat from renewable energy sources and industrial waste heat is attracting a lot of attention in the last years. The organic Rankine cycle (ORC) is one of the technologies that is used for conversion of the low-temperature heat sources into useful power. Usually the low-grade heat sources are not with constant properties (temperature, pressure, mass flow rate), which is one of the obstacles for the evaporator's operation at subcritical conditions and for maximizing the power output. However, the transcritical ORC has a higher potential, because the working fluid temperature transition is above the critical point which allows a better temperature profile match with the heat source temperature glide. The transcritical ORC cycles are mostly studied for utilizing low-temperature heat sources [1–3]. However, the ORC cycle power output depends from the design and selection of proper components, choice of appropriate working fluids [4], the temperature and the stability of the heat source etc. There are several studies related to transcritical ORC's, that use CO_2 as working fluid. Chen et.al [1] did a comparative study of transcritical CO_2 and HFC-123, with respect to convert energy from low-temperature waste heat into usable work. The results show that CO_2 power cycle has slightly higher power output. Other studies [3] [5] do an experimental validation of using CO_2 as working fluid in solar (transcritical) organic Rankine cycles. Cayer et. al reported that HFC-125 and ethane are beneficial fluids that can be used in low-temperature transcritical ORC's. In several comparative studies [4–8], HFC-125 is tested with many other organic fluids including CO_2 for low-temperature (~100°C) power generation in a transcritical ORC. Due to the lower critical pressure the required pumping power is lower compared to the other fluids and HFC-125 is considered as potential medium.

DOI: 10.17185/duepublico/46097

HFC-125 has beneficial thermophysical properties and low critical pressure and temperature (36.2 bar and 66°C).

Furthermore, experimental studies related to heat transfer to supercritical CO_2 for solar transcritical ORC are conducted by Niu et. al [10]. The results show that when CO_2 is near the critical region it has a significant effect on the heat transfer behavior. Moreover, there are several other organic fluids that have been tested (HFC134a, R-404A, R-410A, HCFC-22) under supercritical conditions in either heating or cooling applications as well. Garimella et al. [11] performed experimental investigation regarding supercritical heat transfer to the organic fluids R-404A and R-410A in a horizontal flow and in cooling applications. In his work small diameter tubes in the range between 0.76–3.05 mm were tested. A heat transfer correlation is applicable for pressure 1.0 < pcr < 1.2 was also proposed. An experimental heat transfer investigation of HFC-134a at supercritical pressure between 45–55 bar in cooling application was done by Zhao and Jiang [12]. The inner diameter of the stainless steel tube is 4.01 mm. The tests were done at different mass fluxes and a new correlation is proposed based on the measured data. Furthermore, an experimental investigation of the heat transfer characteristics of HFCF-22 and ethanol in small vertical tubes was done by Jiang et. al [13]. From the results it was concluded that the frictional pressure drop is more significant for HFC-22 than for ethanol, while the local heat transfer coefficient increases as the enthalpy increases for both fluids.

Typical for all fluids at supercritical pressure especially near the critical pressure is the strong variation of the thermophysical properties. Due to a large compressibility and density inhomogeneity the fluid induces strong convective flows within a slight temperature changes. The specific heat capacity reaches a peak at the pseudo-critical temperature T_{pc} and apart from the density the viscosity and the thermal conductivity vary significantly within a small temperature range as well. These changes are presented in Figure 1.

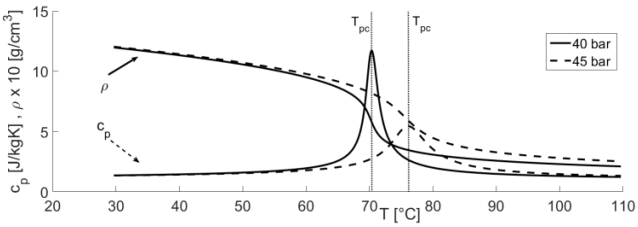

Figure 1: thermophysical property variation of HFC-125.

In order to have optimal operating ORC conditions in the heat exchanger at the hot side it is necessary to determine the behavior of the working fluid at supercritical state in horizontal flow and large tube diameter. Therefore, the main objective of this study is to determine the heat transfer characteristics of HFC-125 at supercritical pressures.

EXPERIMENTAL FACILITY "ISCORE"

An experimental facility "iSCORe" is built at the Ghent University and it consists of a heating loop, a cooling loop and an experimental loop.

A thermal oil heater Vulcanic is part of the heating loop and is depicted with a red line. The heater has a power of 20 kW and is used for providing a heating fluid (synthetic oil) to the test section.

In order to control the temperature of the cold source which is a mixture of water/glycol, a chiller with capacity of 37 kW is used. A 3-way mixing valve is installed in front of the condenser (plate heat exchanger) to control the mass flow rate of the cooling fluid. The sub-cooled working fluid HFC-125 is then provided to the circulation pump.

The experimental loop represents a transcritical organic Rankine cycle (ORC) and is depicted with a green line. This cycle consists of four basic components a pump, two heat exchangers (at the hot and cold side) and an expansion valve. The basic layout of the cycle (experimental facility) is represented in Figure 2a with a corresponding T-s diagram Figure 2b.

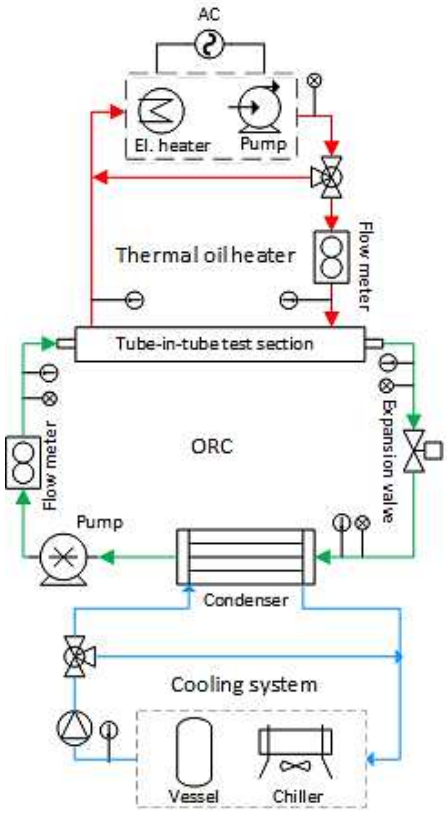

Figure 2a: layout of the experimental facility "iSCORe".

A volumetric (positive displacement) pump (Hydra-cell, G15) is used for circulation of the working fluid HFC-125 and

DOI: 10.17185/duepublico/46097

is controlled by a frequency controller. The working fluid is first pressurized above its critical pressure (1-2) and heated up in the heat exchanger (test section) (2-3). The test section is positioned horizontally and is equipped with pressure and temperature sensors. In the installation there are two tube-in-tube preheaters and one in-line electrical preheater with a capacity of 10kW.

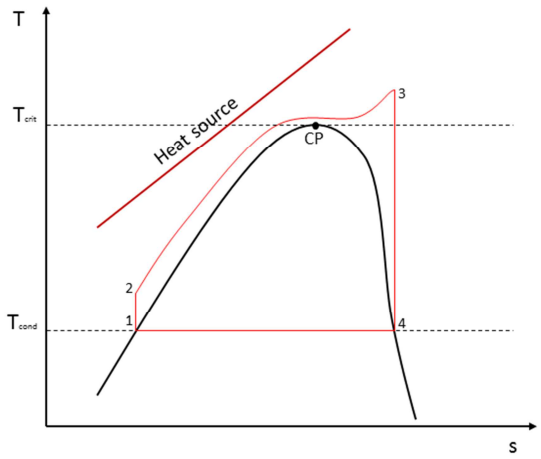

Figure 2b: temperature-entropy T-s diagram.

The tube-in-tube preheaters can be by-passed or used if there is a need. However, the inlet temperature of HFC-125 is controlled by the electrical in-line heater. An expansion valve is used to expand the working fluid (3-4). The working fluid is sub-cooled in the cooling loop (4-1) with which the cycle closes and repeats again. The process is depicted in the T-s diagram. Furthermore, Coriolis mass flow meters (GE, RHM12 and RHM20) are used to measure accurately the mass flow rate of the working and heating fluid respectively.

TEST SECTION

The test section has a configuration of a tube-in-tube heat exchanger which is positioned horizontally and is equipped with a number of sensors. A basic layout of the test section is presented on Figure 3.

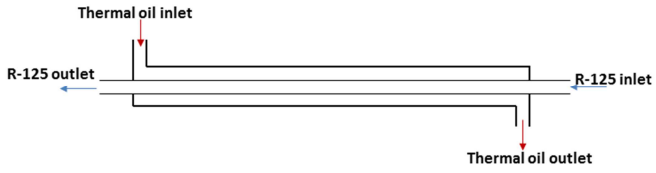

Figure 3: test section layout.

The working fluid HFC-125 circulates in the inner tube and the heating fluid (thermal oil) flows in the annulus. The inner tube is made out of a copper tube with the following dimensions: outer diameter of 28.58 mm, thickness of 1.9 mm and heating length of 4 m (L/Di=162). An unheated adiabatic test section with a length of 1 m is connected to the test section in order to provide fully-developed flow in the test section. The complete installation is insulated in order to reduce the heat losses to the environment. The temperatures at the inlet and the outlet of the test section are measured by four Pt100's. The pressure over the test section is measured by two pressure transducers. In this work, the results from the temperature and pressure measurements obtained at the inlet and outlet of the test section are reported. All signals are collected by a data acquisition system.

DETERMINING THE HEAT TRANSFER COEFFICIENT

The energy balance over the test section is determined by employing the following equations Eq. (1) and Eq. (2).

$$\dot{Q} = \dot{m}_{hf} \cdot c_p (T_{hf,in} - T_{hf,out}) \tag{1}$$

$$\dot{Q} = \dot{m}_{wf} (h_{wf,out} - h_{wf,in}) \tag{2}$$

$\dot{Q}$ is the heat transfer rate, $\dot{m}_{hf}$, and $\dot{m}_{wf}$ are the mass flow rates of the heating and working fluid respectively. The enthalpy changes of the working fluid at the inlet/outlet of the heat exchanger (test section) are given with $h_{wf,in}$ and $h_{wf,out}$. $T_{hf,in}$ and $T_{hf,out}$ are the temperature changes over the test section at the heating fluid side. The c_p is the specific heat capacity of the heating fluid.

The overall heat transfer coefficient U is determined from Eq. (3)

$$Q = U \cdot A \cdot LMTD \tag{3}$$

where A is the total surface area and $LMTD$ (logarithmic mean temperature difference) is calculated with Eq. (4)

$$LMTD = \frac{(T_{hf,in} - T_{wf,out}) - (T_{hf,out} - T_{wf,in})}{ln\left(\frac{T_{hf,in} - T_{wf,out}}{T_{hf,out} - T_{wf,in}}\right)} \tag{4}$$

In order to determine the wall temperatures T_w, $T_{w,o}$ and $T_{w,i}$ at the outer and inner wall of the central tube the following equations were applied:

$$q = htc_o (T_{hf,b} - T_{w,o}) \tag{5}$$

$$q = htc_i (T_{w,i} - T_{wf,b}) \frac{d_i}{d_o} \tag{6}$$

$$T_w = \frac{T_{w,o} + T_{w,i}}{2} \tag{7}$$

In order to determine the Nusselt Nu number of the working fluid, Eq. (8) and (9) were used

$$\frac{1}{UA} = \frac{1}{htc_o A_o} + \frac{\ln(d_o/d_i)}{2\pi\kappa L} + \frac{1}{htc_i A_i} \tag{8}$$

$$Nu = \frac{htc_i \cdot d_{wf,hyd}}{\lambda_{wf,b}} \tag{9}$$

DOI: 10.17185/duepublico/46097

For calculating the annular convective heat transfer coefficient htc_o the heat transfer correlation of Dirker and Meyer [14] was used and is given with Eq. (10)

$$Nu = 0.01069 Re^{0.879} Pr^{1/3} \quad (10)$$

ERROR ANALYSIS

An overview of the experimental uncertainties is presented with Table 1.

Table 1. An overview of the corresponding experimental uncertainties.

Parameter	Range	Relative error (%)
Heat input	5–10 kW	2.62
Pressure	37.5–46 bar	1.5
Temperature	45–100 °C	3.71
Mass flow rate	0.2–2.1 kg/s	2.00

However, it is important to be mentioned that the energy balance deviated less than 5% when the working fluid was away from the (super) critical region. In contrary at near and supercritical operating conditions there was a larger deviation (20%) mainly because of the enthalpy's uncertainties at this state. For determining the property changes Coolprop was used which has employed the correlations of Bell et.al [15]. Uncertainties of the Nusselt number of 9% up to 25% are found from the measurements at supercritical conditions with an average deviation of 12.7%. The mean uncertainty on the resulting overall heat transfer coefficient is 11.9%.

RESULTS AND DISCUSSION

The thermo-physical properties of the working fluid at supercritical pressures strongly depend on the changes at the bulk fluid and wall temperature. Heat transfer deterioration occurs when the bulk temperature of the working fluid is below the pseudo-critical temperature and the wall temperature significantly exceeds the pseudo-critical temperature. According to the results from the measurements, the wall temperature is higher than the bulk fluid temperature of the working fluid.

INFLUENCE OF THE WALL TEMPERATURE TO THE CONVECTIVE HEAT TRANSFER COEFFICIENTS AT VARIOUS HEAT FLUXES

The variation of the convective heat transfer coefficients HTC and the wall temperature with the global enthalpy of the working fluid at the outlet of the heat exchanger at different global heat fluxes and at mass flux of 395 kg/m^{2}s is presented in Fig.4 (a) and (b). At lower enthalpies and lower heat fluxes (9 kW/m^2; 12 kW/m^2) the wall temperature variation determined from Eq's (5-7) from the measurements at the inlet and at the outlet of the test section is not very significant Fig.4 (b). However, the heat transfer coefficients at these heat fluxes are higher which shows that the there is a better heat transfer between the tube wall of the heating fluid and the working fluid. At higher heat fluxes (19 kW/m^2; 22 kW/m^2) the enthalpy rise yields to increased wall temperatures as well. The density and the viscosity of HFC-125 decrease at higher wall temperatures which is especially dominant near the tube wall. This results in lower heat transfer coefficients which are depicted on Fig.4 (a).

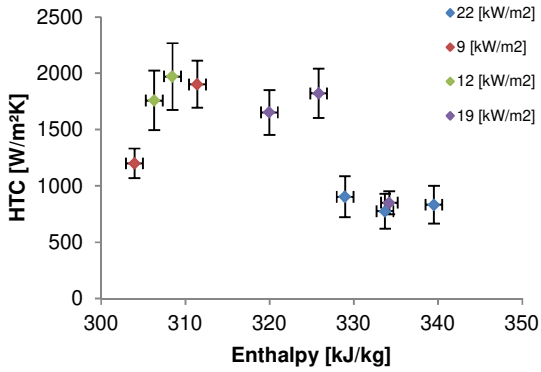

Figure 4a: heat transfer coefficients HTC variations at different heat fluxes and mass flux of 395 kg/m^{2}s.

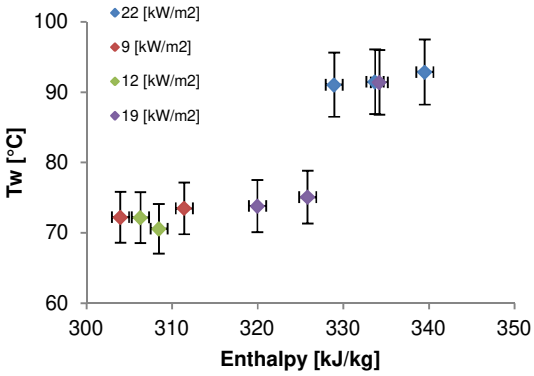

Figure 4b: wall temperatures variations at different heat fluxes and mass flux of 395 kg/m^{2}s.

Similar effects are observed at mass fluxes in the range of 520-625 kg/m^{2}s.

COMPARISON OF THE HEAT TRANSFER COEFFICIENTS WITH DIFFERENT HEATING FLUID TEMPERATURES AND THE RESPECTIVE BULK AND WALL TEMPERATURES

The heat transfer characteristics of a fluid at supercritical pressures differ significantly because of the thermo-physical property variation occurring at these conditions (above critical pressure and temperature). The density and viscosity changes of the fluid with the temperature have a significant influence on the heat transfer coefficients. Furthermore, Fig. 5 (a) and (b) gives an overview of the convective heat transfer coefficients HTC variations with the bulk fluid temperature T_b of HFC-125 and the wall temperature T_w. Higher heat transfer coefficients

DOI: 10.17185/duepublico/46097

are observed at heating fluid temperatures of 80-90°C. At these operating conditions the difference between the bulk temperature of HFC-125 and the wall temperature T_w is in the range of 8-15°C (Fig.5 (b)). At higher heating fluid temperatures of 100°C the wall temperature is higher and the temperature difference with the bulk fluid temperature is larger which can be observed on Fig. 5 (a and b). According to the results from the measurements the temperature difference is in the range of 25-35°C and these results in lower heat transfer coefficients.

However, the thermo-physical property variations of the fluid in radial direction of the tube are important which indicates that the effect of the wall temperature to the heat transfer coefficient is very significant.

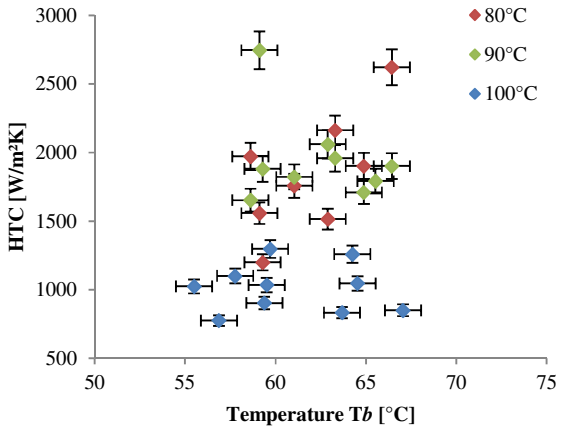

Figure 5a: evaluating the effects of the bulk temperatures to the heat transfer coefficients.

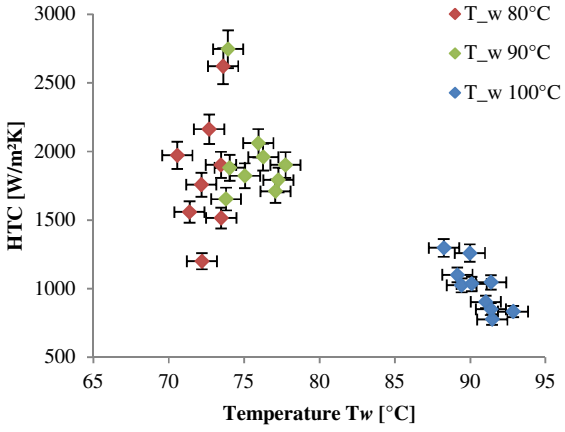

Figure 5b: evaluating the effects of the wall temperatures to the heat transfer coefficients.

DETERMINING THE EFFECTS OF THE WALL TEMPERATURE TO THE DETERIORATED HEAT TRANSFER

Determining if the effect of the heat transfer deterioration will occur at these operating conditions is of great importance. This heat transfer phenomenon (DHT) appears when there is a large increase of the tube wall temperature. An estimation of the wall heat flux at which the deteriorated heat transfer phenomena occur is presented with the Eq. (11) which is proposed by Styriakovich et al. [16]

$$q_{DHT} = 580G\ [W/m^2] \qquad (11)$$

where q is the heat flux at which the DHT appears and G is the mass flux of the working fluid which was developed for water in Eq. (11). During the measurements the mass flux was in the range of 395-625 kg/m^{2}s. According to results calculated with the Eq. (11) the heat flux at which DHT is expected to appear is in the range of 230-360 kW/m^2.

The heat flux obtained from the measurements at the temperatures of the heating fluid in the range of 80-100°C is significantly lower than the maximum heat flux determined by Eq. (11). From the calculations it can be observed that the experimental heat flux is in the range of 9–30 kW/m^2. This shows that a deteriorated heat transfer is not likely to occur at these operating conditions.

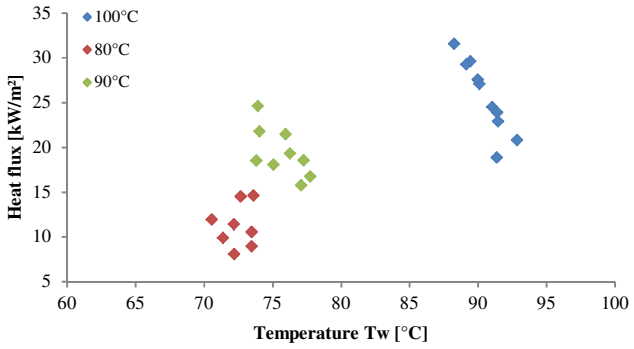

Figure 6: Determining the effects of the wall temperature to the heat flux.

However, as part of the future work is obtaining local heat transfer measurements and analyzing this phenomenon in detail for the particular working fluid and operating conditions.

CONCLUSION

In this article, preliminary results from the forced convection heat transfer measurements at supercritical state, done on the new test set-up are reported. Low-temperature heating fluid in the range of 80°C-100°C was utilized during the measurements. The presented results are all conducted by ensuring supercritical heat transfer at the working fluid side. At higher

DOI: 10.17185/duepublico/46097

mass flow rates the convective heat transfer coefficients reach highest values. However, at supercritical pressure and bulk fluid temperatures close to the pseudo-critical temperature there is a peak of the heat transfer coefficient. Determining the wall effects on the heat transfer mechanisms is also reported where the conclusion is that occurrence of "pseudo-critical" heat flux and hence deteriorated heat transfer is not likely to occur at these operating conditions.

A next step of this research is obtaining local heat transfer measurements and deriving a new heat transfer correlation.

NOMENCLATURE

A	total heat transfer area [m^2]
c_p	specific heat capacity [J/kg K)]
d	tube diameter [mm]
D	shell diameter [mm]
f	friction factor [-]
G	mass flux [kg/m^2s]
htc	heat transfer coefficient [W/m^2K]
h	enthalpy [kJ/kg]
L	length [m]
$\dot{m}$	mass flow rate [kg/s]
p	pressure [bar]
T	temperature [°C]
q	heat flux [W/m^2]
Q	heat transfer rate [kW_{th}]
U	overall heat transfer coefficient [W/m^2K]

Dimensionless numbers

Nu	Nusselt number
Re	Reynolds number
Pr	Prandtl number

Greek letters

Δ	difference
λ	thermal conductivity of the fluid [W/mK]
κ	thermal conductivity of the material [W/mK]
μ	viscosity [kg/ms]
ρ	density [kg/m^3]

Subscripts

a	acceleration
ad	adiabatic
b	bulk
cr	critical
hyd	hydraulic
f	fouling
i	inner
o	outer
in	inlet conditions
out	outlet conditions
wf	working fluid
hf	heating fluid
exp	experimental
ov	overall
w	wall

ACKNOWLEDGEMENTS

The results presented in this paper have been obtained within the frame of the IWT SBO-110006 project The Next Generation Organic Rankine Cycles (www.orcnext.be), funded by the Institute for the Promotion and Innovation by Science and Technology in Flanders. This financial support is gratefully acknowledged.

REFERENCES

[1] Y. Chen, P. Lundqvist, A. Johansson, and P. Platell, "A comparative study of the carbon dioxide transcritical power cycle compared with an organic rankine cycle with R123 as working fluid in waste heat recovery," *Appl. Therm. Eng.*, vol. 26, no. 17–18, pp. 2142–2147, 2006.

[2] Z. Shengjun, W. Huaixin, and G. Tao, "Performance comparison and parametric optimization of subcritical Organic Rankine Cycle (ORC) and transcritical power cycle system for low-temperature geothermal power generation," *Appl. Energy*, vol. 88, no. 8, pp. 2740–2754, 2011.

[3] H. Yamaguchi, X. R. Zhang, K. Fujima, M. Enomoto, and N. Sawada, "Solar energy powered Rankine cycle using supercritical CO2," *Appl. Therm. Eng.*, vol. 26, no. 17–18, pp. 2345–2354, 2006.

[4] B. T. Liu, K. H. Chien, and C. C. Wang, "Effect of working fluids on organic Rankine cycle for waste heat recovery," *Energy*, vol. 29, no. 8, pp. 1207–1217, 2004.

[5] X. R. Zhang, H. Yamaguchi, and D. Uneno, "Experimental study on the performance of solar Rankine system using supercritical CO2," *Renew. Energy*, vol. 32, no. 15, pp. 2617–2628, 2007.

[6] Z. Gu and H. Sato, "Performance of supercritical cycles for geothermal binary design," *Energy Convers. Manag.*, vol. 43, no. 7, pp. 961–971, 2002.

[7] Y. J. Baik, M. Kim, K. C. Chang, and S. J. Kim, "Power-based performance comparison between carbon dioxide and R125 transcritical cycles for a low-grade heat source," *Appl. Energy*, vol. 88, no. 3, pp. 892–898, 2011.

[8] Y. J. Baik, M. Kim, K. C. Chang, Y. S. Lee, and H. K. Yoon, "A comparative study of power optimization in low-temperature geothermal heat source driven R125 transcritical cycle and HFC organic Rankine cycles," *Renew. Energy*, vol. 54, pp. 78–84, 2013.

[9] G. Shu, L. Liu, H. Tian, H. Wei, and X. Xu, "Performance comparison and working fluid analysis of subcritical and transcritical dual-loop organic Rankine cycle (DORC) used in engine waste heat recovery," *Energy Convers. Manag.*, vol. 74, pp. 35–43, 2013.

[10] X. D. Niu, H. Yamaguchi, X. R. Zhang, Y. Iwamoto, and N. Hashitani, "Experimental study of heat transfer characteristics of supercritical CO2fluid in collectors of solar Rankine cycle system," *Appl. Therm. Eng.*, vol. 31, no. 6–7, pp. 1279–1285, 2011.

[11] S. Garimella, B. Mitra, U. C. Andresen, Y. Jiang, and B.

DOI: 10.17185/duepublico/46097

M. Fronk, “Heat transfer and pressure drop during supercritical cooling of HFC refrigerant blends,” *Int. J. Heat Mass Transf.*, vol. 91, pp. 477–493, 2015.

[12] C. R. Zhao and P. X. Jiang, “Experimental study of in-tube cooling heat transfer and pressure drop characteristics of R134a at supercritical pressures,” *Exp. Therm. Fluid Sci.*, vol. 35, no. 7, pp. 1293–1303, 2011.

[13] P. X. Jiang, C. R. Zhao, and B. Liu, “Flow and heat transfer characteristics of r22 and ethanol at supercritical pressures,” *J. Supercrit. Fluids*, vol. 70, pp. 75–89, 2012.

[14] J. Dirker and J. P. Meyer, “Convective heat transfer coefficients in concentric annuli,” *Heat Transf. Eng.*, vol. 26, no. 2, pp. 38–44, 2005.

[15] I. H. Bell, J. Wronski, S. Quoilin, and V. Lemort, “Pure and pseudo-pure fluid thermophysical property evaluation and the open-source thermophysical property library coolprop,” *Ind. Eng. Chem. Res.*, vol. 53, no. 6, pp. 2498–2508, 2014.

[16] M. A. Styriakovich, T. K. Margulova, and Z. L. Miropolskiy, “Problem in the development of designs of supercritical boilers,” *Teploenergetika*, vol. 14, no. 6, pp. 4–7, 1967.

DOI: 10.17185/duepublico/46097